Alma Mater Studiorum – Università di Bologna

DOTTORATO DI RICERCA IN

Ingegneria Civile, Chimica, Ambientale e dei Materiali

Ciclo XXXI

Settore Concorsuale: 09/D2 – Sistemi, Metodi e Tecnologie dell'Ingegneria Chimica e di Processo

Settore Scientifico Disciplinare: ING-IND/24 – PRINCIPI DI INGEGNERIA CHIMICA

Development and Detailed Characterization of Innovative, High-Performance Membrane Materials for CO₂ Capture Processes

Presentata da: Francesco Maria Benedetti

Coordinatore Dottorato

Prof. Luca Vittuari

Supervisore

Prof.ssa Maria Grazia De Angelis

Esame finale anno 2019

To my family:
past, present and future

Development and Detailed Characterization of Innovative, High-Performance Membrane Materials for CO₂ Capture Processes

Abstract

The challenge to mitigate the environmental impact and provide sustainable technologies for gas separation applications is one of the biggest opportunities for fundamental and applied research in chemical engineering. Membrane technologies represent a mature alternative to traditional unit operations such as cryogenic distillation and pressure swing adsorption. For a breakthrough in this field it is essential to develop new materials, which can perform gas and vapor separations in a more efficient way. This work was dedicated to develop and characterize innovative high-performing materials for membrane-based gas separation applications, with particular consideration to CO_2 capture. Composite materials called mixed matrix membranes (MMMs) were obtained by combining poly(2,6-dimethyl-1,4-phenylene oxide) (PPO) and molecular sieves such as Zeolite 3A and ZIF-8. It was possible to tune the separation performance by changing the filler/polymer ratios, enhancing productivity or improving the separation efficiency. For ZIF-8/PPO MMMs, both achievements were obtained, resulting in size-selective membranes with possible application in H_2-purification processes. Mixed-gas sorption experiments were performed in recently developed materials such as PIM-EA-TB, HAB-6FDA polyimide, and its thermally rearranged analogous (*i.e.*, TR450). The goal was to provide a more accurate picture of the membranes performance in more realistic industrial conditions. It was discovered that competition can enhance solubility-selectivity, which in turns controls the separation behavior in

multicomponent conditions over diffusivity-selectivity. This finding provided relevant information for the design of future materials and the further understanding of already characterized ones. A fundamental and systematic approach to the study of CO_2-induced plasticization was carried out on a glassy polyimide, Matrimid®. The findings about the plasticization phenomenon provided awareness on its interpretation and laid the foundation for the prediction of its dependence on operating pressure. It was shown that plasticization pressure changed at different CO_2 downstream pressures. Thus, it is not a property of the material, but rather comes from the contribution of solubility coefficient and diffusivity coefficient, in the framework of the solution-diffusion model. The first specimens of two new families of polymers were developed and investigated: the CANAL ladder polymers, synthesized *via* Catalytic Arene-Norbornene Annulation polymerization, and the ROMP bottlebrush polymers, obtained through Ring-Opening Metathesis Polymerization. The new chemistry allowed the formation of organic materials which were never tested for gas separation applications before. So far ladder polymers were containing Tröger's base- and dioxane-based bridges, the so-called polymers on intrinsic microporosity (PIMs). The CANALs featured norbornyl benzocyclobutene backbone and thereby introduced a third typology of ladder polymers in the gas separation field. The unique purely hydrocarbon and nonpolar rigid backbone of CANALs made them an exceptional model system for fundamental investigations of the structure-property relationships of ladder polymers. The ROMPs have a new architecture made of a flexible backbone which connects rigid ladder side-chains. Ultrahigh CO_2 permeability above 21,000 Barrer was recorded by CF_3-ROMP. All ROMPs revealed to have extremely high plasticization resistance, which made these polymers an interesting new platform for gas separation. Physical aging was monitored with a systematic approach measuring the transport properties and the chain interspacing, and CF_3-ROMP revealed moderate permeability loss over time for smaller gases (*i.e.*, He, H_2). In both classes of new materials, it was revealed that very small changes in functionalities and substituents in the polymer chain affected significantly the transport properties. Therefore, permeability and solubility can be tuned based on the flexibility of the new polymer designs that were developed. Variable-temperature studies were performed at temperatures higher than 35 °C on various materials to allow the evaluation of energetic contributions involved in the separation processes.

9

List of Figures

17

19

20

List of Tables

1. Dissertation Goals

The scope of this dissertation is to study the transport phenomena of small molecules in polymers and membranes for gas separation applications, with particular attention to energy efficiency and environmental sustainability. This work seeks to contribute to the development of new competitive selective materials through the synthesis of novel organic polymers such as CANALs and ROMPs, as well as through the combination of selective materials obtaining MMMs, to make membrane technologies competitive with the traditional ones. Kinetic and thermodynamic aspects of the transport properties were investigated in ideal and non-ideal scenarios, such as mixed-gas experiments. The information we gathered contributed to the development of the fundamental understanding related to phenomenon like CO_2-induced plasticization and physical aging.

1.1. Dissertation Outline

A brief introduction to the concepts of carbon capture and energy efficiency, as well as a conclusion about their challenges, is provided in Chapter 2.

An overview of the current and emerging membrane technologies for carbon capture, hydrogen purification and methane upgrade applications is presented in Chapter 3.

Chapter 4 provides a comprehensive discussion of the theoretical background in the transport of small molecules in dense polymers. The solution-diffusion model[1] is presented, as well as models commonly used to describe the gas sorption in glassy polymeric materials such as the dual-mode sorption (DMS)[2,3] model and the non-equilibrium lattice fluid (NELF)[4] model. The physical aging[5] and plasticization[6] phenomena are also elucidated from the theoretical point of view.

An overview of the experimental methods adopted for collecting the results presented in the dissertation is included in Chapter 5. Membrane preparation techniques, methods to measure permeability, diffusivity and solubility, as well as calorimetric, morphological and analytical techniques are presented.

Chapter 6 focuses on the preparation and characterization of size-selective Mixed Matrix Membranes (MMMs) for H_2 purification and CO_2 removal. The goal of this chapter is to combine commercial materials to improve both permeability and selectivity of the pristine polymers. To accomplish this end, poly(phenylene oxide) (PPO) and two fillers (*i.e.*, Zeolite 3A and a zeolitic imidazole framework, ZIF-8), were mixed to develop composite materials, MMMs, and therefore tailored properties in terms of permeability and selectivity were achieved. The effect of the loading and the temperature were investigated through permeation and sorption experiments.

The solubility of CO_2/CH_4 gas mixtures was studied to investigate the competitive effect upon multicomponent gas sorption and diffusion in membranes[7,8], and is presented in Chapter 7. Different materials were chosen: a polyimide precursor, HAB-6FDA, and its thermally rearranged (TR) derivative TR450[9–11], as well as PIM-EA-TB[12,13]. In addition to measure the deviations from the ideal behavior, the goal was to combine mixed-gas solubility data with mixed-gas permeability data to deduct information on the diffusivity in the multicomponent case.

In Chapter 8 the focus is set on some fundamental aspects of the plasticization phenomenon. The target of this study was to investigate if plasticization represents an intrinsic property of a material or a state of the system, and what is the meaning of the so-called plasticization pressure. To do so, experiments at variable upstream pressure and different downstream pressures, up to 25 bar and 10 bar respectively, were performed on Matrimid®, a glassy polymer known to show plasticization pressure.[14,15]

The goal of Chapter 9 was to expand the structural diversity of microporous ladder polymers such as PIMs[16,17] and explore new strategies to obtain ladder polymers that are able to forms a film. The CANAL polymerization was first reported by Liu *et al.*[18] in 2014, but the gas separation properties of these polymers were not tested due the molecular weight of those species which was too low to form a film (10-40 kDa). The recently optimized polymerization developed in Professor Xia's lab allowed the formation of very high molecular weight polymers. The intention was to investigate the transport properties of unexplored membrane materials. Furthermore, in view of their completely hydrocarbon-based rigid backbone, the goal was to use CANALs as a model system to investigate structure-property correlations. The energetics contributions to the gas transport and sorption, were also studied to

investigate the dual nature of these microporous polymers, being dense polymers but with some microporous material features.

The ROMP polymers presented in Chapter 10, instead, featured a completely new design with flexible backbone and rigid ladder side chains. ROMPs were obtained *via* living polymerization[19] through the procedure recently developed by Zhao and He *et al.*[20]. The focus of this chapter was to show that side chains can induce tunable porosity, revealing ultrapermeable polymers such as CF_3-ROMP. Gas transport properties such as permeability, diffusivity and sorption, as well as aging and plasticization behavior, were studied to a different extent for all the ROMPs, to broadly characterize these new polymers. The studies in Chapters 9 and 10 revel new routes for the preparation of high-performance microporous polymer systems for gas separation. The reason why these new design strategies represent a possible breakthrough in the field of gas separation, is that they are alternative, and highly unexplored, to traditional polymers used or studied so far.

Finally, conclusions and ideas for future research are presented in Chapter 11.

References

[1]   J. G. Wijmans, R. W. Baker, *J. Memb. Sci.* **1995**, *107*, 1.

[2]   W. J. Koros, D. R. Paul, A. A. Rocha, *J. Polym. Sci.* **1976**, *14*, 687.

[3]   D. R. Paul, *J. Polym. Sci. Part A-2 Polym. Phys.* **1969**, *7*, 1811.

[4]   F. Doghieri, G. C. Sarti, *Macromolecules* **1996**, *29*, 7885.

[5]   L. C. E. Struik, *Polym. Eng. Sci.* **1977**, *17*, 165.

[6]   A. Bos, I. G. M. Pünt, M. Wessling, H. Strathmann, *J. Memb. Sci.* **1999**, *155*, 67.

[7]   O. Vopička, M. G. De Angelis, G. C. Sarti, *J. Memb. Sci.* **2014**, *449*, 97.

[8]   O. Vopička, M. G. De Angelis, N. Du, N. Li, M. D. Guiver, G. C. Sarti, *J. Memb. Sci.* **2014**, *459*, 264.

[9]   Z. P. Smith, D. F. Sanders, C. P. Ribeiro, R. Guo, B. D. Freeman, D. R. Paul, J. E. McGrath, S. Swinnea, *J. Memb. Sci.* **2012**, *415–416*, 558.

[10]   D. F. Sanders, Z. P. Smith, C. P. Ribeiro, R. Guo, J. E. McGrath, D. R. Paul, B. D.

Freeman, *J. Memb. Sci.* **2012**, *409–410*, 232.

[11]   K. L. Gleason, Z. P. Smith, Q. Liu, D. R. Paul, B. D. Freeman, *J. Memb. Sci.* **2015**, *475*, 204.

[12]   M. Carta, R. Malpass-Evans, M. Croad, Y. Rogan, J. C. Jansen, P. Bernardo, F. Bazzarelli, N. B. McKeown, *Science (80-.).* **2013**, *339*, 303.

[13]   S. C. Fraga, M. Monteleone, M. Lanč, E. Esposito, A. Fuoco, L. Giorno, K. Pilnáček, K. Friess, M. Carta, N. B. McKeown, P. Izák, Z. Petrusová, J. G. Crespo, C. Brazinha, J. C. Jansen, *J. Memb. Sci.* **2018**, *561*, 39.

[14]   A. Bos, I. G. M. Pünt, M. Wessling, H. Strathmann, *Sep. Purif. Technol.* **1998**, *14*, 27.

[15]   N. R. Horn, D. R. Paul, *Polymer (Guildf).* **2011**, *52*, 1619.

[16]   P. M. Budd, E. S. Elabas, B. S. Ghanem, S. Makhseed, N. B. McKeown, K. J. Msayib, C. E. Tattershall, D. Wang, *Adv. Mater.* **2004**, *16*, 456.

[17]   P. M. Budd, B. S. Ghanem, S. Makhseed, N. B. McKeown, K. J. Msayib, C. E. Tattershall, *Chem. Commun.* **2004**, *4*, 230.

[18]   S. Liu, Z. Jin, Y. C. Teo, Y. Xia, *J. Am. Chem. Soc.* **2014**, *136*, 17434.

[19]   C. W. Bielawski, R. H. Grubbs, *Prog. Polym. Sci.* **2007**, *32*, 1.

[20]   Y. Zhao, Y. He, T. M. Swager, *ACS Macro Lett.* **2018**, *7*, 300.

2. Introduction and Motivations

2.1. Climate Change and CO_2 emission

One of the biggest challenges the modern society is facing nowadays, is to provide energy to more than 7 billion people growing population in a sustainable way, in order to mitigate the impact of the human activity on the Earth. The goal of sustainable development is to meet the needs of people living today without compromising the needs and wellness of future generations. To do this, economic, social and environmental considerations need to be balanced.

The Intergovernmental Panel on Climate Change (IPCC) special report from October 2018, makes it clear that the Earth is warming up faster year after year and "*rapid, far-reaching and unprecedented changes are needed in all areas of society*". The IPCC was invited by the United Nations Framework Convention on Climate Change (UNFCCC) to provide a report on the impacts of global warming of 1.5 °C above pre-industrial levels and related global greenhouse gas emissions pathways. The authors state that if the 1.5-degree target is missed, there is a risk of dramatic consequences for life on earth such as more frequent extreme weather conditions, rising sea levels, the disappearance of the Arctic sea ice and the extinction of lower species. Consequences would be uneven across the globe, and different parts of the world experience impacts differently. For instance, as some places would risk water shortages, others would suffer heavy rainfall events. Therefore, climate change represents an urgent and potentially irreversible threat to human society and is one of the consequences of this intensified energy request.

In recognition of this, the overwhelming majority of countries around the world (around 200 countries) adopted the Paris Agreement[1] in December 2015 in occasion of the United Nations Climate Change conference. The major outcomes of the meeting were to reduce the anthropogenic greenhouse gas emissions and limit global warming to well below 2 °C.

As it can be observed in **Figure 2.1a**, in 2018 human-induced warming has already reached about 1 °C above pre-industrial levels. In fact, if we compare the average temperature of the earth in the pre-

industrial time (1850–1900) to the decade 2006–2015, human activity had warmed the world by 0.87 ± 0.12 °C (**Figure 2.1b**).[2] Assuming the current warming rate continues, it can be determined that the world would reach human–induced global warming of 1.5 °C around 2040.[2]

(a)

(b)
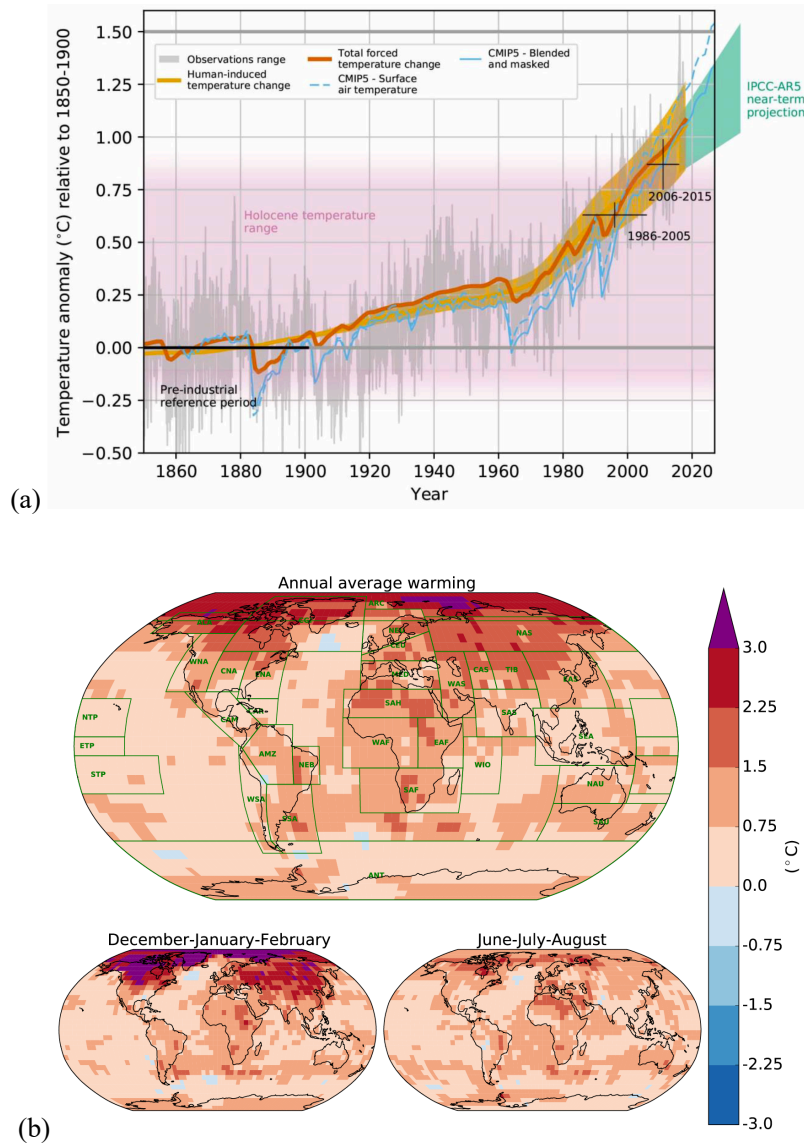
Figure 2.1*: (a) Global Mean Surface Temperature (GMST) over time from the pre-industrial level till today. In yellow, the human-induced contribution, in orange, the total (human + naturally-forced) contribution; (b) Regional warming for the decade 2006-2015, compared to the pre-industrial mean of the 1850-1900 half century. Top view: annual average; bottom view: cold months on the left and hot months on the right.*[2]

There is no definitive way to limit global temperature rise to 1.5 °C above pre-industrial levels, but for sure that the world would need to transform in numerous complex and interconnected ways. *"The coming years are probably the most important in human history"*, states the co-chair of the IPCC Debra Roberts[2], and each of us, from companies to private citizens, could contribute to some extent. In general, lowering as much as possible the energy consumptions would provide access to more possible alternatives to further reduce the impact. However, if we as society use a lot of energy, we also reduce the number of feasible solutions, making technologies that remove carbon dioxide (CO_2) from the atmosphere essential, since its emission directly link to the global warming.[1,3] It is clear that the impact the world will face depends on the specific greenhouse gas emission which, in their turn, will depend on the policies governments and companies adopt.

Anthropogenic emissions of CO_2 can come from many sources, such as combustion of fossil fuels (*e.g.*, coal, natural gas and petroleum), but also biofuels, to produce energy for electricity, industrial processes, and transportation.[4] Chemical and petrochemical industry is responsible for 16% of the total direct CO_2 emission (**Figure 2.2a**).[5] Although it is hard to quantify the global CO_2 emissions, different authors agree that it is above 30 Gt per year (**Figure 2.2b**).[6] According to the US Department of Energy (DOE) Office of Science, in 2007 the global CO_2 emissions reached 37 Gt of CO_2, 85% of which results from energy use.[7] Therefore, the main source of CO_2 emission, one of the most important greenhouse gases, is the power generation sector.[4]

(a)   (b)
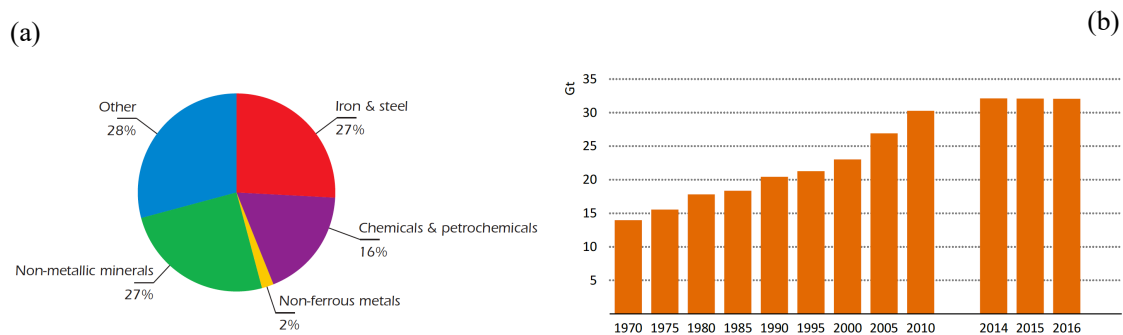
Figure 2.2: (a) CO_2 divided by sectors [5] (b) Global energy-related CO_2 emissions in Gigatonnes (Gt) per year.[6]

2.1.1. Carbon Capture

The expression Carbon Dioxide Removal (CDR) refers to the process of removing CO_2 from the atmosphere. Technologies that remove CO_2 are often described as achieving 'negative emission'. The process is sometimes referred to more broadly as Greenhouse Gas Removal (GGR) if it involves removing gases other than CO_2 such as methane (CH_4) or other hydrocarbons. The implementation of these technologies is considered to be indispensable from the IPCC authors.[2]

CDR technologies are divided into two types. The first one aims to enhance existing natural- or bio-processes that remove carbon from the atmosphere (*e.g.*, by increasing its uptake by trees or soil). The second type is based on the operation of chemical and physical processes to separate CO_2 from gas streams such as diluted emission of a power plant[8–10] and storing it elsewhere (*i.e.*, underground)[11,12], using it to produce other chemicals (*i.e.*, methanol)[13], or using it as a fluid to perform enhanced oil recovery (EOR)[14,15]. All CDR methods are at different stages of development and some are more conceptual than others, as they have not been tested at scale.[16,17]

At the moment, amine absorption is the most mature CO_2 capture technology commercially available. Plants have been built and operate at industrial scale, and more are planned.[18] Mono-, di- and tri-ethanolamine are the most common liquids for acid gas scrubbing because they easily react with CO_2 to separate it from the gas mixture. In a typical configuration, two columns are implemented. In the first column, a gas stream is pressurized and the liquid stream flow counter-currently. The solution absorbs acid components such as CO_2 and H_2S, while heavier hydrocarbons and water are able to be removed from the bottom of the column. This liquid solution is then heated and directed to a stripping column, which operates at lower pressure and higher temperature, thereby the absorbed compounds leave the column from above, while the regenerated solvent is returned to the first absorption column. The main disadvantage is the extremely high energy consumption related to the solvent regeneration at high temperature to remove the CO_2 from the liquid.[8,17,19,20] The regeneration step obtained in a stripping column consumes between 4 and 6 GJ/t_{CO2}, a great energy consumption that needs to be reduced to make

this process economical.[21,22] For these reasons, and because of the high capital and operating costs, the large footprint, the need to handle large amounts of hazardous chemicals as well as the high plant corrosion rate and amine degradation by SO_2, NO_2 and HCl, it is unlike that amine absorption will be widely used as a long-term solution for carbon capture applications.[18] These are motivations that drive the investigation of new technologies to perform the capture of CO_2.

The adsorption in solid porous media is an alternative to absorption. By mean of this technology, gas separation is achieved by the different sorption capacity of the gaseous components in solid.[23,24] A promising adsorbent material should feature good mechanical properties, high selectivity towards CO_2, good adsorption kinetics, thermal stability and large internal surface area.[25] The dimension of the pores is a critical parameter, since it should be designed to allow desired molecules to access the internal structure.[25] Active Carbons (AC) and zeolites were used in industrial applications and designed as fixed-bed columns, in which the gas stream is fed to the porous material, CO_2 is adsorbed into the adsorbent bed and, from the top of the column, the purified gas is recovered.[26] Sorption in porous materials is favored by high pressure and low temperature. As in the case of amine scrubbing, porous materials present the need to be regenerated once the breakthrough limit is reached. Both temperature and pressure can be used to perform the regeneration, thus adsorption technologies are divided in pressure swing adsorption (PSA)[26,27] and temperature swing adsorption (TSA)[28,29], which use lower pressure and higher temperature, respectively, to desorb CO_2. The latter step is usually achieved by hot air or steam that strip the component from the adsorbent. The classic setup of these technologies feature in both processes two columns connected in series to continuously remove CO_2 from the stream. The time required for CO_2 adsorption depends on sorption and desorption kinetics of the gases from the solids, controlling the economic efficiency of the process. To remove undesirable components from the gas mixture, a high affinity of the adsorbent is necessary. On the other hand, the stronger the affinity, the more difficult it is to desorb the gas, and the higher the energy consumption during bed regeneration will be.

Another widely used separation technology is the cryogenic removal of carbon dioxide. Compared to amine scrubbing and absorption techniques, the advantage is that no chemical compound is necessary

to run the process, which operates at atmospheric pressure. On the other hand, the main disadvantage is the low temperature necessary to liquefy CO_2, which makes the operation one of the most energy intensive.[8,17] A typical difficulty encountered in this particular setup is that CO_2 tends to form a solid layer on the surface of the heat exchangers, reducing the heat transfer coefficient and the efficiency of the heat exchange. The necessity to regenerate the apparatus at high temperature, adds yet another cost item.

2.1.2. Energy Efficiency

Figure 2.3: Chemical plant from source[19].

Chemical engineers and industrial chemists devote most of their time investigating efficient ways to separate the components of interest from mixtures of other byproducts.[19] The way these separations are performed impact the quality of products we consume daily, as well as the air we breathe and the water we drink. The traditional unit operations implemented to take care of this industrial aspect such as distillation and absorption, account for the 10-15% of the world energy consumption.[30,31] Nearly half of this energy consumption comes from thermal separation processes that take advantage of differences

in boiling points between components but require high energy input to generate the necessary temperature gradients. Chemical and petrochemical is by far the most demanding industrial sector in terms of energy consumptions, and accounts for 30% of global industrial energy use.[5] As represented in **Figure 2.4**, trends are clear, and energy use increased by a remarkable 61% between 1971 and 2004, which means 2% more each year. Considering that the expected world population will reach about 9.2 billion by 2050 with a resulting equivalent increase of energy consumption from 15 TW (2010) to more than 40 TW, the integration of more energy efficient technologies to provide those separations is one of the crucial aspects to mitigate the environmental impact of human activities.[20] Just by adopting the so-called best practice commercial technologies, the manufacturing industry could increase its energy efficiency by 18 to 26%, and at the same time reducing its sectorial CO_2 emission up to 32%.[5]
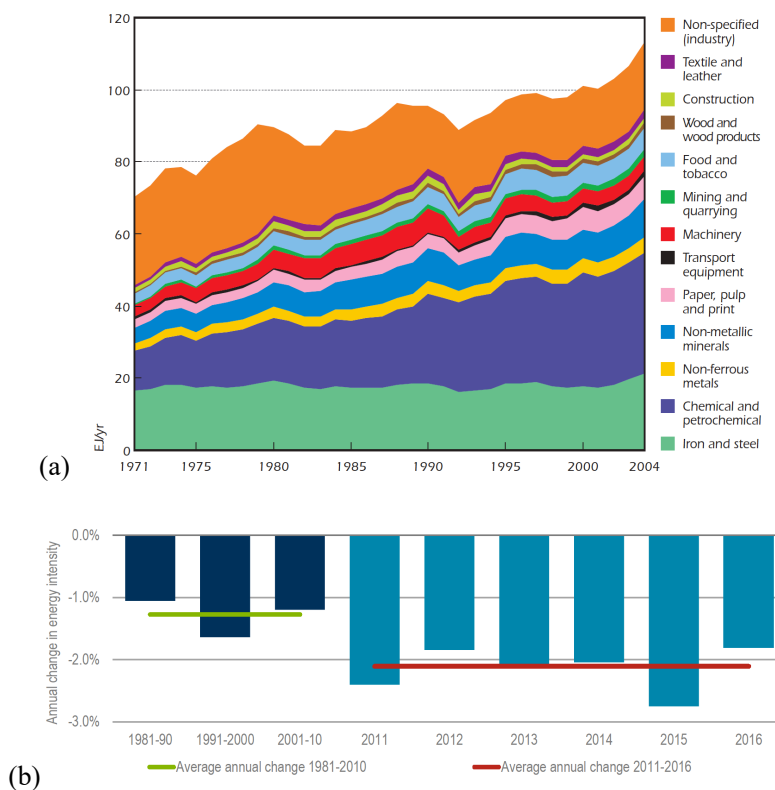
Figure 2.4: *(a) Industrial energy use increase in the period 1971-2004*[5]*, (b) Industrial energy intensity decrease in the period 1981-2016.*[32]

The International Energy Agency (IEA) provided interesting considerations on its Energy Efficiency report from 2017.[32] Although energy consumption is increasing, the integration of more efficient technologies in industry is allowing the decrease of the energy intensity. This means that the amount of energy required to generate a unit of gross domestic product (GDP) is gradually decreasing over time, as represented in **Figure 2.4b**. Since 2010, the intensity has decreased at an average rate of 2.1% per year, a significant increase over the average rate of 1.3% between 1970 and 2010.[32] Without this achievement, the world's population would have consumed 12% more energy since 2000. To give a proportion, this corresponds to an expansion of the global energy market to include another European Union.[32] As the former President of the United States stated in his 2017 Science paper[33], "*The importance of this trend cannot be understated. This decoupling of energy sector emissions and economic growth should put to rest the argument that combatting climate change requires accepting lower growth or a lower standard of living.*". The improvement in intensity varies from country to country, but the greatest impact on global trends came from China recent developments, which effort was 24% of that USD 231 billion global investment.[32] On the other hand, Europe has been more consistent over the last few years, and still remains the largest contributor to global investment (30% of total).[32] Despite these positive effects, more efforts should be made, since energy efficiency helps to improve the global energy system and can really allow the development to be more sustainable.

References

[1]   N. Höhne, T. Kuramochi, C. Warnecke, F. Röser, H. Fekete, M. Hagemann, T. Day, R. Tewari, M. Kurdziel, S. Sterl, S. Gonzales, *Clim. Policy* **2017**, *17*, 16.

[2]   Intergovernmental Panel on Climate Change (IPCC), *Global Warming of 1.5 °C*, **2018**.

[3]   J. Hansen, M. Sato, R. Ruedy, K. Lo, D. W. Lea, M. Medina-Elizade, *Proc. Natl. Acad. Sci.* **2006**, *103*, 14288.

[4]   C. Fu, T. Gundersen, *Energy Procedia* **2012**, *16*, 1806.

[5]   International Energy Agency (IEA), *Tracking Industrial Energy Efficiency and CO2 Emissions*, **2007**.

[6]   Intenational Energy Agency (IEA), *World Energy Outlook 2017*, **2017**.

[7]   P. Alivisatos, M. Buchanan, *Basic Research Needs for Carbon Capture: Beyond 2020*, **2010**.

[8]   A. A. Olajire, *Energy* **2010**, *35*, 2610.

[9]   F. Isa, H. Suleman, H. Zabiri, A. S. Maulud, M. Ramasamy, L. D. Tufa, A. M. Shariff, *J. Nat. Gas Sci. Eng.* **2016**, *33*, 666.

[10]   T. C. Merkel, M. Zhou, R. W. Baker, *J. Memb. Sci.* **2012**, *389*, 441.

[11]   S. M. Benson, F. M. Orr, *MRS Bull.* **2008**, *33*, 303.

[12]   S. Bachu, *Prog. Energy Combust. Sci.* **2008**, *34*, 254.

[13]   M. Pérez-Fortes, J. C. Schöneberger, A. Boulamanti, E. Tzimas, *Appl. Energy* **2016**, *161*, 718.

[14]   Q. M. Malik, M. R. Islam, in *SPE/DOE Improv. Oil Recover. Symp.*, Society Of Petroleum Engineers, **2000**.

[15]   D. W. Green, G. P. Willhite, *Enhanced Oil Recovery*, **2018**.

[16]   C. Song, *Catal. Today* **2006**, *115*, 2.

[17]   H. Yang, Z. Xu, M. Fan, R. Gupta, R. B. Slimane, A. E. Bland, I. Wright, *J. Environ. Sci.* **2008**, *20*, 14.

[18]   M. Galizia, W. S. Chi, Z. P. Smith, T. C. Merkel, R. W. Baker, B. D. Freeman, *Macromolecules* **2017**, *50*, 7809.

[19]   D. S. Sholl, R. P. Lively, *Nature* **2016**, *532*, 435.

[20]   J. K. Adewole, A. L. Ahmad, S. Ismail, C. P. Leo, *Int. J. Greenh. Gas Control* **2013**, *17*, 46.

[21]   R. Bounaceur, N. Lape, D. Roizard, C. Vallieres, E. Favre, *Energy* **2006**, *31*, 2556.

[22]   I. Taniguchi, D. Ioh, S. Fujikawa, T. Watanabe, Y. Matsukuma, M. Minemoto, *Chem. Lett.* **2014**, *43*, 1601.

[23]   C. E. Wilmer, O. K. Farha, Y.-S. Bae, J. T. Hupp, R. Q. Snurr, *Energy Environ. Sci.* **2012**, *5*, 9849.

[24]   C. A. Trickett, A. Helal, B. A. Al-Maythalony, Z. H. Yamani, K. E. Cordova, O. M. Yaghi, *Nat. Rev. Mater.* **2017**, *2*, 17045.

[25]   C.-H. Yu, C.-H. Huang, C.-S. Tan, *Aerosol Air Qual. Res.* **2012**, *12*, 745.

[26]   M. T. Ho, G. W. Allinson, D. E. Wiley, *Ind. Eng. Chem. Res.* **2008**, *47*, 4883.

[27]   K. S. Knaebel, *Pressure Swing Adsorption*, **1989**, US5032150A.

[28]   M. Ali Kalbassi, R. J. Allam, T. C. Golden, *Temperature Swing Adsorption*, **1997**, US5846295A.

[29]   N. Hedin, L. Andersson, L. Bergström, J. Yan, *Appl. Energy* **2013**, *104*, 418.

[30]   none, *Materials for Separation Technologies. Energy and Emission Reduction Opportunities*, **2005**.

[31]   J. L. Humphrey, G. E. Keller, *Separation Process Technology*, McGraw-Hill, **1997**.

[32]   International Energy Agency (IEA), *Energy Efficiency 2017*, **2017**.

[33]   B. Obama, *Science (80-.).* **2017**, *355*, 126.

3. Membrane Technologies for Carbon Capture Applications

The concept of membranes is inspired by biology. Membranes separate the internal environment of a cell from the surroundings, and provide the exchange of chemicals, signals, and chemical elements. Synthetic polymeric membranes can be used to address the problem of a variety of separations, with a very low impact on the environment and the drastic reductions of the energy consumption, up to 90% less than distillation.[1] The applications are almost unlimited, from gas separation[2–6], to water desalination[7–10], ultrafiltration, microfiltration, pervaporation, electrodialysis, and medical applications such as drug delivery. In the framework of gas separation, CO_2 capture to reduce the greenhouse effect, hydrogen purification and methane upgrading from natural gas for energy applications, as well as air separation, are among the most important operations performed. Membranes became an industrial reality because of their ability to control the rate of permeation of different species.[11] Compared to other technologies that perform separations at industrial level, membranes feature different advantages such as lower capital costs given the small dimensions of plants, high energy efficiency, because separations do not rely on phase change, and reliability, because membrane modules do not feature moving parts.[2,11]

The very first studies on the permeability of gases in various materials started long time ago with Thomas Graham.[12] However, gas separation has become a major industrial application of membrane technology only during the past 30 years, a while after Barrer[13], van Amerongen[14], Stern[15], and Meares[16], developed the foundation of the modern approach to the subject (**Figure 3.1**).
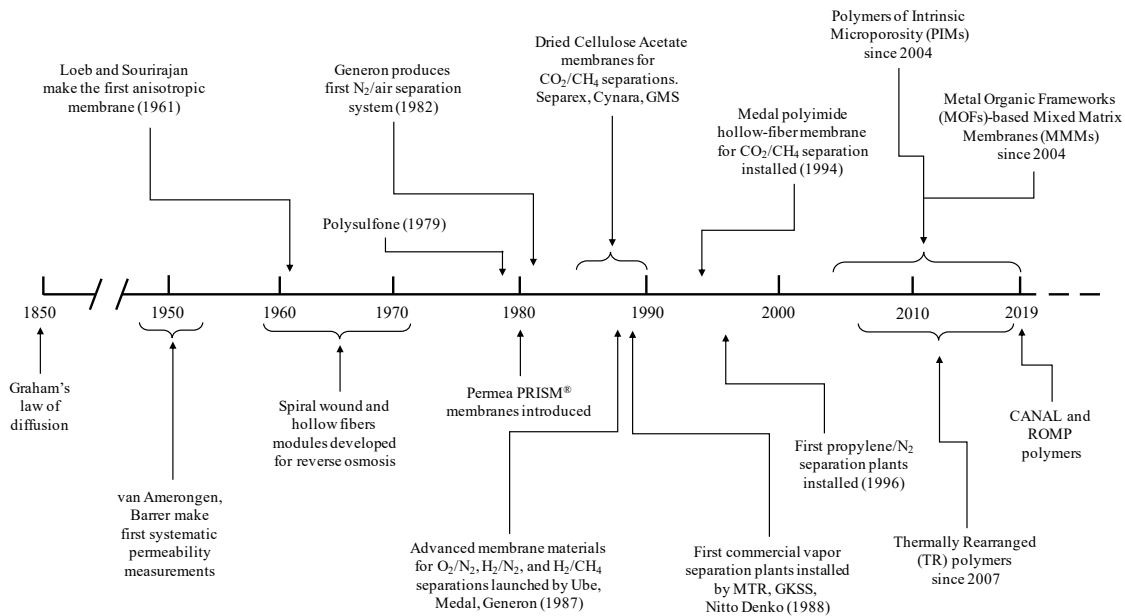
Figure 3.1: *Historical and recent developments of membrane technologies for gas separation applications. Adapted and integrated from references*[3,17].

In a typical configuration like the one represented in **Figure 3.2**, the gas mixture is fed to the separation module at a pressure higher than atmospheric pressure, and two streams are obtained. With respect to the feed, the permeate is enriched with the more permeable component, while the residue (*i.e.*, retentate), is concentrated in the less permeable components. The separation is carried out by a dense membrane that operates as a selective barrier through which components go through at different rates, or are rejected, based on favorable interactions and/or molecular sieving ability of the material.
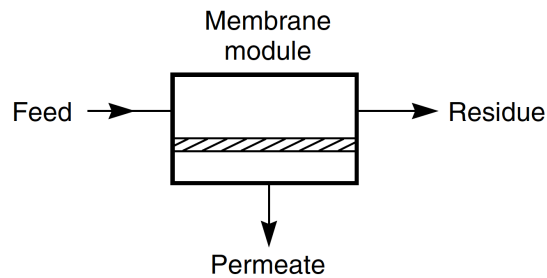
Figure 3.2: *Simplified schematic of a separation performed with a membrane module.*[11]

One of the first documented attempts to provide CO_2 and H_2S separation from natural gas with membrane technologies, was patented in 1977.[18] However, membrane companies such as *Grace Membrane Systems*, *Separex* (today part of *Honeywell UOP, Des Plaines IL USA*) and *Cynara* (today part of *Schlumberger, Huston TX USA*), entered the market just during the early-mid '80s.[19] The breakthrough material at the time was anisotropic cellulose acetate (CA), prepared using the Loeb-Sourirajan technique.[20] Nowadays materials are more diversified, especially because of the research efforts. However, industrial applications still rely just on the few commercial ones, as will be discussed in more detail later. The applications are also getting more diversified, and among the few involving carbon dioxide the most relevant mixtures are CO_2/N_2, CO_2/CH_4, and H_2/CO_2.

CO_2/N_2 is the mixture that best represent the exhaust gases produced at a power plant (*i.e.*, flue gas), as a product of the combustion of fossil fuel or biomass when air is used as an oxidizing agent. This separation process is called post-combustion, and it is important mostly from an ecological and environmental point of view, to prevent CO_2 emission into the atmosphere.[21] Industrially, combustion can be performed with air as an oxidant agent, but also with enriched air such as ~95% O_2 (*i.e.*, oxy-combustion). The latter case is particularly favorable for the application of a membrane process as the partial pressure of CO_2 is significantly higher than the traditional combustion which usually do not exceed 15% of CO_2 in the flue gas.[2] Oxy-fuel combustion provides a stream that generally does not need further treatments before performing CO_2 capture, being it mainly composed by CO_2 and H_2O. Further, for unit of power generated, oxy-combustion produces ~75% less gas to be treated, which makes the membrane section much smaller and cheaper. Usually both pressure and temperature are relatively low being an end-of-pipe separation, and while low temperature is good because it enhances CO_2 solubility, the low pressure is a disadvantage since the driving force is reduced. In 2006, Bounaceur *et al.*[22] performed a parametric study that demonstrated that materials available at that time were not selective enough to meet the standards required by the government regulations in terms of concentration. It was just in 2010 that Tim Merkel and *Membrane Technology & Research Inc.* (*MTR*) developed Polaris™, which featured a CO_2/N_2 of 50 and a permeance 10 times higher than that of commercial membranes.[21] This way also post-combustion became an opportunity for membrane

technologies, which however remains an economical challenge. In fact, by neglecting the environmental impact, at the moment CO_2 sequestration with membrane technology is cost-effective compared to absorption with amines only for high carbon dioxide concentration and low for medium gas flow rates, as shown in **Figure 3.3**.[19]
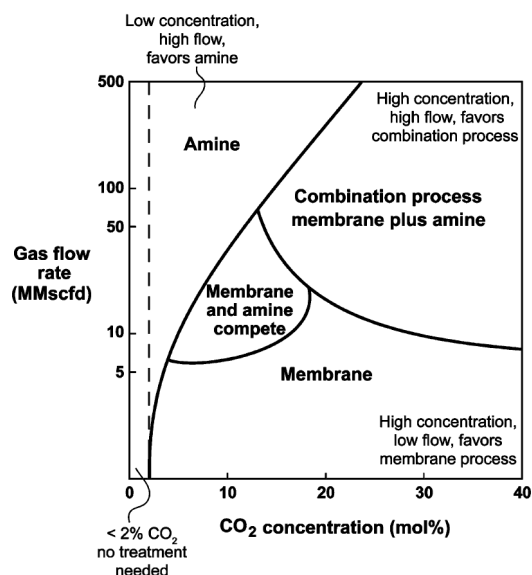
Figure 3.3: *Scheme to compare technologies for CO_2 sequestration in different operating conditions: CO_2 concentration and gas flow. The author, Richard Baker*[19]*, warns that limits are not as strict as in the figure, and choices need to be made looking at specifics and issues of each site.*

Other separations involving CO_2 such as CO_2/CH_4 and H_2/CO_2 will be discussed in the dedicated sections 3.3.1 and 3.3.2, respectively.

3.1. The Upper Bound: membrane permeability and selectivity

About 30 years ago, Robeson developed a way to represent polymers' performance and compare them to one another, which is still the framework used by researchers operating in the membrane-based gas separation to assess the potential of a polymer for the separation of a specific gas pair.[23] This was called the "upper bound" and represented the limit membrane technologies achieved at the time of the publication, in 1991. The fundamental theoretical understanding of this limit, which is not a thermodynamic limit but rather an empirical relation that photograph the state of the art, was developed

by Freeman[24] a few years later. Eventually the upper bound was also updated in the 2008.[25] Since the upper bound represent the material performance at room temperature (*e.g.*, 30 ± 5 °C), Rowe *et al.*[26], based on the understanding provided by Freeman[24], developed a model to evaluate the shift of the upper bound with temperature. Given the extraordinary production of new high-performing materials for gas separation designed mostly by Pinnau, McKeown and Budd research groups, in 2015[27] it was proposed a redefined version of the upper bound for air separation and H_2 purification. However, the latter limit was calculated just based on a few materials such as TPIM-1[28], KAUST-PI-1[29] and PIM-trip-TB[30], developed after 2013.

The separation performance of polymer membranes is characterized by two physical quantities: permeability, P_i, and selectivity, α_{ij}. Permeability is defined as the steady-state flux of species i, J_i, normalized by the ratio of driving force (pressure difference across the membrane, Δp_i) and membrane thickness, l, as follows:

$$\mathcal{P}_i = \frac{J_i l}{\Delta p_i}$$

Eq. (3.1)

Permeability can be expressed in many different units, but the most common in the membrane field for gas separation is the *Barrer*:

$$1 Barrer = 10^{-10} \frac{cm^3(STP) \cdot cm}{cm^2 \cdot cmHg \cdot s}$$

Eq. (3.2)

Ideal selectivity represents the ability of the membrane to separate the components of the mixture, reducing the loss of the component of interest or the emission of the undesired gas, and it is defined as follows:

$$\alpha_{ij} = \frac{y_{i,d}/y_{j,d}}{y_{i,u}/y_{j,u}} \cong \frac{\mathcal{P}_i}{\mathcal{P}_j}$$

Eq. (3.3)

where $y_{i,d}$ and $y_{j,d}$ are the molar fraction in the permeate side of the membrane of gas i and j respectively, while $y_{i,u}$ and $y_{j,u}$ those in the retentate side of the module. $\mathcal{P}_i$ is the permeability of the more permeable gas of the pair and $\mathcal{P}_j$ is the less permeable one. The optimal situation would be having

both high productivity, *i.e.*, high permeate flow, which would lead to smaller membrane skid size and, at the same time, high selectivity, *i.e.*, better separation, which further means a reduced cost of the compression.

The efforts of research have been widely devoted to the development of materials with improved performance, since the success of membrane technologies strongly relies on these features. However, Robeson showed that an increase in permeability is often accompanied by a decrease in selectivity, and *vice versa*.[23,25] In the membrane community, this is known as the *trade-off* . **Figure 3.4** represents the Robeson plot for the CO_2/CH_4 gas pair, in which performance of commercial polymers (white symbols) as well as materials developed more recently (colored solid symbols), are plotted.
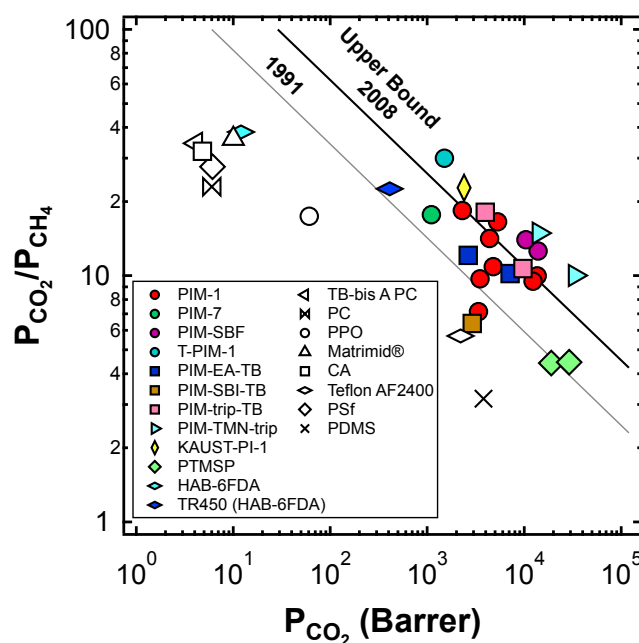
Figure 3.4*: Robeson upper bound for the CO_2/CH_2 gas pair from 1991[23] and 2008[25]. Empty white symbols represent commercial glassy polymers: CA, PSf[31], PPO[32], Matrimid®[33], Teflon AF2400[34], TB-bis A PC, and PC[35]. Solid colored symbols represent some recent Polymers of Intrinsic Microporosity (PIMs)[28,36–40], PIM-polyimide[29], polyimide[41], TR-polymer[41] and PTMSP[42], while the "X" symbol represent the only rubbery polymer on the plot: PDMS[43].*

It is important to notice that in terms of materials used in industrial applications, things have not changed much from the '80s, and cellulose acetate is still one of the few materials used in real-world applications, together with perfluoropolymers and polyimides that more recently gained some room in the field.[19] Just considering the capture of carbon dioxide from high pressure natural gas, CO_2/CH_4 separation, these

commercially available materials have performance far below the 1991 upper limit (**Figure 3.4**).[23] This leads to some considerations, as Galizia *et al.*[3] pointed out in the *Macromolecules* 50th anniversary perspective on gas and vapor separation. New materials perform better, and thereby are likely to reduce the process costs by 5 - 10%, making it more convenient to companies and make a breakthrough. However, this would likely be not enough to gain a significant increase in the market share and replace cryogenic distillation and pressure swing adsorption. The reason behind this, is that usually membranes are characterized at ideal conditions (*i.e.*, pure-gas experiments), without polluting agents, underestimating the mixture-induced competition effects and the importance of mechanical properties even when the thickness of the selective layer of the material is thinner than one micrometer. It is just taking care of these remarkable aspects that better performing materials such as Thermally Rearranged polymers[44,45], Polymers of Intrinsic Microporosity[38,39,46], Metal Organic Frameworks[47], Covalent Organic Frameworks[48] and Mixed Matrix Membranes[49,50] will become a commercial reality.[3]

3.2. Membrane Modules

At the laboratory scale, polymer membranes are commonly prepared by means of the solution-casting or casting-knife techniques.[11] After casting, the solution is left to rest, and the solvent evaporates to create a thin, uniform polymer film. Usually these techniques do not allow to cast membranes thinner than a few microns. Alternatives to coat porous supports with thinner selective dense layers are spin coating, dip coating, and spray coating. A requirement for these techniques is that the polymer is soluble in a solvent, feature that makes the polymer inclined to swell in the presence of a condensable gas of vapor, which leads to a separation-performance drop due to plasticization.[51] The plasticization phenomenon will be detailed discussed in section 4.3.3.

Nowadays, membranes used for gas separation applications are produced as flat sheets packaged as spiral-wound modules[52] (**Figure 3.5a**) or as hollow fibers[53,54] (**Figure 3.5b**). These geometries allow for an intensification of the membrane process (*i.e.*, more active area per volume occupied by the equipment), leading to economic benefits because high $A_{membrane}/V_{equipment}$ ratios, reduce the

footprint of the membrane installation required to treat a given amount of gas. For relatively clean gas streams like N_2 separation from air or O_2-enrichment, hollow fiber modules represent the most compact and efficient solution. However, for other growing applications involving membrane technology, such as natural gas sweetening or H_2-purification in power plants in which gas streams are highly contaminated and may also contain solid particulate, flat sheet membranes assembled as spiral wound modules are more recommended.

(a)

(b)
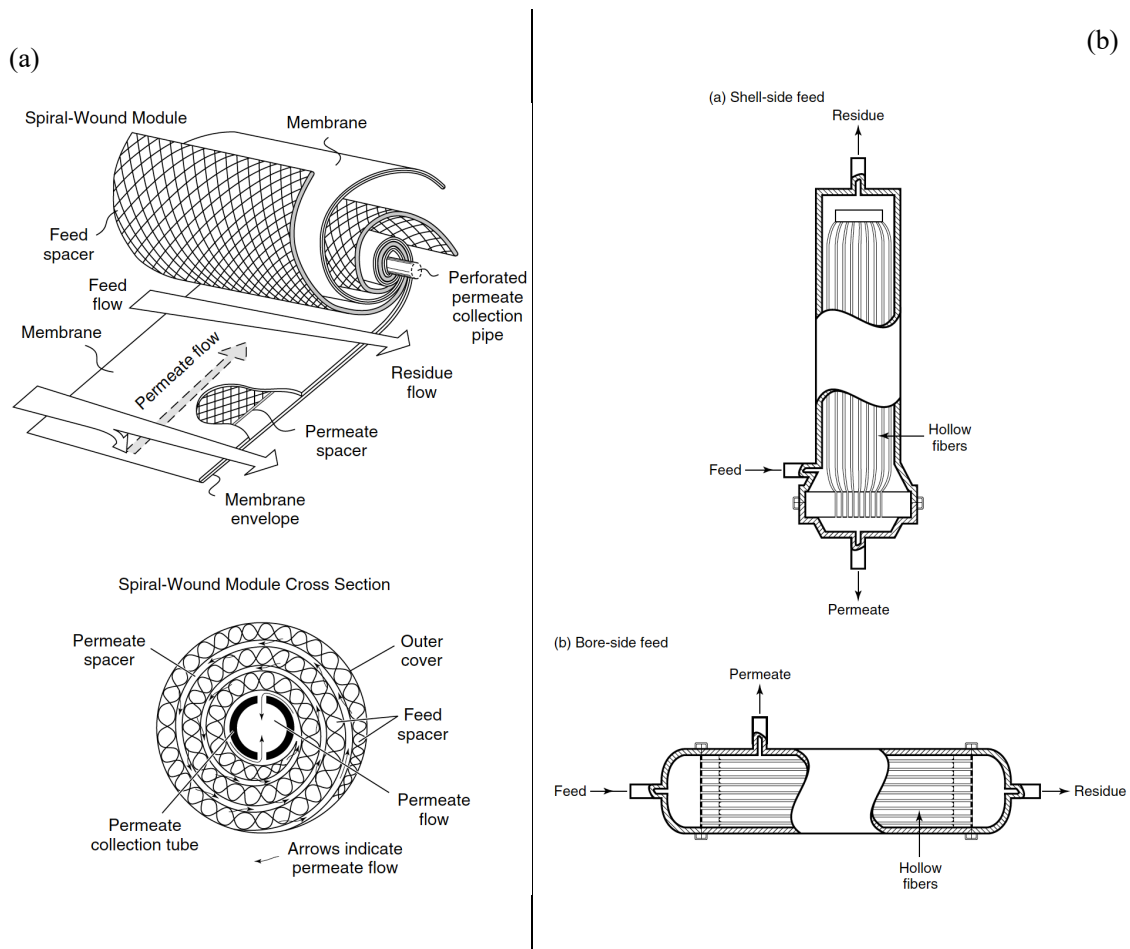
Figure 3.5: *(a): Schematic representation of a spiral-wound membrane module: detail of each layer (top) and cross-section (bottom).*[11] *(b) Different configurations of hollow-fibers modules for the treatment of gas streams.*[11]

3.3. Other Important Separations for Membrane Technologies

3.3.1. Natural Gas Upgrade

Natural gas is one of the most important source of power generation. Just in the US, it accounted for ~21% of electricity generation in 2008, and in 2017 it increased up to 33%, rising almost exclusively as a result of the shift from higher-emission coal to lower-emission natural gas, caused mainly by the availability of low-cost gas due to advances in production technologies.[55] In fact, the cost of generating electricity from natural gas is predicted to remain relatively low compared to coal, and build coal-fired power plants would be more costly than natural gas plants.[56]

Natural gas (NG) is a complex mixture of methane, ethane, carbon dioxide, heavier hydrocarbons, hydrogen sulfide, and traces of many other compounds including toluene, benzene and xylene.[19] The composition of natural gas can significantly vary depending on the oil well, and it is mandatory to treat NG to some extent before delivering the gas to the pipeline grid. Remove carbon dioxide from NG streams and meet the American standard maximum content of CO_2 (*i.e.*, 2 mol.%) is necessary to increase the calorific value and prevent pipe corrosion. Corrosive solutions could be generated by the simultaneous presence of acid gases and water in the gas stream, since NG is often saturated with water after extraction from a well.[2,57] Thus, another pipeline specification to meet is on H_2S, which is allowed up to 4 ppm.[19] Further, upon cooling, water may condense and form solid hydrates with hydrocarbons in the NG stream that can harm the equipment.[17,58]

It is clear how many separation processes are necessary to be performed to make natural gas usable. According to Baker[19], natural gas is potentially the biggest market for industrial gas separation, but membranes just account for about a 5% share. Traditionally, water is removed from NG by means of glycol dehydrators, in which tri-, di-, mono-ethylene glycol solutions are used to absorb water and higher hydrocarbons.[17] As for CO_2 capture with amines absorption, glycols need to be regenerated boiling the liquid mixture with some related costs. However, these units are less expensive than the amines analogous, both from the operation costs and the equipment investment point of view, thus are widely diffused.[17] Membrane technologies can be an alternative since many materials used to build membrane

modules present high H_2O/CH_4 selectivity, allowing to limit the methane loss with the permeate water.[19] As discussed above, also CO_2 can be removed from natural gas with membrane technologies, as well as another acid gas: H_2S. This is another growing area in the membrane field.

In **Figure 3.6** two alternative schemes to perform natural gas upgrading using membrane technologies are represented. The alternative in one-stage features no moving parts, which is a remarkable aspect in terms of compression cost reductions and stability over time. This set up is particularly competitive with traditional technologies when the permeate can be directly used at low pressure. On the other hand, the two-stage plant provides a much better yields in terms of methane recovery, but it is more expensive since a compressor is required to pressurize the permeate coming from the first stage. Using more complex multi stage systems, recovery of natural gas higher than 95% can be achieved.[2]
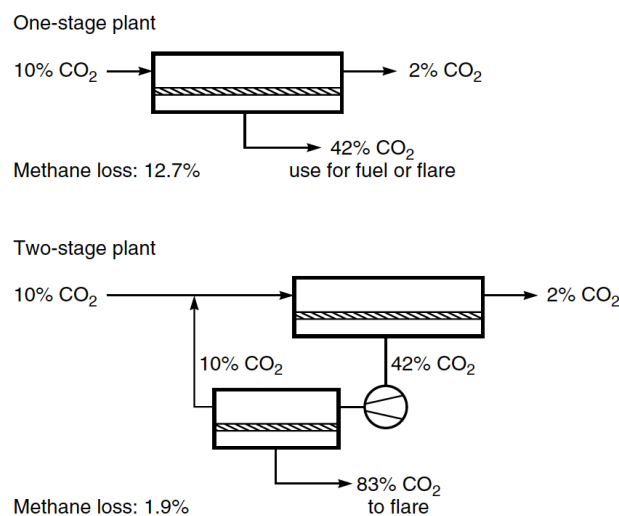
Figure 3.6: Scheme of a membrane separation plan to treat natural gas and remove carbon dioxide: (a) one-stage, and (b) two-stage plant.[11]

As also previously indicated in **Figure 3.3** and highlighted by Bernardo *et al.*[2], membrane technologies become more competitive than amine scrubbing, or other more traditional solutions, for small applications in which less than 6,000 Nm^3/h need to be treated. Offshore plants usually need to deal with very limited space available on the platform, and given the compactness of membrane modules (**Figure 3.5**), this technology became competitive with amine sorption also at higher flow rates up to

50,000 Nm^3/h. **Figure 3.7** clearly shows how much a membrane plant can be smaller compared to other technologies while treating the same amount of CO_2. In particular, the *MTR* system represented can capture 20 tons per day of CO_2, while the amine absorption plant indicated in white, has half of the capacity, but much bigger dimensions hard to fit when space is limited.

One of the largest membrane systems for NG sweetening was installed in 2007 on an offshore platform in the Malaysia Thailand Joint Development Area in the Gulf of Thailand called the *Cakerawala* production platform (**Figure 3.8**). The 16-inch modules can treat 830,000 Nm^3/h.[59] and reduce the amount of CO_2 in the stream from 36% to 16%, to meet the 23% CO_2 emission limit required by law in Southeast Asia. The 16-inch module has 17.5 times the feed capacity of a 5-inch module, while the latest development, the 30-inch module, can get up to 62.5 times the feed capacity of the smallest module, reducing weight and space by more than 90%.[2]

Figure 3.7: *Representation of the compactness of membrane technologies compared to other competitive technologies for carbon capture. 20 tons per day membrane system by MTR (green), amine absorption columns 20 tons per day (green), and 10 tons per (yellow).*[60]

Figure 3.8: The Cakerawala natural gas production platform and one of the Cynara-NATCO cellulose triacetate 16-inch modules installed to perform CO_2 capture.[59]

CO_2 enhanced oil recovery (EOR) to increase recovery rates from a well is another application in which membrane technologies can be beneficial to separate the CO_2 that otherwise would be wasted from natural gas. High CO_2 concentrations, typically > 50%, and high pressure up to 140 bar which these processes produce, are favorable conditions for membrane, but they need to be plasticization resistant to prevent loss in mixed-gas selectivity.[2] A remarkably successful installation was develop in 1983 by Cynara in Texas. The membrane system was originally designed to reduce CO_2 from 45% to 28%, to treat 60,000 Nm^3/h in 160 modules (5 in × 12 in), but then the capacity doubled, and the CO_2-content reduction provided is from 80% to 10%.[2]

Another mixture of interest that the natural gas industry is often required to separate is CH_4/N_2, for instance in nitrogen-rich gas reserves. *MTR* for instance provides the *NitroSep* system that features composite material with enhanced properties, since methane and nitrogen often have similar permeability, thus it is difficult to separate them with polymer membranes. Alternative materials such as carbon molecular sieves (CMS) have been investigated to separate this particular mixture given the industrial interest.[61]

NG is not the only source of methane. Biogas is a renewable energy source produced by anaerobic degradation of organic matter operated by microorganisms.[62] Just considering India, over 250 million

cattle produce lots of dung, and if just one third of it would be used for biogas production, more than 12 million biogas plants could be installed.[63] The biogas treatment represents an important area for the development and application of CO_2 capture technology. After the microbial fermenter, the CO_2 level is approximately 25-50%, which makes the CO_2/CH_4 separation step necessary.[64,65]

3.3.2. Hydrogen Purification

Hydrogen is a perfect target for membrane separation since its small dimensions and low condensability confer high diffusivity and, as a consequence, high permeability. For these reasons, it is easy to separate it from many gas mixtures.[2–4,66] As also highlighted in **Figure 3.1**, *Permea* pioneered commercially available membrane-based technologies for gas separation in the early '80s, with the very first commercialization on 1979.[67] The separation was focused on H_2 separation from N_2, Argon, and CH_4 in ammonia plant purge gas.[68] The applications quickly expanded to different sectors such as oil and gas, in which H_2 was separated from light hydrocarbons (ethane, propane etc.), or in synthesis plants, in which membranes were used to adjust the ratio between H_2 and CO streams coming from gasification plants.[3] Membrane technologies can be applied also directly to integrated-gasification combined cycle (IGCC) plants[69]. As it can be observed in **Figure 3.9**, membrane technologies can be featured at different stages of the process. Right after the gasification step, temperatures and pressure are higher, and the gas stream brings along impurities, such as particulate, that can harm the membrane module, but still H_2/CO separation can be performed. To increase the yield of H_2, water gas shift reaction can be performed, providing the need to separate H_2 from CO_2 as a product of the carbon monoxide oxidation. In this case, pre-combustion separation has the double role to purify H_2 to be used as fuel for power generation, as well as to capture CO_2 to prevent its emission. This would also require the development of technologies for the separation at high temperatures of acid gases (*i.e.*, H_2S) usually part of the mixture, since absorption is more effective at low temperatures, and membrane modules that could also provide this kind of separation, would be beneficial to the overall efficiency of the process.[70,71]
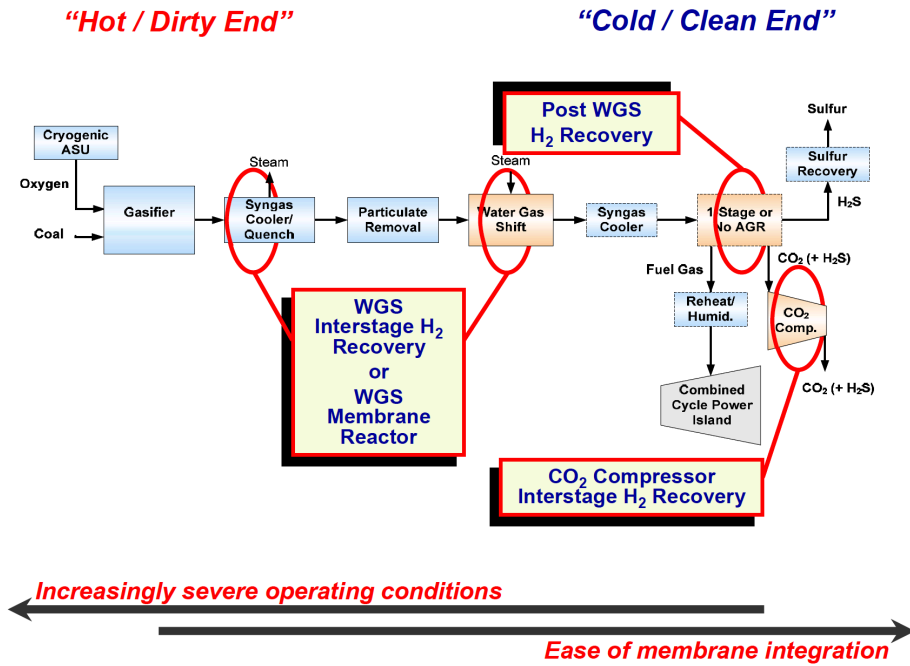
Figure 3.9: Integration of membrane technologies with the Integrated-Gasification Combined-Cycle.[72]

Working at high temperatures increase the efficiency of the process, so it would be beneficial that polymer materials could be able to operate at 150 – 200 °C, and many recent developments especially in the field of polyimides allow for that. Studies carried out in the literature showed that, from an economic point of view, it is equivalent to choose between H_2-selective and CO_2-selective materials to be implemented in an IGCC gasification plant. In his study[69], Merkel concludes that, in the case of a single-stage process, a H_2-selective membranes is preferable because it allows to operate at high temperature, reducing the cost of gas cooling, being H_2/CO_2 separation enhanced at high temperature. H_2-selective membranes allow to keep CO_2 in the retentate side obtaining CO_2 at high pressure. This way, no further compression is needed to meet the requirements necessary for the geological storage of carbon dioxide. In addition, H_2 concentration required on the permeate side for turbine feed (*i.e.,* 44 - 80%)[72] can be achieved by the use of membrane technologies. If a solubility-controlled CO_2-selective membrane was preferred, it would minimize or eliminate H_2 recompression, but a CO_2 compression step would be necessary to add.

Steam reforming of natural gas is another process which involves hydrogen separation, since it leads to gas mixtures consisting mainly of hydrogen, carbon dioxide and carbon monoxide. Similar considerations hold for the choice of the membrane. Hydrogen membrane rejection and contaminant permeation are currently investigated for H_2 purification, mostly with carbon-based membranes.[66]

3.3.3. Air Separation

Nitrogen production represents the most important application in terms of market size, with about $800 million per year, about half of the total membrane-based gas separation business.[3] Some of the most relevant applications consistent with the degree of purity membrane technology can provide include combustion/reaction processes, inerting and refrigeration.[73] Materials such as Polysulfone (PSf), Polycarbonate (PC) and its substituted, Poly(phenylene oxide) (PPO), and various polyimides have been used since 30-40 years.[3,74] However, novel polymer of intrinsic microporosity have shown promising properties in terms of O_2/N_2 separation[28,36,38], which use would be able to significantly reduce both the operation costs and the initial investment on a membrane-based plant. As for other membrane-based applications, most of the costs are concentrated in the necessary compressors, and in the N_2-enrichment field they can account for 2/3 of the total cost.[17] **Figure 3.10** shows the approximate economic range for various separation processes used to achieve N_2 purities at a specified flowrate. It is clear how membranes are suitable for a wide range of specifics, especially if purities are kept between about 95 and 99%. A strategy to improve N_2 purity using membranes was developed by adding a deoxygenation system, which purpose is to remove the oxygen excess from N_2/O_2 mixture coming from a membrane separation unit using H_2 and a noble metal catalyst, followed by H_2 and H_2O removal from the product stream.[74] Competing technologies such as cryogenic distillation and PSA, are used to process higher gas flowrates and, for cryogenic distillation, to achieve higher purity N_2, but the energy inefficiency of this process has been already discussed previously in this dissertation. This high-purity N_2 finds application in gas feeds for the electronics industry, enhanced oil recovery and metallurgical processes. As for the graph in **Figure 3.3**, also for **Figure 3.10** it is important to realize that many

different characteristics of the site can influence the limits represented, which should not be interpreted strictly.
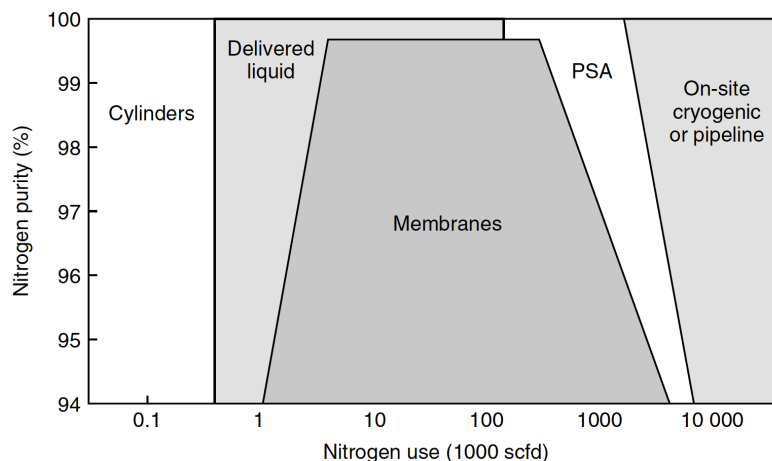
Figure 3.10*: Approximate range in which membrane technologies are competitive with traditional solutions. Figure from reference* [11].

References

[1]   D. S. Sholl, R. P. Lively, *Nature* **2016**, *532*, 435.

[2]   P. Bernardo, E. Drioli, G. Golemme, *Ind. Eng. Chem. Res.* **2009**, *48*, 4638.

[3]   M. Galizia, W. S. Chi, Z. P. Smith, T. C. Merkel, R. W. Baker, B. D. Freeman, *Macromolecules* **2017**, *50*, 7809.

[4]   W. J. Koros, R. Mahajan, *Mahajan J Membr Sci Vol 175 p 181* **2000**, *175*, 181.

[5]   D. F. Sanders, Z. P. Smith, R. Guo, L. M. Robeson, J. E. Mcgrath, D. R. Paul, B. D. Freeman, **2013**, *54*, 4729.

[6]   B. D. Freeman, Y. Yampolskii, I. Pinnau, *Materials Science of Membranes for Gas and Vapor Separation*, John Wiley & Sons, Ltd, Chichester, UK, **2006**.

[7]   L. F. Greenlee, D. F. Lawler, B. D. Freeman, B. Marrot, P. Moulin, *Water Res.* **2009**, *43*, 2317.

[8]   J. Kamcev, M. Galizia, F. M. Benedetti, E.-S. Jang, D. R. Paul, B. D. Freeman, G. S. Manning, *Phys. Chem. Chem. Phys.* **2016**, *18*, 6021.

[9]   M. Galizia, F. M. Benedetti, D. R. Paul, B. D. Freeman, *J. Memb. Sci.* **2017**, *535*, 132.

[10]   E. Drioli, A. Criscuoli, E. Curcio, *Desalination* **2002**, *147*, 77.

[11]   R. W. Baker, *Membrane Technology and Applications*, **2004**.

[12]   T. Graham, *Philos. Trans. R. Soc. London* **1866**, *156*, 399.

[13]   R. M. Barrer, *Diffusion In and Through Solids*, Cambridge University Press, London, **1951**.

[14]   G. J. van Amerongen, *J. Appl. Polym. Sci.* **1950**, *5*, 307.

[15]   S. A. Stern, *Proc. Symp. South. Res. Inst.* **1966**, 196.

[16]   P. Meares, *J. Am. Chem. Soc.* **1954**, *76*, 3415.

[17]   R. W. Baker, *Ind. Eng. Chem. Res.* **2002**, *41*, 1393.

[18]   A. B. Coady, T. E. Cooley, *Removal of H2S and/or CO2 from a Light Hydrocarbon Stream by Use of Gas Permeable Membrane*, **1977**, CA1080133A.

[19]   R. W. Baker, K. Lokhandwala, *Ind. Eng. Chem. Res.* **2008**, *47*, 2109.

[20]   H. Strathmann, P. Scheible, R. W. Baker, *J. Appl. Polym. Sci.* **1971**, *15*, 811.

[21]   T. C. Merkel, H. Lin, X. Wei, R. Baker, *J. Memb. Sci.* **2010**, *359*, 126.

[22]   R. Bounaceur, N. Lape, D. Roizard, C. Vallieres, E. Favre, *Energy* **2006**, *31*, 2556.

[23]   L. M. Robeson, *J. Memb. Sci.* **1991**, *62*, 165.

[24]   B. D. Freeman, *Macromolecules* **1999**, *32*, 375.

[25]   L. M. Robeson, *J. Memb. Sci.* **2008**, *320*, 390.

[26]   B. W. Rowe, L. M. Robeson, B. D. Freeman, D. R. Paul, *J. Memb. Sci.* **2010**, *360*, 58.

[27]   R. Swaidan, B. Ghanem, I. Pinnau, *ACS Macro Lett.* **2015**, *4*, 947.

[28]   B. S. Ghanem, R. Swaidan, X. Ma, E. Litwiller, I. Pinnau, *Adv. Mater.* **2014**, *26*, 6696.

[29]   B. S. Ghanem, R. Swaidan, E. Litwiller, I. Pinnau, *Adv. Mater.* **2014**, *26*, 3688.

[30]   I. Rose, M. Carta, R. Malpass-Evans, M. C. Ferrari, P. Bernardo, G. Clarizia, J. C. Jansen, N. B. McKeown, *ACS Macro Lett.* **2015**, *4*, 912.

[31]   A. J. Erb, D. R. Paul, *J. Memb. Sci.* **1981**, *8*, 11.

[32]   F. M. Benedetti, M. G. De Angelis, M. Degli Esposti, P. Fabbri, G. Cucca, A. Masili, A. Orsini, A. Pettinau, *To be Submitt.* **n.d.**

[33]   L. Ansaloni, M. Minelli, M. Giacinti Baschetti, G. C. Sarti, *Oil Gas Sci. Technol. – Rev. d'IFP Energies Nouv.* **2015**, *70*, 367.

[34]   T. C. Merkel, V. Bondar, K. Nagai, B. D. Freeman, Y. P. Yampolskii, *Macromolecules* **1999**, *32*, 8427.

[35]   N. Muruganandam, W. J. Koros, D. R. Paul, *J. Polym. Sci. Part B Polym. Phys.* **1981**, *25*, 1999.

[36]   M. Carta, M. Croad, R. Malpass-Evans, J. C. Jansen, P. Bernardo, G. Clarizia, K. Friess, M. Lanč, N. B. McKeown, *Adv. Mater.* **2014**, *26*, 3526.

[37]   P. Li, T. S. Chung, D. R. Paul, *J. Memb. Sci.* **2013**, *432*, 50.

[38]   M. Carta, R. Malpass-Evans, M. Croad, Y. Rogan, J. C. Jansen, P. Bernardo, F. Bazzarelli, N. B. McKeown, *Science (80-.).* **2013**, *339*, 303.

[39]   I. Rose, C. G. Bezzu, M. Carta, B. Comesanã-Gándara, E. Lasseuguette, M. C. Ferrari, P. Bernardo, G. Clarizia, A. Fuoco, J. C. Jansen, K. E. Hart, T. P. Liyana-Arachchi, C. M. Colina, N. B. McKeown, *Nat. Mater.* **2017**, *16*, 932.

[40]   Y. He, F. M. Benedetti, S. Lin, C. Liu, Y. Zhao, H.-Z. Ye, T. Van Voorhis, M. G. De Angelis, T. M. Swager, Z. P. Smith, *Submitt. to Adv. Mater.* **2019**.

[41]   D. F. Sanders, Z. P. Smith, C. P. Ribeiro, R. Guo, J. E. McGrath, D. R. Paul, B. D. Freeman, *J. Memb. Sci.* **2012**, *409–410*, 232.

[42] T. Mizumoto, T. Masuda, T. Higashimura, *J. Polym. Sci. Part A Polym. Chem.* **1993**, *31*, 2555.

[43] T. C. Merkel, V. I. Bondar, K. Nagai, B. D. Freeman, I. Pinnau, *J. Polym. Sci. Part B Polym. Phys.* **2000**, *38*, 415.

[44] H. B. Park, C. H. Jung, Y. M. Lee, A. J. Hill, S. J. Pas, S. T. Mudie, E. Van Wagner, B. D. Freeman, D. J. Cookson, *Science (80-.).* **2007**, *318*, 254.

[45] Z. P. Smith, D. F. Sanders, C. P. Ribeiro, R. Guo, B. D. Freeman, D. R. Paul, J. E. McGrath, S. Swinnea, *J. Memb. Sci.* **2012**, *415–416*, 558.

[46] P. M. Budd, E. S. Elabas, B. S. Ghanem, S. Makhseed, N. B. McKeown, K. J. Msayib, C. E. Tattershall, D. Wang, *Adv. Mater.* **2004**, *16*, 456.

[47] O. M. Yaghi, M. O'Keeffe, N. W. Ockwig, H. K. Chae, M. Eddaoudi, J. Kim, *Nature* **2003**, *423*, 705.

[48] A. P. Côté, H. M. El-Kaderi, H. Furukawa, J. R. Hunt, O. M. Yaghi, *J. Am. Chem. Soc.* **2007**, *129*, 12914.

[49] H. Yehia, T. J. Pisklak, K. J. Balkus, I. H. Musselman, in *Polym. Prepr. - Am.*, **2004**, pp. 35–36.

[50] A. F. Bushell, M. P. Attfield, C. R. Mason, P. M. Budd, Y. Yampolskii, L. Starannikova, A. Rebrov, F. Bazzarelli, P. Bernardo, J. Carolus Jansen, M. Lanč, K. Friess, V. Shantarovich, V. Gustov, V. Isaeva, *J. Memb. Sci.* **2013**, *427*, 48.

[51] A. Bos, I. G. M. Pünt, M. Wessling, H. Strathmann, *J. Memb. Sci.* **1999**, *155*, 67.

[52] D. T. Bray, D. H. Hopkins, *Spiral Wound Membrane*, **1988**, US4842736A.

[53] N. Peng, N. Widjojo, P. Sukitpaneenit, M. M. Teoh, G. G. Lipscomb, T.-S. Chung, J.-Y. Lai, *Prog. Polym. Sci.* **2012**, *37*, 1401.

[54] C. F. Wan, T. Yang, G. G. Lipscomb, D. J. Stookey, T.-S. Chung, *J. Memb. Sci.* **2017**, *538*, 96.

[55] US Energy Information Administration, *Monthly Energy Review, November 2016*, Washington, DC, **2016**.

[56] B. Obama, *Science (80-.).* **2017**, *355*, 126.

[57] J. K. Adewole, A. L. Ahmad, S. Ismail, C. P. Leo, *Int. J. Greenh. Gas Control* **2013**, *17*, 46.

[58] D. W. Choi, *Hydrocarb. Process.* **2006**, *85*, 69.

[59] A. Callison, G. Davidson, *Oil Gas J.* **2007**, *105*.

[60] T. C. Merkel, R. W. Baker, in *Membr. Gas Sep.*, San Francisco, **2017**.

[61] X. Ning, W. J. Koros, *Carbon N. Y.* **2014**, *66*, 511.

[62] Yadvika, Santosh, T. R. Sreekrishnan, S. Kohli, V. Rana, *Bioresour. Technol.* **2004**, *95*, 1.

[63] D. . Kashyap, K. . Dadhich, S. . Sharma, *Bioresour. Technol.* **2003**, *87*, 147.

[64] Z.-M. Xia, X.-S. Li, Z.-Y. Chen, G. Li, K.-F. Yan, C.-G. Xu, Q.-N. Lv, J. Cai, *Appl. Energy* **2016**, *162*, 1153.

[65] Z. Bacsik, O. Cheung, P. Vasiliev, N. Hedin, *Appl. Energy* **2016**, *162*, 613.

[66] N. W. Ockwig, T. M. Nenoff, *Chem. Rev.* **2007**, *107*, 4078.

[67] Air Products and Chemicals, "PRISM® Membranes, Air Products division," can be found under http://www.airproducts.com/Products/Gases/supply-options/prism-membranes.aspx, **1996**.

[68] W. Bollinger, D. MacLean, R. Narayan, *Chem. Eng. Prog.* **1982**, *78*.

[69] T. C. Merkel, M. Zhou, R. W. Baker, *J. Memb. Sci.* **2012**, *389*, 441.

[70] G. George, N. Bhoria, S. AlHallaq, A. Abdala, V. Mittal, *Sep. Purif. Technol.* **2016**, *158*, 333.

[71] C. A. Scholes, G. Q. Chen, W. X. Tao, J. Bacus, C. Anderson, G. W. Stevens, S. E. Kentish, *Energy Procedia* **2011**, *4*, 681.

[72] J. J. Marano, J. P. Ciferino, *Energy Procedia* **2009**, *1*, 361.

[73] P. S. Puri, **n.d.**, pp. 215–244.

[74] R. Prasad, F. Notaro, D. R. Thompson, *J. Memb. Sci.* **1994**, *94*, 225.

4. Theoretical Background

4.1. The Solution-Diffusion Model

The fundamental theory that supports research in the membrane science field, can be found in the transport phenomena literature.[1,2] Dense membranes are commonly used in the field of gas separation, and the formulation of the gas transport theory in these peculiar materials has been developed by many authors.[3–11] It mainly involves the study of diffusion and sorption of small molecules in organic solids such as polymers that can form a film. The diffusion of penetrants through the dense layer, is originated by the presence of a gradient that can be of different kinds: pressure, concentration or electrical potential.[12] Considering a typical configuration in which a membrane separates two environments at different pressure and composition (**Figure 4.1**), the transport mechanism is carried out by means of a first stage of adsorption of the supplied gas on one side of the membrane (the one at higher pressure), followed by a diffusion stage up to desorption on the opposite side (the one at low pressure).
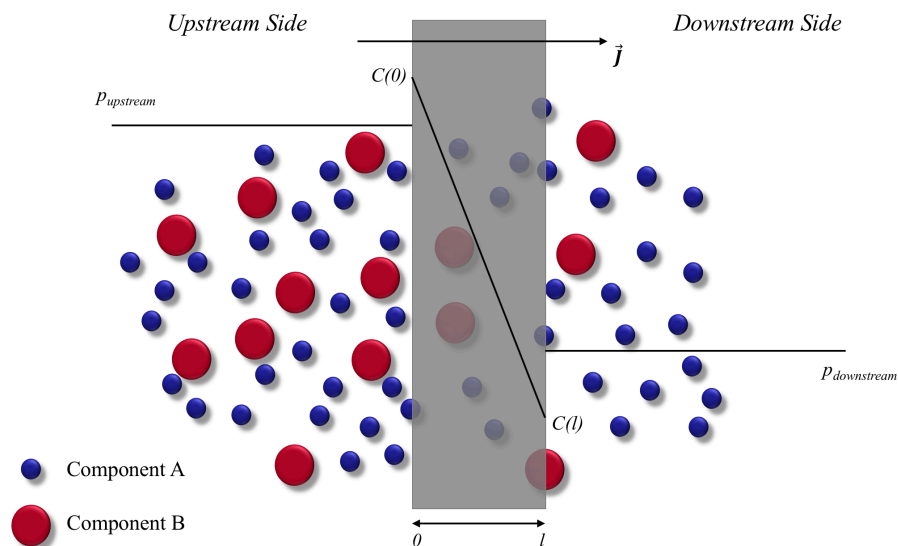
Figure 4.1: *Illustration of the solution-diffusion transport mechanism.*

These two contributions, solution and diffusion, define the transport rate of each penetrant within the membrane, thus, their possibility to be separated. The two distinct processes can be mathematically described through the *Henry's law of solubility* and the *Fick's law of mass diffusion* as follows:

$$C = \mathcal{S}p \qquad\qquad \text{Eq. (4.1)}$$

$$\bar{J} = -\mathcal{D}\bar{\nabla}C \qquad\qquad \text{Eq. (4.2)}$$

where C is the concentration of the penetrant in the film, $\mathcal{S}$ the solubility coefficient, p the pressure, $\bar{J}$ the penetrant flux through the membrane, and $\mathcal{D}$ the diffusion coefficient.

Eq. (5.8) can be rewritten in its integral form for a single penetrant i, under the hypothesis of steady state and unidirectional flux, in the following fashion:

$$J_i = \mathcal{D}_i \frac{(C_{i,1} - C_{i,2})}{l} = \mathcal{D}_i \mathcal{S}_i \frac{(p_{i,1} - p_{i,2})}{l} \qquad\qquad \text{Eq. (4.3)}$$

where l is the dimension of the membrane barrier that separates the two environment, thus the thickness.

By recalling the definition of permeability given in the previous chapter:

$$\mathcal{P}_i = \frac{J_i l}{\Delta p_i} \qquad\qquad \text{Eq. (4.4)}$$

and combining it with Eq. (4.3), we can obtain a very important relationship in the gas separation field, the *Solution-Diffusion* model.[5]

$$\mathcal{P}_i = \mathcal{D}_i \mathcal{S}_i \qquad\qquad \text{Eq. (4.5)}$$

In view of the result in Eq. (4.5), the ideal selectivity (*i.e.*, permselectivity) defined in the previous chapter, can be decoupled in two contributions, the diffusivity-selectivity ($\alpha_\mathcal{D}$), and the solubility-selectivity ($\alpha_\mathcal{S}$):

$$\alpha_\mathcal{P} = \frac{y_{i,d}/y_{j,d}}{y_{i,u}/y_{j,u}} \cong \frac{\mathcal{P}_i}{\mathcal{P}_j} = \frac{\mathcal{D}_i}{\mathcal{D}_j} \cdot \frac{\mathcal{S}_i}{\mathcal{S}_j} = \alpha_\mathcal{D} \cdot \alpha_\mathcal{S} \qquad\qquad \text{Eq. (4.6)}$$

Graham was the first one that made considerations that today still relate to the modern understanding of the solution-diffusion model. He started conducting permeation experiments in 1829, and in 1866

postulated very important observations that still hold with good approximation.[3,13] He understood that permeation was occurring by means of a dissolution step followed by a diffusion under gradient, that differences in permeability could be exploited for application in gas separation, that permeability was fairly independent on pressure, that the intrinsic properties of the membrane were independent of the thickness, and that higher temperature was increasing permeability although reducing solubility.[14]

The overall permeability, which can be easily measured with techniques described in chapter 5, depends on two terms: the thermodynamic factor, $\mathcal{S}_i$, and the kinetic factor, $\mathcal{D}_i$. Diffusivity is the kinetic parameter which quantifies the mobility of molecules through polymer chains. Being the membrane generally an isotropic medium in which molecules do not have a preferred direction of motion, each gas molecule is in constant random motion (**Figure 4.2**). What gives a direction to the transport phenomenon is the gradient under which molecules move, and this comes from simple statistics considerations.[12] The mechanism that explains how small molecules diffuse through polymer chains is often described as a sequence of distinct jumps between one cavity and another, space in which the gas molecule spends some time before thermal motion of polymer chains creates the opportunity for the molecule to jump to the adjacent cavity.[15] Diffusion is an activated process, which means that it is always enhanced by temperature. Other factors that influence diffusivity are the gas molecule size and polymer fractional free volume, as shown in **Figure 4.3a**.
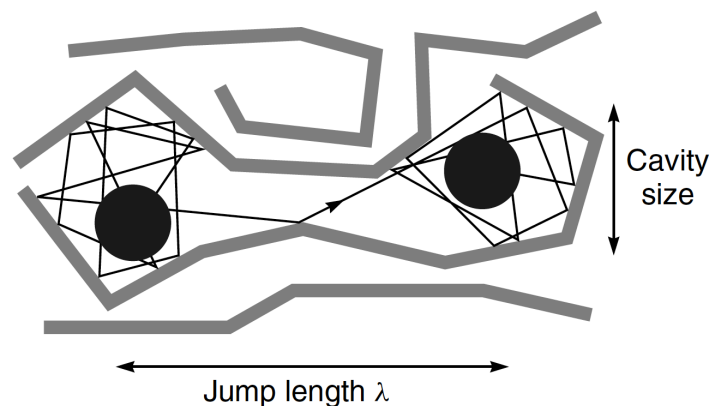
Figure 4.2: *Representation of the random motion of a gas molecule in a polymer matrix.* [15]

Solubility, instead, is the thermodynamic parameter of the permeation process. It is strongly related to the condensability of the gas molecule (*i.e.*, to its critical temperature, T_C). **Figure 4.3b** illustrates the exponential dependence between S, the solubility coefficient, and T_C. Each polymer provides a different capacity to host the penetrant, and this is based on chemical affinity, superficial adsorption and bulk absorption. Solubility gives information about the sorption uptake of the gas in the polymer. The study of solubility in polymer materials, and the ability to model and predict solubility isotherms, *i.e.*, curves in which solubility is plotted as a function of pressure at equilibrium or pseudo-equilibrium conditions, has been one of the most challenging and fascinating topics in the membrane fields. Before deepening this topic, it is important to introduce the differences between rubbery and glassy polymers, as will be done in the following section of this chapter.
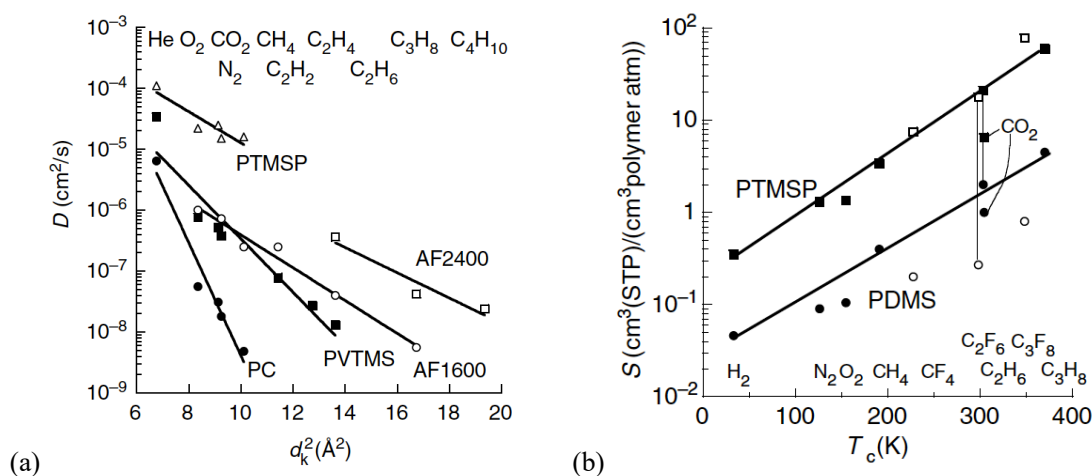
Figure 4.3: (a) Relationship between the diffusion coefficient and the kinetic diameter of different gas in glassy polymers: PTMSP, Teflon AF2400 e AF1600, PC e PVTMS; (b) Dependence of the low-pressure-limit solubility coefficient with the gas critical temperature.[16]

The solution-diffusion model breaks down when the dimension of the pores is bigger than about 10 Å, because then the free volume elements dimension is no longer within the range of the thermal motion of the polymer chains from which the membrane is made.[6,12] As represented in **Figure 4.4**, when pores' dimension increase, there is a transition from transient to permanent pores, thus from the solution-diffusion model to the pore-flow model.[12] In this case, the transport of penetrants is pressure-driven,

and the regime is not diffusion anymore, but it convection. The basic equation that describes this kind of mechanism, is *Darcy's law*, which can be written as follows:

$$\bar{J} = -K'C\bar{\nabla}p \qquad\qquad\qquad \text{Eq. (4.7)}$$

where K' is a coefficient that depends on the nature of the medium.
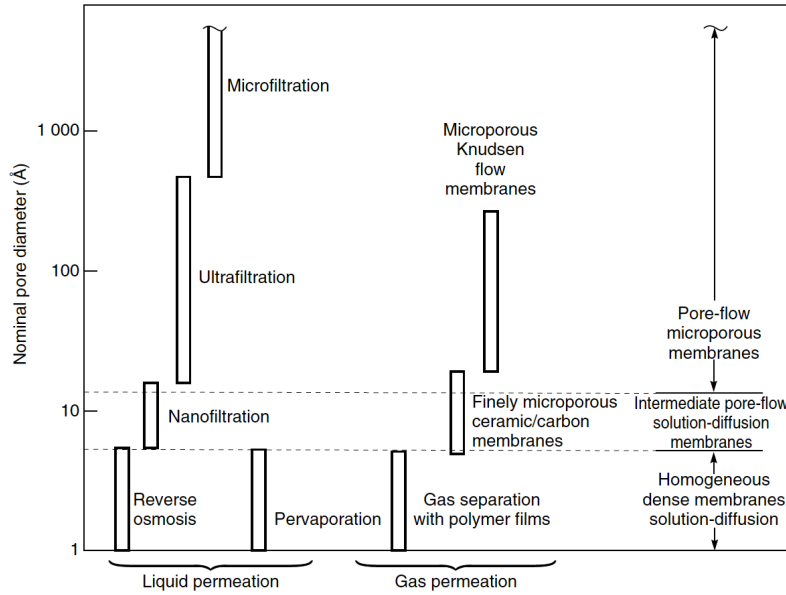
Figure 4.4*: Summary of different types of membranes based on the nominal pore size, and best theoretical model to describe the transport of penetrants therein.*

4.1.1. Energetics of Permeation, Diffusion and Sorption

As previously anticipated, diffusion and sorption depend on temperature, thus also permeability will be a function of temperature. In view of this, it is important to evaluate the energetic contributions of the diffusion, sorption and permeation processes. Diffusivity and permeability can be described by an *Arrhenius-like equation*, while sorption dependency on temperature can be formulated according to the *van't Hoff equation*, as discussed by many authors.[17–26] Analog formulations can be provided as follows:

$$\mathcal{D} = \mathcal{D}_\infty exp\left(-\frac{E_\mathcal{D}}{RT}\right) \qquad\qquad\qquad \text{Eq. (4.8)}$$

$$S = S_\infty exp\left(-\frac{\Delta H_S}{RT}\right)$$ <div align="right">Eq. (4.9)</div>

$$P = P_\infty exp\left(-\frac{E_P}{RT}\right)$$ <div align="right">Eq. (4.10)</div>

where T is the temperature and R the universal constant of gas. E_D is the activation energy of the diffusion process, the barrier that needs to be overcome for a gas molecule to make a diffusive jump from one cavity to another, and D_∞ is the temperature independent pre-exponential term, which represent the diffusion coefficient at infinite temperature. Similar considerations hold for permeability, with the essential difference that permeation is not an activated process, and different trends can be experienced as a function of temperature, since permeability results as a combination between a kinetic and a thermodynamic factor. However, the energetics of permeation, E_P, can be calculated by means of Eq. (4.10), and the pre-exponential factor, P_∞, as for diffusion, is temperature independent and represent the permeation coefficient at infinite temperature. ΔH_S is the sorption enthalpy, and it is related to the heat of absorption involved during the dissolution of gas molecules in the polymer matrix. S_∞ is the pre-exponential factor, and it stands for the solution coefficient at infinite dilution. While E_D is always a positive value, being diffusion an activated process always enhanced by increasing temperature, ΔH_S is a negative quantity since the sorption event is always exothermic. The latter statement can be explained by looking at Eq. (4.11), that comes from the definition of the Gibbs free energy:

$$\Delta G = \Delta H - T\Delta S$$ <div align="right">Eq. (4.11)</div>

When a molecule is adsorbed in solid media, it experiences a limitation of its movement, leading to a decrease of the entropy of the gas molecule since entropy is a measure of the randomness of the system, namely, ΔS is negative. Sorption is a spontaneous process, therefore it features a negative ΔG. As a consequence, from Eq. (4.11), ΔH of sorption must be negative.

In the framework of the solution-diffusion model, recalling Eq. (4.5) and combining it with Eq. (4.8), Eq. (4.9) and Eq. (4.10), the following equation can be obtained:

$$E_P = E_D - \Delta H_S$$ <div align="right">Eq. (4.12)</div>

Another equation used sometimes in the literature to evaluate the activation energy of the diffusion process, is the *Eyring equation*:

$$D \; = \; \lambda^2 \frac{k_B T}{h} e^{\frac{\Delta S_{\mathcal{D}}}{R}} e^{\frac{-\Delta H_{\mathcal{D}}}{RT}} \qquad\qquad \text{Eq. (4.13)}$$

where λ is the average jump length of the penetrant in each diffusion event, k_B is the Boltzmann constant, and h is Planck's constant. λ can be assumed to be a certain value[24], or can be estimated with molecular simulations.[27–29] Usually the average jump length is the higher the bigger the gas molecule, as well as the time the molecule spends trapped in the cavity, because statistically it is harder for a bigger species to find an opened path to diffuse in. Even though $E_{\mathcal{D}}$ and $\Delta H_{\mathcal{D}}$ do not have the same physical meaning, they are numerically very similar and both represent the enthalpic component of the diffusion barrier. Small differences in $E_{\mathcal{D}}$ and $\Delta H_{\mathcal{D}}$ come from the fact that the pre-exponential factor in the Arrhenius-like equation, $\mathcal{D}_\infty$, is assumed to be invariant over temperature, while, the front factor in the Eyring equation, $\lambda^2 \frac{k_B T}{h} e^{\frac{\Delta S_{\mathcal{D}}}{R}}$, clearly has a temperature dependence. In this dissertation, all the energetics consideration will be elaborated using the Arrhenius-like equation approach, since it is the most widely disseminated in the literature to which we compare our results.

4.2. Glassy and Rubbery Polymers

Polymers for gas separation divide in two big families of materials: glassy and rubbery. Each polymer can be either on its rubbery or glassy state, as long as the glass transition temperature, T_g, is not higher than the decomposition temperature. In that case, the material can be found just in its glassy state, below its T_g, thus it would never reach thermodynamic equilibrium.

Rubbery materials are characterized by a flexible "liquid-like" structure. From the thermodynamic point of view, they are material at equilibrium. This means that they occupy space in the most efficient way, and their density (*i.e.*, specific volume), is the one that minimizes the Gibbs free energy. No evolution over time is then expected for these materials. Probably the most studied rubber is

poly(dimethylsiloxane), PDMS[30], one of the most permeable of its category and one of the few used in industrial vapor separation application.[31]

Glassy materials, instead, are stiff and rigid. The first polymers used for gas separation applications were glassy polymer such as cellulose acetate (CA)[32] and polysulfone (PSf).[33] The transition to the glass state occurs typically when a polymer is cooled down from the melted or also from the rubber state, down to the glass transition temperature and below. This transition can be measured with different techniques, among which the most common could be *differential scanning calorimetry* (DSC). The transition from rubbery to glassy state involves change in heat capacity, but does not involve latent heat because there is no phase change, contrary to melting or crystals formation. For this reason, it is a second order transition. In a specific volume-temperature graph, **Figure 4.5**, it can be seen that it appears as a discontinuity in the slope of specific volume, v, departing from the set of values in red that represent the specific volume at equilibrium. Struik[34] defined glassy amorphous materials as *solidified supercooled liquids*, for whom available thermal energy is not enough to allow chain motion to reach equilibrium. As a consequence, these materials are not at the thermodynamic equilibrium, and their structure and properties, subsequently, change in a measurable manner over time. This phenomenon is called physical aging and it will be further discussed in the following section.
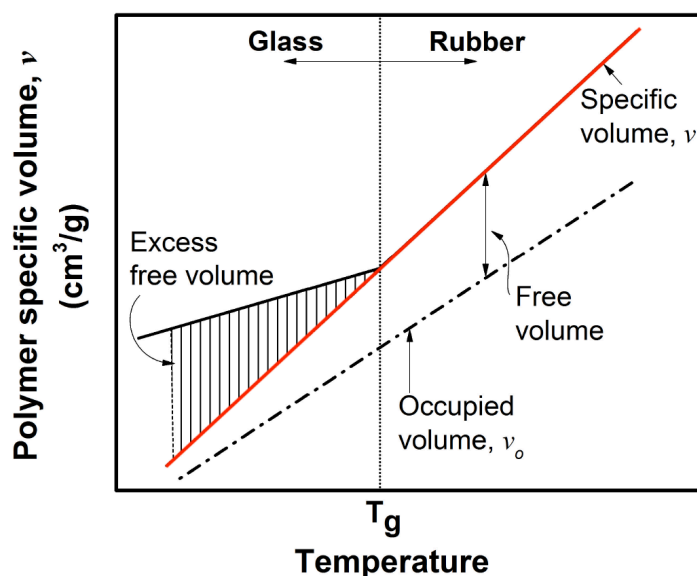
Figure 4.5: *Specific volume of the polymer as a function of temperature, above and below the glass transition.*

Glassy and rubbery polymers have very different transport properties. In **Figure 4.6** three plots are shown from Freeman and Pinnau[31] in which the authors compared a glassy polymer, PSf, and a rubbery material, PDMS, to summarize the main differences. Rubbery materials have weak size-sieving ability, as can be seen in **Figure 4.6a**, while thanks to rigidity of the polymer chains, glassy materials can efficiently separate molecules based on their size. In terms of diffusivity, PSf covers 6 orders of magnitude from the quickest and smallest gas, helium, to butane, the biggest and slowest penetrant tested. Diffusivity is lower in glassy polymers because molecules need to wait for the internal motion of the rigid polymer chains to move from a free volume element to another. In terms of solubility, many polymers reveal that the logarithmic of gas solubility coefficients, follows a linear trend when plotted against critical temperature over short ranges of penetrant condensability (**Figure 4.6b**). PSf and PDMS have similar solubility-selectivity, since the slope of the two fitting lines is comparable. However, the glassy material has higher solubility coefficient. The combination of the two quantities described contribute to the overall permeability observed in **Figure 4.6c**. As for diffusivity, PSf revealed to be less permeable, but at the same time much more selective than PDMS. Recent developments in the synthesis of glassy polymers, provided the membrane science community with materials capable of surpassing most of the rubbery polymers such as PDMS both in terms of selectivity and permeability.
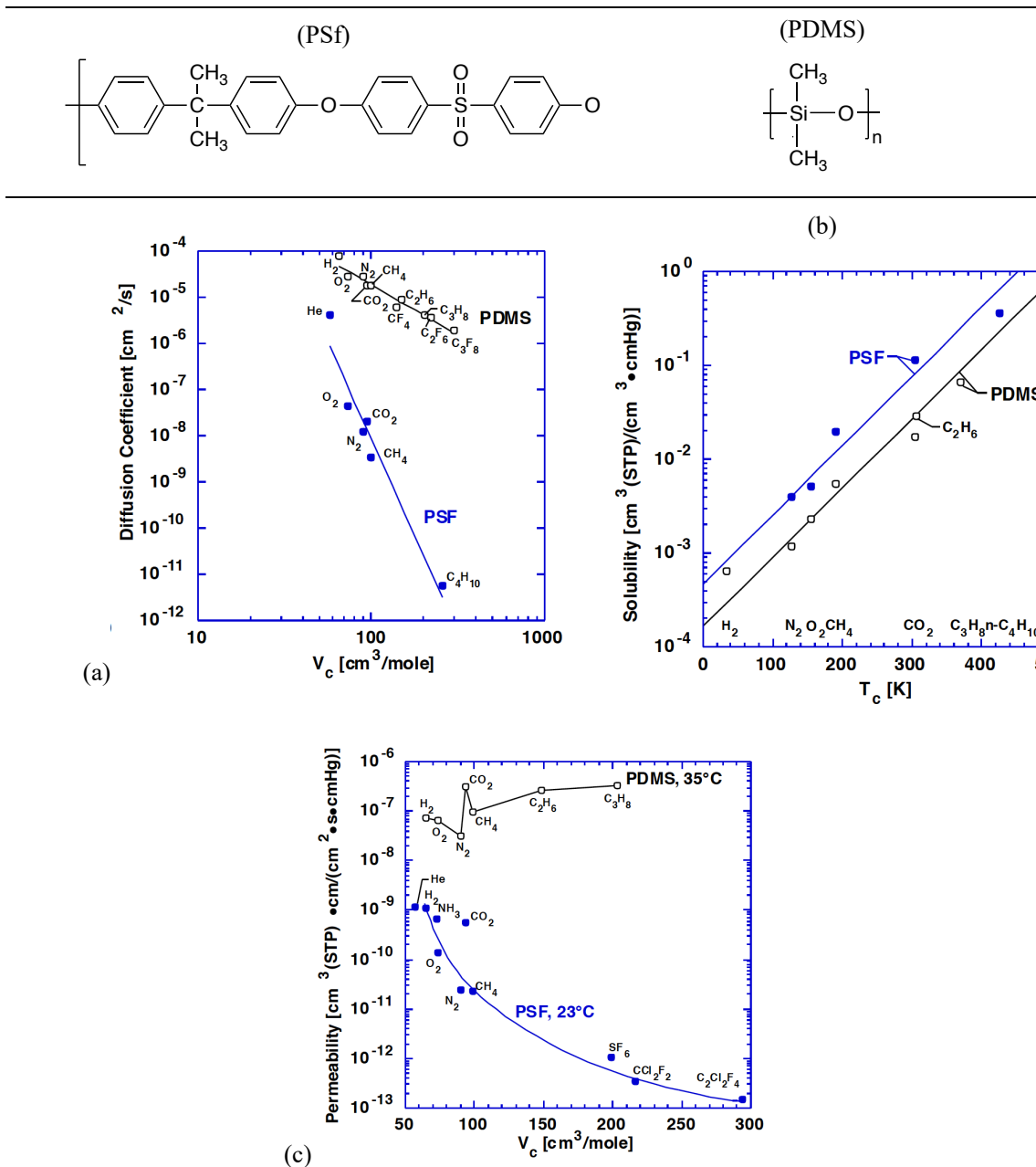
Figure 4.6: *Differences between the transport propertied of a rubbery polymer, PDMS, and glassy polymers, PSf: (a) diffusivity, (b) solubility, and (c) permeability.*[31] *Chemical strictures of the polymers represented on top of the figure.*

4.2.1. Physical Aging

Long-term stability is one of those features, besides high permeability and selectivity, that companies are looking for when it comes to gas separation application with membrane technologies. However, the non-equilibrium state that glassy polymers feature, as discussed in the previous section, causes physical properties, including gas transport properties, to drift with time towards a seemingly unattainable equilibrium in a process known as physical aging.[34–43] The easiest way to visualize this phenomenon, is describing it as a densification process of the polymer matrix from the non-equilibrium density to the thermodynamic equilibrium specific volume, represented by the red line in **Figure 4.5**. Many studies had tried to mitigate the aging to happen[44–46], however aging is still a non-solved problem, besides being an interesting phenomenon to be studied from the fundamental point of view.

The fractional free volume (FFV) is defined as follows:

$$FFV = \frac{v - v_0}{v}$$

Eq. (4.14)

where v is the specific volume of the material that can be experimentally measured, while v_0 is the volume theoretically occupied by the polymer chains, that can be calculated by mean of the group contribution theory proposed by Bondi.[47] In this framework, v_0 is calculated by considering the van der Waals volume of the polymer chain as $1.3v_{pol}^{vdW}$, where the constant 1.3 comes from the Bondi's approximation, and derives from the packing density estimation. As illustrated by the most simple formulation of the *Free Volume Theory* (FVT)[48–51], FFV can be correlated to the transport properties as follows:

$$\mathcal{D}_i = \mathcal{D}_{i,0} exp\left(-\frac{\beta_i}{FFV}\right)$$

Eq. (4.15)

$$\mathcal{P}_i = A_i exp\left(-\frac{B_i}{FFV}\right)$$

Eq. (4.16)

where B_i is the penetrant-free volume interaction parameter, $\mathcal{D}_{i,0}$ and β_i are specific parameters for the gas-polymer pair considered. The pre-exponential factor A_i can be further elaborated as follows:

$$A_i = A_{i,0} exp \left(-\frac{E_{p,i}}{RT} \right)$$ Eq. (4.17)

where $A_{i,0}$ represent the specific parameter for the gas-polymer pair and $E_{p,i}$, as already seen in the previous section, is the energetic contribution associated to the permeation process.

An important technology to evaluate FFV that makes a step further and allows for the determination of its distribution in space providing essential information related to the connectivity of the free volume elements, is the positron annihilation lifetime spectroscopy (PALS).[52–54]

The most permeable polymer ever synthesized[55], poly(1-trimethylsilyl-1-propyne), PTMSP, has never found a suitable industrial application because of the rapid physical aging that can occur for years after casting into films.[42] The main reason why this happens, is because this polymer features a very high excess fractional free volume, well represented in **Figure 4.5**, that tends to relax over time even at temperature far below T_g.[56] In the case of PTMSP, almost one-third of its volume consists in unoccupied space.[56] Even though Olivieri *et al.*[46] proposed a strategy that could reduce its aging behavior, still it is not completely eradicated. Newly synthesized polymers of intrinsic microporosity (PIMs), which exceptional properties made a breakthrough in the last 15 years, particularly suffer from this evolution of properties over time.[56] They are sometimes categorized as "super-glassy" materials containing significantly larger excess free volumes than conventional low-free-volume polymers, and have an extremely high T_g that in most of the cases cannot be measured with the traditional differential scanning calorimetry (DSC) approach, since higher than the decomposition temperature.[57] In the case of PIMs, the innovative ladder-type structure limits the chain mobility while packing during film formation, providing contorted backbones that pack inefficiently and generating a continuous network of interconnected intermolecular voids.[58]

In general, the permeability loss experienced while the polymer is aging, is bigger when the thickness of the film is smaller, as shown by Huang *et al.* in series of studies.[36–38] This is not convenient for industrial applications since thinner thicknesses are preferred to increment the flux, and makes this problem one of the most important to be addressed by the membrane science community. In this dissertation, aging studies were performed on new synthesized materials obtained through the catalytic

arene-norbornene annulation (CANAL) polymerization reaction[59–61], and through ring-opening metathesis polymerization (ROMP).[62–64]
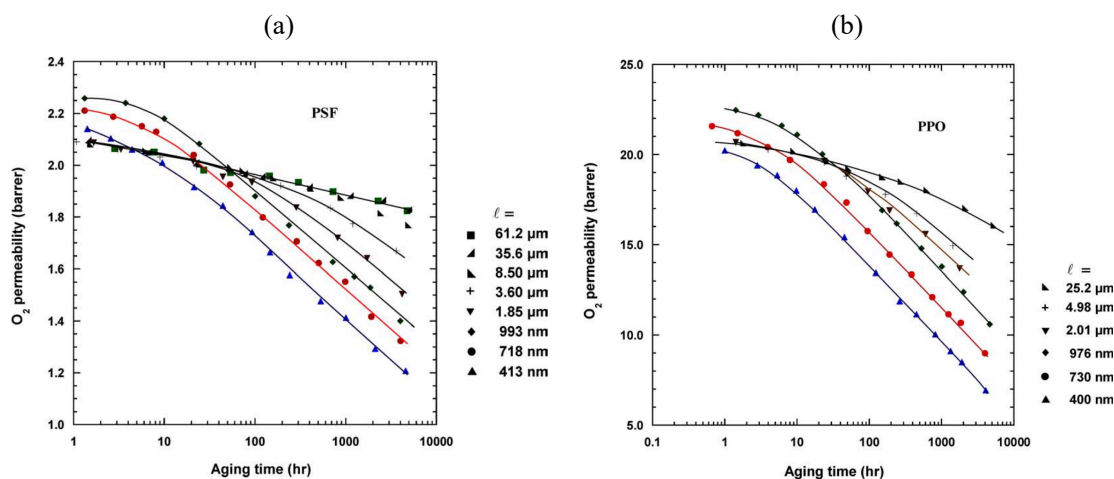
Figure 4.7: *Evolution of O$_2$ permeability over time due to physical aging as a function of the thickness for two glassy polymers: (a) Polysulfone, and (b) Poly(phenylene oxide).*[36]

4.3. Sorption in Polymers

Together with diffusion, sorption is the most fundamental property to study transport in polymer materials. It is the thermodynamic contribution to the overall flux that a membrane can provide. The adsorption stage of a penetrant in a polymer film can be described as the combination of two processes, *i.e.*, the condensation of the gas up to the conditions of saturated liquid (defined by the operating temperature), and the subsequent mixing with the polymeric phase.[65] This implies that the enthalpy of absorption, ΔH_S, can be deconvolute into a term related to the penetrant condensation, ΔH_{cond}, and a contribution of the mixing event, ΔH_{mix}. The latter term is related to the non-ideal behavior of the mixture formed by the polymer and the penetrant.

$$\Delta H_S = \Delta H_{cond} - \Delta H_{mix} \qquad \text{Eq. (4.18)}$$

The gas/polymer penetrant system can be considered at equilibrium when it minimizes its Gibbs free energy, meaning $(dG)_{T,p} = 0$. This is directly correlated to the chemical potential, μ_i, which is defined

77

as the partial molar Gibbs free energy, $\tilde{G}_i$, at fixed temperature, T, pressure, p, and quantity of all the components different than i, $n_{i \neq j}$, as follows:

$$\mu_i = \tilde{G}_i = \left(\frac{\partial G}{\partial n_i} \right)_{T,p,n_{i \neq j}}$$

Eq. (4.19)

where n_i is the number of moles of the component i. If we consider a gas phase in equilibrium with a polymer/gas phase, combining Eq. (4.19) and the constraint for the Gibbs free energy at equilibrium, the following equation holds at equilibrium:

$$\mu_i^G(T,p) = \mu_i^S(T,p,\omega_i)$$

Eq. (4.20)

where μ_i^G is the chemical potential of species i in the gas phase, μ_i^S is the chemical potential of species i in the polymer/gas phase, and ω_i is the mass fraction in the polymer phase. **Figure 4.8** represents the situation described above, where C_i^G and C_i^S are the concentration of the penetrant i in the gas phase and in the polymer/gas phase, respectively. The sorption problem is symmetric, thus l represent the thickness of the film.
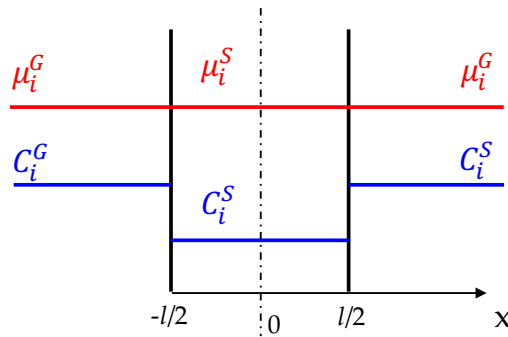
Figure 4.8:Concentration and chemical potential profile of a gas phase in equilibrium with a polymer/gas phase.

4.3.1. Lattice Fluid Models: Equilibrium and Non-Equilibrium

4.3.1.1.   Flory Huggins and Sanchez Lacombe EoS

The formulation of equilibrium described in the previous section implies that, once temperature and pressure are assigned, the specific volume of a system, v, is uniquely defined. This is the typical case of rubbery polymers, being materials at equilibrium, as described in section 4.2. Sorption in these systems can be evaluated properly by means of Equations of State (EoS) and Activity Coefficient approaches.

For the first time in the '40s, Flory and Huggins[66–68] proposed a description of polymer solutions as a lattice. The problem was approached making use of statistical mechanics and not classical thermodynamics. It was assumed a potential with rigid, hard spheres with a face centered cubic closed packed geometry, and the compressibility was ascribed to the volume change of the cells. A relevant hypothesis was the absence of empty spaces in the lattice, since the focus was on liquid systems. Sanchez and Lacombe[69,70] in the '70s, improved the Flory-Huggins theory, introducing the possibility of having empty spaces in the lattice (**Figure 4.9**). This allowed for predictions also in the vapor phase. Following this approach, it was possible to calculate heat and volume of mixing, lower critical solution temperature and the enthalpic and entropic components of the chemical potential. The system was considered compressible, and the specific volume (or density) can be evaluated under the hypothesis of thermodynamic equilibrium.
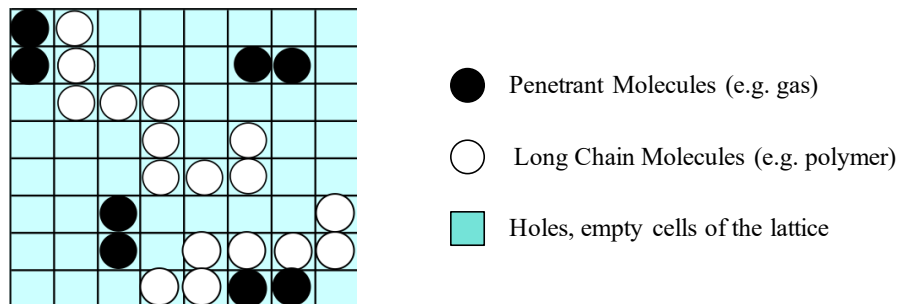
Figure 4.9: Lattice fluid representation of matter: Sanchez-Lacombe approach.

An expression for the chemical potential in the framework of the LF EoS, under the approximation of random mixing of molecules and vacant sites, is given by the following equation[70]:

$$\mu = rN\varepsilon^* \left[-\tilde{\rho} + \tilde{p}\tilde{v} + \tilde{T}\tilde{v} \left[(1 - \tilde{\rho}) \, ln(1 - \tilde{\rho}) + \frac{\tilde{\rho}}{r} \, ln \, (\tilde{\rho}) \right] \right]$$

<div align="right">Eq. (4.21)</div>

where N is the number of molecules, each of which occupies r sites in the lattice, and ε^* is the non-bounded interaction energy between two lattice cells, the energy required to create a vacancy in the lattice. The quantities $\tilde{\rho}$, $\tilde{T}$, and $\tilde{p}$ are reduced density, temperature, and pressure, respectively, and are defined as follows:

$$\tilde{T} \equiv \frac{T}{T^*}$$

<div align="right">Eq. (4.22)</div>

$$\tilde{p} \equiv \frac{p}{p^*}$$

<div align="right">Eq. (4.23)</div>

$$\tilde{\rho} \equiv \frac{\rho}{\rho^*} = \frac{1}{\tilde{v}}$$

<div align="right">Eq. (4.24)</div>

where ρ^*, T^*, and p^* are the lattice fluid parameters for the pure component: the characteristic density, temperature, and pressure of the system, respectively. In particular, ρ^* represent the close-pack mass density, which can be considered the density of the crystal as a first approximation. The LF parameters can be defined in their turn:

$$T^* \equiv \frac{\varepsilon^*}{k_b}$$

<div align="right">Eq. (4.25)</div>

$$p^* \equiv \frac{\varepsilon^*}{v^*}$$

<div align="right">Eq. (4.26)</div>

$$\rho^* \equiv \frac{M}{rv^*}$$

<div align="right">Eq. (4.27)</div>

where k_b is the Boltzmann constant and v^* represent the volume of a hole of the lattice site, and can be calculated as $v^* = RT^*/p^*$.

A substance is completely characterized from the thermodynamics point of view by either the three molecular parameters (the microscopic ones), ε^*, v^*, and r, or the three scale parameters (the macroscopic ones), T^*, p^*, and ρ^*. The LF parameters can be retrieved from experimental data. In the case of gases and liquids, usually liquid-vapor equilibrium (LVE) data are used (**Figure 4.10a**), while

for polymers, it depends on the glass transition temperature of the material. For rubbery polymers and for some of the glassy polymers, pVT equilibrium data can be measured and parameters calculated (**Figure 4.10b**), while for ultra-glassy polymers whose glass transition temperature exceeds the decomposition temperature, an alternative way to determine T^*, p^*, and ρ^*, is through infinite dilution solubility data.[71]
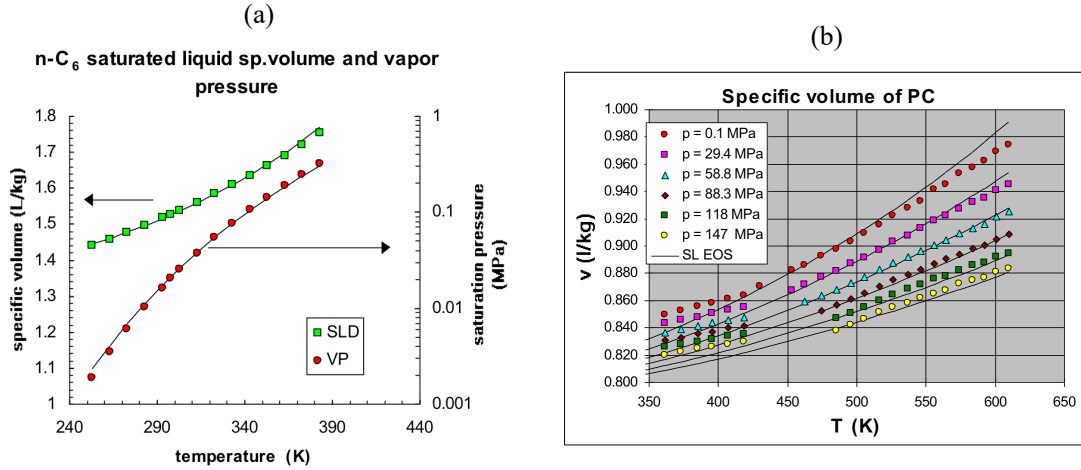
Figure 4.10: (a) LVE data for n-C6, and (b) pVT data for polycarbonate.[72,73]

When it comes to evaluate the EoS for the gas/polymer mixture, mixture LF parameters need to be evaluated from pure-component ones through with mixing rules:

$$\frac{1}{\rho^*} = \frac{\phi_1}{\rho_1^*} + \frac{\phi_2}{\rho_2^*}$$

Eq. (4.28)

$$T^* = \frac{p^*}{\rho^* \left(\frac{p_1^* \phi_1}{T_1^* \rho_1} + \frac{p_2^* \phi_2}{T_2^* \rho_2}\right)}$$

Eq. (4.29)

$$p^* = \phi_1 p_1^* + \phi_2 p_2^* - \phi_1 \phi_2 \Delta p^*$$

Eq. (4.30)

in which ϕ_1 and ϕ_2 are the volume fraction in the closed packed conditions for components 1 and 2, either gas or polymer, respectively, and Δp^* can be determined as the geometric mean as first approximation: $\Delta p^* = \sqrt{p_1^* \cdot p_2^*}$. Now all the information needed to solve the system are available. The three unknowns are the density of the gas, ρ_{gas}, the density of the polymer at equilibrium, ρ_{pol}, and the

volume fraction of the gas/polymer mixture, ϕ_i. This method can describe and predict with great accuracy solubility isotherms for rubbery polymers.

4.3.1.2. Doghieri-Sarti Non-Equilibrium Lattice Fluid (NELF)

A different approach needs to be adopted to predict the penetrant solubility in glassy polymers because equations of state cannot be applied since they are not materials at thermodynamic equilibrium. Sarti and Doghieri[7,74] revisited the LF EoS for isotropic, amorphous and homogeneous glassy polymers. The new approach resulted in the development of an expression of the Gibbs free energy of non-equilibrium, to evaluate and predict solubility in glassy materials: the Non-Equilibrium Lattice Fluid model. The approach was also generalized to other equations of state, developing a framework for the calculation of the solubility of low molecular weight species in glassy polymers called the Non-Equilibrium Thermodynamics for Glassy Polymers (NET-GP).[75] The glassy polymer/penetrant system is characterized by temperature, pressure, and composition, as for the EoS approach, plus the actual non-equilibrium (NE) density of the polymer, ρ_{pol}, to account for the NE state of the system. The actual density of the polymer is an order parameter, thermodynamically treated as a true internal state variable, which accounts for the thermal history and formation of the polymer film. The time rate of change of the order parameter is assumed to depend on the state of the system itself:

$$\frac{d\rho_{pol}}{dt} = f(T, p, \Omega_{sol}, \rho_{pol})$$

Eq. (4.31)

where Ω_{sol} is the solute-to-polymer mass ratio. The system is considered to be at its pseudo-equilibrium, which refers to a gas phase at thermodynamic equilibrium and a polymer phase which is actually not $\left((\partial G / \partial \rho_{pol})_{T,p,n_{j\neq i}} \neq 0 \right)$, but whose evolution over time is slow enough to be considered constant during the time frame of a sorption experiment: $\frac{d\rho}{dt} = f\left(T, p, \Omega_{sol}, \rho_{pol}\right) \approx 0$. Pseudo-equilibrium does not occur at a specific value of NE density, but rather it can be established in the entire range of possible

NE density values, that depend on T, p, composition, and history. Calculations are performed by imposing the equality of the chemical potentials for a fixed value for the order parameter as follows:

$$\mu_i^{NE(pol/gas)}\left(T,p,\Omega_{sol},\rho_{pol}\right) = \mu_i^{Eq(gas)}(T,p,y) \qquad \text{Eq. (4.32)}$$

where y represents the composition vector of the gas phase, $\mu_i^{NE(pol/gas)}$ is the chemical potential of species i in the polymer/gas phase, and $\mu_i^{Eq(gas)}$ is the chemical potential of species i in the gas phase. An expression for the chemical potential written for the case of N_p penetrants in the non-equilibrium polymeric phase, is given by the following equation:

$$\begin{aligned}\frac{\mu_i^{NE}}{RT} &= ln(\tilde{\rho}\phi_i) - ln(1-\tilde{\rho})\left[r_i^0 + \frac{r_i + r_i^0}{\tilde{\rho}}\right] - r_i \\ &\quad - \tilde{\rho}\frac{r_i^0 v_i^*}{RT}\left[p_i^* + \sum_{j=1}^{N_p+1}\phi_i(p_j^* - \Delta p_{i,j}^*)\right] + 1\end{aligned} \qquad \text{Eq. (4.33)}$$

An expression for the term $\Delta p_{i,j}^*$ can be the following:

$$\Delta p_{12}^* = p_1^* + p_2^* - 2(1-k_{ij})\sqrt{p_1^* \cdot p_2^*} \qquad \text{Eq. (4.34)}$$

where k_{ij} is the binary interaction parameter, which measures the departure of polymer-penetrant interactions from the geometric mixing rule predicted by Hildebrand's regular solution theory.[76,77] It can be retrieved from the analysis of pure-gas experimental data.

It is well known that polymer density changes upon sorption of big amount of condensable penetrants, such as CO_2 or vapors. Therefore, when modelling sorption of such molecules, it is important to know how density varies at different content of penetrants. Experimentally, this can be determined with dilation measurements. As an alternative to the latter, a linear relation between the polymer specific volume and the partial pressure of the penetrants can be assumed, as it is often observed experimentally for light gases.[49,78–81]

$$v_{pol} = v_{pol}^0\left(1 + \sum_{i=1}^{N_p} k_{sw,i}p_i\right) \qquad \text{Eq. (4.35)}$$

where v_{pol}^0 is the specific volume of the penetrant-free polymer, v_{pol} is the specific volume of the dilated polymer, p_i is the partial pressure of each gas in the gas phase, and $k_{sw,i}$ is the swelling coefficient. The value of $k_{sw,i}$ can be obtained fitting the pure-gas sorption isotherm in the high-pressure range where the swelling is more pronounced, after the appropriate value of k_{ij} is obtained. **Figure 4.11** shows how the proper use of density through the application of Eq. (4.35) and a non-zero $k_{sw,i}$, can improve the quality of the modelling results.
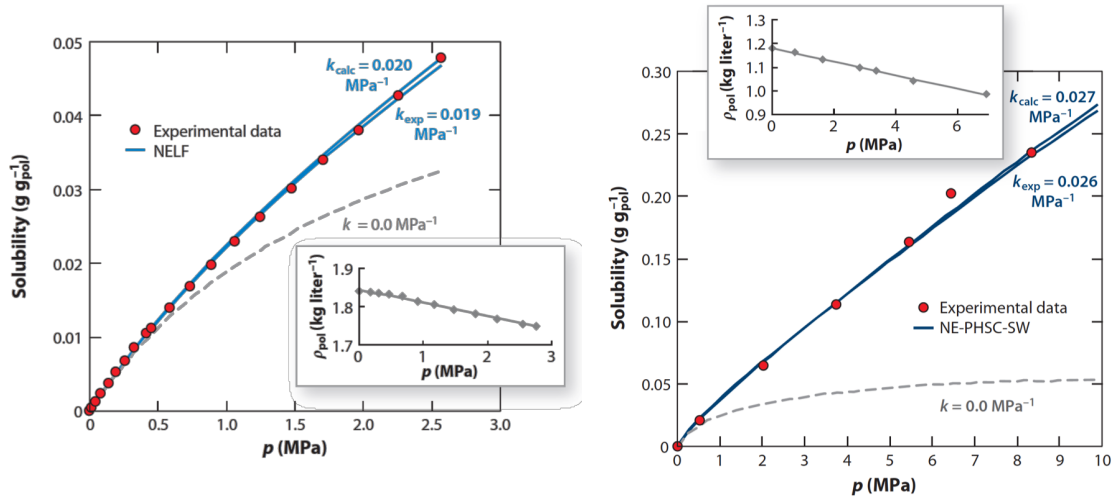
Figure 4.11: *Effect of the polymer dilation and swelling coefficient on the prediction of the solubility of CO_2 in (a) poly(methyl methacrylate) (PMMA), and (b) Teflon® AF1600.*[73]

As a final comment, from the knowledge of pure-gas data, which allows to determine k_{ij} and $k_{sw,i}$, and assuming negligible gas-gas interaction compared to gas/polymer interactions (*i.e.*, $k_{gas1/gas2} = 0$), it is possible to predict the mixed gas solubility.[82] This is a very powerful tool considering that mixed gas sorption experiments are very time consuming.

4.3.2. Dual Mode Sorption Model

The dual mode sorption (DMS) model was the first framework introduced to describe and correlate the sorption behavior of small molecules in glassy polymers.[9,83–86] The formulation is based on the

assumption that sorbed gas molecules divide in two populations, one that dissolves in the dense phase of the polymer following a liquid-like *Henry's law* equation, and one occupying the nonequilibrium excess free volume, which obeys the Langmuir curve:

$$C_i = k_{D,i}p_i + \frac{C'_{H,i}b_ip_i}{1 + b_ip_i}$$

Eq. (4.36)

where C_i is the concentration of penetrant i in the polymer, $k_{D,i}$ is the Henry coefficient, $C'_{H,i}$ is the Langmuir capacity, b_i is the affinity constant, and p_i is pressure (which can be also replaced by fugacity if high pressure makes the gas non-ideal). $k_{D,i}$ can be evaluated at the high-pressure asymptote, while $C'_{H,i}$ measures the sorption ability of the excess free volume. In fact, $C'_{H,i}$ goes to zero if T tends to T_g. The Langmuir capacity constant is usually fitted onto the low-pressure data, since Langmuir sites are favorable sorption sites and get occupied first. The three adjustable parameters need to be evaluated for each gas/polymer couple and come from a non-linear least-square best fit of experimental data. This makes the DMS model an empirical and non-predictive model. The parameters are function of temperature and they depend on the range of pressure investigated. **Figure 4.12** represents a CO_2 sorption isotherm at 35 °C in Matrimid® polyimide, measured in our laboratory in Bologna, with explicitly reported Langmuir and Henry contributions.
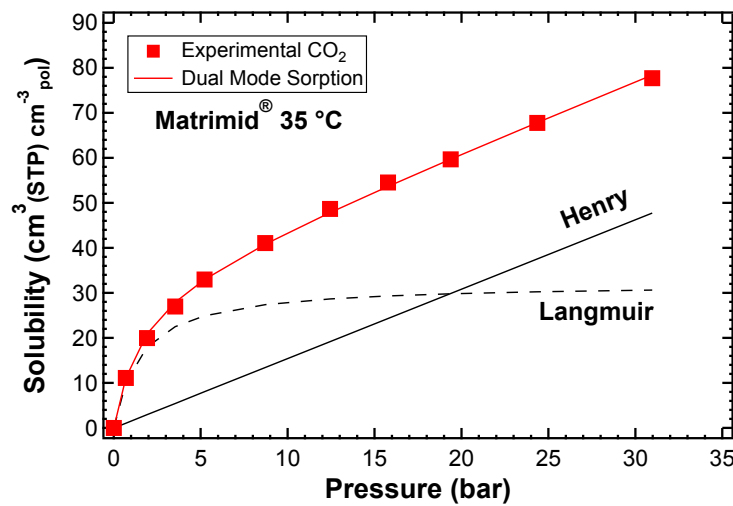
Figure 4.12: *CO_2 sorption isotherm in Matrimid® polyimide, and decoupling of the Henry and Langmuir contribution in the Dual Mode Sorption framework.*[87]

The DMS model became widely accepted by the community because it is easy to use, being explicit with respect to the concentration. Recalling Eq. (4.5) in the framework of the solution-diffusion model, the DMS model can be written also in terms of the solubility coefficient, S_i:

$$S_i = k_{D,i} + \frac{C'_{H,i} b_i}{1 + b_i p_i} \qquad \text{Eq. (4.37)}$$

4.3.3. CO_2-induced Plasticization

Plasticization is a largely investigated phenomenon in the field of membrane science.[88–91] It is related to a large amount of gas, vapor or liquid penetrant absorbed in the polymer matrix, which contributed to generate free volume in the polymer and increase the polymer chain mobility.[16] It is typically recognized through a decrease in glass transition temperature (*i.e.* softening)[88,92,93] and an increase in gas permeability as the upstream pressure increases (**Figure 4.13**).[94,95] In view of this, Koros and Hellums in the Encyclopedia of Polymer Science and Engineering defined plasticization in the following way: *"In membrane studies, plasticization is generally defined as an increase in the segmental motion of polymer chains, due to the presence of one or more sorbates, such that the permeability of both components increases and the selectivity decreases".*[96] Among small molecules commonly used to characterize materials for gas separation applications such as He, H_2, N_2, O_2, and CH_4, CO_2 is the most condensable one, *i.e.,* highest critical temperature (31.1 °C). For this reason, plasticization becomes very relevant when operating high pressure feed streams as in natural gas applications and CO_2 enhanced oil recovery (EOR).[97]
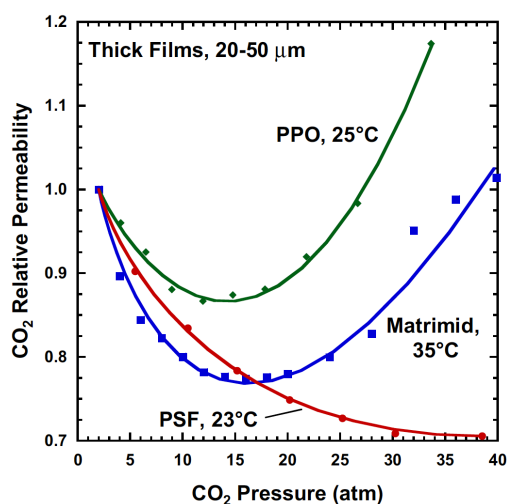
Figure 4.13: *Permeability as a function of CO_2 upstream pressure for three glassy polymers: Poly(phenylene oxide) (green diamonds), Matrimid® (blue squares), and Polysulfone (red circles).*[95]

Plasticization is often a detrimental phenomenon. One of the most undesirable consequences of plasticization, is a significant reductions of the membrane mixed gas selectivity, which makes the separation module operating out of specification.[98,99] It is important to determine to which extent materials can resist plasticization, to guarantee steady and reliable performance even when plasticizing agents can be found in high concentrations in the stream to be treated. In **Figure 4.13**, for instance, three glassy polymers which permeability was studied while exposed to increasing CO_2 pressure, can be observed. PPO and Matrimid® show the typical trend for glassy polymers that plasticize, showing a minimum in the permeability function at a pressure called *plasticization pressure*.[95] PSf, however, do not show any minimum, revealing to be more resistant to plasticization up to 40 bar. To compare different glassy polymers and define the state of the art in terms of plasticization resistance, a broad collection of CO_2-induced plasticization data are reported in **Table 4.1**. In the second column, CO_2 permeability from the first point of the plasticization curve, which usually was collected at an upstream pressure between 1 and 2 bar, is reported to give a sense of the performance of different polymers, which ranges over 5 orders of magnitude (*i.e.*, $0.5 - 35,500$ Barrer). Before the recent findings related to extremely high plasticization-resistant ROMP polymers in the framework of this PhD, polysulfone (PSf) had the highest plasticization pressure for thick films (34 bar)[89] and thin films (24 bar)[95]. A method

often used to make polymers more resistant to plasticization, is crosslinking. For instance, the permeability of a crosslinked Matrimid® film (treated at 350 °C for 30 minutes), plateaus at 3.5 Barrer at 44 bar, but there is no evidence of its behavior at higher pressures that, for instance, CF_3-ROMP reached successfully without showing the typical increasing trend.[98] More details about plasticization in ROMPs and CANALs will be provided in the following chapters.

Table 4.1: *Comprehensive review on CO_2 plasticization pressure in glassy polymers. Data refer both to data collected in the framework of this PhD (bold) and from the literature. Readapted from the SI of reference* [100].

Polymer	CO_2 Permeability @ 1-2 bar (Barrer)	Peculiarities (treatment, thickness, aging)	Plasticization pressure	Reference
CF_3-ROMP	**14477**	**119 μm, ethanol treatment, 2100 h aged**	**> 51 bar**	[100]
OMe-ROMP	**1425**	**153 μm, ethanol treatment, 300 h aged**	**> 51 bar**	[100]
PIM-1	**10558**	**119 μm, ethanol treatment, 2000 h aged**	**~27.5 bar**	[100]
Matrimid®	**9.5**	**45 μm, 200 °C overnight**	**11.6 bar**	[87]
CANAL-Me-*co*-PEO (3%)	**2120**	**87 μm, vap. methanol treat., 60 °C under vacuum overnight**	**~17.5 bar**	[101]
CANAL-trip-Et (50%)	**4900**	**184 μm, methanol treatment, 250 h aged**	**> 31 bar**	/
6FDA-1,4-trip_CF_3	19.7		> 17 bar	[102]
6FDA-1,4-trip_CH_3	9		> 17 bar	[102]
6FDA-1,4-trip_para	14.4		> 17 bar	[102]
6FDA-6FmDA	5.5		~21 atm	[103]
6FDA-6FpDA	75.5		~10 atm	[103]
6FDA-6FpDA	75.5	50/50 CO_2/CH_4	~13 atm	[103]
6FDA-6FpDA	78		~16.5 bar	[99]
6FDA-6FpDA/DABA 2:1	47	Uncrosslinked	~10.3 bar	[99]
6FDA-6FpDA/DABA 2:1	32	Crosslinked with ethylene glycol	~27.5 bar	[99]
6FDA-6FpDA/DABA 2:1	30	Crosslinked with aluminum	~15.2 bar	[99]
6FDA-6FpDA/DABA 2:1	32	Uncrosslinked, 50/50 CO_2/CH_4	~13.8 bar	[99]

6FDA-6FpDA/DABA 2:1	39	Crosslinked with ethylene glycol, 50/50 CO_2/CH_4	> 27.5 bar	[99]
6FDA-6FpDA/DABA 2:1	36	Crosslinked with aluminum, 50/50 CO_2/CH_4	~16.5 bar	[99]
6FDA-DAM:DABA 2:1			~27.5 bar	[104]
6FDA-DAM:DABA 2:1		Rapid quench from Tg+15 °C	~34.5 bar	[104]
AD 60	400	Annealed above Tg, 335 nm	~8 bar	[105]
AF 2400	2400	As-cast, 258 nm	~12 bar	[105]
AF 2400	3800	Annealed above Tg, 17 μm	~10 bar	[105]
BCPC	26		> 20 atm	[106]
BPA-PC	7.5		~31 bar	[89]
BPZ-PC	2.5		~24 bar	[89]
C-CoPIM-TB-1	5400	Pure-gas and 50/50 CO_2/CH_4	> 20 atm	[107]
C-CoPIM-TB-2	4200	Pure-gas and 50/50 CO_2/CH_4	> 20 atm	[107]
CA	6.5 - 9		11-13 bar	[89,108]
CTA	8		~10 bar	[89]
HFPC	34		~21 bar	[109]
KAUST-PI-1	2400	Pure-gas and 50/50 CO_2/CH_4	< 2 bar	[108]
KAUST-PI-5	1500	Pure-gas and 50/50 CO_2/CH_4	~12 bar	[108]
Matrimid®	9	182 nm	~6 atm	[94]
Matrimid®	9.2	20 μm	~14 atm	[94]
Matrimid®	5	Crosslinked, 30' at 350 °C	> 44 bar	[98]
P84	1		~22 bar	[89]
PC	7.5	127 μm	~34 bar	[109]
PEI	1		~28 bar	[89]
PES	3.4		~27 bar	[89]
PH	0.5		> 17 bar	[110]
PIM-1	450	200 nm	< 2 bar	[40]
PIM-1	10600	30 μm	~8 bar	[40]

PIM-1	5500-5600	50-102 μm	> 10 bar	[111,112]
PIM-Trip-TB	8400	Pure-gas and 50/50 CO_2/CH_4	> 20 atm	[107]
PMMA	0.5		< 2 bar	[113]
PPO	95	18 – 45 μm	~14 bar	[89]
PPO	41.5	192 nm	~6 bar	[95]
PSf	4.7	18 – 45 μm	~34 bar	[89]
PSf	9.2	191 nm	~24 bar	[95]
PTMSP	35500	115 μm	> 28 atm	[20]
PVF_2	0.95		< 2 bar	[113]
TMBPA-PC	15		~13 bar	[89]
TMPC	22.5		~21 bar	[109]
TPIM-1	1500	Pure-gas and 50/50 CO_2/CH_4	< 2 bar	[111]
TPIM-2	450	Pure-gas and 50/50 CO_2/CH_4	N/A, constant profile up to 15 bar	[111]

An interesting aspect of plasticization is the conditioning that high CO_2 pressure induces in the polymer matrix. Jordan *et al.*[109], investigated the hysteresis in permeation, sorption, and volume dilation in substituted polycarbonates after exposing films up to 62 bar of CO_2. In **Figure 4.14a** hysteresis occur just after a certain pressure is reached. In particular, conditioning at 300 psia is not enough to induce hysteresis, and decreasing pressure permeability follows the same trend that was observed increasing it. After reaching 600 psia, and even more after 900 psia, permeability follows a different trend, indicating that the polymer structure has changed due to plasticization. Similar conclusions apply when the property monitored is sorption, as shown in **Figure 4.14b**.
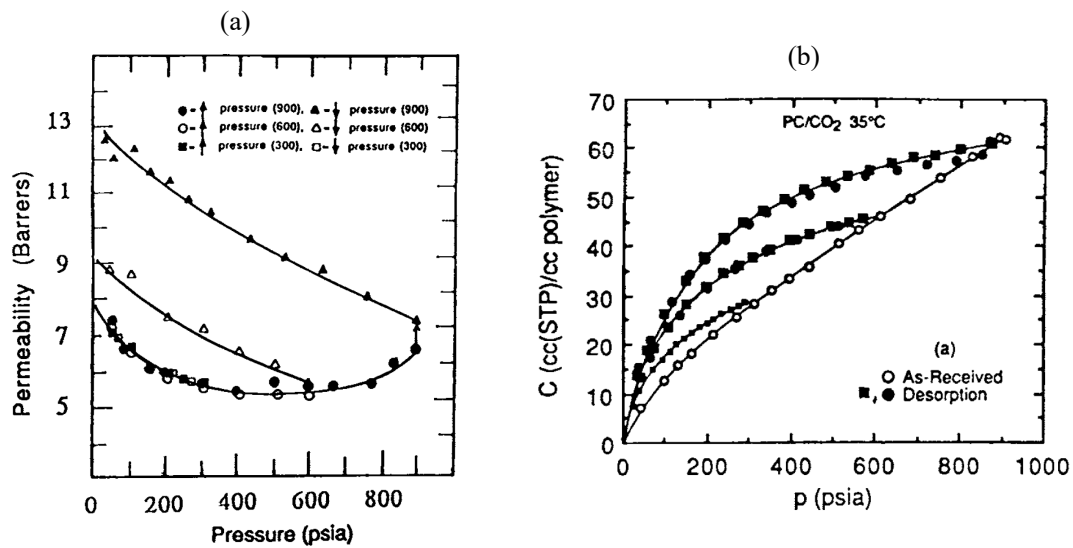
Figure 4.14: CO₂-conditioning experiments in polycarbonate (PC) at different pressures monitoring (a) permeability, and (b) solubility.[109]

4.4. Models for Permeability in Mixed Matrix Membranes

The combination of polymeric materials and inorganic or metal-organic fillers to form mixed matrix membranes (MMMs), is often indicated as one of the most promising alternatives in the field of gas separations.[114–118] A schematic representation of a MMM is reported in **Figure 4.15**. They combine the superior transport properties of fillers without compromising the processability and the mechanical properties of polymer systems. Typical fillers used given their sieving capability and sorption selectivity are zeolites[119,120] and metal organic frameworks[121,122]. Other materials investigated in the literature are fumed silica[123], graphene and graphene oxide[46,124] and covalent organic frameworks.[125]
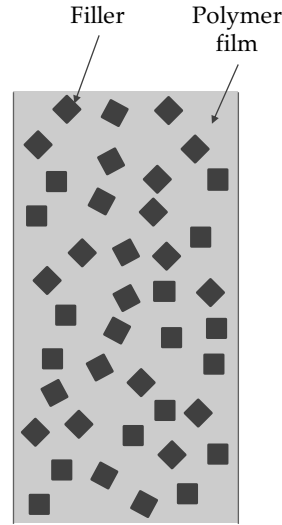
Figure 4.15*: Schematic representation of a mixed matrix membrane.*

A way to investigate the mechanism of the permeability behavior is to compare experimental data collected for MMMs and the theoretical prediction provided by several different models reported in the literature.[126,127] So far, different models have been developed for the prediction of the performance of MMMs by various theoretical expressions. The most widely used are: Maxwell-Wagner-Sillar[126], Bruggeman[128,129], and Lewis-Nielsen.[127,129,130] The Maxwell-Wagner-Sillar model was initially introduced to study electrical conductivity in composite materials.[131] It applies when the filler loading is low (*i.e.*, up to ~20 wt.%), under the assumption that the local flow path around a particle is not affected by the presence of adjacent particles. Furthermore, it is necessary that the aspect ratio of the dispersed phase is close to 1. Bouma *et al.*[132] adapted the Maxwell equation to study the permeability in composite materials (Eq. (4.38)). The Maxwell-Wagner-Sillar provides the simplest quantitative and explicit framework to predict the permeability of MMMs related to the permeabilities of the pure components and the dispersed phase (filler) volume fraction. The generalized equation looks as follows:

$$P_{MMM} = P_{pol}\left[\frac{nP_{fil} + (1-n)P_{pol} + (1-n)(P_{fil} - P_{pol})\phi_{fil}}{nP_{fil} + (1-n)P_{pol} - n(P_{fil} - P_{pol})\phi_{fil}}\right] \qquad \text{Eq. (4.38)}$$

where P_{MMM} is the permeability of the mixed matrix membrane, while P_{pol} and P_{fil} those of the pure polymer and the pure filler, respectively. ϕ_{fil} is the volume fraction of the filler, and n is the shape factor. When $n = 1/3$, Eq. (4.38) reduces to the original Maxwell equation and the filler is considered to be spherical. For $0 \leq n \leq 1/3$, we refer to prolate ellipsoids, namely the longest axis of the filler is in the same direction of the pressure gradient applied, while for $1/3 \leq n \leq 1$, we consider oblate ellipsoids, meaning the shortest axis is in the same direction of the pressure gradient applied. $n = 1$ and $n = 0$ refer respectively to a series and a parallel two-layer model.

When the particle loading is higher that 20 wt.%, different models must be considered. The Bruggeman model was originally developed for the prediction of the dielectric constant in composite materials.[128] It is an implicit model, as reported in Eq. (4.39) that show the formulation of the model when adapted for the case of MMMs, thus it must be solved numerically.

$$P_{MMM} = P_{pol} \frac{1}{(1 - \phi_{fil})^3} \left[\frac{\frac{P_{MMM}}{P_{pol}} - \frac{P_{fil}}{P_{pol}}}{1 - \frac{P_{fil}}{P_{pol}}} \right]^3 \qquad \text{Eq. (4.39)}$$

In this framework, a random dispersion of spherical particles is considered, and the aggregation is not taken into account. On the other hand, it takes into account that nearby particles influence the flow pattern, and this is the reason why it can be applied when the particle loading is slightly higher than 20 wt.%.

The Lewis-Nielsen model, Eq. (4.40), originally developed for the prediction of the elastic modulus of particulate-reinforced composites[130], can be adapted for the prediction of the permeability of MMMs at high particle loadings as follows:

$$P_{MMM} = P_{pol} \left[\frac{1 + 2\phi_{fil} \frac{(P_{fil}/P_{pol}) - 1}{(P_{fil}/P_{pol}) + 2}}{1 - \psi\phi_{fil} \frac{(P_{fil}/P_{pol}) - 1}{(P_{fil}/P_{pol}) + 2}} \right] \qquad \text{Eq. (4.40)}$$

where,

$$\psi = 1 + \left(\frac{1 - \phi_m}{\phi_m{}^2}\right)\phi_{fil} \qquad\qquad \text{Eq. (4.41)}$$

In Eq. (4.41), ϕ_m represents the maximum achievable volume fraction of the filler in the MMM. For random close packing of spheres, the value of ϕ_m is 0.64, while for loose random packing of spheres the value equals 0.59.[129]

References

[1]   R. B. Bird, W. E. Stewart, E. N. Lightfoot, *Transport Phenomena*, John Wiley & Sons, Inc., **2002**.

[2]   W. M. Deen, *Analysis of Transport Phenomena*, Oxford University Press, **2011**.

[3]   T. Graham, *Philos. Trans. R. Soc. London* **1866**, *156*, 399.

[4]   A. Fick, *London, Edinburgh, Dublin Philos. Mag. J. Sci.* **1855**, *10*, 30.

[5]   J. G. Wijmans, R. W. Baker, *J. Memb. Sci.* **1995**, *107*, 1.

[6]   B. D. Freeman, Y. Yampolskii, I. Pinnau, *Materials Science of Membranes for Gas and Vapor Separation*, John Wiley & Sons, Ltd, Chichester, UK, **2006**.

[7]   F. Doghieri, G. C. Sarti, *Macromolecules* **1996**, *29*, 7885.

[8]   J. Crank, *The Mathematics of Diffusion*, Oxford University Press, **1975**.

[9]   W. J. Koros, D. R. Paul, A. A. Rocha, *J. Polym. Sci.* **1976**, *14*, 687.

[10]   D. R. Paul, W. J. Koros, *J. Polym. Sci. Polym. Phys. Ed.* **1976**, *14*, 675.

[11]   R. M. Barrer, J. A. Barrie, J. Slater, *J. Polym. Sci.* **1958**, *27*, 177.

[12]   R. W. Baker, *Membrane Technology and Applications*, **2004**.

[13]   V. Stannett, *J. Memb. Sci.* **1978**, *3*, 97.

[14]   E. C. Suloff, Sorption Behavior of an Aliphatic Series of Aldehydes in the Presence of Poly(Ethylene Terephthalate) Blends Containing Aldehyde Scavenging Agents., Virginia Polytechnic Institute and State University, **2002**.

[15]   E. Smit, M. H. V. Mulder, C. A. Smolders, H. Karrenbeld, J. van Eerden, D. Feil, *J. Memb. Sci.* **1992**, *73*, 247.

[16]   S. Matteucci, Y. Yampolskii, B. D. Freeman, I. Pinnau, *Mater. Sci. Membr. Gas Vap. Sep.* **2006**, 1.

[17]   P. Meares, *J. Am. Chem. Soc.* **1954**, *76*, 3415.

[18]   T. Masuda, Y. Iguchi, B.-Z. Tang, T. Higashimura, *Polymer (Guildf).* **1988**, *29*, 2041.

[19]   T.-H. Kim, W. J. Koros, G. R. Husk, *J. Memb. Sci.* **1989**, *46*, 43.

[20]   R. Srinivasan, S. R. Auvil, P. M. Burban, *J. Memb. Sci.* **1994**, *86*, 67.

[21]   P. Li, T. S. Chung, D. R. Paul, *J. Memb. Sci.* **2014**, *450*, 380.

[22] W. . Koros, D. . Paul, G. . Huvard, *Polymer (Guildf).* **1979**, *20*, 956.

[23] Y. Yampolskii, S. Shishatskii, A. Alentiev, K. Loza, *J. Memb. Sci.* **1998**, *148*, 59.

[24] R. M. Barrer, *Trans. Faraday Soc.* **1942**, *38*, 322.

[25] M. Moaddeb, W. J. Koros, *J. Memb. Sci.* **1997**, *125*, 143.

[26] P. M. Budd, N. B. McKeown, B. S. Ghanem, K. J. Msayib, D. Fritsch, L. Starannikova, N. Belov, O. Sanfirova, Y. Yampolskii, V. Shantarovich, *J. Memb. Sci.* **2008**, *325*, 851.

[27] D. Hofmann, L. Fritz, J. Ulbrich, C. Schepers, M. Bhning, *Macromol. Theory Simulations* **2000**, *9*, 293.

[28] D. Hofmann, L. Fritz, J. Ulbrich, D. Paul, *Comput. Theor. Polym. Sci.* **2000**, *10*, 419.

[29] W. Fang, L. Zhang, J. Jiang, *Mol. Simul.* **2010**, *36*, 992.

[30] T. C. Merkel, V. I. Bondar, K. Nagai, B. D. Freeman, I. Pinnau, *J. Polym. Sci. Part B Polym. Phys.* **2000**, *38*, 415.

[31] B. D. Freeman, I. Pinnau, *Trends Polym. Sci.* **1997**, *5*, 167.

[32] H. Strathmann, P. Scheible, R. W. Baker, *J. Appl. Polym. Sci.* **1971**, *15*, 811.

[33] A. J. Erb, D. R. Paul, *J. Memb. Sci.* **1981**, *8*, 11.

[34] L. C. E. Struik, *Berichte der Bunsengesellschaft für Phys. Chemie* **1978**, *82*, 1019.

[35] L. C. E. Struik, *Polym. Eng. Sci.* **1977**, *17*, 165.

[36] Y. Huang, D. R. Paul, *Polymer (Guildf).* **2004**, *45*, 8377.

[37] Y. Huang, D. R. Paul, *Macromolecules* **2005**, *38*, 10148.

[38] Y. Huang, D. R. Paul, *J. Polym. Sci. Part B Polym. Phys.* **2007**, *45*, 1390.

[39] B. W. Rowe, B. D. Freeman, D. R. Paul, *Polymer (Guildf).* **2009**, *50*, 5565.

[40] R. R. Tiwari, J. Jin, B. D. Freeman, D. R. Paul, *J. Memb. Sci.* **2017**, *537*, 362.

[41] L. Ansaloni, M. Minelli, M. Giacinti Baschetti, G. C. Sarti, *Oil Gas Sci. Technol. – Rev. d'IFP Energies Nouv.* **2015**, *70*, 367.

[42] K. Nagai, B. D. Freeman, A. J. Hill, *J. Polym. Sci. Part B Polym. Phys.* **2000**, *38*, 1222.

[43] A. Brunetti, M. Cersosimo, J. S. Kim, G. Dong, E. Fontananova, Y. M. Lee, E. Drioli, G. Barbieri, *Int. J. Greenh. Gas Control* **2017**, *61*, 16.

[44] C. H. Lau, X. Mulet, K. Konstas, C. M. Doherty, M. A. Sani, F. Separovic, M. R. Hill, C. D. Wood, *Angew. Chemie - Int. Ed.* **2016**, *55*, 1998.

[45] C. H. Lau, P. T. Nguyen, M. R. Hill, A. W. Thornton, K. Konstas, C. M. Doherty, R. J. Mulder, L. Bourgeois, A. C. Y. Liu, D. J. Sprouster, J. P. Sullivan, T. J. Bastow, A. J. Hill, D. L. Gin, R. D. Noble, *Angew. Chemie - Int. Ed.* **2014**, *53*, 5322.

[46] L. Olivieri, S. Ligi, M. G. De Angelis, G. Cucca, A. Pettinau, *Ind. Eng. Chem. Res.* **2015**, *54*, 11199.

[47] A. Bondi, *J. Phys. Chem.* **1964**, *68*, 441.

[48] Y. Huang, X. Wang, D. R. Paul, *J. Memb. Sci.* **2006**, *277*, 219.

[49] S. S. Jordan, W. J. Koros, *Macromolecules* **1995**, *28*, 2228.

[50] A. Thran, G. Kroll, F. Faupel, *J. Polym. Sci. Part B Polym. Phys.* **1999**, *37*, 3344.

[51] A. Y. Alentiev, Y. . Yampolskii, *J. Memb. Sci.* **2000**, *165*, 201.

[52]   A. J. Hill, in *Polym. Charact. Tech. Their Appl. to Blends*, Oxford University Press, **2003**, pp. 401–435.

[53]   Y. C. Jean, P. E. Mallon, D. M. Schrader, *Principles and Applications of Positron and Positronium Chemistry*, World Scientific, **2003**.

[54]   K. ichi Okamoto, K. Tanaka, M. Katsube, O. Sueoka, Y. Ito, *Radiat. Phys. Chem.* **1993**, *41*, 497.

[55]   Y. Hu, M. Shiotsuki, F. Sanda, B. D. Freeman, T. Masuda, *Macromolecules* **2008**, *41*, 8525.

[56]   Z.-X. Low, P. M. Budd, N. B. McKeown, D. A. Patterson, *Chem. Rev.* **2018**, *118*, 5871.

[57]   H. Yin, Y. Z. Chua, B. Yang, C. Schick, W. J. Harrison, P. M. Budd, M. Böhning, A. Schönhals, *J. Phys. Chem. Lett.* **2018**, *9*, 2003.

[58]   N. B. McKeown, *ISRN Mater. Sci.* **2012**, *2012*, 1.

[59]   S. Liu, Z. Jin, Y. C. Teo, Y. Xia, *J. Am. Chem. Soc.* **2014**, *136*, 17434.

[60]   H. W. H. Lai, Y. C. Teo, Y. Xia, *ACS Macro Lett.* **2017**, *6*, 1357.

[61]   H. W. H. Lai, S. Liu, Y. Xia, *J. Polym. Sci. Part A Polym. Chem.* **2017**, *55*, 3075.

[62]   Y. Zhao, Y. He, T. M. Swager, *ACS Macro Lett.* **2018**, *7*, 300.

[63]   C. W. Bielawski, R. H. Grubbs, *Prog. Polym. Sci.* **2007**, *32*, 1.

[64]   S. T. Nguyen, L. K. Johnson, R. H. Grubbs, J. W. Ziller, *J. Am. Chem. Soc.* **1940**, *62*, 995.

[65]   G. Gee, *Q. Rev. Chem. Soc.* **1947**, *1*, 265.

[66]   P. J. Flory, *J. Chem. Phys.* **1942**, *10*, 51.

[67]   M. L. Huggins, *Ann. N. Y. Acad. Sci.* **1942**, *43*, 1.

[68]   P. J. Flory, *Principles of Polymer Chemistry*, Cornell University Press, **1953**.

[69]   I. C. Sanchez, R. H. Lacombe, *J. Phys. Chem.* **1976**, *80*, 2352.

[70]   I. C. Sanchez, R. H. Lacombe, *Macromolecules* **1978**, *11*, 1145.

[71]   M. Galizia, K. A. Stevens, Z. P. Smith, D. R. Paul, B. D. Freeman, *Macromolecules* **2016**, *49*, 8768.

[72]   P. Zoller, *J. Polym. Sci. Polym. Phys. Ed.* **1982**, *20*, 1453.

[73]   M. G. De Angelis, G. C. Sarti, *Annu. Rev. Chem. Biomol. Eng.* **2011**, *2*, 97.

[74]   F. Doghieri, G. C. Sarti, *J. Memb. Sci.* **1998**, *147*, 73.

[75]   F. Doghieri, M. Quinzi, D. G. Rethwisch, G. C. Sarti, in *Mater. Sci. Membr. Gas Vap. Sep.* (Eds.: B.D. Freeman, I. Pinnau, Y.P. Yampolskii), John Wiley & Sons, Ltd, **2006**, pp. 137–158.

[76]   J. H. Hildebrand, *J. Chem. Phys.* **1947**, *15*, 225.

[77]   J. H. Hildebrand, *Annu. Rev. Phys. Chem.* **1981**, *32*, 1.

[78]   M. G. De Angelis, T. C. Merkel, V. I. Bondar, B. D. Freeman, F. Doghieri, G. C. Sarti, *Polymer (Guildf).* **1999**, 3011.

[79]   D. S. Pope, G. K. Fleming, W. J. Koros, *Macromolecules* **1990**, *23*, 2988.

[80]   M. G. De Angelis, T. C. Merkel, V. I. Bondar, B. D. Freeman, F. Doghieri, G. C. Sarti, *Macromolecules* **2002**, *35*, 1276.

[81]   R. G. Wissinger, M. E. Paulaitis, *Ind. Eng. Chem. Res.* **1991**, *30*, 842.

[82]   M. Minelli, S. Campagnoli, M. G. De Angelis, F. Doghieri, G. C. Sarti, *Macromolecules* **2011**, *44*, 4852.

[83]   D. R. Paul, *J. Polym. Sci. Part A-2 Polym. Phys.* **1969**, *7*, 1811.

[84]   G. H. Fredrickson, E. Helfand, *Macromolecules* **1985**, *18*, 2201.

[85]   W. R. Vieth, J. M. Howell, J. H. Hsieh, *J. Memb. Sci.* **1976**, *1*, 177.

[86]   H. L. Frisch, *Polym. Eng. Sci.* **1980**, *20*, 2.

[87]   F. M. Benedetti, M. Minelli, G. C. Sarti, *To be Submitt.* **n.d.**

[88]   J. S. Chiou, J. W. Barlow, D. R. Paul, *J. Appl. Polym. Sci.* **1985**, *30*, 2633.

[89]   A. Bos, I. G. M. Pünt, M. Wessling, H. Strathmann, *J. Memb. Sci.* **1999**, *155*, 67.

[90]   T. Visser, M. Wessling, *Macromolecules* **2007**, *40*, 4992.

[91]   A. F. Ismail, W. Lorna, *Sep. Purif. Technol.* **2002**, *27*, 173.

[92]   Y. P. Handa, S. Lampron, M. L. O'neill, *J. Polym. Sci. Part B Polym. Phys.* **1994**, *32*, 2549.

[93]   Z. Zhang, Y. P. Handa, *J. Polym. Sci. Part B Polym. Phys.* **1998**, *36*, 977.

[94]   N. R. Horn, D. R. Paul, *Polymer (Guildf).* **2011**, *52*, 1619.

[95]   N. R. Horn, D. R. Paul, *Polymer (Guildf).* **2011**, *52*, 5587.

[96]   W. J. Koros, M. W. Hellums, *Encyclopedia of Polymer Science and Engineering*, John Wiley And Sons, New York, **1989**.

[97]   P. Bernardo, E. Drioli, G. Golemme, *Ind. Eng. Chem. Res.* **2009**, *48*, 4638.

[98]   A. Bos, I. G. M. Pünt, M. Wessling, H. Strathmann, *Sep. Purif. Technol.* **1998**, *14*, 27.

[99]   J. D. Wind, C. Staudt-Bickel, D. R. Paul, W. J. Koros, *Ind. Eng. Chem. Res.* **2002**, *41*, 6139.

[100] Y. He, F. M. Benedetti, S. Lin, C. Liu, Y. Zhao, H.-Z. Ye, T. Van Voorhis, M. G. De Angelis, T. M. Swager, Z. P. Smith, *Submitt. to Adv. Mater.* **2019**.

[101] H. W. H. Lai, F. M. Benedetti, M. G. De Angelis, Z. P. Smith, Y. Xia, *To be Submitt.* **n.d.**

[102] J. R. Wiegand, Z. P. Smith, Q. Liu, C. T. Patterson, B. D. Freeman, R. Guo, *J. Mater. Chem. A* **2014**, *2*, 13309.

[103] M. R. Coleman, W. J. Koros, *Macromolecules* **1999**, *32*, 3106.

[104] A. M. Kratochvil, W. J. Koros, *Macromolecules* **2008**, *41*, 7920.

[105] R. R. Tiwari, Z. P. Smith, H. Lin, B. D. Freeman, D. R. Paul, *Polymer (Guildf).* **2015**, *61*, 1.

[106] P. C. Raymond, D. R. Paul, *J. Polym. Sci. Part B Polym. Phys.* **1990**, *28*, 2103.

[107] C. Zhang, L. Fu, Z. Tian, B. Cao, P. Li, *J. Memb. Sci.* **2018**, *556*, 277.

[108] R. Swaidan, B. Ghanem, M. Al-Saeedi, E. Litwiller, I. Pinnau, *Macromolecules* **2014**, *47*, 7453.

[109] S. M. Jordan, G. K. Fleming, W. J. Koros, *J. Polym. Sci. Part B Polym. Phys.* **1990**, *28*, 2305.

[110] T. A. Barbari, W. J. Koros, D. R. Paul, *J. Polym. Sci. Part B Polym. Phys.* **1988**, *26*, 709.

[111] R. Swaidan, B. Ghanem, E. Litwiller, I. Pinnau, *Macromolecules* **2015**, *48*, 6553.

[112] P. Li, T. S. Chung, D. R. Paul, *J. Memb. Sci.* **2013**, *432*, 50.

[113] J. S. Chiou, D. R. Paul, *J. Appl. Polym. Sci.* **1986**, *32*, 4793.

[114] D. Bastani, N. Esmaeili, M. Asadollahi, *J. Ind. Eng. Chem.* **2013**, *19*, 375.

[115] R. Adams, C. Carson, J. Ward, R. Tannenbaum, W. Koros, *Microporous Mesoporous Mater.* **2010**, *131*, 13.

[116] M. A. Aroon, A. F. Ismail, T. Matsuura, M. M. Montazer-Rahmati, *Sep. Purif. Technol.* **2010**,

75, 229.

[117] J. Dechnik, J. Gascon, C. J. Doonan, C. Janiak, C. J. Sumby, *Angew. Chemie Int. Ed.* **2017**, *56*, 9292.

[118] B. Zornoza, C. Tellez, J. Coronas, J. Gascon, F. Kapteijn, *Microporous Mesoporous Mater.* **2013**, *166*, 67.

[119] A. L. Khan, A. Cano-Odena, B. Gutiérrez, C. Minguillón, I. F. J. Vankelecom, *J. Memb. Sci.* **2010**, *350*, 340.

[120] Y. Li, H.-M. Guan, T.-S. Chung, S. Kulprathipanja, *J. Memb. Sci.* **2006**, *275*, 17.

[121] A. F. Bushell, M. P. Attfield, C. R. Mason, P. M. Budd, Y. Yampolskii, L. Starannikova, A. Rebrov, F. Bazzarelli, P. Bernardo, J. Carolus Jansen, M. Lanč, K. Friess, V. Shantarovich, V. Gustov, V. Isaeva, *J. Memb. Sci.* **2013**, *427*, 48.

[122] T. Yang, Y. Xiao, T.-S. Chung, *Energy Environ. Sci.* **2011**, *4*, 4171.

[123] M. C. Ferrari, M. Galizia, M. G. De Angelis, G. C. Sarti, *Ind. Eng. Chem. Res.* **2010**, *49*, 11920.

[124] K. Althumayri, W. J. Harrison, Y. Shin, J. M. Gardiner, C. Casiraghi, P. M. Budd, P. Bernardo, G. Clarizia, J. C. Jansen, *Philos. Trans. R. Soc. A Math. Phys. Eng. Sci.* **2016**, *374*, 20150031.

[125] Z. Kang, Y. Peng, Y. Qian, D. Yuan, M. A. Addicoat, T. Heine, Z. Hu, L. Tee, Z. Guo, D. Zhao, *Chem. Mater.* **2016**, *28*, 1277.

[126] S. Rafiq, A. Maulud, Z. Man, M. I. A. Mutalib, F. Ahmad, A. U. Khan, A. L. Khan, M. Ghauri, N. Muhammad, *Can. J. Chem. Eng.* **2015**, *93*, 88.

[127] H. Vinh-Thang, S. Kaliaguine, *Chem. Rev.* **2013**, *113*, 4980.

[128] D. A. G. Bruggeman, *Ann. Phys.* **1935**, *416*, 636.

[129] G. Dong, H. Li, V. Chen, *J. Mater. Chem. A* **2013**, *1*, 4610.

[130] T. B. Lewis, L. E. Nielsen, *J. Appl. Polym. Sci.* **1970**, *14*, 1449.

[131] J. C. Maxwell, *A Treatise on Electricity and Magnetism*, Oxford: Claredon Press, London, **1873**.

[132] R. H. B. Bouma, A. Checchetti, G. Chidichimo, E. Drioli, *J. Memb. Sci.* **1997**, *128*, 141.

5. Experimental Methods

5.1. Membrane Preparation

The formation of a homogeneous and defect-free film is a crucial part on which the quality of all the transport results rely on. Polymers were casted into thick film (*i.e.*, 50 to 200 µm) by means of the solution casting technique. Thin films were not tested since most of the polymers and the composite materials investigated were novel materials never characterized before. The preparation and characterization of thin films would be for future developments.

5.1.1. PPO-based Mixed Matrix Membranes (MMMs)

Self-standing PPO (**Figure 5.1**) and MMMs films were obtained through solution casting technique. From the information regarding the particle size distribution of Zeolite 3A and ZIF-8 (see section 5.1.1.1), a thickness ranging from 80 to 120 µm was selected to be achieved. This technique requires the use of a solvent able to solubilize the polymer, to evaporate easily during the film formation, and to be completely removed from the final membrane. Chloroform, 1,1,2-trichloroethylene (TCE) and toluene were widely tested under different conditions both for polymeric membranes and for composite materials, since the choice of the solvent has been shown to affect the performance of the membranes in terms of gas separation.[1–3] Studies on PPO membranes formation have shown that a decrease in the boiling point (BP) of the solvent leads to a decrease of permeability and an increase of selectivity.[1] In addition, PPO may form crystals if the evaporation is too slow, thus a more volatile solvent ensures the formation of fully amorphous membranes.[1] In the end, chloroform (*Sigma Aldrich*, purity ≥ 99.8%) was selected as the optimal solvent, according to the criteria previously mentioned. Therefore, a similar methodology to the one developed by Aguilar-Vega and Paul[4] was applied to PPO and extended to the MMMs.

The preparation of each solution in this work began dissolving a 5 wt.% of PPO in chloroform. The use of a concentrated solution significantly reduced the sedimentation and the agglomeration of the particles during the casting step. That was because the high viscosity of the suspension could sufficiently reduce the particle mobility, as suggested by Das *et al.*.[5] The complete dissolution of the polymer in the solvent was reached through magnetic stirring for at least 2 h. This solution may be used as such to prepare pure PPO membranes and as a precursor in which adding different quantities of particle to obtain MMMs in various percentages by weight of filler in PPO. Prior to use, ZIF-8 was activated at 200 °C under vacuum overnight. Zeolite, instead, was dried in a muffle furnace at 500 °C for 4 h, as suggested by Khan *et al.*.[6] At the end of the thermal treatment, the powders were promptly mixed with the polymeric solution under stirring. When the suspension reached a homogeneous aspect, it was further sonicated for at least 4 h (*Lavo, Ultrasonic Vibrator ST-3*). The suspension was poured onto Petri dish with a diameter of 10 cm, to make sure a large area of the membrane was not affected by the edge, which is never as flat as the center of the sample. The Petri dish was heated on a hot plate at 50 °C to induce quick evaporation of the solvent (*i.e.*, 15 minutes film formation), necessary to obtain a defect-free film with a good particle dispersion and to ensure the formation of fully amorphous membranes, as revealed by DSC experiments.
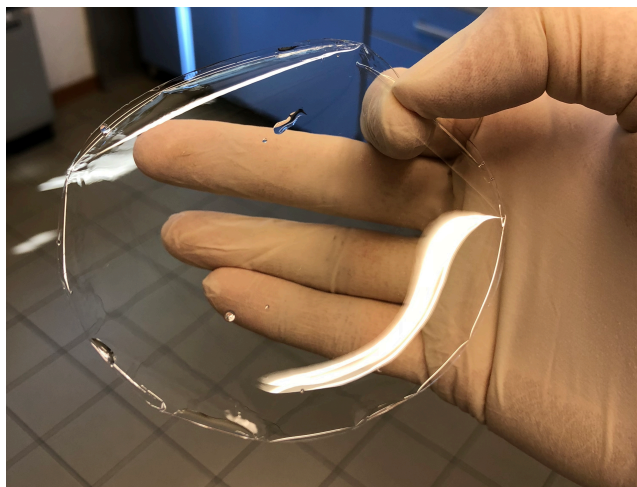
Figure 5.1: *As casted film of amorphous PPO.*[7]

5.1.1.1. Particle Size Distribution

The dimensions and the distribution of the particle size was measured by means of a laser diffraction particle size analyzer (*Fritsch, Laser Particle Sizer Analysette 22*). Zeolite 3A presented a value of the particle diameter at 50% in the cumulative distribution (*i.e.*, D50) of 4.84 µm and a D90 equal to 12.11 µm. On the other hand, *Sigma Aldrich* provided particle size information for ZIF-8 which had a D50 of 4.90 µm, quite the same of that of the zeolite. No further grinding was performed on the fillers eventually used to produce MMMs, because preliminary results showed small improvements (*i.e.*, small decrease of particle size) as a result of quite invasive milling processes which might risk to break the regular crystal cages of the materials. An estimation of the particle size can also be made through the Scanning Electron Microscopy (SEM) images as will be discussed later.

5.1.2. CANALs, ROMPs, and PIMs

CANALs, ROMPs, and PIMs all required a different approach with respect to PPO and PPO-based MMMs. For a typical polymer casting, 250 mg of polymer was dissolved in 12 g of chloroform (~2 wt. % solution), and the solution was transferred into a flat, 5-cm Petri dish with a Norton® fluorinated ethylene propylene liner (*WELCH Fluorocarbon, Inc.*). The use of the fluorinated liner was essential to prevent the polymer to stick on the glass, which sometimes could lead to a fractured film. The polymer could break because these microporous materials need to rearrange in space and they need to be free to do so. For instance, the diameter of the resulting films was 1-2 cm smaller than the diameter of the Petri dish. For some ROMP polymers, aluminum dishes were also used.[8] The Petri dish was covered with a piece of aluminum foil and a glass cover to slow down the evaporation at room temperature (**Figure 5.2**). The aluminum foil could be perforated or not, depending on the evaporation rate it was necessary to achieve. On average, the solvent evaporated in 3-5 days to form a flat film.
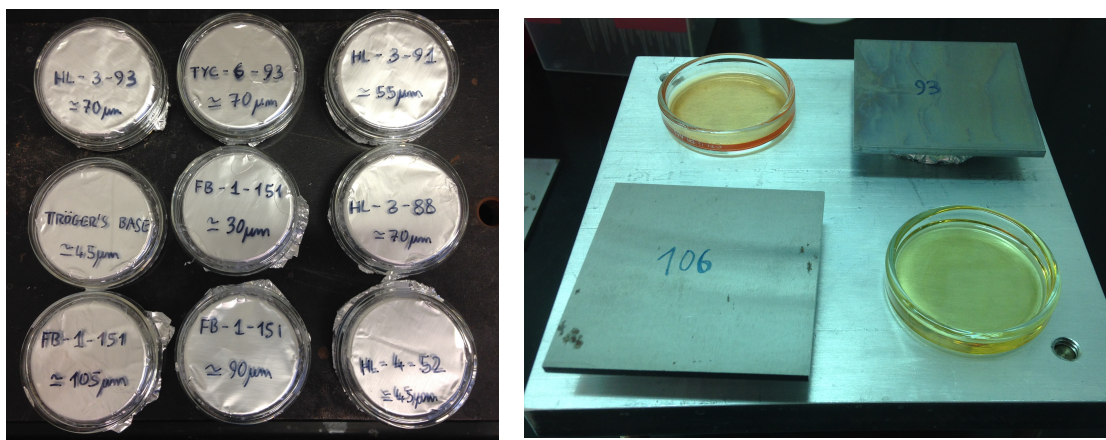
Figure 5.2:Set of Petri dishes used to prepare CANAL films through solution casting technique.

5.1.3. Post-Casting Treatments

Films need to undergo a post-casting treatment which goal is to prepare the polymer for each following test. One alternative was to perform a thermal treatment at temperature that ranged from 60 to 200 °C, depending on the material, to remove residual casting solvent and, in certain cases, also accelerate physical aging to reduce the property variation over time while testing.[9–11] An alternative very diffused in the world of PIMs is to soak polymer films in non-solvents like alcohols (*i.e.*, methanol or ethanol).[12] This is used both to remove residual solvent from the matrix when TGA experiments proves that a thermal treatment is not enough to do so, and/or to erase thermal or casting history from the film and test membranes in similar conditions.[12] Also the combination of alcohol-treatment and thermal-treatment could be an option. Some of the new polymers could not resist to be soaked in a liquid, especially before the optimization of the synthesis procedure, thus it was necessary to come up with a new technique to erase history from films. The protocol established was: thermal treatment at 120 °C for 24 h under full vacuum, vapor methanol treatment at 200 mbar (partial pressure of methanol) for 12 h, and drying step under full vacuum at 100 °C for 12 h (**Figure 5.3**).
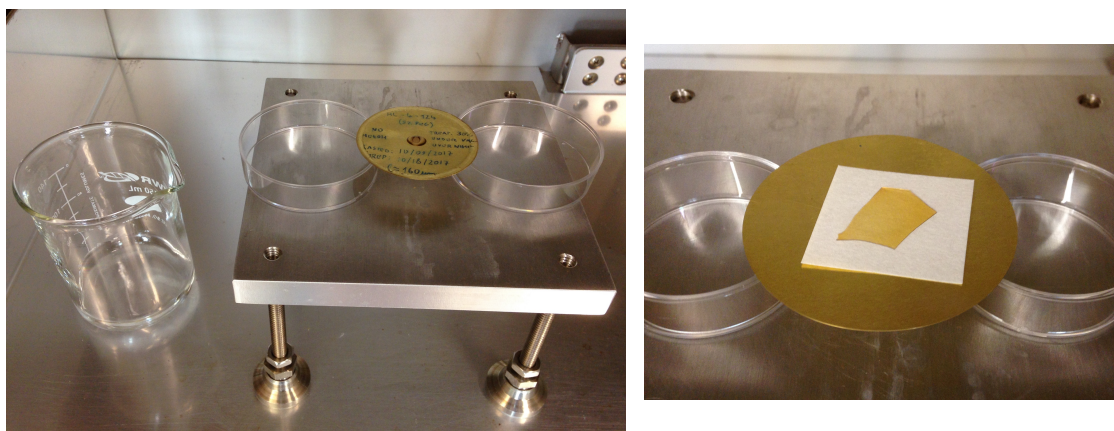
Figure 5.3:Vapor methanol treatment setup. Liquid methanol was placed next to the polymer in a Becher. The film could be already glued on the brass support (left) or not (right).

When establishing protocols, post-casting treatments were often followed by thermogravimetric analysis.

5.2. Thermogravimetric Analysis (TGA)

Thermal gravimetric analysis (*TA Instrument – 550 & Q50*) experiments were performed to investigate the thermal stability of newly synthesized materials, commercial polymers and mixed matrix membranes. While establishing new protocols for thermal treatments and solvent removal, TGA is also a remarkable tool to investigate whether residual solvent and/or humidity is still trapped in the film. Samples of about 5 to 10 mg were held in a platinum pan and were heated up to 800 – 900 °C in nitrogen atmosphere at a constant rate of 10 °C/min.

5.3. Differential Scanning Calorimetry (DSC)

Differential scanning calorimetry (*TA Instrument – Q20*) was mainly used to optimize the annealing procedure and to evaluate the presence of residual solvent and humidity in polymers and composite materials, as well as in MOFs and zeolites powders. In addition, DSC was used to evaluate the glass

transition temperature, T_g, where possible, and assess the variation of the chain mobility in mixed matrix membranes. Further, DSC provided information to determine whether the material was amorphous or semi-crystalline. The experiments were performed under N_2 flux performing two identical cycles sequentially for each sample. Each cycle consisted of heating the sample from 25 to 300 °C at a rate of 10 °C/min, then cooling it down from 300 to 25 °C at 20 °C/min and repeating it twice.

5.4. Scanning Electron Microscope (SEM)

Gas transport properties in composite membranes significantly depend on the filler distribution within the matrix and on the adhesion between the particles and the polymer. To evaluate these morphological features, field-emission gun - scanning electron microscopy (FEG – SEM) was used (*Fei Company – Bruker Corporation*, *Nova NanoSEM 450*) (**Figure 5.4**). All the film samples were fractured in liquid nitrogen, causing a brittle fracture of the membranes by bending them immediately after re-emerging from nitrogen. Being careful not to touch the cross-section of the samples, they were placed vertically each on its stub using an adhesive aluminum tape (**Figure 5.4**). The samples were metallized using a gold sputter coater (*Emitech K550*) providing a uniform dispersion of gold to make them conductive. The sprayed gold particle size was sufficiently fine (*i.e.* ≈ 10 nm) to perform magnifications up to 160,000 x, preserving the image quality.
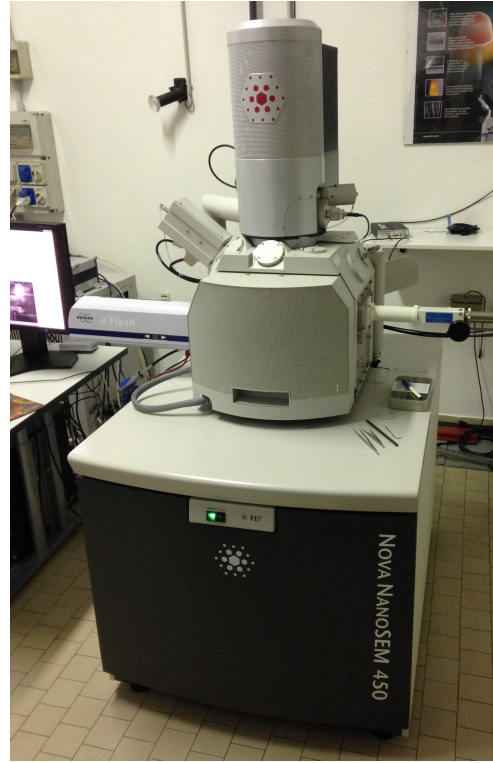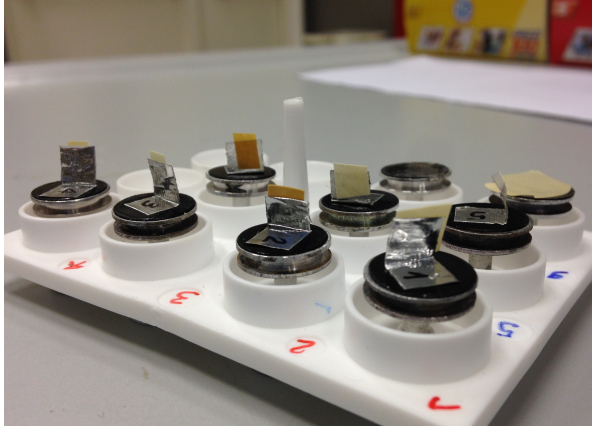
Figure 5.4: *Samples ready to be tested with FEG – SEM and Nova NanoSEM 450 equipment.*

5.5. Density Measurement

The determination of the density of the membranes, ρ_{mem}, was performed by means of the buoyancy method (Archimedes' principle), using a density kit (*MS-DNY-54*) on a high precision balance (*Mettler Toledo, NewClassic MF MS105DU*). Deionized water (*Culligan, M1 Series Commercial Reverse Osmosis Water System*) was used to determine the hydrostatic weight of the sample. A wetting agent (*Pervitro 75% 72409*) was used to avoid the formation of air bubbles on the submerged film which might compromise the measurements, introducing a negligible change in the water density. The temperature of the fluid was monitored with a thermometer (± 0.1 °C) to determine the proper density, ρ_{H_2O}, taken from the Perry's tables[13], to calculate the sample density as follows:

$$\rho_{mem} = \frac{m_{mem}^{Air}}{\left(m_{mem}^{Air} - m_{mem}^{H_2O}(T)\right)} \rho_{H_2O}(T)$$

Eq. (5.1)

where m_{mem}^{Air} is the weight of the sample measured in air while $m_{mem}^{H_2O}$ that measured when soaked in water. Accurate density values are essential to determine the volume occupied by the polymer in a pressure decay equipment while performing sorption experiments, as well as to investigate the volumetric behavior of the polymer-filler mixtures when working with mixed matrix membranes (MMMs). Further, models such as NELF[14] and Maxwell-Wagner-Sillar[15], require the knowledge of the polymer density, or the exact volumes occupied by the two phases in a composite material.

5.6. Permeability

To perform permeability measurements, the fixed-volume variable-pressure manometric technique was used.[16,17] The system was designed in-house, and the essential layout of the equipment is shown in **Figure 5.5**.
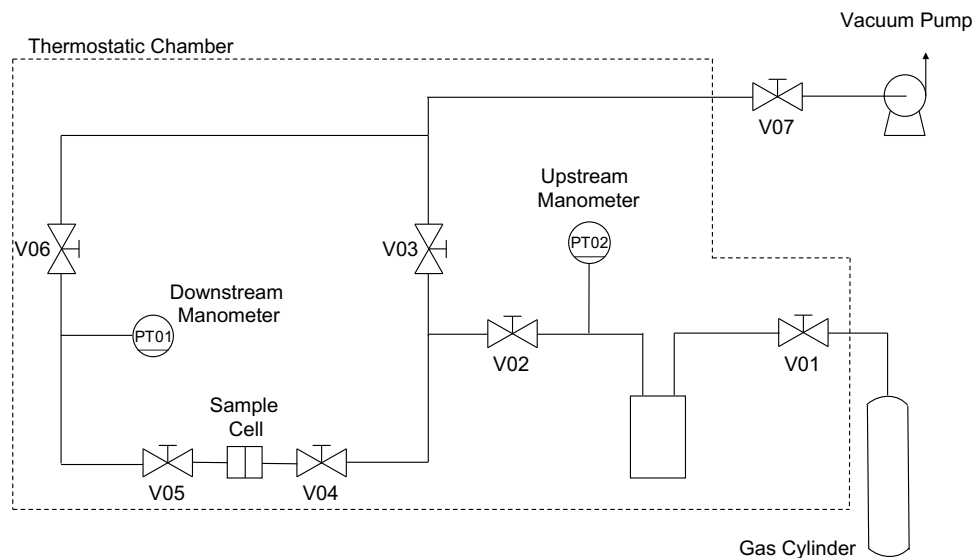
Figure 5.5*: Layout of a fixed-volume variable-pressure permeation equipment. The black dashed line indicates the volume in which temperature is controlled.*

In a typical experiment, a circular self-standing film is placed in the sample holder, a stainless-steel cell, and sealed by means of an o-ring made of Viton® to ensure the system was leak-tight. The specimen was conditioned under dynamic vacuum for at least 8 hours to remove any possible species from the

matrix such as gases and humidity coming from the exposition to air after the specific treatment the membrane underwent depending on the material. Therefore, by closing valves V06, V04 and eventually V03, the sample was isolated at static vacuum. The volume delimited by V01, V03 and V04, which contains the penetrant reservoir, was fed with the gas from the gas cylinder up to the desired upstream pressure, p_u. Once equilibrium conditions were achieved, V04 was opened to start the experiment, exposing the upstream side of the membrane to the gas. Accordingly, pressure values in the downstream side of the film started to be collected in the same moment. The upstream volume was large enough to consider p_u constant with time, despite a small physiological decrease due to gas permeation. The increase of the downstream pressure in the calibrated closed volume, V_d, between the sample holder and V06 was monitored by a capacitance manometer (PT01 – *Edwards Barocel®*) with a sensitivity of 10^{-2} mbar and an accuracy of 0.15% of the reading. In **Figure 5.6** it is represented the typical result of a permeation experiment in which the variation of downstream pressure is reported in red, and the slope of the permeation curve, dp/dt, necessary to calculate permeability as indicated in Eq. (5.5), is reported in black. The two dashed lines represent the steady-state slope dp/dt that is clearly reached after a certain time. The black line can be used to evaluate the time-lag as the intercept with the x-axis, as will be discussed in the following section.
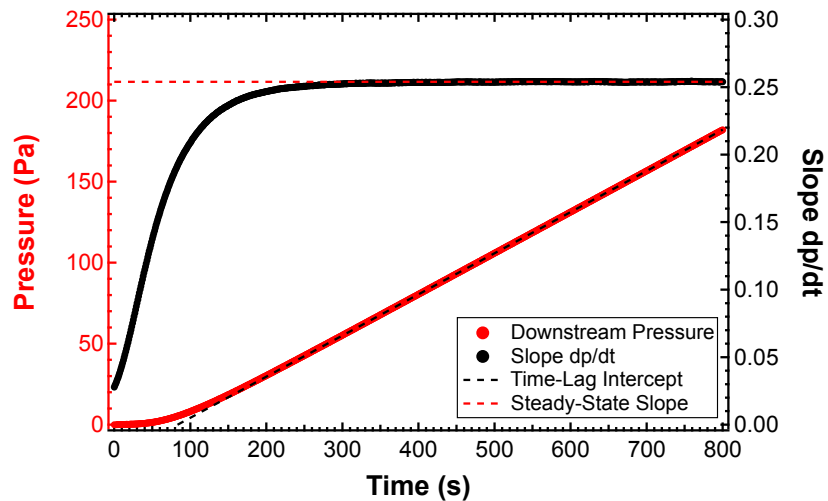
Figure 5.6: *Typical result of a permeation experiment conducted in a fixed-volume variable-pressure permeation equipment.*

Recalling some of the elements introduced in the theoretical background chapter, an expression to calculate permeability can be derived by simply solving the following set of equations:

$$\frac{dn_i}{dt} = J_i A \qquad \text{Eq. (5.2)}$$

$$p_i V_d = n_i RT \qquad \text{Eq. (5.3)}$$

$$\mathcal{P}_i = \frac{J_i l}{(p_{i,u} - \bar{p}_{i,d})} \qquad \text{Eq. (5.4)}$$

which are expressions for the flux of the penetrant i, Eq. (5.2), the ideal gas law, Eq. (5.3), and the definition of permeability ($\mathcal{P}_i$), Eq. (5.4). R is the gas constant, T is the operative temperature, l is the membrane thickness, A the membrane area, J_i the penetrant flux through the membrane, n_i the moles of the component i, $\bar{p}_d$ the average downstream pressure of the gas considered, and $p_{i,u}$ the upstream pressure. When the initial downstream pressure, p_d, is the vacuum, permeability can be evaluated at the steady-state from the linear portion of the pressure versus time (**Figure 5.6**) by using the following equation:

$$\mathcal{P} = \frac{V_d}{RT} \frac{l}{A} \frac{1}{(p_u - \bar{p}_d)} \left(\frac{dp_d}{dt}\right)_{t \to \infty} \qquad \text{Eq. (5.5)}$$

A forced ventilation thermostatic chamber (*MPM Instruments srl – Type M 150-TBR*) able to control the air temperature with an accuracy of $\pm\, 0.1$ °C was used. The uncertainty on the permeability values was calculated by considering the error committed in measuring experimentally l, $\bar{p}_d$ and V_d, by means of the propagation of error approach. The ideal permselectivity between gas A and B, $\alpha_{A/B}$, is calculated as illustrated in the introduction of this dissertation:

$$\alpha_{A/B} = \frac{y_{A,d}/y_{B,d}}{y_{A,u}/y_{B,u}} \cong \frac{\mathcal{P}_A}{\mathcal{P}_B} \qquad \text{Eq. (5.6)}$$

in which $y_{A,d}$ and $y_{B,d}$ are the molar fraction in the downstream side of the membrane of gas A and B respectively, while $y_{A,u}$ and $y_{B,u}$ those in the upstream side of the film. $\mathcal{P}_A$ is the permeability of the more permeable gas of the pair, and $\mathcal{P}_B$ is the less permeable one. $\alpha_{A/B}$ can be evaluated for each

possible gas pair, combining permeability of all the species tested. According to the solution-diffusion model, it can be divided in two contributions; the diffusivity-selectivity, $\alpha_{A/B}^D$, and the solubility-selectivity, $\alpha_{A/B}^S$, as follows:

$$\alpha_{A/B} \cong \frac{\mathcal{P}_A}{\mathcal{P}_B} = \frac{\mathcal{D}_A}{\mathcal{D}_B}\frac{\mathcal{S}_A}{\mathcal{S}_B} = \alpha_{A/B}^D \alpha_{A/B}^S \qquad\qquad \text{Eq. (5.7)}$$

Permeability of different gases such as He, H_2, CH_4, N_2, O_2, and CO_2, was measured in the framework of this dissertation at temperature ranging from 35 °C to 65 °C. The purity of gases was at or above 99.99% and they were always used as received. The order in which gases were tested, depended on the experimental details, but in a typical set up in which the transport properties of different gases were screened to provide a general characterization, the order was following the critical temperature of gases, meaning He, H_2, N_2, O_2, CH_4, and CO_2. Testing gases in membranes going from the least condensable to the more condensable, prevent any conditioning effect of the sample, since polymers undergo plasticization when exposed to high pressure of CO_2.[18–22] However, always in the framework of the general characterization, each permeability experiment was performed at an absolute upstream pressure of 1.1-1.3 bar, thus pressure was conveniently low to neglect the plasticization effect. To make sure that the membrane permeability was consistent after testing with CO_2, small gases like He and H_2 were tested again at the same conditions. Especially when working with brittle membranes, it is important to check that the film is defect-free, to consider data reliable. The technique that was adopted to verify the integrity of films, was to test gases at increasing pressures after the data acquisition was completed, then check the permeability trend. Since all the polymers tested were glassy polymers, what was expected from a defect-free film were slightly decreasing values of permeability while pressure was increasing. The decreasing trend is in general more pronounced for CO_2, given the solubility coefficient contribution that decreases more quickly than for the less condensable gases, because of the higher Langmuir capacity, especially at low pressure. **Figure 5.7** shows results from a pinhole test performed on a defect-free CANAL-10% PEO-Me copolymer film, to provide an example.[23]
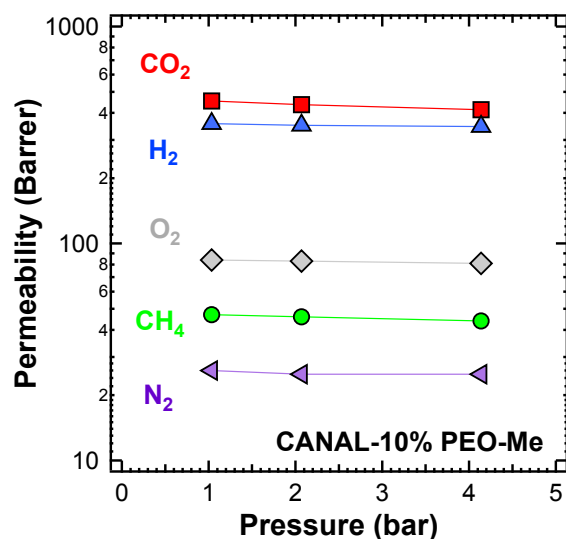
Figure 5.7*: Typical result of a pinhole test for a defect-free film.*[23]

5.6.1. Maxwell Robotics Automated System

The use of an automated permeation system (**Figure 5.8**) was implemented to perform CO_2-induced plasticization studies on ROMP polymers and CANAL ladder polymers. Being plasticization a time-dependent experiment, it is very important to control accurately the upstream pressure and the duration of each step of the curve, to get consistent data. A software developed from *Maxwell Robotics* allows to program a series of tests without the need for the operator to be in the laboratory. This way, each 30 – 60 minutes, pressure can be increased and decreased, as well as gases can be changed, so that experiment can safely run also overnight. In this particular configuration, polymer films used for permeation tests were supported by brass shim stock disks (*McMaster-Carr, 9011K4*). For the brass disks, these supports were machined to fit precisely into a 47 mm diameter filter holder (*Millipore, XX4504700*) used as a permeation cell (**Figure 5.9**). Concentric holes were bored through the disks, and polymer films were attached to the shim stock supports with 5-minute epoxy glue (*McMaster-Carr, Devcon 14240*). A series of other experiments besides plasticization were performed on ROMP and CANAL films while at the *Massachusetts Institute of Technology*, which will be reported in chapter 9 and 10.

Figure 5.8: *Maxwell Robotics automated permeation systems.*
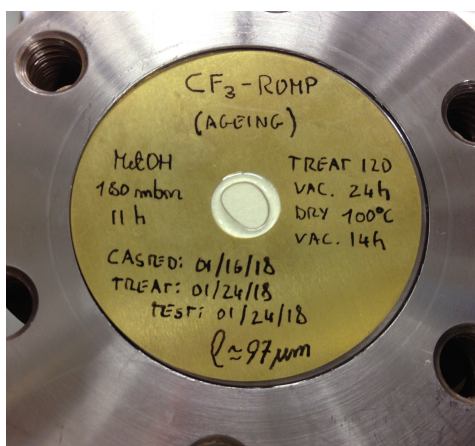
Figure 5.9: *ROMP and CANAL samples to be tested in the Maxwell Robotics apparatus. Films were glued on brass disks and placed in the cell.*

5.6.2. Diffusivity: Time-Lag Method

As discussed in the theoretical background chapter, the diffusion process can be described with the *Fick's law of diffusion*, by analogy to the *Fourier's law of heat conduction*.[24,25] The first law of diffusion can be recalled as follows:

$$\bar{J} = -\mathcal{D}\bar{\nabla}C$$

Eq. (5.8)

where $\bar{J}$ is the rate of mass transfer per unit area, C is the concentration of the diffusing penetrant, and $\mathcal{D}$ the diffusion coefficient. From Eq. (5.8), the fundamental equation of diffusion in an isotropic medium can be derived, obtaining Eq. (5.9)[25]:

$$\frac{\partial C}{\partial t} = \mathcal{D} \cdot \left(\frac{\partial^2 C}{\partial x^2} + \frac{\partial^2 C}{\partial y^2} + \frac{\partial^2 C}{\partial z^2} \right)$$

Eq. (5.9)

which can be reduced to the second law of diffusion if the diffusion is one-dimentional, namely the gradient concentration is only along the x-axis:

$$\frac{\partial C}{\partial t} = \mathcal{D} \cdot \frac{\partial^2 C}{\partial x^2}$$

Eq. (5.10)

The solution of Eq. (5.10) depends on the problem it is applied to. In the case of a permeation experiment, we consider a film that is in contact with gas at a certain pressure, p_1, on the upstream side, and on the other side it has full vacuum, $p_2 = 0$. At each time < 0, the concentration is considered to be uniform and equal to zero, $C_0 = 0$, across the thickness of the membrane, l. The assumption is reasonable considering that the film is kept under full vacuum for at least 8 hours before performing a permeation test. At $t = 0$, the upstream side of the film is put in contact with the gas at p_1, and the concentration at the interface, $x = 0$, is assumed to be identical to the concentration at equilibrium for that gas in that polymer at that pressure and temperature: $C_1 = C_1(p_1, T)$. The penetrant diffusion starts at $t = 0$, and the shape of the concentration profile in the film starts changing as shown in **Figure 5.10**, until reaching a pseudo-state equilibrium. To derive an equation that describes that evolution of the concentration profile that depends on position and time, $C = C(x, t)$, Eq. (5.10) needs to be solved using the following boundary conditions:

$$\begin{cases} \dfrac{\partial C_i}{\partial t} = \mathcal{D}_{i,j} \cdot \dfrac{\partial^2 C_i}{\partial x^2} \\ C = C_0, t = 0, 0 < x < l \\ C = C_1, t \geq 0, x = 0 \\ C = C_2, t \geq 0, x = l \end{cases}$$
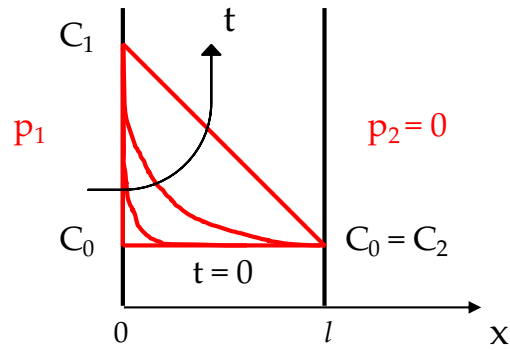
Figure 5.10: *Illustration of the transient process occurring during a permeation experiment from C_0 across the thickness of the film at time zero, to C_1 on a side and C_2 on the other side at steady state. Boundary conditions to solve the second law of diffusion are reported.*

There are two options to solve Eq. (5.10): (1) separation of variables and (2) the Laplace transform. The general solution of the equation, $C = C(x,t)$, is given in the form of a trigonometrical series.[25] Its partial derivative, $\partial C_i/\partial x$, can be calculated and substituted in the first law of diffusion for a one-dimentional problem calculated at $x = l$ to evaluate the flux at the downstream interface, $J_{x=l}$:

$$J_{x=l} = -\mathcal{D}_{i,j}\left(\frac{\partial C_i}{\partial x}\right)_{x=l} \qquad\qquad \text{Eq. (5.11)}$$

An equation for the total amount of diffusing penetrant passed through the membrane from time zero to t, Q_t, can be then calculated by integrating the equation of local flux:

$$Q_t = \int_0^t J_{x=l} \cdot dt \qquad\qquad \text{Eq. (5.12)}$$

As previously indicated, in a typical permeation experiment, it can be assumed that $C_0 = C_2 = 0$. After implementing the latter boundary condition, a solution of the equation for $t \to \infty$ can be found, and approaches asymptotically the following expression:

$$Q_t = \frac{\mathcal{D}C_1}{l}\left(t - \frac{l^2}{6\mathcal{D}}\right) \qquad\qquad \text{Eq. (5.13)}$$

The intercept of this equation with the time-axes can be observed in **Figure 5.11** and is the following equation:

$$\theta_L = \frac{l^2}{6\mathcal{D}}$$

Eq. (5.14)

which is the expression more often implemented to calculate the diffusion coefficient, $\mathcal{D}$, with the time lag method.
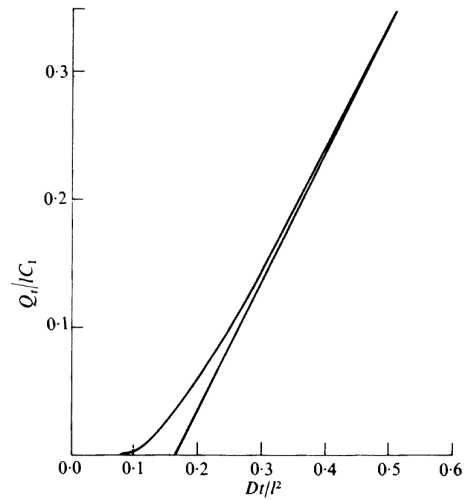
Figure 5.11: Transient flow of a penetrant through a plane sheet approaching steady-state for the case in which $C_0=C_2=0$.[25]

The time-lag, θ_L, can be evaluated for all the gases by extrapolating the linear portion of the pressure versus time graph to the time axis, as it was shown in **Figure 5.6**. It is a measure of the characteristic time required to the gas molecule to dissolve in the polymer matrix and to diffuse through it. Thus, θ_L can be related to the diffusivity, $\mathcal{D}$, through the following equation:

$$\mathcal{D} = \frac{l^2}{6\theta_L}$$

Eq. (5.15)

5.7. Solubility

Solubility experiments were performed both in the pure-gas and the mixed-gas cases. In particular, He, H_2, N_2, O_2, CH_4, and CO_2 sorption isotherms were determined in a series of polymers and mixed matrix

membranes, while the only mixture tested was CO_2/CH_4 on a selection of polymers that will be discussed in the dedicated chapter.

5.7.1. Single-Gas Pressure Decay

The single gas solubility measured for different gases in different materials, was evaluated at 35 °C by means of an in-house pressure decay apparatus which scheme is represented in **Figure 5.12**.[26–28] It is a manometric technique, and the amount of gas sorbed is determined by recording the decrease of pressure in a closed volume while the gas diffuses into the sample. In a typical configuration, about 0.3 - 0.6 g of sample were placed in the sample chamber and degassed for at least 8 hours. When the sample was free or residual species, the experiment starts by feeding a known amount of gas in the pre-chamber. After having reached the equilibrium, namely the pressure measured was constant with time, valve V03 was opened allowing the gas to expand in the sample chamber. The gas uptake was measured indirectly with a mass balance (Eq. (5.16)) by measuring the pressure decrease due to the sorption, and the solubility at equilibrium was determined when the mass uptake reached an asymptotic value, as shown in **Figure 5.13**. To accurately describe a sorption isotherm that covers the desired pressure range, a sufficient number of sorption points need to be measured. To do so, the strategy normally implemented because it allows saving time without losing accuracy, is performing so-called *differential experiments*, in which sorption is not measured each time on degassed fresh sample. In this configuration, once the equilibrium is reached at a given pressure, V03 is closed to isolate the sample, and more gas is loaded in the pre-chamber, stabilized, and then expanded in the sample chamber to get another equilibrium point at higher pressure. It is called "differential" because it does not measure the absolute number of moles in the polymer, but just the difference from the previous step at equilibrium, as indicated in Eq. (5.16).

$$n_i^{pol} = n_{i-1}^{pol} + n_{i-1}^{sc} + n_{i-1}^{pre} - n_i^{tot} \qquad \text{Eq. (5.16)}$$

were the step *i* represent the system after V03 opens to reach the new equilibrium and *i-1*, instead, represents the system before V03 opens. As an example, $n_i^{tot} = \left[p_{EQ,i}(V_{tot} - V_{pol})\right]/\left[Z(p_{EQ,i}; T)RT\right]$,

and represent the moles of gas contained in the total volume, V_{tot}, (delimited by PT01, PT02, sample chamber and V02), minus the volume occupied by the polymer, V_{pol}, placed in the sample chamber, after V03 opens to expand the gas previously fed in the pre-chamber. The compressibility factor, $Z(p; T)$, was calculated with the Peng-Robinson equation of state (PR-EoS)[29]. Similarly, n_{i-1}^{pre} represent the number of moles contained in the pre-chamber and fed in it before opening V03, and n_{i-1}^{sc} is the volume of gas left in the sample chamber from the previous step, in equilibrium with the polymer but not sorbed in it. On the other hand, n_{i-1}^{pol} is the number of moles already sorbed by the polymer in the previous step, while n_i^{pol} is the amount of gas sorbed by the sample after reaching equilibrium subsequently opening V03. The concentration of gas in the polymer, C_i^{pol}, is usually reported in $cm^3(STP)/cm_{pol}^3$, and is calculated as follows:

$$C_i^{pol} = \frac{n_i^{pol}\tilde{v}(STP)}{V_{pol}}$$
Eq. (5.17)

where $\tilde{v}(STP)$ is the molar volume of gas in standard temperature and pressure, $\sim$22,413 cm³.

Therefore, consecutive sorption tests were performed to evaluate the whole sorption isotherm by increasing the operative pressure step-by-step up to 35 - 50 bar (depending on the equipment used). In *Bologna*, two pressure transducers (*Honeywell – Super TJE*) were used for this purpose, one with a full-scale (FS) of 200 psia (PT02) and one with a FS of 500 psia (PT01), to cover a wide pressure range without compromising the accuracy of the measurements. Both transducers feature 0.05% accuracy and zero temperature error of less than 0.0015% FS/°F. The temperature of the system was controlled by using the same kind of air incubator described above for the permeation system. For CO_2, the most soluble gas among those that were studied, the de-sorption isotherm was also often measured to investigate hysteresis behavior.
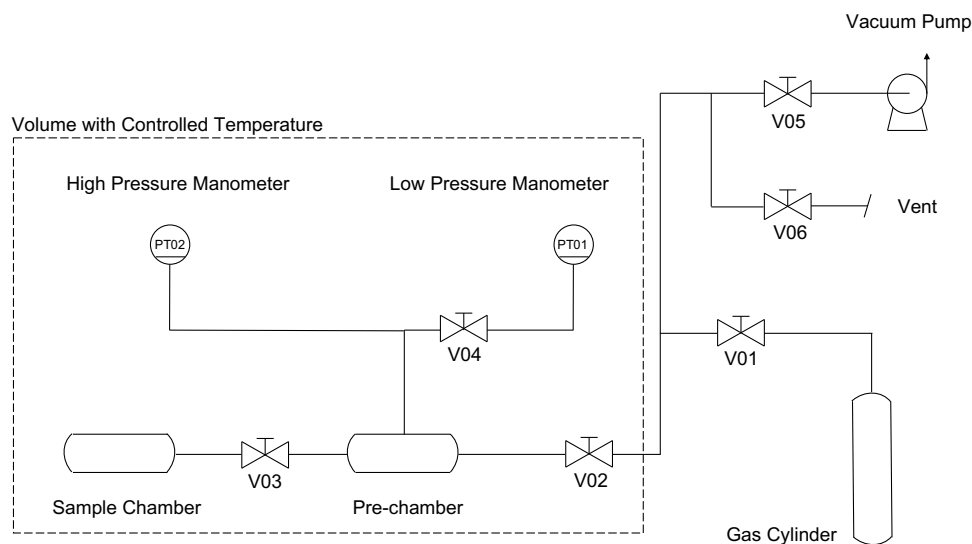
Figure 5.12*: Scheme of the in-house designed single gas pressure decay apparatus.*

5.7.1.1.   Diffusivity: Sorption Kinetics Method

Besides the time-lag technique previously described, the diffusion coefficient can be evaluated also through the analysis of the sorption data, fitting the experimental transient mass uptake data to the solution of the local mass balance reported in Eq. (5.18), and as illustrated in **Figure 5.14b**. **Figure 5.14a** reports the pressure decrease recorded during a gas sorption step in polymer film from which the mass uptake can be calculated as a function of the time. The average diffusion coefficient is obtained as a function of the average concentration reached in the polymer between one equilibrium point and the next. To properly evaluate the sorption kinetics, a uniform thickness sample needs to be selected. Mathematically the problem is analogous to the permeation experiments, but boundary conditions are different, as illustrated in **Figure 5.13**, because the concentration is the same on both sides of the film and the problem is symmetric. Furthermore, the boundary conditions change with time in terms of concentration at the interface, because while the pressure decay is occurring, by definition the pressure decreases over time at the interface. Crank[25] provided the solution for the problem with variable boundary conditions, and this solution was implemented to perform calculations in this dissertation.

However, for simplicity, the cartoon and the formulation of the problem reporter in **Figure 5.13** shows

the case in which $C\left(\frac{l}{2}\right) = C\left(-\frac{l}{2}\right) = C_1 \; \forall \; t \geq 0$.

$$
\begin{cases}
\dfrac{\partial C_i}{\partial t} = \mathcal{D}_{i,j} \cdot \dfrac{\partial^2 C_i}{\partial x^2} \\[2mm]
C = C_0, t = 0, -l/2 < x < l/2 \\[2mm]
C = C_1, t \geq 0, x = -l/2 \\[2mm]
C = C_1, t \geq 0, x = l/2
\end{cases}
$$
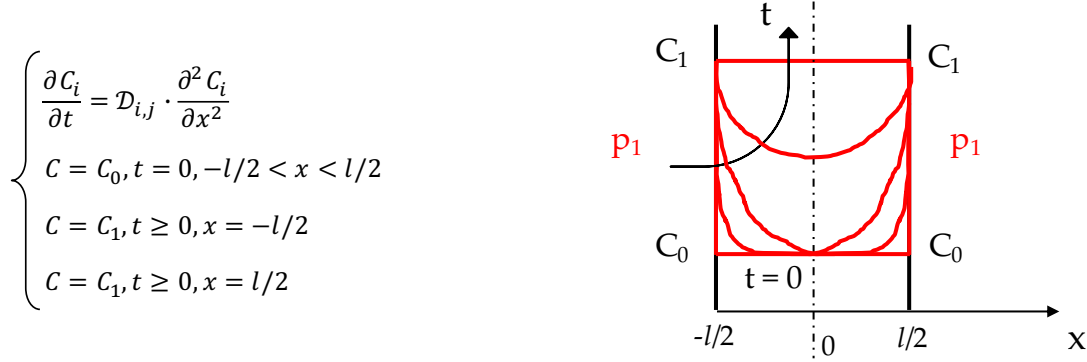
Figure 5.13: *Illustration of the transient process occurring during a sorption experiment from C_0 at time zero all across the film, to C_1 at the steady state. Boundary conditions to solve the second law of diffusion are provided.*
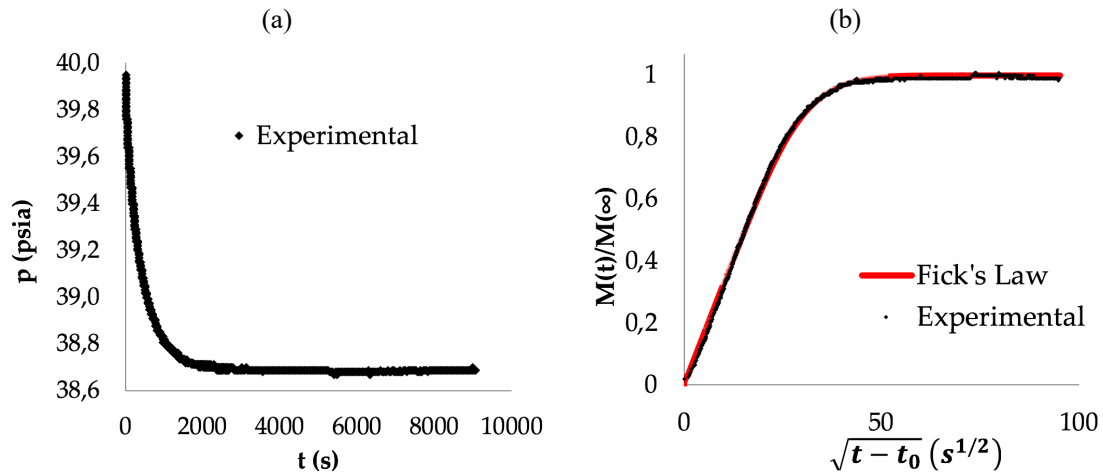
Figure 5.14: *(a) pressure decay recorded during a gas sorption step in polymer film, (b) modeling of the sorption kinetics measured through the gas uptake with Fick's law.*

Once the system is solved, the following equation is obtained[25]:

$$
\frac{M^i(t) - M_0^i}{M_\infty^i - M_0^i} = 1 - \sum_{n=1}^{\infty} \frac{2\alpha(1+\alpha)}{1 + \alpha + \alpha^2 q_n^2} exp\left(-\frac{\mathcal{D} q_n^2 t}{\left(l/2\right)^2}\right) \qquad \text{Eq. (5.18)}
$$

where M_0^i and M_∞^i are the initial and final mass uptake in step "i" respectively and $M^i(t)$ is the expression of the mass uptake as a function of the time. α is the ratio between the volume of the gas phase and that of the polymer, corrected for the partition coefficient of gas between the gaseous phase and the polymeric phase, while q_n are the positive, non-zero, solutions of the equation $\tan(q_n) = -\alpha q_n$.[26]

5.7.2. Mixed-Gas Pressure Decay

Mixed-gas sorption tests in polymers have been performed by means of an in-house built pressure decay apparatus, based on the same principles of the pure-gas pressure decay.[27,30,31] However, in addition, the mixed-gas equipment is coupled with a gas chromatographer (*Varian Inc. – CP-4900 Micro GC*) that allows for the measurement of the composition of the mixture. The system is represented schematically in **Figure 5.15**. It can operate with any gas pair, as long as concentrations are in the range for which the GC is calibrated, but in the framework of this dissertation, just CO_2/CH_4 mixtures were tested.
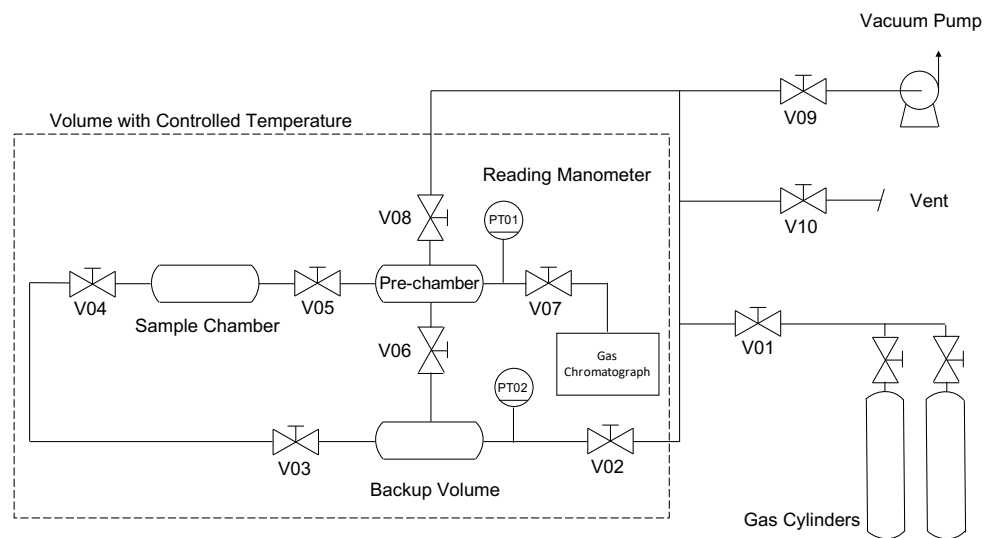
Figure 5.15: Scheme of the in-house designed mixed-gas pressure decay apparatus.

The apparatus was thermostatted by submersion in a water bath and can work in a wide range of pressures $(0-35\text{ bar})$, temperatures $(25-65\,^{\circ}\text{C})$ and compositions $(0-100\text{ mol.\%}\ CO_2)$. A

Honeywell-Super TJE pressure transducer (PT01) with a full-scale of 500 psia was used to measure the pressure. To stabilize the pressure reading with respect to temperature fluctuations, the part of the manometer which was not soaked in the water bath was further insulated using a heating coil in which the fluid of the bath was continuously recirculated. The details of the measurement protocol adopted for mixed-gas tests with this apparatus were optimized to maximize the flexibility of the equipment.

The first step of a mixed-gas equilibrium point measurement required to pressurize the pre-chamber with the more condensable gas (CO_2), after keeping the sample under vacuum overnight. The reason why the order we feed each gas is important, is because the two gases have a different conditioning effect on the membrane structure. CO_2 is the first gas that the polymer is exposed to because it is the one more responsible for the polymer dilation (*i.e.*, relaxation of the polymer chains upon sorption of a condensable gas). When the second gas, CH_4, is loaded in the system, the polymer is already relaxed to an extent that is reasonably close to that it would achieve if constantly exposed to a mixture contacting CO_2 at the equilibrium composition. This way the amount of CH_4 that can be absorbed is closer to the one we would experience in a real-world membrane separation apparatus. Operating the other way around, CH_4 would not be able to swell the polymer to the same extent, and the overall amount of CH_4 absorbed would be underestimated.

Once CO_2 was expanded in the sample chamber and a constant pressure was reached, V05 was closed and the pre-chamber was evacuated. This first part of the experiment coincides with a pure-gas pressure decay sorption experiment step, thus CO_2-sorption information can be determined also while performing mixed-gas experiments. Subsequently, the second less condensable gas, CH_4, was loaded in the pre-chamber at the desired pressure, and V05 was opened to allow the two gases to mix. When a constant pressure was reached, the polymer sample was isolated (V05 was closed) to avoid any further change in composition and the gas mixture at the equilibrium pressure and composition was collected from the pre-chamber to the backup volume. The composition was then measured with the gas chromatograph (GC), as it was necessary to calculate the amount of each gas sorbed by the sample. The GC test was repeated at least 10 times for each point to ensure that the composition was properly measured, and

standard deviation was acceptable (**Figure 5.16**). The error made on the composition was always kept smaller than 0.5%.
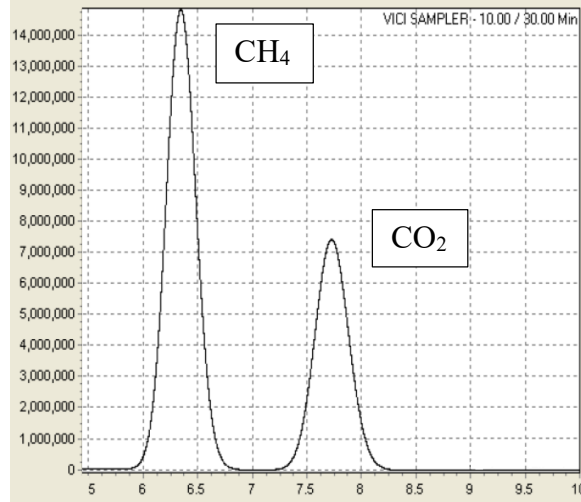
Figure 5.16*: Typical chromatogram from the Micro GC analysis of a 30% CO₂, 70% CH₄ mixed-gas composition.*

In mixed-gas tests, the vacuum is pulled after each equilibration stage, therefore a sorption isotherm is obtained through a series of so-called *integral steps*, progressively increasing the equilibrium pressure. In order to obtain the same equilibrium mixture composition at the end of each step of the sorption isotherm (e.g., $10 - 30 - 50$ mol.% of CO₂), the loading pressures of both gases, $p_{CO_2}^0$ and $p_{CH_4}^0$, need to be estimated according to the following set of equations:

$$n_{CO_2}^1 = \frac{p_{CO_2}^0 V_{pre}}{Z(p_{CO_2}^0;T)RT} - \frac{p_{CO_2}^{Eq,1}(V_{pre} + V_{sc}+V_v - V_{pol})}{Z(p_{CO_2}^{Eq,1};T)RT} \qquad \text{Eq. (5.19)}$$

$$n_{CO_2}^{\prime 1} = \frac{p_{CO_2}^0 V_{pre}}{Z(p_{CO_2}^0;T)RT} - \frac{p_{CO_2}^{post,1}(V_{pre} + V_{sc} - V_{pol})}{Z(p_{CO_2}^{post,1};T)RT} \qquad \text{Eq. (5.20)}$$

$$n_{CH_4}^2 = \frac{p_{CH_4}^0 V_{pre}}{Z(p_{CH_4}^0;T)RT} - \frac{p_{CH_4}^{Eq}(V_{pre} + V_{sc}+V_v - V_{pol})}{Z(p_{CH_4}^{Eq};T;y_{CO_2})RT} \qquad \text{Eq. (5.21)}$$

$$n_{CO_2}^{tot} = n_{CO_2}^{\prime 1} + \frac{p_{CO_2}^{post}(V_{sc} - V_{pol})}{Z(p_{CO_2}^{post};T)RT} - \frac{p_{CO_2}^{Eq,2}(V_{pre} + V_{sc}+V_v - V_{pol})}{Z(p_{CO_2}^{Eq,2};T;y_{CO_2})RT} \qquad \text{Eq. (5.22)}$$

$$C^1_{CO_2} = k_{DCO2} p^{Eq,1}_{CO_2} + \frac{C'_{H,CO_2} b_{CO_2} p^{Eq,1}_{CO_2}}{1 + b_{CO_2} p^{Eq,1}_{CO_2}}$$

Eq. (5.23)

$$C^1_{CO_2} = \frac{n^1_{CO_2} \tilde{v}(STP)}{V_{pol}}$$

Eq. (5.24)

$$C'^1_{CO_2} = k_{DCO2} p^{post,1}_{CO_2} + \frac{C'_{H,CO_2} b_{CO_2} p^{post,1}_{CO_2}}{1 + b_{CO_2} p^{post,1}_{CO_2}}$$

Eq. (5.25)

$$C'^1_{CO_2} = \frac{n'^1_{CO_2} \tilde{v}(STP)}{V_{pol}}$$

Eq. (5.26)

$$C^{tot}_{CO_2} = k_{DCO2} p^{Eq,2}_{CO_2} + \frac{C'_{H,CO_2} b_{CO_2} p^{Eq,2}_{CO_2}}{1 + b_{CO_2} p^{Eq,2}_{CO_2} + b_{CH_4} p^{Eq}_{CH_4}}$$

Eq. (5.27)

$$C^{tot}_{CO_2} = \frac{n^{tot}_{CO_2} \tilde{v}(STP)}{V_{pol}}$$

Eq. (5.28)

$$C^2_{CH_4} = k_{DCH4} p^{Eq}_{CH_4} + \frac{C'_{H,CH_4} b_{CH_4} p^{Eq}_{CH_4}}{1 + b_{CO_2} p^{Eq,2}_{CO_2} + b_{CH_4} p^{Eq}_{CH_4}}$$

Eq. (5.29)

$$C^2_{CH_4} = \frac{n^2_{CH_4} \tilde{v}(STP)}{V_{pol}}$$

Eq. (5.30)

where $n^1_{CO_2}$ is the number of moles of CO_2 that were sorbed in the first sorption step, which corresponded to the first equilibrium pressure $(p^{Eq,1}_{CO_2})$, $n'^1_{CO_2}$ is the number of moles of CO_2 that were sorbed in the first sorption step, which corresponded to the first post-equilibrium pressure, $(p^{post,1}_{CO_2})$, and $n^{tot}_{CO_2}$ is the total number of moles of CO_2 that were sorbed after the second sorption step, which corresponded to the final equilibrium pressure $(p^{Eq,2}_{CO_2})$. $n^{tot}_{CO_2}$ represents the difference between the moles of CO_2 sorbed in the first sorption step and the moles desorbed in the second sorption step. $n^2_{CH_4}$ instead is the number of moles of CH_4 that were sorbed in the second sorption step, which corresponded to the final equilibrium pressure $(p^{Eq}_{CH_4})$. $C^1_{CO_2}$, $C'^1_{CO_2}$, $C^{tot}_{CO_2}$, and $C^2_{CH_4}$ are the gas concentrations that can be evaluated from the knowledge of the moles above listed and described. V_{pre}, V_{sc}, and V_v, are the volume of the pre-chamber,

the sample chamber, and the valve V04, as indicated in **Figure 5.15**. $k_{D_{CO_2}}$, C'_{H,CO_2}, and b_{CO_2} are the dual mode sorption parameters of CO_2 retrieved from pure-gas sorption experiments, while $k_{D_{CH4}}$, C'_{H,CH_4}, and b_{CH_4} are those of CH_4. Future developments will be featuring the use of the NELF model for the calculation of the concentration, especially in place of Eq. (5.27) and Eq. (5.29) where the competitive effect between CO_2 and CH_4 needs to be properly evaluate to predict accurately the final concentration in the polymer.[32,33] y_{CO_2} is the mole fraction of CO_2 in the final equilibrium mixture, measured *via* GC analysis.

5.8. Polymer Synthesis

5.8.1. Catalytic Arene-Norbornene Annulation (CANAL) Ladder Polymers

The contribution of the candidate on the organic synthesis of new CANAL ladder polymers was limited to the assistance provided to Holden W. H. Lai while at *Stanford University*. The generic procedure and all the different steps required to get from commercial chemicals to in-house synthesized monomers and to synthesize the final polymers, were learned and performed by the candidate a few times, but the vast majority of polymers eventually tested where prepared by Holden W. H. Lai while the candidate was testing transport properties at *MIT*. Continuous feedback was provided to optimize the polymerization to obtain eventually polymer that could form a film and be tested in different circumstances.

Figure 5.17: *Fume hood in which reactions were performed at Stanford University. [photo credit Professor Xia Lab Website]*

5.8.1.1. Benzocyclobutene CANAL Ladder Polymers

To synthesize CANAL ladder polymers, HPLC-grade Tetrahydrofuran (THF) was purchased from *Fisher Scientific* (*Hampton, NH USA*) and sparged with nitrogen to remove dissolved O_2 before being transferred into the nitrogen glovebox and used for polymerization reactions. All other reagents were obtained from commercial vendors and used as received. On the other hand, 2,5-dibromo-1,4-diethylbenzene (1-Et)[34], 2,5-dibromo-1,4-diisopropylbenzene (1-iPr)[35], and diisopropyldinorbornene (2-iPr)[36] were synthesized according to literature procedures.

Diethyldinorbornene (2-Et), was synthesized using a literature procedure.[36] To a flame-dried 75-mL glass pressure tube used as a reactor, it was added: 1-Et (2.92 g, 10 mmol), Pd(OAc)$_2$ (44 mg, 0.02 mmol), and PPh$_3$ (104 mg, 0.4 mmol). Pd(OAc)$_2$ is the catalyst, but PPh$_3$ is needed to coordinate the palladium to form the actual catalyst PPh$_3$-Pd-PPh$_3$ that takes part to the reaction mechanism. The tube was transferred into a nitrogen-filled glovebox to make sure the environment is oxygen-free before adding Cs$_2$CO$_3$ (6.5 g, 20 mmol) and 15 mL of 1,4-dioxane. Cs$_2$CO$_3$ is used to neutralize HBr that is formed in the reaction. The reactor atmosphere and its reagents need to be oxygen-free because O_2 can

harm the catalyst when the solution is warmed up. The tube was then sealed with a Teflon valve and taken out of the glovebox. The mixture was then stirred at 150 °C for 24 h, it was cooled to room temperature and then passed through a pipette filled with Celite, $(CaO)_3Al_2O_3$, to remove inorganic salt, which was washed with chloroform (3 × 15 mL). Filtered solution was concentrated by means of a rotavap and purified by silica chromatography (see following dedicated section) using hexanes as the mobile phase to yield 2-Et as a white solid.

The general procedure used to synthesize CANAL ladder polymers was following the scheme represented in **Figure 5.18**. Some of the considerations made for the synthesis of 2-Et hold also for the synthesis of the polymers and will not be repeated in this context. To a flamed-dried 15-mL glass pressure tube, dibromoarene monomer was added, indicated as "**1**" in **Figure 5.18** (0.5 mmol), dinorbornene, indicated as "**2**" (0.5 mmol), Pd(OAc)$_2$ (2.2 mg, 0.01 mmol), and PPh$_3$ (5.2 mg, 0.02 mmol). The functionalities R_1 and R_2 could be short-chain of hydrocarbons such as methyl (-Me), ethyl (-Et), and isopropyl (-iPr). More details will be provided in the results section. The tube was then transferred into a nitrogen-filled glovebox, and Cs$_2$CO$_3$ (330 mg, 1 mmol), THF (1 mL), and butylated hydroxytoluene (1 mg) were added. The tube was sealed with a Teflon valve and removed from the glovebox. The reaction mixture was heated to 150 °C for 24 h. The mixture was then cooled to room temperature and passed through Celite to remove inorganic salts. Chloroform (3 × 5 mL) was used to wash the residue. The filtrate was concentrated and dissolved in a minimum amount of chloroform, which was then precipitated into ethyl acetate given its opposite polarity. The precipitated polymer was collected by centrifugation, washed with ethyl acetate, and dried under vacuum.
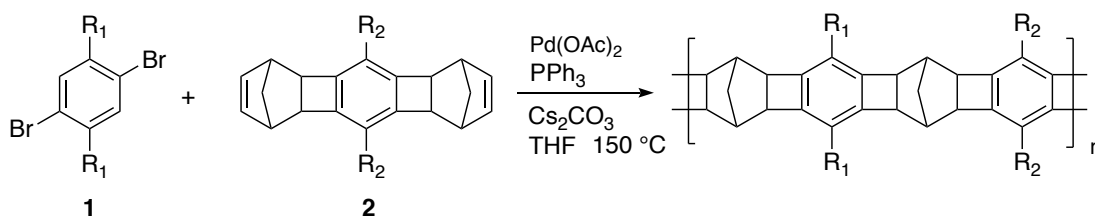
Figure 5.18: *General reaction scheme for the synthesis of CANAL ladder polymers.*[37]

5.8.2. Ring Opening Metathesis Polymerization (ROMP) Polymers

Polymers obtained through ring opening metathesis polymerization technique, were synthesized following the procedure recently reported in the literature from Zhao and He *et al.*.[38] The first reaction represented in **Figure 5.19** is the oligomer formation through a *Diels-Alder reaction*, while the second reaction is the actual ROMP polymerization. The flexible design allows to easily vary the pendent group (*i.e.*, –X). The main part of this investigation was performed on two species ROMP polymers featuring the following functionalities: –CF$_3$ and –OMe.
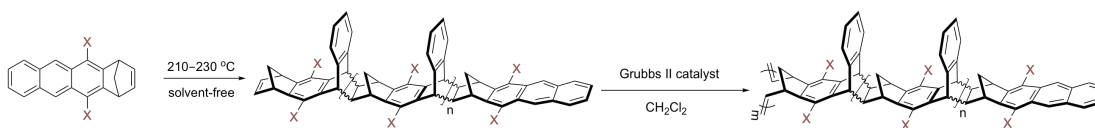
Figure 5.19: Generalized synthetic procedure for ROMP porous polymers.[8]

5.9. Silica Chromatography Purification

While synthesizing CANAL ladder polymers, different reactions were performed to produce intermediates, monomers, and the final polymers. Usually there was never just one single product obtained from the reaction, and the desired one needed to be isolated from the byproducts by means of the silica chromatography technique, as illustrated in **Figure 5.20**. The column was filled by silica in powder form, and a solution of ethyl acetate (ETAC) and hexane was poured inside to saturate the column with the liquid. The ratio hexane/ ETAC of the elution solution depends on the components that need to be separated and the degree of polarity to be conferred to the column, because changing the polarity changes the affinity towards certain components, to tune the separation efficiency. Often the ratios used were richer in hexane (*i.e.*, 80 to 100 vol.% of hexane). The more polar the molecule, the slower the passage through the column, because the affinity with the column is higher. The products of the reaction were then added on top of the silica column and then more liquid solution was poured. The liquid mixture was collected in 50 to 70 culture tubes. It usually took around 30 minutes to run a column, as it can be seen in **Figure 5.20** in which the color variation over time correspond to the motion of different components and their separation.
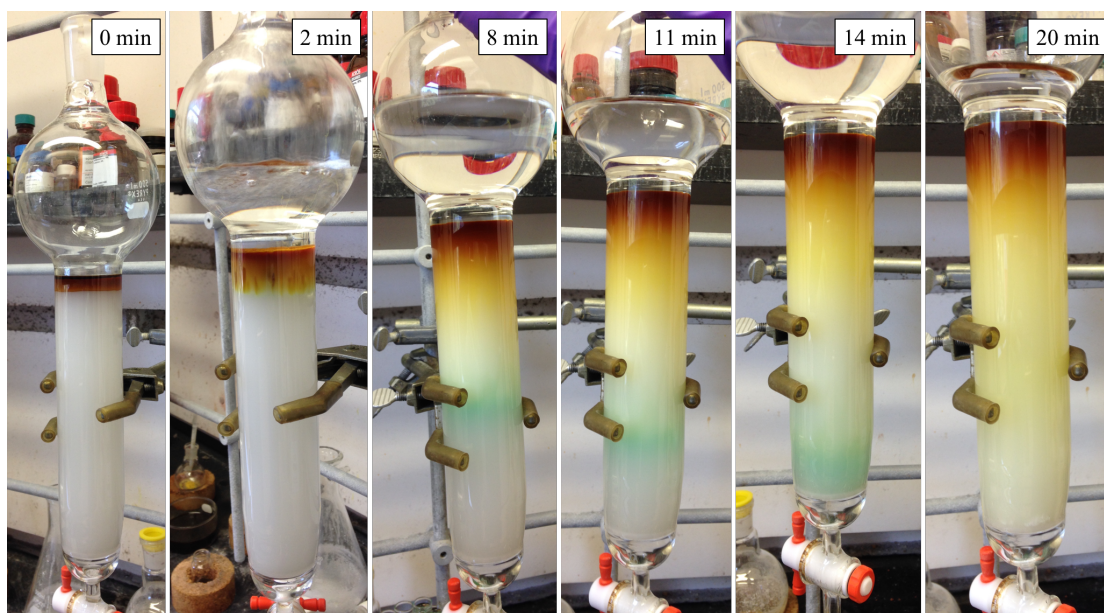
Figure 5.20:Separation of a monomer through silica chromatography technique.

If the separation was properly designed in terms of length of the column and polarity of the elution solvent, the product was present just in some of the many tubes. To assess in which tubes the product was, and if it was the only one in there, thin layer chromatography (TLC) technique was used. A drop of solution from different tubes was put on the baseline of an aluminum foil covered with a thin layer of silica gel (**Figure 5.21**). The first 2 millimeters of the TLC film was soaked in the same liquid solution, that via capillary action goes from bottom to top of the plate. Different components ascend the TLC plates at different rates, reaching different heights. Once identified in which culture tubes the product was, the liquid solution ETAC/hexane containing the product was collected in a flask and allowed to evaporate at the rotavap. The following step was then to assess via proton nuclear magnetic resonance (^{1}H NMR) if the compound isolated was actually what we expected it to be.
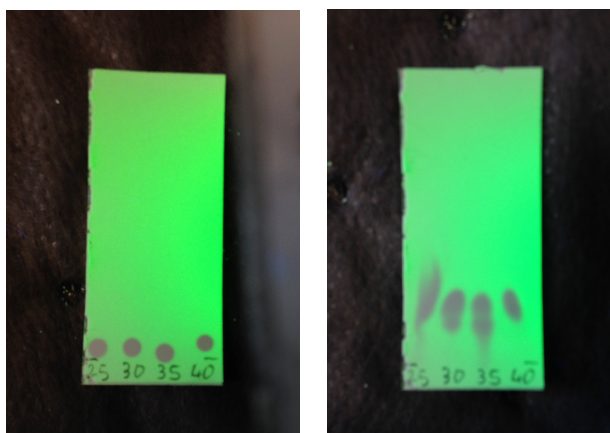
Figure 5.21: *Fluorescent Thin Layer Chromatography (TLC) under a UV light.*

5.10.   Proton Nuclear Magnetic Resonance (^{1}H NMR)

A small quantity of the solid product was dissolved in deuterated chloroform ($CDCl_3$) to be analyzed at the proton nuclear magnetic resonance (^{1}H NMR). Deuterated solvents, thus solvents in which deuterons are in place of hydrogens, are used to prevent a very intense signal coming from the proton of $CHCl_3$. Usually NMR tubes were 5 mm diameter, so 0.6-0.7 ml of sample solution was enough to cover the detected region of the machine. Good-quality clean tubes with homogeneous wall thickness and straight shape with no bends or bows, are essential to prevent spinning and shimming problems. Different NMR equipment were used, *Varian Mercury 300 MHz NMR*, *Varian 400 MHz NMR* with *Oxford NMR AS400 magnet*, and *Bruker Avance Spectrometer 100* and *400 MHz*. The principle on which ^{1}H NMR is based is that when a molecule is exposed to a magnetic field, it makes the protons in the molecule spinning at a certain frequency. A spinning charge generates a magnetic field that can be detected to produce a spectrometer that provides information about the structure of the molecule, and can be read as the fingerprint of the molecule. Even though the magnetic field changes (*i.e.*, 300, 400, 500 MHz), thus the frequency to which protons spin changes accordingly, the frequency can be normalized according to Eq. (5.31) to evaluate the chemical shift, δ, of each type of proton in the molecule, so that the spectrum obtained is independent from the intensity of the magnetic field of the equipment.

$$\delta \, (ppm) = \frac{Observed \; shift \; from \; standard \;\; (MHz)}{NMR \; spectrometer \; frequency \; (MHz)}$$

Eq. (5.31)

The chemical shift is characteristics of each type of hydrogen present in the molecule and depends on the environment that surrounds the proton. In general, more shielded protons show lower spinning frequency, less intense magnetic field, and lower chemical shift, and vice versa. The standard to which zero chemical shift is attributed (*i.e.*, 0 ppm) is tetramethylsilane (TMS), whose protons are far more shielded than any other organic compound. Since often deuterated solvents contain trace amounts of the protiated solvents (*i.e.*, chloroform in the case of $CDCl_3$), another standard reference that can be used to report the chemical shift, is the peak of the protiated solvent ($CHCl_3$ ^{1}H NMR: 7.26 ppm).

(a)

(b)

(c)

Figure 5.22: NMR facility at (a), (b) Stanford University, (c) MIT.

5.11.   Gel Permeation Chromatography (GPC)

Gel permeation chromatography (GPC) for CANAL ladder polymers was carried out to determine the average molecular number (M_n) and average molecular weight (M_w). The polydisperdity index (PDI) was calculated as the ratio M_w/M_n according to those measurements.

For CANAL ladder polymers, GPC was performed in tetrahydrofuran (THF) on two PolyPore columns (*Agilent*) connected in series with a DAWN multiangle laser light scattering (MALLS) detector and an Optilab T-rEX differential refractometer (both from *Wyatt Technology*). No calibration standards were used, and dn/dc values were obtained for each injection by assuming 100% mass elution from the columns.

For ROMP polymers, measurements were carried out in HPLC-grade THF using an *Agilent 1260 Infinity* system with variable-wavelength diode array (254, 450 and 530 nm) and refractive index detectors, guard column (*Agilent* PLgel; 5μm; 50 x 7.5 mm), and three analytical columns (*Agilent* PLgel; 5μm; 300 x 7.5 mm; 105, 104, and 103 Å pore sizes). The instrument was calibrated with narrow-dispersity polystyrene standards between 1.7 and 3150 kg/mol. All runs were performed at 1.0 mL/min

flow rate and 35 ºC. Molecular weight values were calculated using *Chemsta-tion GPC Data Analysis Software* (Rev. B.01.01) based on the refractive index signal.

5.12. Wide-angle X-ray Scattering (WAXS)

Wide-angle X-ray scattering (WAXS) experiments were performed to gather information about the structure and the chain packing of polymers, measuring the interchain distance between polymer chains. Microporosity and free volume elements can be observed as scattering features in a WAXS spectrum. Experiments were performed also to study how the structure was evolving over time, providing additional information that can be coupled with permeation experiments to get more insights on physical aging.[39] WAXS experiments were performed under vacuum on a system with a Rigaku 002 Cu microfocus X-ray source with an Osmic staggered parabolic multilayer optics. The WAXS instrument was equipped with the Dectris Pilatus 300K detector. To gather information about the distance, d, we need to collect the momentum transfer data interfaced by the apparatus, q, and calculate the Bragg spacing as follows:

$$d = \frac{2\pi}{q}$$

Eq. (5.32)

The equipment shown in **Figure 5.23** can perform WAXS but also SAXS (Small-angle X-ray Scattering). What changes between the two analysis is just the distance between the detector and the sample, which allows for the possibility to investigate porosities of different dimensions (*i.e.*, from 3 Å to 2300 Å). In particular, WAXS was performed by placing the sample very close to the detector (~110 mm), to detect small porosities (bigger q), while with SAXS we can identify bigger pores (smaller q) by increasing the distance between the sample and the detector (up to 1.5 m).
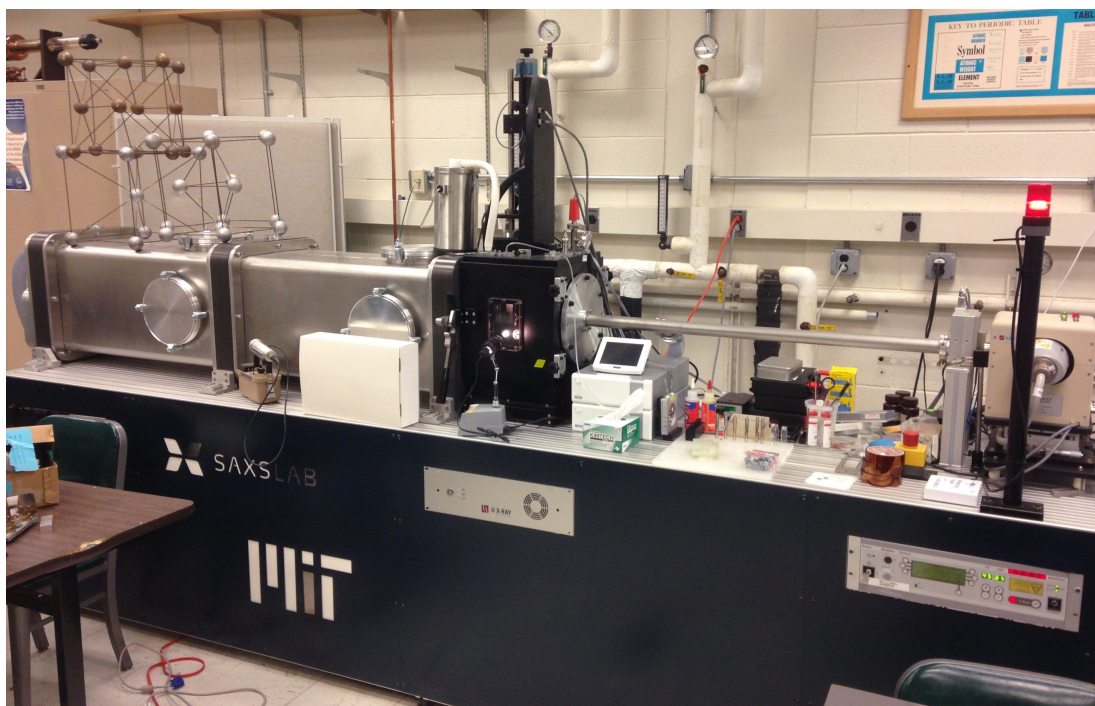
Figure 5.23*:Wide-angle X-Ray Scattering equipment at MIT.*

References

[1]   K. C. Khulbe, T. Matsuura, G. Lamarche, H. J. Kim, *J. Memb. Sci.* **1997**, *135*, 211.

[2]   M. Khayet, J. P. G. Villaluenga, M. P. Godino, J. I. Mengual, B. Seoane, K. C. Khulbe, T. Matsuura, *J. Colloid Interface Sci.* **2004**, *278*, 410.

[3]   P. Li, T. S. Chung, D. R. Paul, *J. Memb. Sci.* **2013**, *432*, 50.

[4]   M. Aguilar-Vega, D. R. Paul, *J. Polym. Sci. Part B Polym. Phys.* **1993**, *31*, 1577.

[5]   M. Das, J. D. Perry, W. J. Koros, *Ind. Eng. Chem. Res.* **2010**, *49*, 9310.

[6]   A. L. Khan, A. Cano-Odena, B. Gutiérrez, C. Minguillón, I. F. J. Vankelecom, *J. Memb. Sci.* **2010**, *350*, 340.

[7]   F. M. Benedetti, M. G. De Angelis, M. Degli Esposti, P. Fabbri, A. Masili, A. Orsini, A. Pettinau, *To be Submitt. to J. Membr. Sci.* **2019**.

[8]   Y. He, F. M. Benedetti, S. Lin, C. Liu, Y. Zhao, H.-Z. Ye, T. Van Voorhis, M. G. De Angelis, T. M. Swager, Z. P. Smith, *Submitt. to Adv. Mater.* **2019**.

[9]   L. Ansaloni, M. Minelli, M. Giacinti Baschetti, G. C. Sarti, *Oil Gas Sci. Technol. – Rev. d'IFP Energies Nouv.* **2015**, *70*, 367.

[10]   A. C. Savoca, A. D. Surnamer, C. Tien, *Macromolecules* **1993**, *26*, 6211.

[11]   Y. Huang, D. R. Paul, *Macromolecules* **2005**, *38*, 10148.

[12] C. R. Mason, L. Maynard-Atem, N. M. Al-Harbi, P. M. Budd, P. Bernardo, F. Bazzarelli, G. Clarizia, J. C. Jansen, *Macromolecules* **2011**, *44*, 6471.

[13] R. H. Perry, D. W. Green, in *Perry's Chem. Eng. Handb.* (Ed.: McGraw-Hill), **1999**, p. 2.91-2.93.

[14] F. Doghieri, G. C. Sarti, *Macromolecules* **1996**, *29*, 7885.

[15] S. Rafiq, A. Maulud, Z. Man, M. I. A. Mutalib, F. Ahmad, A. U. Khan, A. L. Khan, M. Ghauri, N. Muhammad, *Can. J. Chem. Eng.* **2015**, *93*, 88.

[16] H. Lin, B. D. Freeman, in *Springer Handb. Metrol. Test.* (Eds.: H. Czichos, T. Saito, L. Smith), Springer US, New York, **2006**, pp. 371–387.

[17] M. Minelli, M. G. De Angelis, F. Doghieri, M. Marini, M. Toselli, F. Pilati, *Eur. Polym. J.* **2008**, *44*, 2581.

[18] A. Bos, I. G. M. Pünt, M. Wessling, H. Strathmann, *J. Memb. Sci.* **1999**, *155*, 67.

[19] N. R. Horn, D. R. Paul, *Polymer (Guildf).* **2011**, *52*, 5587.

[20] N. R. Horn, D. R. Paul, *Polymer (Guildf).* **2011**, *52*, 1619.

[21] Y. P. Handa, P. Kruus, M. O'Neill, *J. Polym. Sci. Part B Polym. Phys.* **1996**, *34*, 2635.

[22] Z. Zhang, Y. P. Handa, *J. Polym. Sci. Part B Polym. Phys.* **1998**, *36*, 977.

[23] H. W. H. Lai, F. M. Benedetti, M. G. De Angelis, Z. P. Smith, Y. Xia, *To be Submitt.* **n.d.**

[24] A. Fick, *London, Edinburgh, Dublin Philos. Mag. J. Sci.* **1855**, *10*, 30.

[25] J. Crank, *The Mathematics of Diffusion*, Oxford University Press, **1975**.

[26] M. C. Ferrari, M. Galizia, M. G. De Angelis, G. C. Sarti, *Ind. Eng. Chem. Res.* **2010**, *49*, 11920.

[27] O. Vopička, M. G. De Angelis, G. C. Sarti, *J. Memb. Sci.* **2014**, *449*, 97.

[28] E. S. Sanders, W. J. Koros, H. B. Hopfenberg, V. T. Stannett, *J. Memb. Sci.* **1984**, *18*, 53.

[29] D.-Y. Peng, D. B. Robinson, *Ind. Eng. Chem. Fundam.* **1976**, *15*, 59.

[30] O. Vopička, M. G. De Angelis, N. Du, N. Li, M. D. Guiver, G. C. Sarti, *J. Memb. Sci.* **2014**, *459*, 264.

[31] A. E. Gemeda, M. G. De Angelis, N. Du, N. Li, M. D. Guiver, G. C. Sarti, *J. Memb. Sci.* **2017**, *524*, 746.

[32] E. Ricci, F. M. Benedetti, M. E. Dose, M. G. De Angelis, B. D. Freeman, D. R. Paul, *To be Submitt.* **n.d.**

[33] F. M. Benedetti, E. Ricci, M. Carta, M. G. De Angelis, N. B. McKeown, *To be Submitt.* **n.d.**

[34] J. Frey, C. Tock, J.-P. Collin, V. Heitz, J.-P. Sauvage, K. Rissanen, *J. Am. Chem. Soc.* **2008**, *130*, 11013.

[35] K. Ohuchi, M. Soga, *Metaphenylene Polymer Compound and Light Emitting Device Using the Same*, **2011**, US20110272686A1.

[36] H. W. H. Lai, Y. C. Teo, Y. Xia, *ACS Macro Lett.* **2017**, *6*, 1357.

[37] H. W. H. Lai, F. M. Benedetti, Z. Jin, Y. C. Teo, A. X. Wu, M. G. De Angelis, Z. P. Smith, Y. Xia, *To be Submitt. to Macromol.* **2019**.

[38] Y. Zhao, Y. He, T. M. Swager, *ACS Macro Lett.* **2018**, *7*, 300.

[39] A. G. McDermott, P. M. Budd, N. B. McKeown, C. M. Colina, J. Runt, *J. Mater. Chem. A* **2014**, *2*, 11742.

6. Size-Selective Mixed Matrix Membranes (MMMs)

This chapter describes the results obtained from the development of size-selective Mixed Matrix Membranes (MMMs) for H_2-purification and CO_2 separation. A commercial polymers (Poly(phenylene oxide)) and different fillers (ZIF-8 and Zeolite 3A), were combined to develop composite materials. This technique was adopted to tailor membrane properties in terms of permeability and selectivity, by changing materials to be combined, loadings, and operating conditions.

Hydrogen purification was among the first commercial applications that provided potential for large-scale membrane gas separation technologies.[1–5] Polymers entered that market in the '70s due to low cost, processability and mechanical properties. However, for polymeric membranes a tradeoff exists between the permeability, that defines the productivity of the process, and the selectivity, that determines the process efficiency.[6,7] Consequently, there is an upper bound to the polymeric membranes performance, which makes it difficult to enhance the permeability and selectivity at the same time. Research on membrane technologies is constantly seeking for new materials to improve the membrane performance.[8–12] One way to circumvent the intrinsic limit of the polymers, is to combine polymeric materials with selective nanoporous particles. Such fillers can improve the polymer permeability and/or selectivity given their intrinsic superior properties, without compromising those features that make polymeric systems the first choice. The composite membranes thus obtained are usually called Mixed-Matrix Membranes (MMMs). Many different materials have been dispersed in organic polymers such as silica particles, zeolites, graphene sheets, carbon molecular sieves (CMS), carbon nanotubes, metal organic frameworks (MOFs), and more recently also covalent organic frameworks (COFs).[13–21]

Despite all those alternatives, the choice of readily available, commercial materials as fillers and polymers to be combined in MMMs with enhanced properties, can answer the urgent request to apply membrane technologies on an industrially relevant scale.[5,22,23]

6.1. ZIF-8/PPO Composite Materials

This section has been partially adapted from the following reference: F.M. Benedetti, M.G. De Angelis, M. Degli Esposti, P. Fabbri, G. Cucca, A. Orsini, A. Pettinau, *Enhancing the separation performance of glassy PPO: I) Gas permeability, diffusivity, and selectivity at various temperature*; to be submitted to the Journal of Membrane Science.

6.1.1. Introduction and Motivations

Since the discovery of MOFs by Yaghi and co-workers about 15 years ago[24], such materials attracted the attention of the scientific community because of their exceptional properties and their structural tunability, that opens a virtually infinite range of design. In particular, they revealed to be great materials for gas storage and separation applications.[23,25] The first MMM containing a MOF (*i.e.*, Cu BPDC-TED/PAET) was reported in 2004, and it was tested via single gas permeation measurements.[26] A crucial aspect in the fabrication of MMMs is to ensure a good adhesion between the two phases, to prevent the formation of non-selective voids at the interface, that can cause an undesired loss in selectivity.[27,28] On the other hand, it is essential to avoid interpenetration between the two phases keeping filler porosities available for gas diffusion, to fully exploit their separation ability. MOFs proved to have higher affinity with organic polymer matrices with respect to zeolites, given the organic nature of the linkers that connect the metal clusters to one another.[29] Nevertheless, different strategies have been developed to even further increase the interfacial compatibility between the components of MOF-based MMMs.[30,31]

ZIFs (Zeolitic Imidazole Frameworks) belong to a particular class of MOFs that presents an isomorphism with zeolites.[32] However, the completely inorganic aluminum-silicate structure is replaced by imidazole organic linkers coordinated with metal ions to form ordered frameworks. The crystallographic structure of these ZIFs provides them with a monomodal pore size distribution, which is a remarkable feature to separate small gas molecules in the Angstrom scale.[33,34] However, pure MOF

membranes cannot reach the expected ideal selectivity towards molecule smaller than the pore diameter because the presence of imperfections such as pinholes and cracks is hard to be completely avoided.[29] Such drawback can be avoided by dispersing ZIFs into a polymer matrix, but also in this case the theoretical separation, obtained based on pore dimension considerations, is impossible to be reached experimentally due to the flexibility of the metal-organic cage, explained by the so-called breathing phenomenon.[35,36] Like all the MOFs, ZIFs provide a wide range of designs that can be obtained changing the imidazolate/imidazolate-like linkers and the coordination metal (*e.g.*, zinc(II) or cobalt(II)).[32] This leads to different topologies (*e.g.*, *SOD*, *RHO*, *LTA*, *GME*, *GIS* etc…) and to different dimensions of the pores, that range from 0.7 Å in the case of ZIF-61 and 13.1 Å in the case of ZIF-70. ZIF-8, in particular, features a dimeter of the pore (*i.e.*, diameter of the largest sphere that can pass through the entrance) of 3.4 Å, exactly in between the effective diameter of H_2 (*i.e.*, 2.90 Å) and that of gases like CO_2, N_2 and CH_4 (*i.e.*, 3.63, 3.66 and 3.81 Å).[37] As a consequence, ZIF-8 turns out to be H_2-selective in terms of permeability over those gases.[38–42] Furthermore, ZIF-8 is commercially available, produced by *BASF* and sold by *Sigma Aldrich*. The combination of this features led us to the choice of ZIF-8 as filler in the development of H_2-selective mixed matrix membranes. The polymer chosen as matrix, poly(2,6-dimethyl-1,4-phenylene oxide) (PPO), is also commercial and it is already used in some industrial gas separation membrane modules. It is a glassy amorphous polymer with good thermal resistance and high permeability in comparison to the materials industrially used for gas separations.

The aim of the study was to develop thermally resistant, H_2-selective materials to be used in the purification of syngas in processes like, for instance, the Integrated Gasification Combined Cycle (IGCC). As described in chapter 3.3.2., membrane technologies can be implemented in different sections of an IGCC plant. However, operating conditions become more favorable for membrane technologies once the gas stream reaches the pre-combustion section of the plant, and the implementation of membranes can reduce the energy consumption associated to the compression of CO_2 and provide a hydrogen-enriched stream ready to be used as a fuel for power generation.[43,44]

The membrane preparation was optimized to allow the formation of films up to 45 wt.% of filler, a remarkably high amount considering that embrittlement and agglomeration formation became harder to

be prevented at high loadings.[16,45] Permeation and diffusion of He (used as a model for H_2), N_2, CH_4, CO_2 were investigated at 35, 50 and 65 °C to allow for the calculation of activation energy. This is of great importance while studying membranes for pre-combustion separation applications, because it allows for the extrapolation of transport properties at temperatures higher than the experimental ones. Furthermore, pure and composite materials were characterized from the morphological and calorimetrical point of view through SEM, TGA and DSC analysis. Microscope images allowed assessing the dispersion and the adhesion of the MOF to PPO in the composite films. The absence of voids was also verified performing density measurements on the composite films at different loadings, by comparing the extrapolated value of pure ZIF-8 with that of the theoretical crystal.[46] With TGA and DSC scans, we could verify the thermal resistance and the hydrophobicity of the MMMs, as well as having access to information related to the variation of the rigidity of the polymer with increasing filler loading. Eventually, simple mathematical models such as Maxwell and Bruggeman were applied to assess if the MMMs were following the theoretical behavior.[16,47]
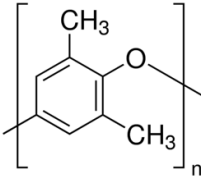
6.1.2. Materials

Poly(2,6-dimethyl-1,4-phenylene oxide), purchased from *Sigma Aldrich* (*St. Louis, MO USA*), commonly indicated as poly(phenylene oxide) or PPO, is a commercial aromatic amorphous glassy polymer. In the literature, it was also referred to by other acronyms such as PDMPO or PMPO.[48,49] PPO has been widely studied in the framework of gas separations because of its excellent sorption and transport properties.[48,50–52] As mentioned by Toi *et al.*[51], PPO shows higher rate of permeability and sorption than others glassy polymers with rigid chain backbone. The high extent of sorption can be ascribed to the high glass transition temperature $(T_g \approx 213°C)$[48,51,52], which indicates a high amount of non-equilibrium excess free volume. The high permeability is related to the high diffusion coefficients of low-weight penetrants, properties that stem from the high Fractional Free Volume (FFV) of the polymer, found to be about 19% by Huang and Paul.[52] Along with these properties, other features that make PPO suitable for industrial applications are its relatively low cost, compared to others common techno-polymers, and the possibility to work at high temperature.[53] This is quite an important aspect

when the separation process is controlled by the diffusivity of the gas species in the membrane, as in this case.

Little information is available about the behavior of PPO in the presence of water. An experimental water vapor permeability was reported by Jia *et al.* to be equal to 2,000 Barrer at 30 °C and 0.04 bar.[54] Some of the relevant physical properties of this material are summarized in **Table 6.1**.

Table 6.1: PPO bulk physical properties.

Polymer	ρ (25°C)	T_g	%FFV [52]	T_m	Refractive index[52]	Average Molecular Weight[53]
PPO	g/cm^3	°C	/	°C	/	g/mol
	1.06	213	19	268	1.573	59,000

Despite gas permeability values showing discrepancies in the literature, different studies revealed that PPO is highly permeable to H_2 (*i.e.*, 86.9-112.8 Barrer), showing instead a moderate selectivity for the H_2/CO_2 pair at room temperature (*i.e.*, ideal perm-selectivity range between 1.49-1.54).[49,55,56] PPO, in particular, behaves as a molecular sieve, indeed permeability values result to be in the following order: $\mathcal{P}_{H_2} > \mathcal{P}_{He} > \mathcal{P}_{CO_2} > \mathcal{P}_{N_2} \cong \mathcal{P}_{CH_4}$, almost the opposite trend of the kinetic diameter, $d_{He} < d_{H_2} < d_{CO_2} < d_{N_2} < d_{CH_4}$.[48,49] It is worth pointing out that hydrogen is the most permeable gas in PPO although helium has a smaller kinetic diameter.

The commercial sieve selected to produce our MMMs was a metal organic framework belonging to the ZIFs family: ZIF-8 (*Basolite® Z1200, Cat. 691348* produced by *BASF*). ZIF-8 presents a regular zeolite-like sodalite (*SOD*) structure and it is H_2-selective over other common light gases (*i.e.*, N_2, CH_4, O_2 and CO_2). In **Figure 6.1** it is shown the structure of ZIF-8: On the right the six-membered ring in which the six ZnN_4 tetrahedra (represented in green) are bounded each other through organic linkers, 2-

methylimidazolate. Carbon atoms are in black, in blue nitrogen and in white hydrogen atoms. Yellow spheres represent the net center, the empty space on the largest cage of the MOF, which provides the very high sorption capacity of the material.
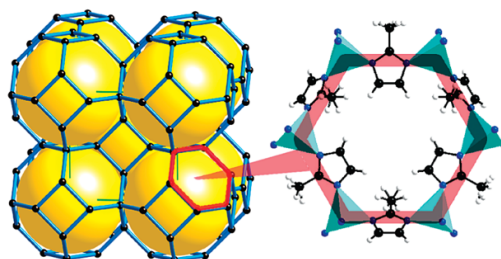
Figure 6.1: Expanded sodalite framework of ZIF-8 from reference [38].

Despite of the similar topology, zeolites and ZIFs have a very different chemistry. Zeolites are aluminum-silicate, therefore, fully inorganic materials.[57] Conversely, ZIF-8 is a hybrid organic-inorganic material in which Zn^+ metal cations are linked by organic molecules (*i.e.*, 2-methylimidazolate) to form a crystalline and regular structure.[29,32,38,46] ZIF-8 is easier to be embedded into organic polymers, compared with purely inorganic materials, due to the organic part. The vast and recent literature regarding MMMs made using ZIF-8 as a filler is an evidence of the last statement.[45,58–66] Both ZIFs, such as ZIF-7 and ZIF-8, and Zeolite 3A, have pore sizes that approach the size of the gas molecules, a feature that makes them theoretically capable of performing gas separation with very high selectivity towards smaller gases. In particular, for ZIF-8, the diameter of the apertures is estimated to be 3.4 Å from crystallographic data, thus larger than H_2 effective diameter, but smaller than that of CO_2, N_2 and CH_4. Bux *et al.*[38,40], as well as McCarthy *et al.*[39], reported that ZIF-8 is an H_2-selective material, as far as H_2/CO_2 separation is concerned, having performed experiments with both pure and mixed-gases. Those measurements have shown that there is no sharp cut-off between those molecules smaller and those bigger than the pores. The fact that molecules with a kinetic diameter larger than the pores can permeate through MOFs was studied in detail by Jürgen Caro.[29] He found out that MOFs often exhibit a pronounced structural flexibility, which makes the framework of these material less rigid than that of zeolites. Furthermore, Bux and coworkers[38] noticed that the H_2 flux in ZIF-8 membranes in the

presence of co-permeating CH_4 was just slightly affected by the presence of the larger molecule in the mixture, and permeation results were comparable with those of single-gas permeability. This behavior was ascribed to the fact that, even though the pore size of ZIF-8 is small, the space inside the largest cage of the system is far larger, so to accommodate a sphere with a diameter as big as 11.6 Å. The values of d_a (diameter of the aperture by which molecules can enter the framework) and d_p (diameter of the largest sphere that can fit into the largest cavity of the crystalline structure) are reported in **Table 6.2**.[32] Therefore, once CH_4 entered the cage, the 3.4 Å-wide pore of ZIF-8 was free and H_2 could diffuse through the network. The organic nature of the filler makes the framework flexible, causing values of selectivity lower than expected. However, its organic nature is essential to have a better compatibility with the polymer.[35,36]

Table 6.2: Physical properties, composition and reticular structure of ZIF-8.

Filler	Composition	Net	d_a	d_p	Surface Area (BET)	Density	Thermal Stability	Hydrophilicity
		/	Å	Å	m^2/g	g/cm^3	°C	/
ZIF-8	$Zn(MeIM)_2$ [46]	sod	3.4 [32]	11.6 [32]	1,630 [46]	theoretical 0.93[64] theoretical 0.95[58]	550 [46]	Hydrophobic [46][67]

The permeability across pure ZIF-8 membrane was measured by various authors and the results were reported in **Table 6.3**. The H_2 permeability values ranged between 4,916 and 10,333 Barrer. Selectivity values were modest, though, possibly due to the flexible morphology of this material.

Table 6.3: *Pure ZIF-8 membranes single-gas permeability and ideal selectivity.*[58]

Thickness (µm)	~30	~20	~20
Ref.	[38]	[39]	[40]
Permeance (10^{-8} mol m^{-2} s^{-1} Pa^{-1})			
H_2	6.04	17.3	8.23
N_2	0.52	1.49	0.69
CH_4	0.48	1.33	0.63
CO_2	1.33	4.45	/
Permeability (Barrer)			
H_2	5411	10333	4916
N_2	466	890	412
CH_4	430	794	376
CO_2	1192	2658	/
Ideal selectivity			
H_2/CO_2	4.54	3.89	/
CO_2/N_2	2.56	2.99	/
CO_2/CH_4	2.77	3.35	/
H_2/CH_4	12.6	13.0	13.1
H_2/N_2	11.6	11.6	11.9

Applications at industrial scale require materials capable of resisting in harsh operative conditions, which can preserve their initial properties over time. Park *et al.*[46] investigated the thermal and chemical stability of some zeolitic imidazole frameworks, focusing on ZIF-8 for its exceptional properties. ZIF-8 demonstrated to possess high hydro-thermal stability, maintaining its architecture as shown by the PXRD analysis, and its porosity (*i.e.*, sorption capacity) after being exposed to 550 °C in N_2 atmosphere and after boiling in water for 7 days. The latter experiment underlined the exceptional hydrophobicity of ZIFs which can repel water molecules, avoiding the attack of ZnN_4 units, which would jeopardize the framework integrity. Küsgens *at al.*[67] also reported the water sorption isotherm of ZIF-8, resulting in a negligible amount of water adsorbed up to p_w/p_w^0=0.6, where p_w is the actual partial pressure and p_w^0 is the saturation partial pressure of water vapor. The behavior was also successfully modeled by using molecular simulation.[68] Finally, the higher Brunauer, Emmett and Taller (BET) surface area of ZIF-8,

allows the MOF to have higher sorption capacity. For instance, H_2 uptake has been reported to be equal to 145 cm^3(STP)/g when the adsorbate pressure is 1 atm.[46]

6.1.3. MMMs Preparation

The production of homogeneous and stable membranes with good mechanical properties, and the implementation of a simple and reproducible protocol, has been a crucial step of this study. To achieve this goal, it was necessary to optimize several factors such as the size of the filler particles, the solvent, the solvent evaporation temperature, which directly affects the evaporation rate during the casting, and finally, the thermal annealing treatment conditions.

6.1.3.1. Casting and Aspect of MMMs

The PPO-based MMMs at different loadings of ZIF-8 were prepared following the optimized protocol described in the experimental methods section 5.1.1. of this dissertation. In **Figure 6.2** it is possible to appreciate the transparency of pure PPO membranes, while MMMs with ZIF-8 developed a slight haze due to the presence of the fillers. Composite membranes were found to be macroscopically homogeneous, testifying the overall good dispersion of the particles inside of the polymer matrix.
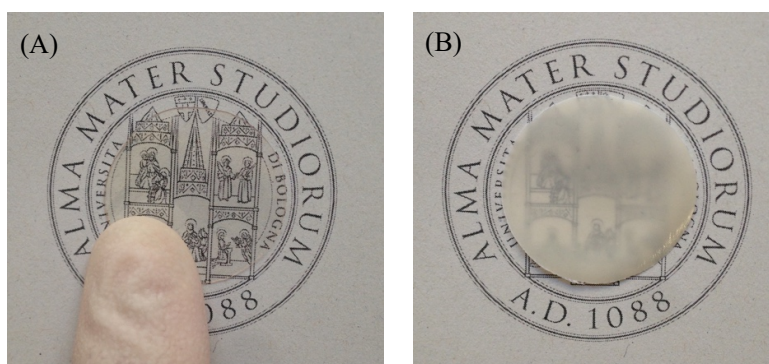
Figure 6.2: Membrane samples pure PPO (A) and ZIF-8/PPO (25 wt.%) (B).

Membranes made of polymer only offer high bending capacity. MMMs with a filler content up to 15 wt.% were still mechanically robust and preserved this feature. At intermediate loads (*e.g.* 25 wt.%), membranes started losing some of their mechanical properties, but could still be easily bended (**Figure 6.3**). Films began to become more brittle when the particle content increased up to 45 wt.%. These materials revealed lower resistance to bending, which was expected since, for instance, a ZIF-8/PPO membrane at 45 wt.% contains about a 48% in volume of the MOF.
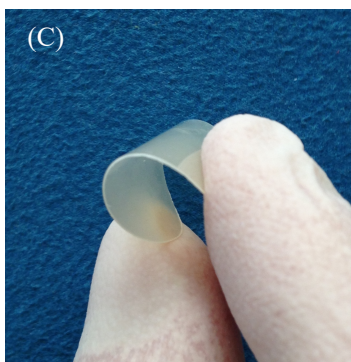
Figure 6.3*:Flexibility of ZIF-8/PPO MMMs at 25 wt.% of ZIF-8.*

6.1.3.2. Thermal Annealing

Physical aging is a phenomenon that occurs to all amorphous materials in the glassy state which evolve towards an equilibrium point and is accelerated by high temperatures. Indeed, it was shown by Ansaloni *et al.*[69] who performed studies on another glassy polymer, Matrimid® polyimide, that the increase of the thermal treatment temperature led to a larger reduction of the FFV and to a stabilization of transport properties over time. Savoca *et al.*[70] observed a considerable decrease of permeability in PTMSP films by increasing the temperature of the thermal treatment, testifying that the sample returned to its original permeability after dissolving and recasting the membrane. Hung and Paul studies have decreed that the aging rate of PPO is faster the higher the aging temperature, and slower the thicker the membrane, by monitoring key parameters such as FFV, gas permeability and refractive index of the polymer.[52,71,72] At 35 °C, a PPO film which thickness was ≈ 400 nm, experienced a loss of permeability of ≈ 65% over 4,000 h (≈ 6 months), conversely a ≈ 25 µm film revealed a decrease of ≈ 20% over

10,000 h ($\approx$ 14 months).[71] Although the membranes produced in this study are rather thick (*i.e.*, 80-120 µm), thus they are subject to a slow ageing, we decided to perform a thermal treatment, in order to induce an accelerated ageing process and be sure to have stable transport properties during the experimental campaign. This protocol also ensures to remove all traces of solvent. The temperature of the thermal treatment was chosen testing He and CO_2 permeability of PPO membranes after being thermally treated at 100, 150, 200, and 250 °C (the latter above T_g). The results of gas permeability versus pretreatment temperature are reported in **Figure 6.4** and showed that permeability decreased with increasing treatment temperature, due to the accelerated ageing induced by such high temperatures, and reaches a plateau at a temperature of 200 °C, which is also below the T_g of PPO, and was chosen as the optimal one in this work.
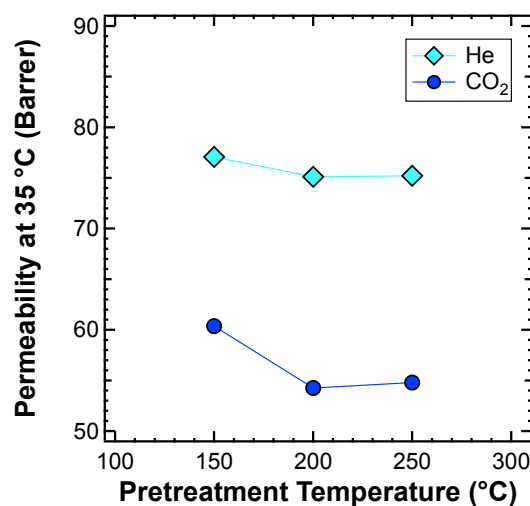
Figure 6.4: Effect of thermal annealing temperature on pure PPO permeability at 35 °C.

6.1.4. Considerations on the Density of MMMs

The density values of pure materials and composite membranes are reported in **Figure 6.5** versus filler content. The density of the mixed matrix membranes decreased with increasing ZIF-8 loading. By plotting the same data in terms of specific volume of each film as a function of weigh filler loading, the expected linear correlation ($\hat{v}_{MMM} = w_{PPO}\hat{v}_{PPO} + w_{ZIF}\hat{v}_{ZIF}$) was obtained with a correlation coefficient $R^2 = 0.98$ (represented with a dashed line in **Figure 6.5**). Hence, it was possible to estimate the density

of ZIF-8 by extrapolating the linear function. Surprisingly, ZIF-8 density resulted to be 0.96 g/cm^3, a value very close to that of the theoretical density of the regular ZIF-8 crystal, *i.e.* 0.93-0.95 g/cm^3.[46,58,64] This may indicate that the presence of voids inside the MMMs is negligible, since those interfacial adhesion defects would be indicated by lower values of density of the membranes. It must be noticed that this value of density is very different from the crystallographic density provided by *BASF* (*i.e.*, 0.35 g/cm^3). The additive rule for composite materials is shown in Eq. (6.1):

$$\rho_{MMM} = \frac{\rho_{PPO}\rho_{ZIF}}{w_{PPO}\rho_{ZIF} + w_{ZIF}\rho_{PPO}} \qquad \text{Eq. (6.1)}$$

It is represented as a solid red line in **Figure 6.5** and was implemented to compare the experimental values with the ones predicted by the ideal combination of the two phases. The consistency between the additive rule and the actual density of the composites indicates that the polymer and filler phase have overall a good adhesion.
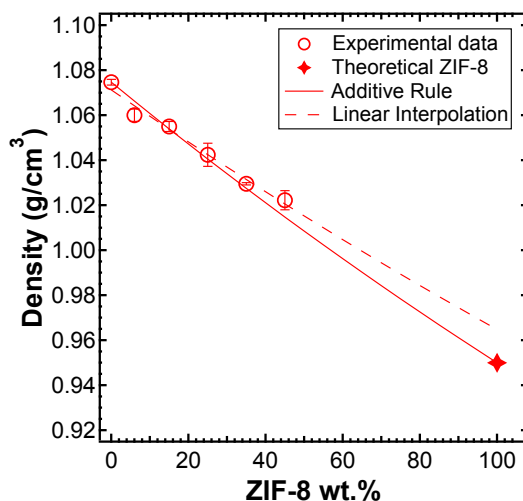
Figure 6.5: *Density of the mixed matrix membranes versus ZIF-8 weight fraction in the film (empty circles), measured with the buoyancy technique in water. Solid line represents the additive rule and was evaluated from the experimental density of PPO and the theoretical density of ZIF-8. Dashed line represents the linear interpolation of the experimental values measured, extrapolated up to pure ZIF-8.*

6.1.5. Morphology: SEM

The morphology of ZIF-8/PPO mixed matrix membranes was investigated at different loadings of the MOF by means of SEM analysis. This enabled to determine the quality of the adhesion between the

particles and the polymer matrix, as well as to evaluate the dispersion of the filler. The SEM images are reported in **Figure 6.6**, and generally show that ZIF particles and the polymer are compatible and had good adhesion. This is consistent with the partially organic nature of the filler which improves the affinity with the polymer matrix as above described. However, detachment appear to happen in some cases, and this could be ascribed to the phenomena described in the following. It is common knowledge that glassy polymers with a rigid backbone and a high glass transition temperature, such as PPO, vitrify when the solvent evaporates.[18] The evaporation-induced transition from rubbery state to glassy state can cause significant stress to the system. As also pointed out by Koros *et al.*[27], this phenomenon could happen during the composite membrane formation before all the solvent has left the film, making further evaporation beyond this point crucial for the detachment of the polymer chain from the filler. This could lead to the formation of non-selective voids which might prevent the membranes to be as selective as expected but, on the other hand, more permeable. In this work, slight delamination between the two phases can be seen especially at high loadings (*i.e.*, ≥ 25 wt.%). However, the presence of non-selective voids can be excluded since no anomalous selectivity loss was observed with increasing filler loading, as will be discussed in section 6.1.7.1, and composites density follow closely the volume additivity as shown above. As pointed out by Ordonez *et al.*[45], delamination can be also induced by fracturing with liquid nitrogen the membranes prior to the SEM analysis. The latter contribution would not affect the transport properties, being caused artificially during the preparation of the sample for the analysis. However, we believe that mechanical stress imposed to break the films and expose the cross-sections would be responsible for the detachment just to some extent.

Chung *et al.*[18] reported that the use of higher-than-ambient temperature to promote fast evaporation during film formation, and in the case here reported, generate a net heat flux and a temperature gradient between bottom and top of the nascent membrane. This way of heating was found to promote convective fluxes inside the fluid suspension, leading to inhomogeneous thicknesses and irregular distribution of the filler in the resulting MMMs, but this kind of consequences were not experienced by the ZIF-8/PPO membranes, probably because of the high viscosity of the casting solution. The distribution of the filler within the matrix was overall ubiquitous, although in a minor number of cases larger aggregates were

visible. This occurred although membrane formation after the solution casting was very quick (*i.e.,* 15 minutes) and the solution viscous, providing less time for the filler to aggregate and limiting the mobility of the particles in the media, respectively. Nevertheless, the majority of the particles was smaller (*e.g.,* 1-4 µm) and also many ZIF nanocrystal cubes with a side of ≈200 nm can be observed.
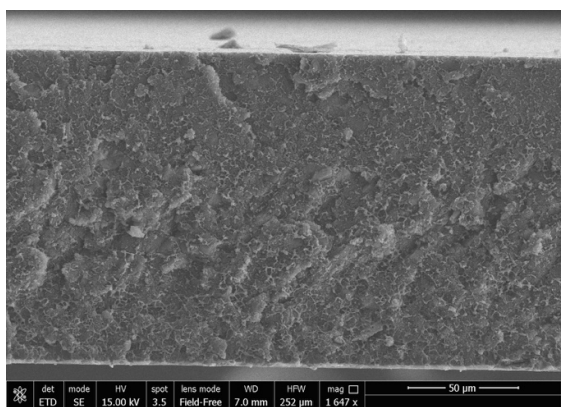
(a) 25%   (b) 10%
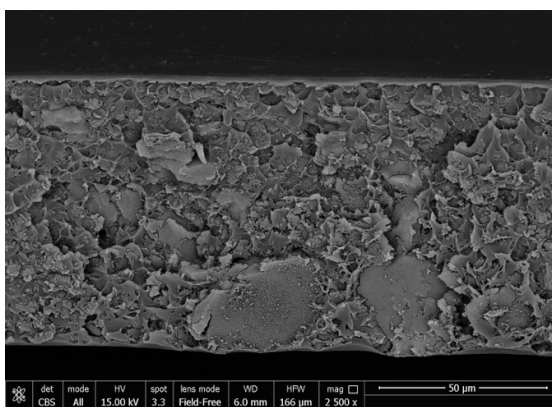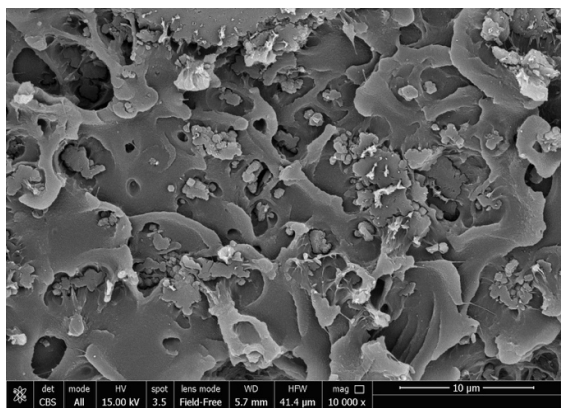
(c) 10%   (d) 45%
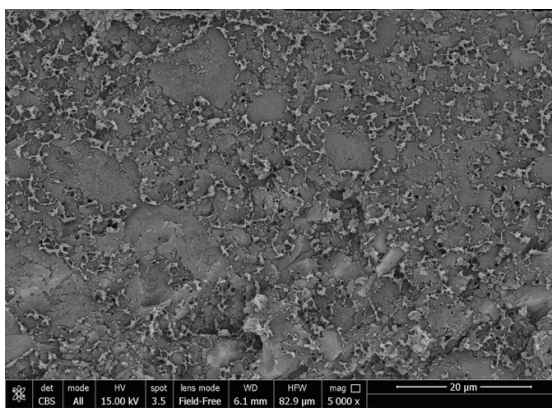
(e) 25%   (f) 25%
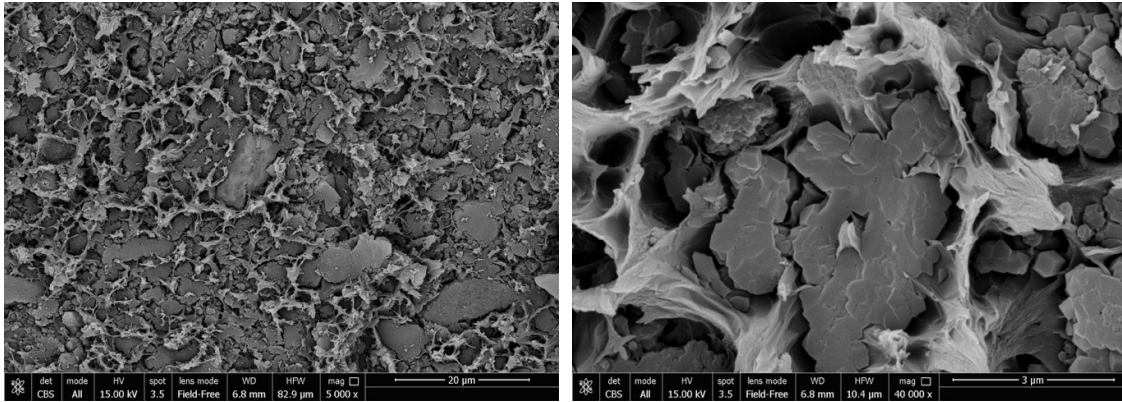
(g) 10%

(h) 25%
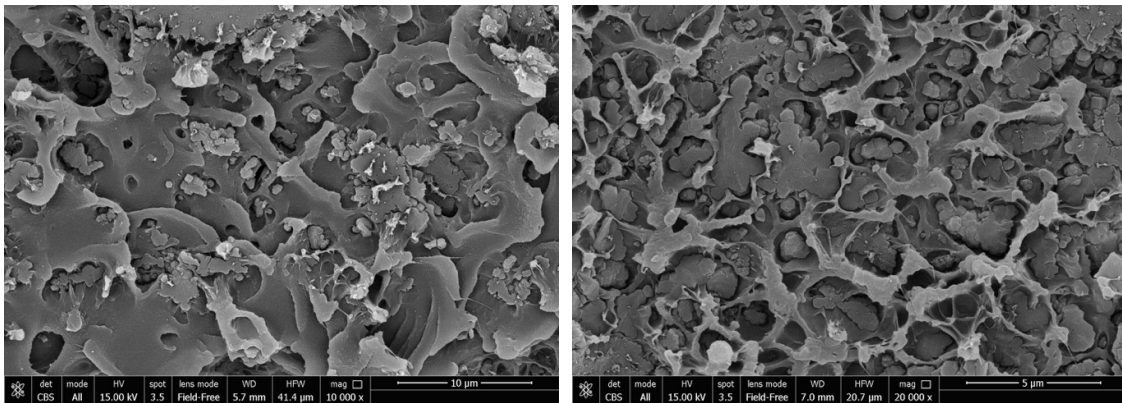
(i) 25%

(j) 10%
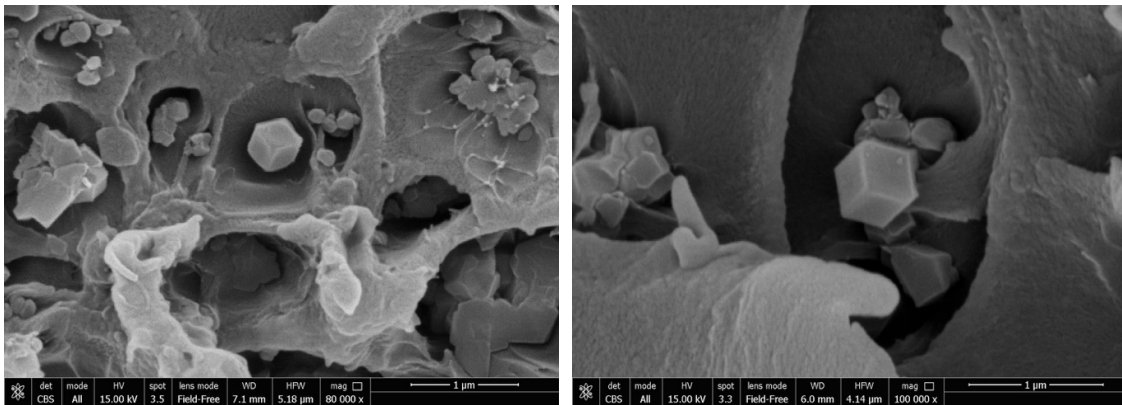
Figure 6.6: *SEM images of the cross-section of ZIF-8/PPO mixed matrix membranes at different loadings and magnitudes: (a) 25 wt.%, 1,647 ×; (b) 10 wt.%, 2,500 ×; (c) 10 wt.%, 10,000 ×; (d) 45 wt.%, 5,000 ×; (e) 25 wt.%, 5,000 ×; (f) 25 wt.%, 40,000 ×; (g) 10 wt.%, 10,000 ×; (h) 25 wt.%, 20,000 ×; (i) 25 wt.%, 80000 ×; (j) 10 wt.%, 100000 ×.*

6.1.6. Calorimetric Results

6.1.6.1. Differential Scanning Calorimetry

The Differential Scanning Calorimetry (DSC) analysis was carried out in two subsequent runs on pure amorphous films of PPO, pure ZIF-8 powder as received, and mixed matrix films between 25 °C and 300 °C. Differences between two subsequent scans can indicate degradation or chemical modification of the sample induced by temperature, presence of residual moisture or solvent.

From **Figure 6.8a**, it is evident that pure PPO films obtained via solvent casting in chloroform at 50 °C were fully amorphous, as they showed the typical glassy transition peak at about 213 °C, consistent with literature values, in both scans.[48,53] It must be noticed, however, that slower casting at room temperature (*i.e.*, complete evaporation in 3 days) resulted in the formation of semi-crystalline PPO samples, as verified via DSC analysis (**Figure 6.7a**), and rupture of the membrane during film formation (**Figure 6.7b**). The polymer was not transparent as for the amorphous one showed in **Figure 6.2a**, but white, which is consistent with the formation of crystal domains.

(a)

(b)
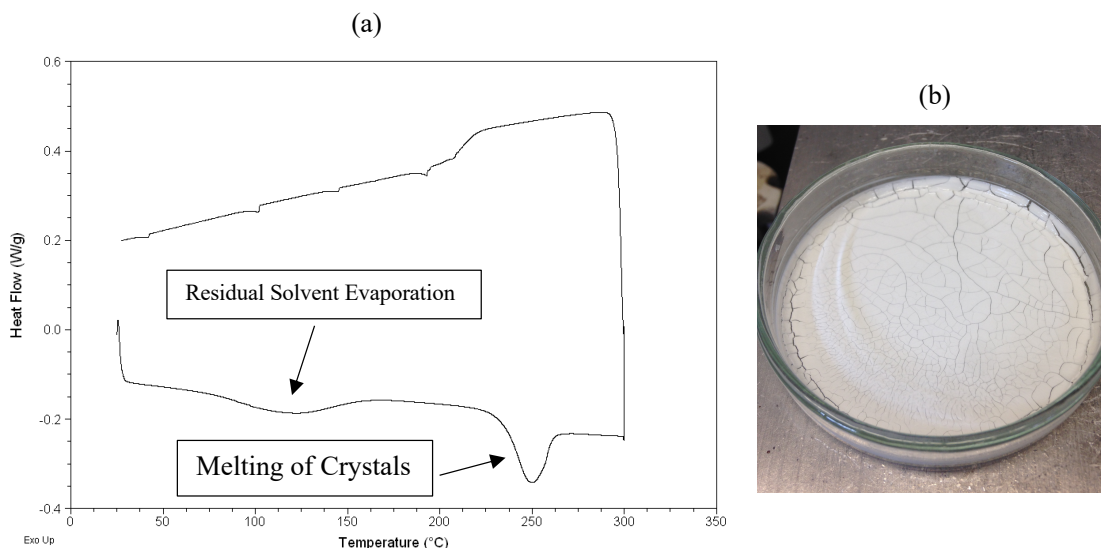
Figure 6.7: First DSC scan of a sample of PPO casted inducing slow solvent evaporation, with subsequent formation of crystal domains and rupture of the membrane. Before performing DSC the film was not pre-treated.

A specific analysis was carried out in this work on the effect of casting temperature on the final properties, although not reported here because beyond the scope of the paper: the value of 50 °C appears to be the optimal one in order to have robust and amorphous PPO films. There is almost no difference between the 1st and 2nd scan in the amorphous PPO, because such sample was previously treated at 200 °C under vacuum, proving that the treatment can remove any residual solvent. Almost no difference was observed also between the two scans carried out on ZIF-8, which indicates that the material is perfectly hydrophobic as indicated in the literature (**Figure 6.8b**).[46,67,68] The observation comes from the fact that hydrophilic materials such as zeolites, show broad endothermic peaks in DSC scans performed in the same range of temperatures, also when the specimens were stored at environmental conditions prior to test.

The same analysis was carried out on mixed matrix membranes containing PPO and different amounts of ZIF-8. In **Figure 6.8c** we reported the results relative to the sample containing 25 wt.% of ZIF-8. One can notice a sharper peak upon transition in the 1st scan, which may be indicative of the presence of some ordered regions in the polymeric part of this membrane. Such sharp peak disappears in the second scan, where the transition is perfectly glassy as in the case of pure amorphous PPO.
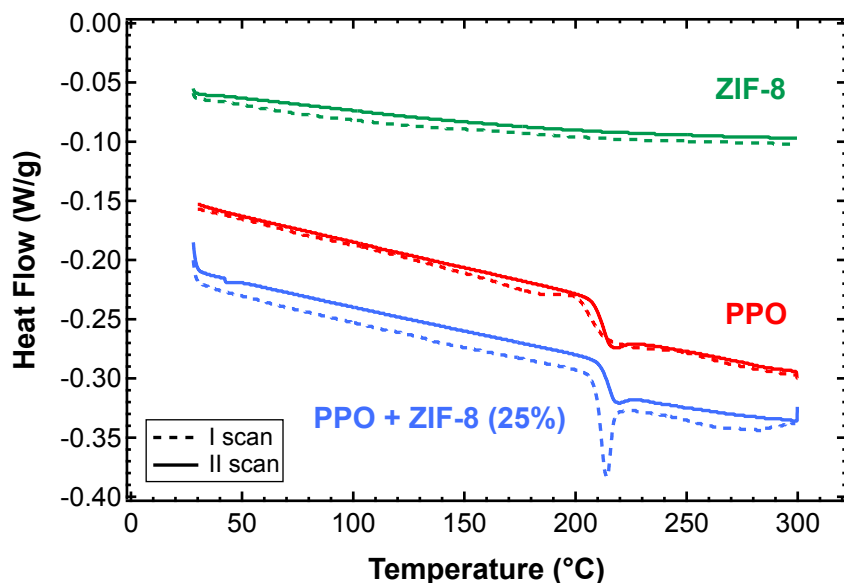
Figure 6.8: *DSC tests on: pure amorphous PPO film after a thermal annealing treatment at 200 °C under vacuum (red), ZIF-8 powder as received (green), and 25 wt.% ZIF-8/PPO mixed matrix film after undergoing a thermal annealing treatment at 200 °C under vacuum (blue).*

Tests carried out on other MMM samples containing different amounts of ZIF-8 allowed to locate the glass transition temperature for each sample. In particular, it was shown that the addition of increasing amount of ZIF-8 increases, albeit slightly, the glass transition temperature of the membrane, as shown in **Figure 6.9**. Therefore, the presence of the MOF in the membranes led to a monotonous increase of the rigidity of the polymer matrix, reducing the mobility of the polymeric chains. This, in turn, can be related also to the appearance of imperfect adhesion with increasing loading in the SEM images in **Figure 6.6**.

Previous works that tried to correlate the variation of permeability and selectivity to the variation of T_g of mixed matrix membranes do not provide clear and univocal conclusions. In particular, Moaddeb et al.[73] observed that the reduction in 6FDA-IPDA chains mobility conferred an enhanced O_2/N_2 selectivity, while permeability was barely altered or negligibly reduced. The opposite was observed by Song et al..[58] In the latter work, ZIF-8/Matrimid® membranes showed enhanced permeability up to about 3-4 times than that of pure Matrimid®, while H_2/CO_2 selectivity remained constant with the filler loading (*i.e.* with the increasing T_g). These results are in contrast to those reported by Díaz et al. for ZIF-8/PPEES systems, where no changes of the T_g was observed.[63]

In the case of the systems studied in the present work, we believe that the slight increase of rigidity testified by the increase of T_g, might reduce to some extent the polymer diffusivity and thus permeability. However, due to the high intrinsic diffusivity of the filler, it is reasonable that the effect induced by the rigidification in the transport properties is negligible.
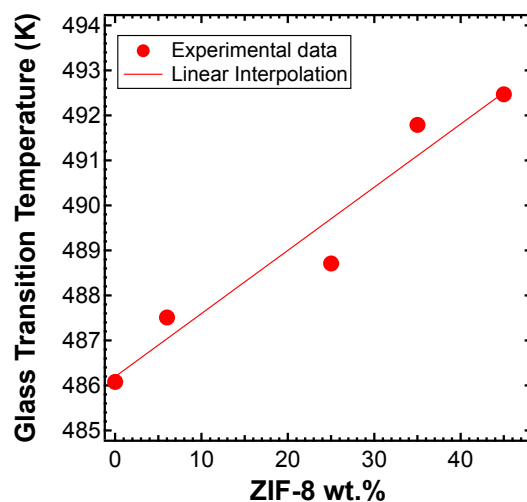
Figure 6.9: Trend of the glass transition temperature in ZIF-8/PPO MMMs as a function of the filler loading.

6.1.6.2.　　TGA

Thermogravimetric analysis was already performed on ZIF-8 by other authors. Park *et al.*[46] reported a weight loss of 28.3% once the temperature reached 450 °C, while the commercial ZIF-8 used in this work showed almost no weight loss up to the same temperature (**Figure 6.10**). This was addressed by the authors as an escape of the residual molecules from the as-synthesized MOF (*e.g.*, DMF, H_2O, calcd.) while the commercial one comes already purified. However, the two materials interfaced the same behavior from 600 °C to 800 °C. Zhang *et al.*[62] tested the same ZIF-8 we used in this work below its decomposition temperature, previously saturated in water vapor. Water-saturated ZIF-8 lost only a 3% of its weight, as a proof of its hydrophobic behavior and great thermal stability. Along with the MOF, PPO revealed a surprisingly high integrity up to 400 °C as shown in **Figure 6.10**, corroborating that ZIF-8/PPO MMMs are suitable for high temperature applications.
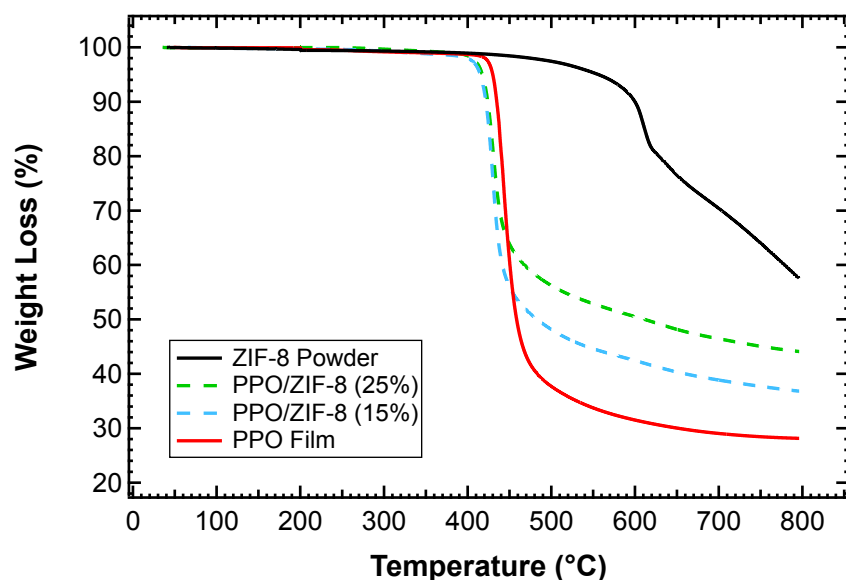
Figure 6.10*: TGA analysis results of PPO (red), ZIF-8 (black), ZIF-8/PPO (15 wt.%) (blue) and ZIF-8/PPO (25 wt.%) (green). Tests were performed in nitrogen atmosphere. PPO and MMMs were pre-treated at 200 °C overnight and then normally exposed to air for days/weeks, while ZIF-8 powder was tested as received.*

6.1.7. Transport Properties

6.1.7.1. Effect of the Filler Loading and of the Temperature on Permeability

Pure-gas permeability tests with He, N_2, CH_4 and CO_2 were performed for several membranes at 35 °C, covering the whole range of filler loadings investigated, namely 0, 3, 6, 10, 15, 25, 35 and 45 wt.%. The mixed matrix membranes, as well as the pure polymer, were treated at 200 °C under vacuum overnight prior to perform experiments. **Figure 6.11** shows that permeability increases monotonously with the filler loading. As one can see, the permeability enhancement is extremely high and, in particular, adding 45 wt.% of ZIF-8 to PPO enhances the He permeability by a factor of about 8. **Table 6.4** presents also the ideal selectivity for relevant gas pairs (*i.e.*, He/CO_2, CO_2/N_2, CO_2/CH_4, He/CH_4, He/N_2). The uncertainty of the calculated permeability was primarily originated from the variation of membrane thickness. Anyhow, the overall error was always kept within ± 3% form MMMs up to 25 wt.% and within ± 8% for higher loadings.
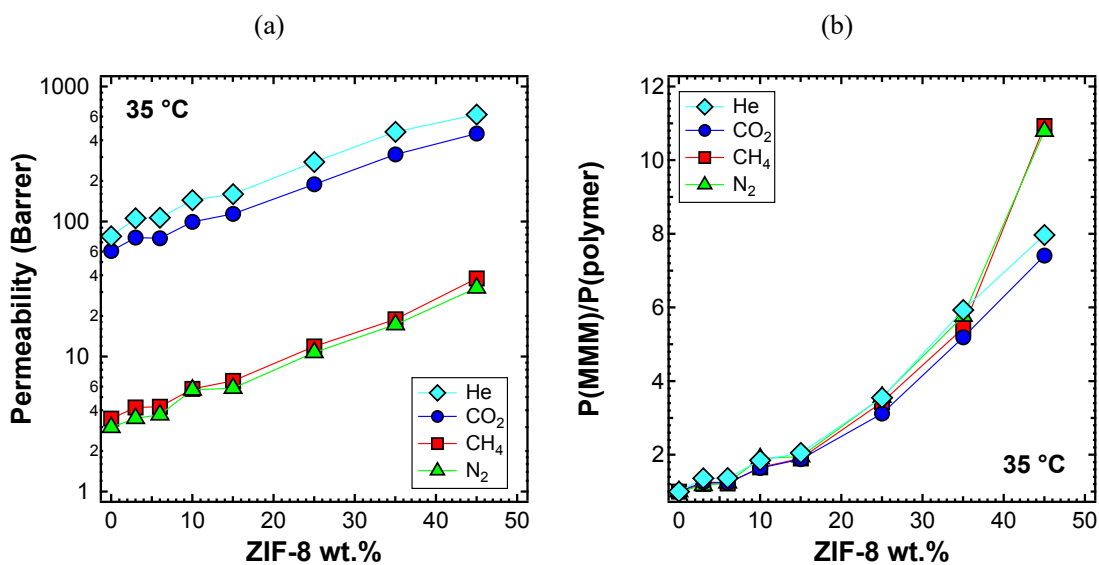
Figure 6.11: (a) Permeability and (b) relative permeability increase of various gases at 35 °C with an upstream pressure of 1.3 bar in ZIF-8/PPO mixed matrix membranes (MMMs).
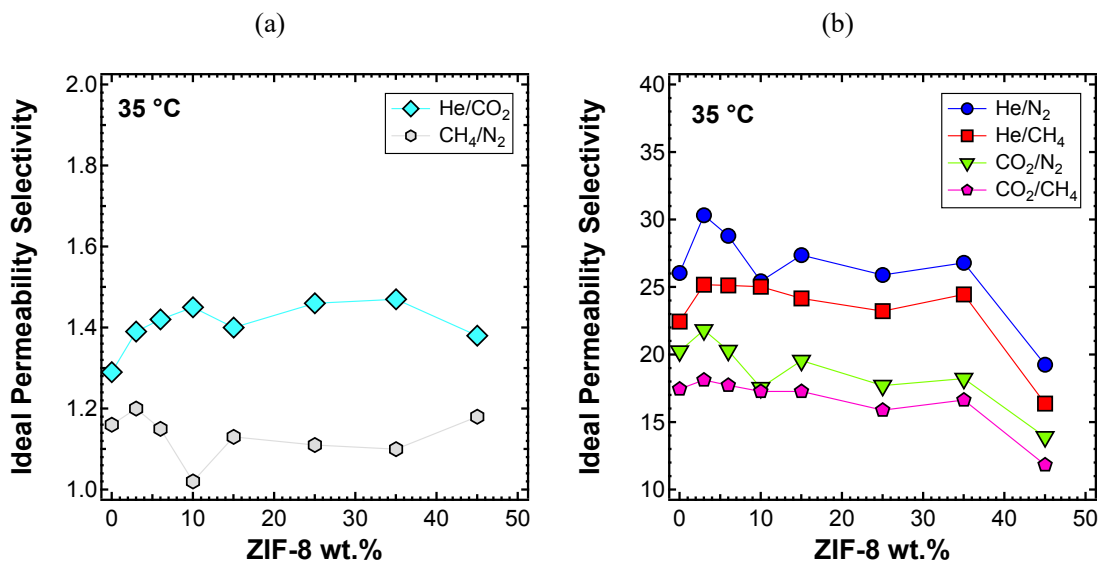
Figure 6.12: Ideal Selectivity for (a) He/CO$_2$ and (b) other gas couples at 35 °C with an upstream pressure of 1.3 bar in ZIF-8/PPO mixed matrix membranes (MMMs).

The significantly enhanced permeability was accompanied by a modest increase in selectivity for the He/CO$_2$ gas pair (*i.e.*, up to 15% more than that of pure PPO). Similar results were achieved also by other authors.[58,59,63,74] The MMMs permeability results are in line to what expected from the transport properties of pure PPO measured in this work, and ZIF-8 permeability and ideal selectivity data from

the published literature summarized in **Table 6.3**. In fact, the remarkable enhancement of permeability can be attributed to the very high permeability of ZIF-8, which is about two orders of magnitude higher than that of pure PPO. Furthermore, ZIF-8 shows higher H_2/CO_2 ideal selectivity and this led to a small improvement of He/CO_2 selectivity also in the ZIF-8/PPO composite membranes (**Figure 6.12a**). Conversely, CO_2/N_2, CO_2/CH_4, He/CH_4 and He/N_2 ideal selectivity for ZIF-8 was lower than that of PPO, thus an almost constant selectivity was shown by MMMs at low loadings, while at higher loadings a slight decrease was observed (**Figure 6.12b**).

Table 6.4: *Pure-gas permeability and ideal selectivity in PPO and ZIF-8/PPO mixed matrix membranes. Tests were performed at 35 °C and 1.3 bar as the upstream pressure.*

ZIF-8 loading (wt.%)	Pure-gas permeability (Barrer[a])				Ideal selectivity				
	He	N_2	CH_4	CO_2	He/CO_2	CO_2/N_2	CO_2/CH_4	He/CH_4	He/N_2
0 (PPO)	77.9 ± 2.25	2.99 ± 0.07	3.47 ± 0.09	60.6 ± 1.52	1.29	20.2	17.4	22.3	26.0
3	105.8 ± 2.51	3.49 ± 0.08	4.20 ± 0.10	76.1 ± 1.85	1.39	21.8	18.1	25.2	30.3
6	106.7 ± 2.39	3.71 ± 0.08	4.25 ± 0.10	75.3 ± 1.71	1.42	20.3	17.7	25.4	28.8
10	144.3 ± 3.56	5.67 ± 0.13	5.76 ± 0.14	99.5 ± 2.44	1.45	17.5	17.3	24.9	25.4
15	159.7 ± 1.54	5.83 ± 0.06	6.61 ± 0.07	114.1 ± 1.12	1.40	19.6	17.3	24.2	27.4
25	276.4 ± 10.4	10.7 ± 0.41	11.9 ± 0.46	189.0 ± 7.23	1.46	17.7	15.9	23.2	25.9
35	462.0 ± 31.0	17.2 ± 1.14	18.9 ± 1.27	314.2 ± 21.0	1.47	18.2	16.6	24.4	26.8
45	620.9 ± 54.0	32.3 ± 2.81	37.9 ± 3.28	448.7 ± 38.9	1.38	13.9	11.8	16.4	19.2

[a]Barrer: 10^{-10} cm^3 cm cm^{-2} s^{-1} (cmHg)$^{-1}$

To conclude, the permeability enhancement obtained by adding ZIF-8 to PPO was extremely high for all gases, and was consistent with the high permeability measured in the literature for ZIF-8.[38–40] This result demonstrates that the filler contributes actively to the transport of gas molecules and that its pores are not blocked by the polymer phase. The selectivity enhancement is more limited, and was observed only for loadings of ZIF-8 below 35 wt.%, because at 45 wt.% the formation of a small amount of non-selective voids can be assumed. This is further confirmed by looking at the anomalous permeability

increase for N_2 and CH_4, the bigger gas molecules, in **Figure 6.11b** which led to the selectivity drop observed in **Figure 6.12b**. This result is consistent with the published ideal selectivity values for a pure membrane of ZIF-8, which are generally lower than those of pure PPO for all the gas couples inspected. The only exception is the H_2/CO_2 pair, which is higher than the one evaluated in pure PPO in this work for He/CO_2, as expected. Indeed, He/CO_2 selectivity of MMMs is higher than that of pure PPO.

Permeability tests were also performed at 50 and 65 °C on a selected list of MMM samples. When analyzing the behavior at different temperatures, one can notice that the qualitative trends were similar, albeit with generally higher values of permeability, which are shown in **Figure 6.13a** (50 °C) and **Figure 6.14a** (65 °C). The relative increase of permeability, that is displayed in **Figure 6.13b** (50 °C) and **Figure 6.14b** (65 °C) was slightly lower than what observed at 35 °C. In particular, we noticed that at higher temperatures, the effect of adding ZIF-8 on the permeability was around the same for He and CO_2, while less marked for N_2 and CH_4.

(a)   (b)
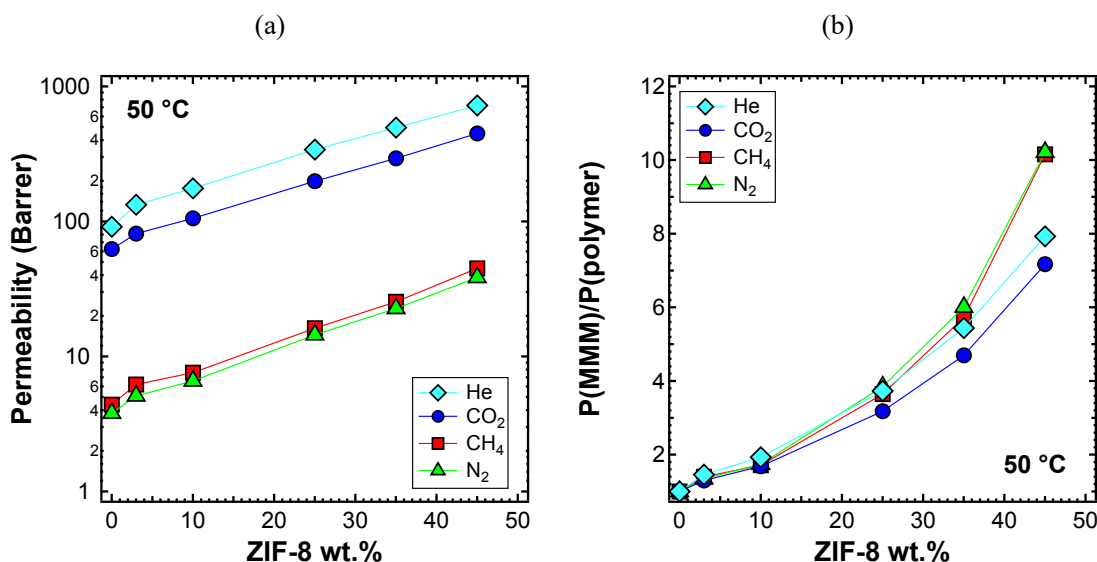
Figure 6.13: (a) Permeability and (b) relative permeability increase of various gases at 50 °C with an upstream pressure of 1.3 bar in ZIF-8/PPO mixed matrix membranes (MMMs).
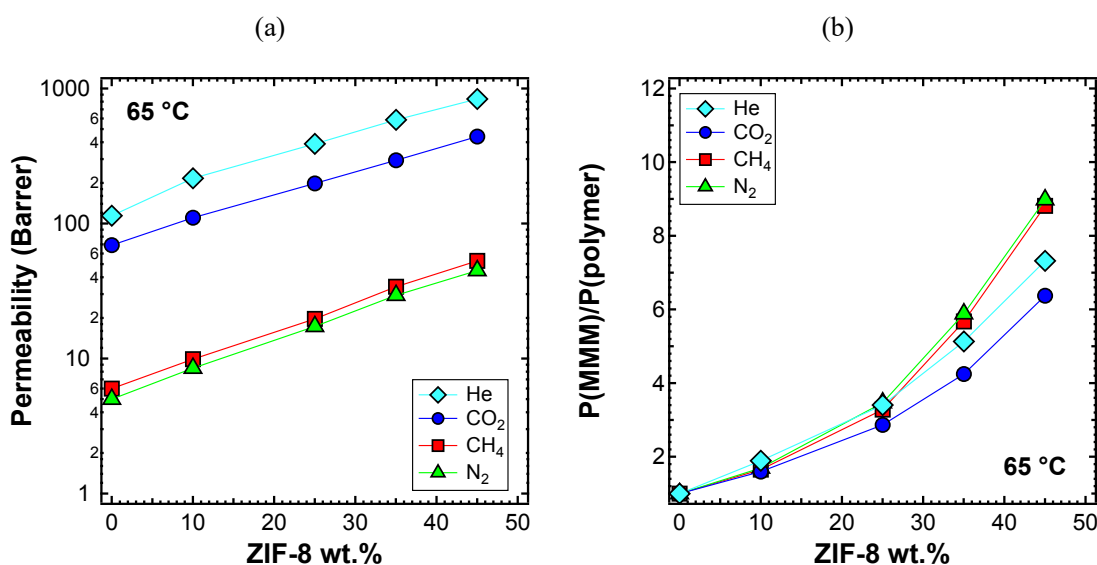
Figure 6.14: *(a) Permeability and (b) relative permeability increase of various gases at 65 °C with an upstream pressure of 1.3 bar in ZIF-8/PPO mixed matrix membranes (MMMs).*

The ideal selectivity was also estimated at 50 and 65 °C. In **Figure 6.15a** we reported the He/CO_2 selectivity versus filler loading at the three different temperatures inspected: one can notice the monotonous increase of the curve with temperature. The shape of the curve remains similar at all temperatures, with an initial higher increase of selectivity for loadings below 10 wt.%, followed by a stable trend and then a slight decrease at a filler loading of 45 wt.%, for the reasons mentioned above. He/CO_2 is the only gas pair which selectivity is enhanced by temperature.[75] This is because of the different nature of the two gases. Helium is a very small and non-condensable ($T_c = 5.2$ K) gas which permeability is controlled by diffusivity. CO_2 is bigger and much more condensable ($T_c = 304.2$ K) and its permeability is controlled by solubility. Temperature enhances diffusivity, being a kinetic property, while compromises solubility, the thermodynamic contribution. Overall, this leads to the results observed.

The selectivity of the MMMs inspected with respect to other gas couples is reported in **Figure 6.15b** and **c** for the temperatures of 50 °C and 65 °C, respectively. The optimal selectivity is obtained for a filler loading of 10% at both temperatures, for the gas He/CH_4 and He/N_2, respectively. On the other hand, the CO_2/N_2 and CO_2/CH_4 selectivity decreases with filler content at both temperatures.

158

(a)

(b)   (c)
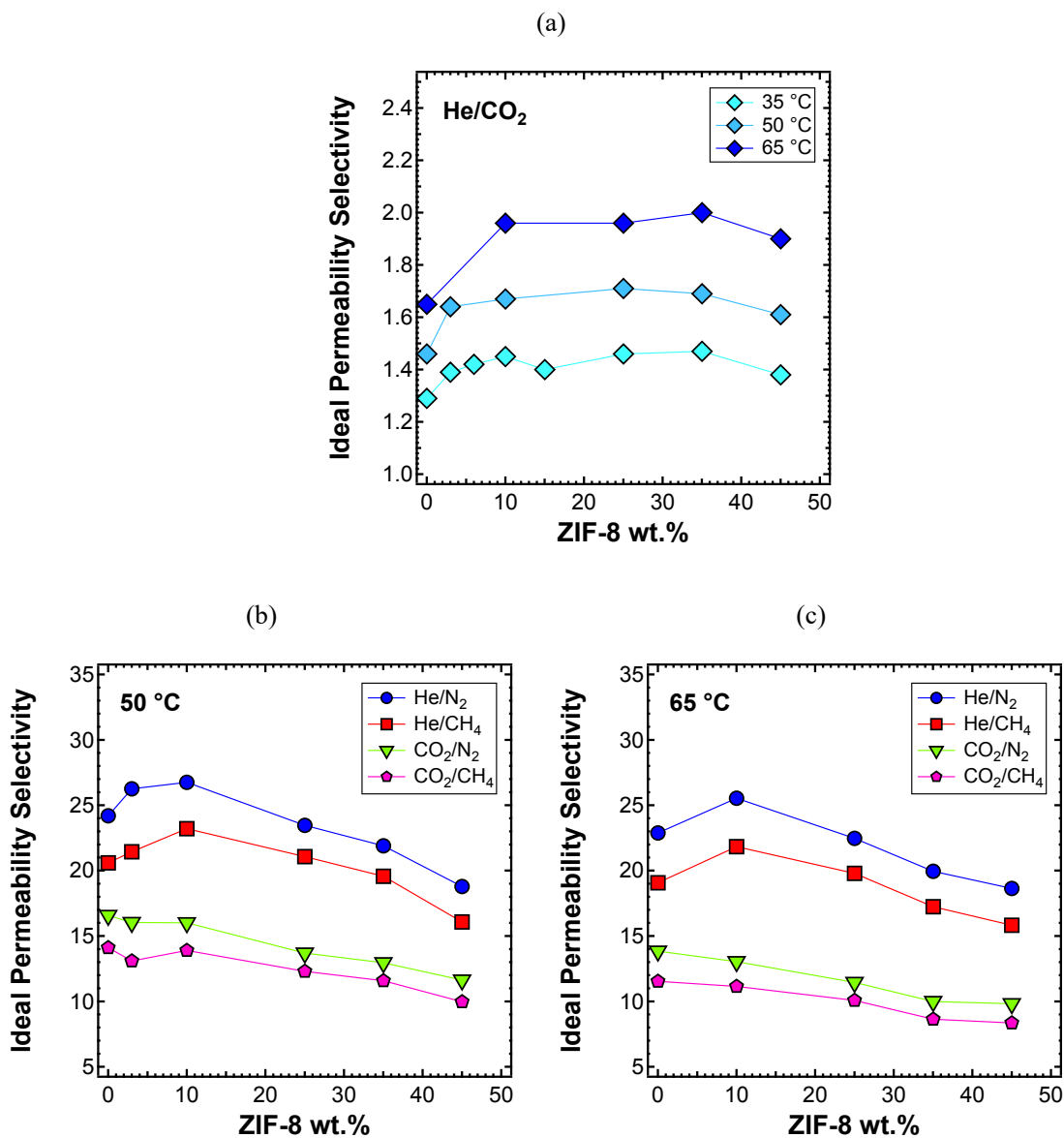
Figure 6.15: Ideal Selectivity values for (a) He/CO$_2$ at 35, 50 and 65 °C, (b) other gas pairs of interest at (b) 50 °C and (c) 65 °C in ZIF-8/PPO mixed matrix membranes (MMM) with an upstream pressure of 1.3 bar.

6.1.7.1.1.   MMMs Modeling

Permeability results at 35 °C were modeled to investigate the transport mechanism occurring in MMMs. An overview of the possible models was addressed in the theoretical background chapter. Results are reported for Maxwell-Wagner-Sillar[47,76] As shown in **Figure 6.16**, the model was able to fit successfully the experimental permeability values for each gas up to 15 wt.% of the filler. The shape

factor was considered 1/6 and the filler density equal to 0.96 g/cm³, as previously determined by extrapolating the experimental density values of MMMs.
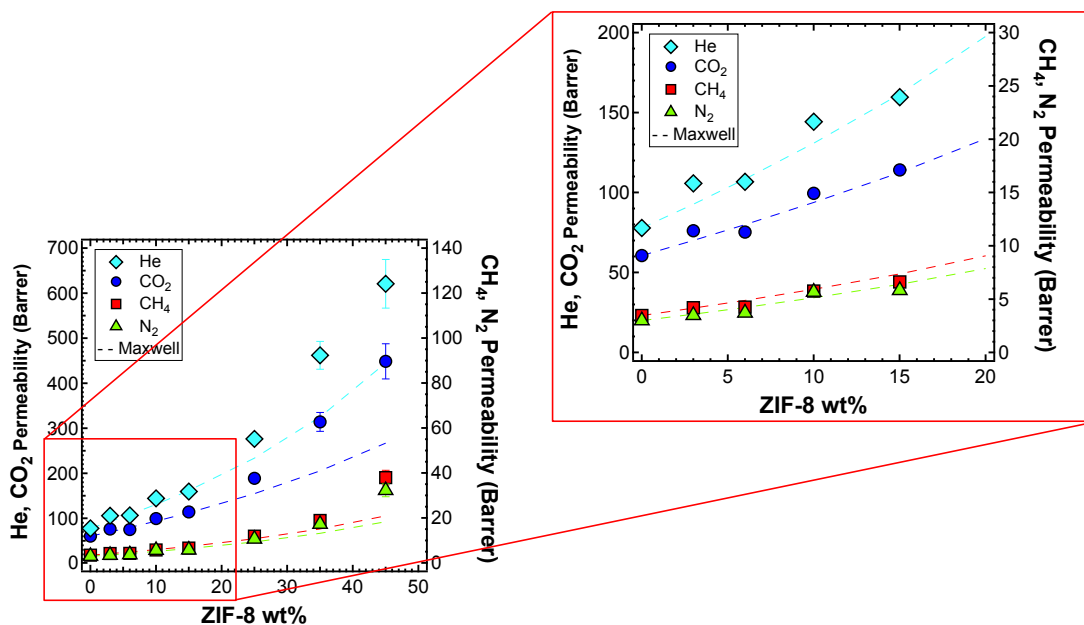
Figure 6.16*: Markers represent the experimental permeability, while dashed lines represent the results of the Maxwell-Wagner-Sillar model prediction when n=1/6 and ρ_{ZIF-8}=0.96 g/cm³. PPO single-gas permeability are from this work, while ZIF-8 pure-gas permeance are from Bux et al.[38] Song et al.[58] derived the permeability from the latter. The inset focuses the results obtained at filler loadings lower than 20%, the range in which the Maxwell model can be applied successfully.*

At filler contents higher than 20 wt.%, the model is not able to predict the gas permeability as expected. In particular, the Maxwell model underestimates the experimental data. Similar results were achieved also implementing models designed to predict permeability at higher filler loadings: Bruggeman[16,77], and Lewis-Nielsen.[16,78,79] This behavior can be addressed by considering two different phenomena: the presence of voids at the interphase between the polymer and the ZIF and/or the achievement of a certain percolation threshold.[80] The occurrence of voids cannot be excluded a priori, but can be considered as a minor effect, since the measured gas ideal selectivity follows the expected trend with increasing filler loading as can be observed in **Figure 6.17**. Conversely, as previously discussed, He/CO_2 selectivity slightly increase and the decreasing selectivity at high filler loadings for other gas pairs is physiological, in accordance with the less-selective nature of the ZIF-8 with respect to PPO towards gas pairs such as CO_2/N_2 and CO_2/CH_4. **Figure 6.17** shows how the trend of the ideal selectivity is in good agreement

with the one predicted with the Maxwell model, which considers defect-free MMMs, at least up to 35wt.%. The Maxwell model was also modified by Mahajan and Koros[28] to consider the potential interfacial voids formation between the two phases that may occur in complex systems such as MMMs. This model, also known as the *sieve-in-a-cage* model, for instance applied successfully by Li *et al.*[81], relies on an accurate determination on the effective defect dimension, which is hard to be established in heterogeneous systems like these ZIF-8/PPO MMMs.
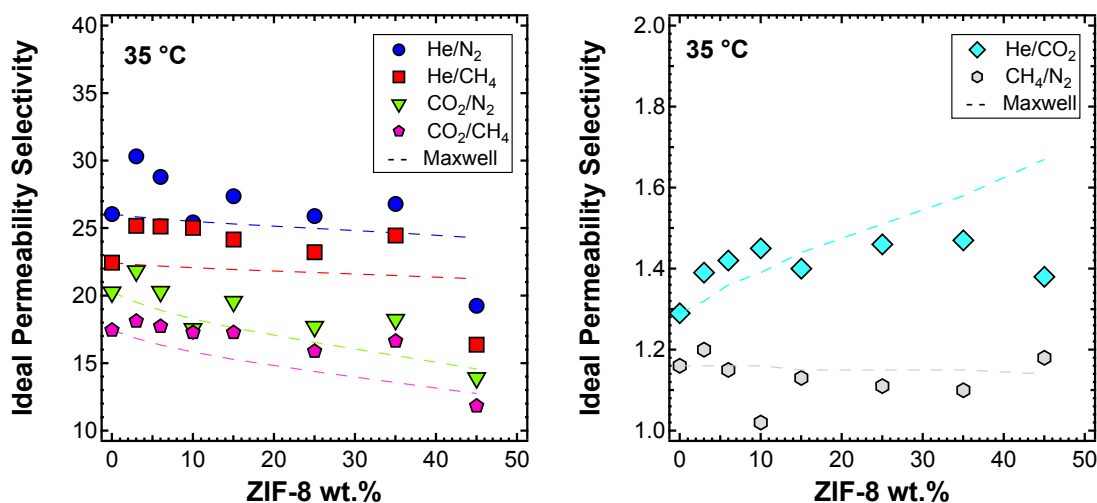
Figure 6.17*: Markers represent the experimental permselectivity, while dashed lines represent the ideal selectivity calculated from the Maxwell-Wagner-Sillar model.*

As above mentioned, another possible interpretation is that the high ZIF-8 volume fraction (*i.e.*, up to 48%) may provide the formation of channels made of a continuous phase of metal organic framework crystals across the whole membrane thickness. Gas molecules can take advantage of these preferential flow paths and a percolation mechanism for gas transportation may occur as illustrated in **Figure 6.18**. This results in MMMs with permeability higher than that expected from the simple combination of the two pristine materials. This explanation is consistent with the observations made on the FEG-SEM images, where at high filler loadings it is clear how the ZIF-8 phase can be the predominant one. Similar results were also obtained by other authors.[59,60]
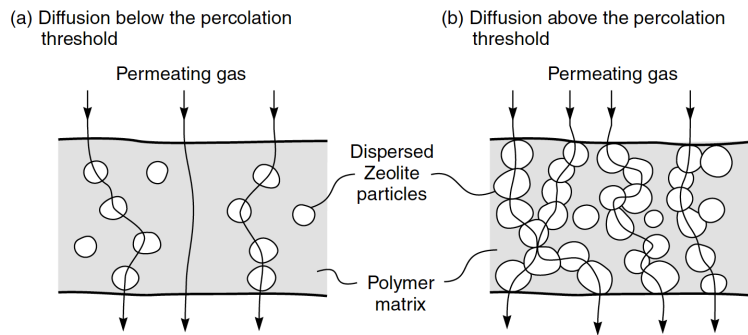
Figure 6.18: Illustration of the different transport mechanisms in MMMs, (a) with or (b) without reaching the percolation threshold. Figure from reference [82].

6.1.7.2.   Energetics of the Permeation Process

The effect of temperature on the transport properties was also investigated plotting permeability data as a function of temperature for various filler loadings. This is reported in **Figure 6.19** for the different gases. It can be noticed that the permeability of CO_2, as expected, was the one that was less affected by temperature: this happened because the permeability of such gas is strongly affected by solubility, that decreases with temperature.
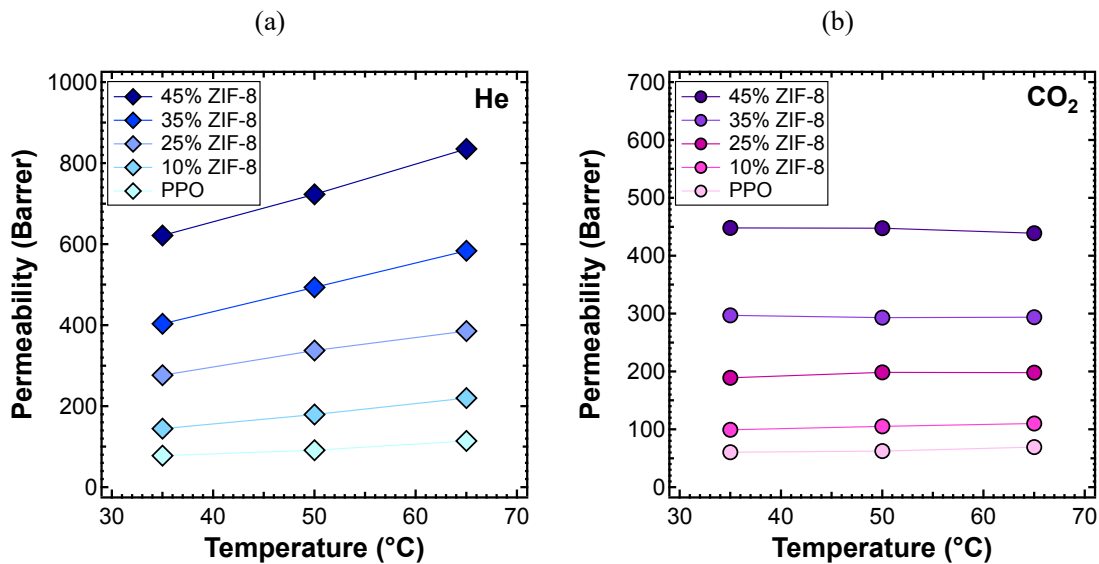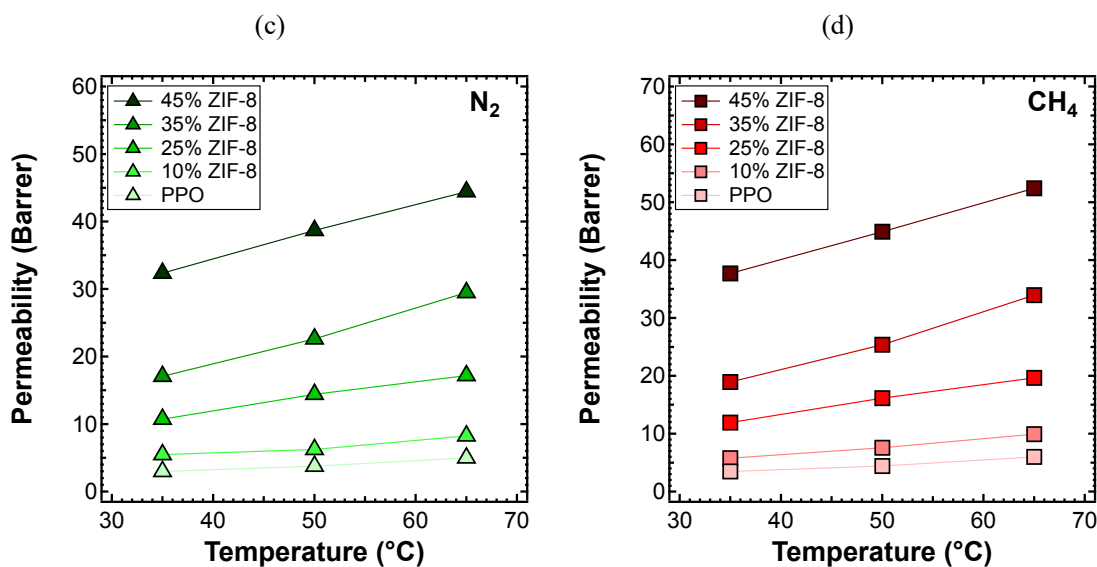
Figure 6.19: *Permeability of (a) He, (b) CO₂, (c) N₂, (d) CH₄ at different temperatures, in the ZIF-8/PPO MMMs of different weight fractions of ZIF-8, from 0 to 45%.*

Those data can be further elaborated to obtain a more quantitative indication of the effect of temperature on permeability, namely the energy contributions associated to the permeation process. This quantity can be estimated as reported in the theoretical background chapter. The values were calculated based on data measured at three different temperatures, just in case they showed good agreement with the Arrhenius-type behavior, and are reported in **Figure 6.20** and in **Table 6.5**.

It can be noticed that the addition of ZIF-8 particles made the membranes permeability a weaker function of the temperature. The plot indicates clearly that CO_2 has a very slight dependence on temperature (*i.e.*, smaller values of E_P), that becomes negligible at high filler loadings. At 35 and 45 wt.%, E_P revealed to have negative values, which means that permeability decreases with increasing temperature. This further enhances He/CO_2 selectivity since helium permeability has a larger dependence on temperature and keeps remarkably increasing with it.[60,63,75,83] The main reason why CO_2 permeability behaves this way, is because ZIF-8 provides a large sorption contribution at high loadings, and the loss of sorption overweighs the increase of diffusion while temperature increases. Further analysis of the sorption behavior will be provided in the following section. N_2 and CH_4 permeability show similar values, with CH_4 having a slightly higher value of activation energy. All values drop in the case of the

membrane containing 45 wt.% of ZIF-8, which is also the one characterized by the lowest selectivity and possibly presents some non-selective voids as discussed above.
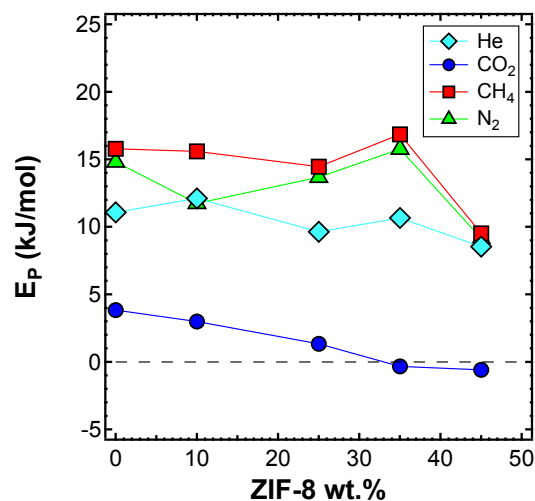
Figure 6.20*: Activation energy of permeability as measured in the interval 35-65 °C for four gases in the MMMs inspected, as a function of filler loading.*

Table 6.5*: Activation energy of permeability in the range 35-65 °C of ZIF-8/PPO mixed matrix membranes at different filler loadings.*

ZIF-8 loading (wt.%)	E_P (kJ/mol)			
	He	N_2	CH_4	CO_2
0[48]	9.7	9.8	12.1	1.5
0	11.07	14.81	15.78	3.84
10	12.11	11.74	15.59	2.99
25	9.64	13.68	14.46	1.34
35	10.66	15.76	16.85	-0.33
45	8.53	9.15	9.52	-0.59

6.1.7.3.   Diffusivity

The diffusivity of the different gases in the various mixed matrix membranes was estimated from the permeation output through the time-lag method. For helium, the time-lag was short, often less than 2-3 seconds, and difficult to be estimated accurately. In **Figure 6.21a** we reported the diffusivity at 35 °C

for the various mixed matrices. The diffusivity followed a slightly different order than permeability, in PPO and in all the studied MMMs. In particular, $D(He) > D(CO_2) > D(N_2) > D(CH_4)$, which is consistent with the values of the effective diameter of all the gas molecules investigated. On the other hand, for permeability it was $P(He) > P(CO_2) > P(CH_4) \geq P(N_2)$. However, the permeability of CH_4 and N_2 was in all cases very similar, and the higher values recorded for CH_4 permeability was due to its higher solubility in the membrane. In **Figure 6.21b** we reported the diffusivity ratio between each mixed matrix membrane and the polymeric phase. The diffusivity ratio was higher than unity for all gases and all filler loadings, indicating that the addition of filler enhanced, as expected, the diffusion coefficient of gases, which possibly take advantage of the fastest filler diffusive paths. This seemed to be particularly remarkable for helium. However, the enhancement of diffusivity induced by the filler addition is not as high as the one recorded for permeability: such phenomenon indicates that the filler also enhances the membrane solubility.

In **Figure 6.22** we reported the estimated values of diffusivity-selectivity for the couples CO_2/N_2 and CO_2/CH_4; the data relative to other couples involving helium were not provided, due to the high error associated to estimation of He diffusivity. In both cases it can be seen that diffusivity-selectivity is lower than the overall selectivity (**Figure 6.12b**), due to the fact that solubility also plays a strong role in separations involving CO_2. There is also a trend of the selectivity with the ZIF content, which is slightly decreasing for both CO_2/CH_4 and CO_2/N_2 separations.
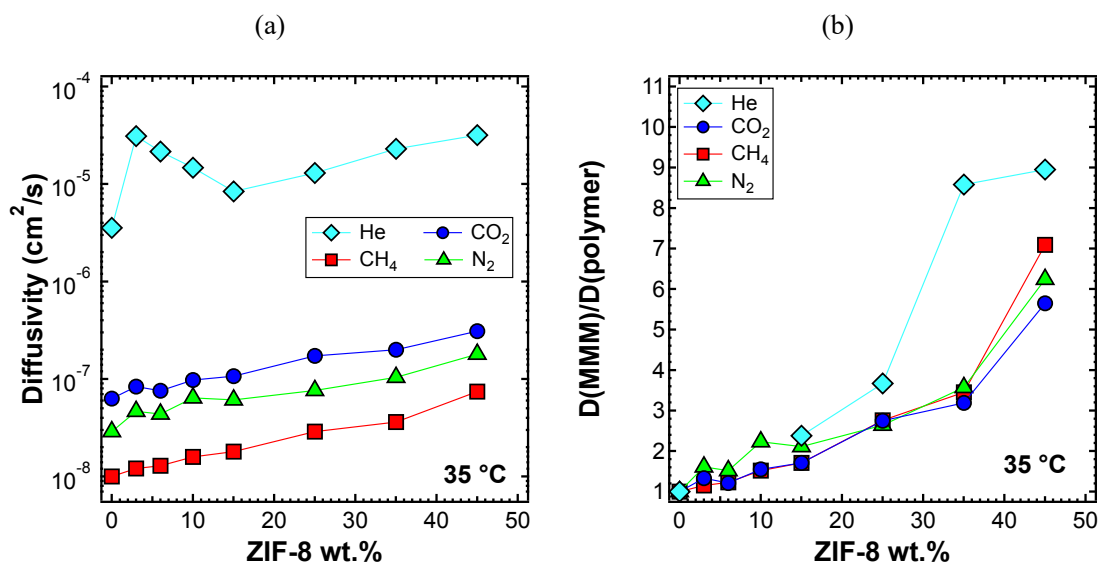
Figure 6.21: *(a) Diffusivity and (b) relative diffusivity increase of various gases at 35°C in ZIF-8/PPO mixed matrix membranes (MMM), estimated with the time-lag method.*
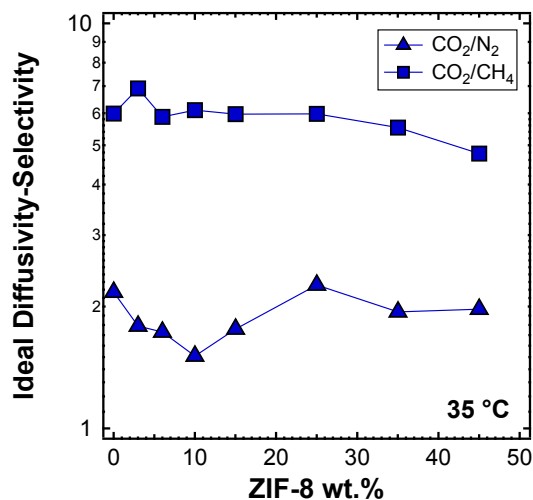
Figure 6.22: *Ideal Diffusivity-Selectivity for CO_2/N_2 and CO_2/CH_4 at 35 °C in ZIF-8/PPO mixed matrix membranes (MMM).*

The diffusivity was also estimated with the time-lag method at higher temperatures, namely 50 and 65 °C and reported in **Figure 6.23a** and **Figure 6.24a**, respectively. We also reported in **Figure 6.23b** and **Figure 6.24b** the values of diffusivity ratio between the mixed matrix material and the pure polymer at 50 and 65 °C, respectively. It can be noticed, from a qualitative point of view, that the diffusivity followed a similar behavior at all temperatures. However, the enhancement of diffusivity induced by the

filler seems less remarkable at the higher temperatures. This could be explained by means of a lower activation energy of diffusion for the mixed matrices than for the polymer, which is indeed an aspect that will be analyzed quantitatively in the next section.

(a)   (b)
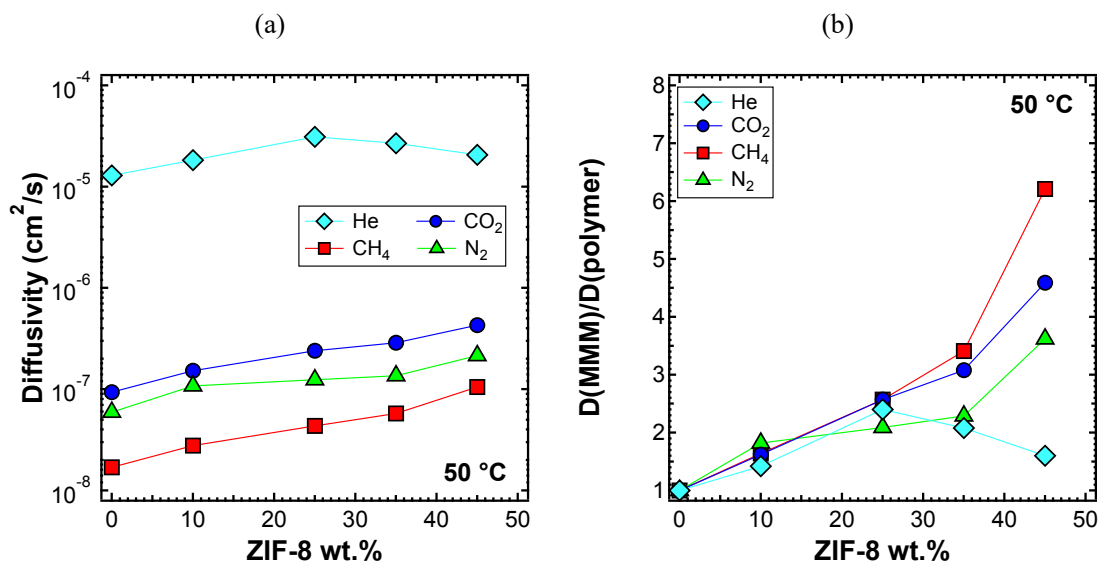
Figure 6.23: (a) Diffusivity and (b) relative diffusivity increase of various gases at 50 °C in ZIF-8/PPO mixed matrix membranes (MMM), estimated with the time-lag method.

(a)   (b)
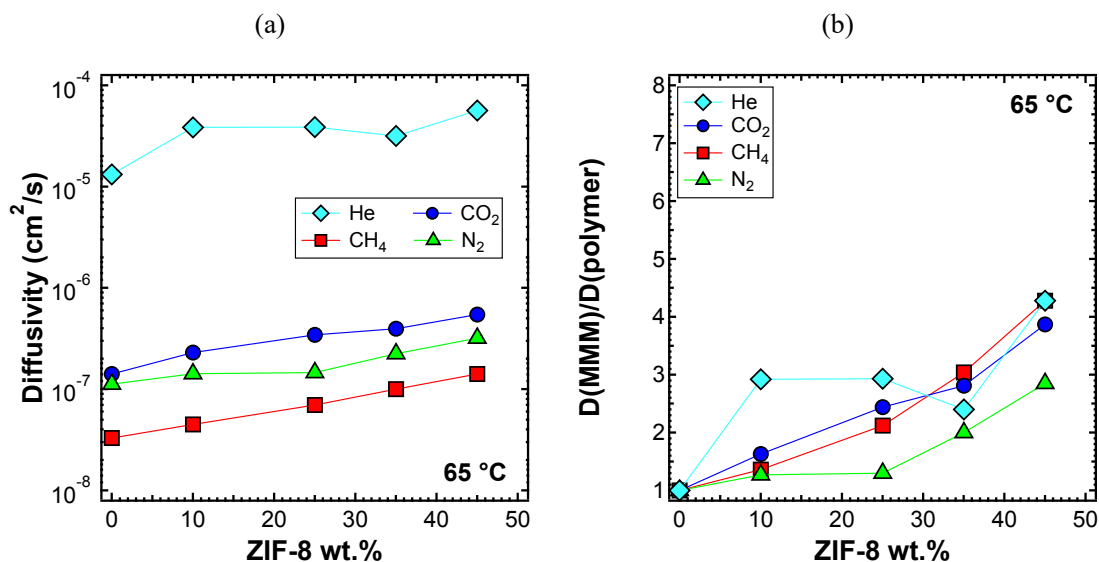
Figure 6.24: (a) Diffusivity and (b) relative diffusivity increase of various gases at 65 °C in ZIF-8/PPO mixed matrix membranes (MMM), estimated with the time-lag method.

6.1.7.3.1.   Dependence of Diffusivity on Temperature and E_D

(a)

(b)

(c)
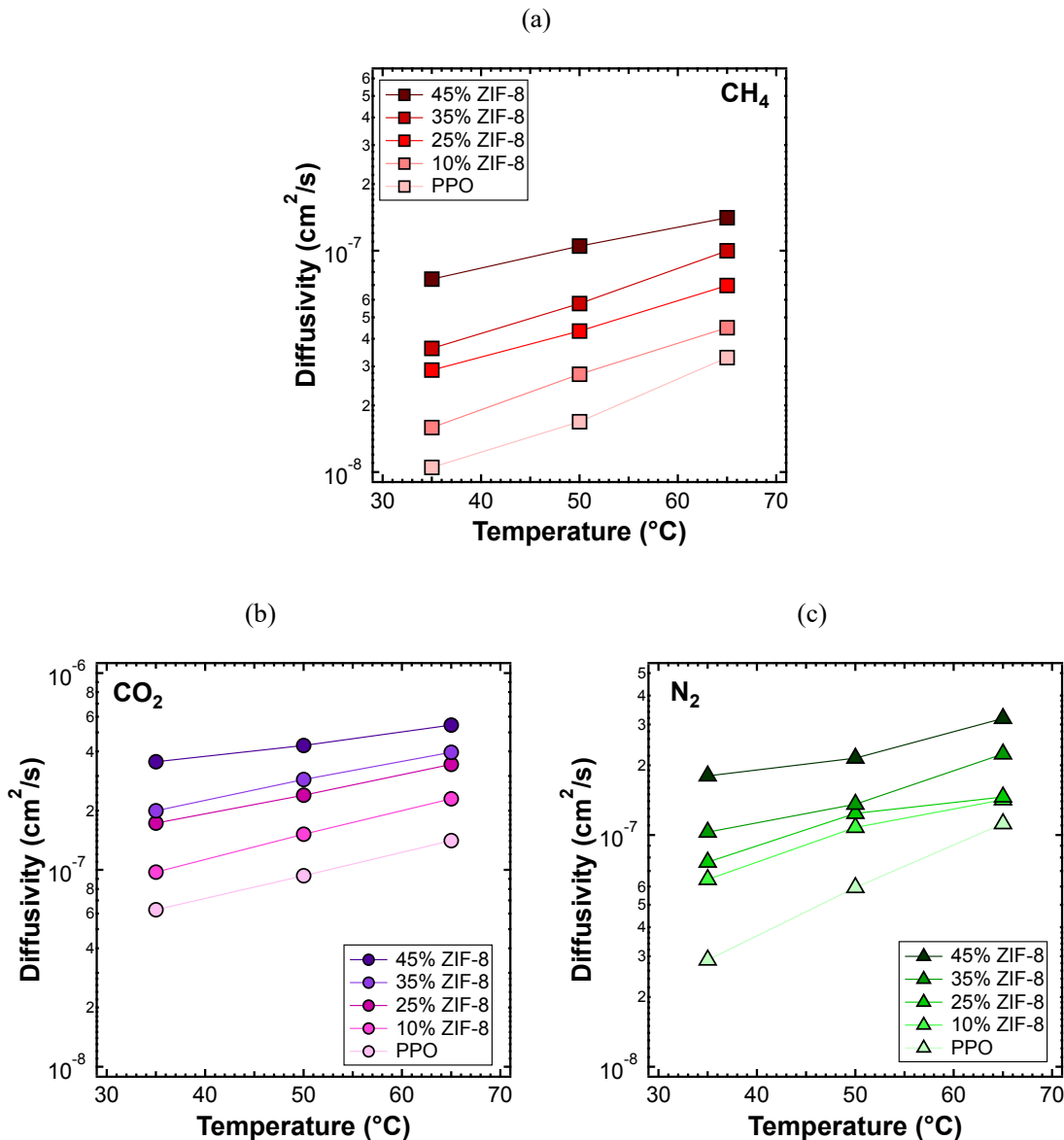
Figure 6.25: Diffusivity of (a) CH₄, (b) CO₂, (c) N₂ at different temperatures, in the ZIF-8/PPO MMMs of different weight fractions of ZIF-8, from 0 to 45%.

In **Figure 6.25** we reported the diffusivity as a function of temperature, for the various mixed matrices inspected and all gases except helium. In this latter case indeed, the experimental error was rather high and the data could not be interpreted according to the Arrhenius law. On the other hand, the diffusivity of the other gases, with a few exceptions, followed Arrhenius law in all the mixed matrices considered.

Therefore, we were able to calculate the activation energy of diffusion, that is reported in **Figure 6.26** and **Table 6.6**. First of all, one can notice that the values of activation energy for diffusion were higher than the respective values of permeation activation energy, due to the negative sorption enthalpy which is typical of gas sorption in polymers. Furthermore, also in this case, as in the case of activation energy of permeation, the values decreased with increasing ZIF content. This aspect indicates that the addition of filler to the polymer lowered the energetic barrier of the diffusion process, possibly due to the presence of the filler pores available for diffusion.
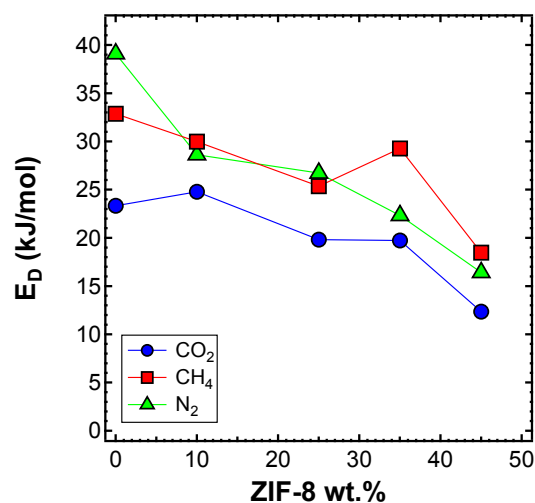
Figure 6.26 *Activation energy of diffusion measured in the interval 35-65 °C for 3 gases in the various MMMs inspected, as a function of filler loading.*

Table 6.6: *Activation energy of diffusion in the range 35-65 °C of ZIF-8/PPO mixed matrix membranes at different filler loadings.*

ZIF-8 loading (wt.%)	E_D (kJ/mol)			
	He	N_2	CH_4	CO_2
0[48]	n.a.	22.4	29.4	23.4
0	n.a.	39.10	32.87	23.33
10	n.a.	28.62*	29.99	24.78
25	n.a.	26.73*	25.37	19.82
35	n.a.	22.32	29.28	19.73
45	n.a.	16.42	18.47	12.35

*Activation energy of diffusion was calculated using diffusivity data at 35 and 50 °C

6.1.7.3.2. Permeability Vs Diffusivity Enhancement

In this section we compare the effect of filler addition on the permeability and the diffusivity. In particular, the idea is to see whether the permeability behavior is uniquely correlated to the diffusivity, or there is also an effect of the filler addition on the solubility, which will be reported in the part II of this work. To do so, in **Figure 6.27** we have plotted against each other the permeability enhancement and the diffusivity enhancement induced by the filler in the various mixed matrices analyzed at 35 °C for the various gases considered. In particular, it can be seen that for helium all the data but one fall exactly on the parity line, indicating that the filler enhances the permeability of helium essentially by acting on the diffusivity, and not the solubility. For all the other cases, the permeability enhancement is equal to the diffusivity enhancement at the low filler loadings up to 15 wt.%, but becomes larger for larger filler loadings. This behavior indicates that, for such gases, the filler also enhances the solubility of the polymer to a significant extent.

(a)   (b)
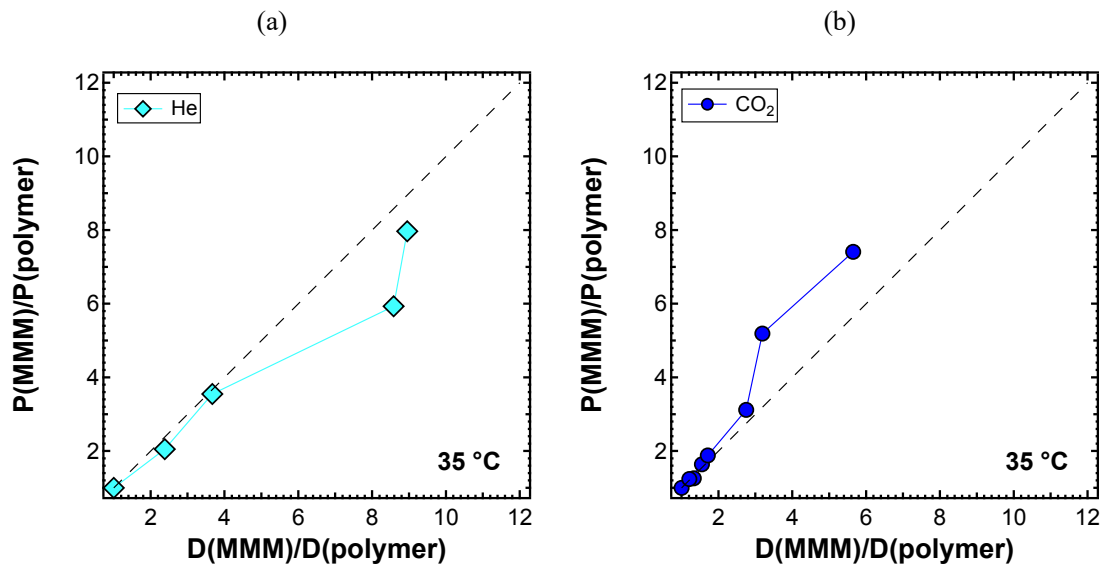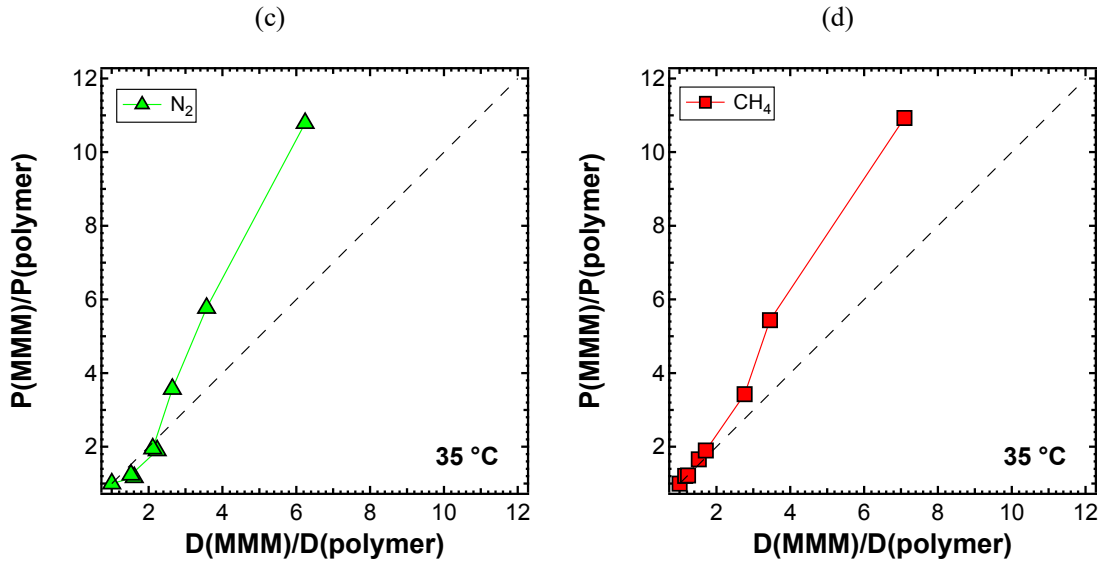
Figure 6.27: Parity plot between diffusivity enhancement and permeability enhancement due to addition of ZIF-8 to PPO at 35 °C for (a) He, (b) CO₂, (c) N₂, (d) CH₄.

6.1.7.4. Solubility

6.1.7.4.1. Solubility from Solution-Diffusion Model and Sorption Enthalpy

Although the gas solubility will be measured directly and analyzed in detail in section 6.1.7.4.2 of this dissertation, we estimated in this section the values of solubility coefficient as the ratio between permeability and diffusivity, assuming the validity of the solution-diffusion model. The values are reported, for the temperature of 35 °C in **Figure 6.28a**. We can notice a slight increase of the solubility coefficient at high filler loadings. From **Figure 6.28b** it is evident that CO_2, N_2 and CH_4 experienced a similar enhancement of solubility, while for He there was no such effect. Such behavior will be further compared to direct sorption data in part II of this work. The data indicate that the filler enhances the gas permeability of the polymer by acting mainly on the diffusivity but also, to a not negligible extent, on the ability of the membrane to absorb gas.
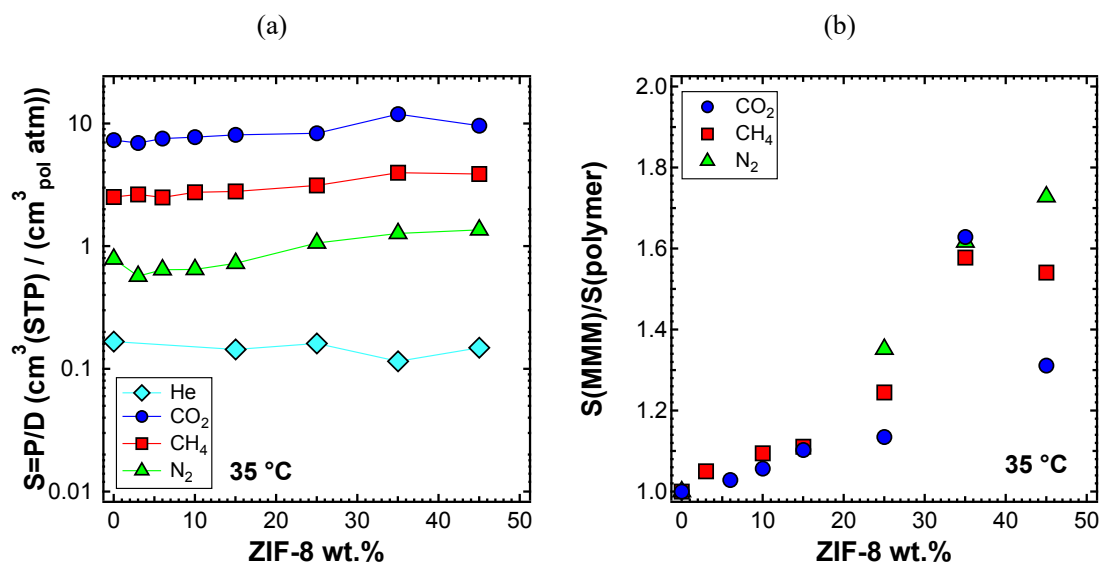
Figure 6.28: (a) Solubility coefficient calculated by means of the solution-diffusion model approach, and (b) normalized solubility in ZIF-8/PPO MMMs. Results were calculated at 35 °C.

By subtracting the activation energy of diffusion to that of permeation, one can estimate the heat of sorption and evaluate its trend with filler content. This was done in **Figure 6.29** and **Table 6.7**. It can be seen that CO_2 showed on average the most negative values (more favorable sorption) among all gases, as expected being the most soluble gas as observed in **Figure 6.28a**. The absolute value of the sorption enthalpy decreases with increasing filler content. Again, the addition of filler makes the solubility a weaker function of temperature with respect to the pure polymer.
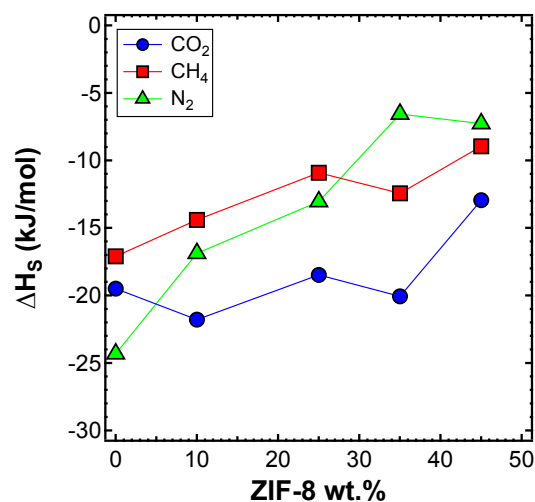
Figure 6.29: *Heat of sorption estimated in the interval 35-65 °C for three gases in ZIF-8/PPO MMMs as a function of filler loading.*

Table 6.7: *Heat of sorption ΔH_S in the range 35-65 °C of ZIF-8/PPO mixed matrix membranes at different filler loadings.*

ZIF-8 loading (wt.%)	ΔH_S (kJ/mol)			
	He	N_2	CH_4	CO_2
0[48]	n.a.	-12.6	-17.3	-21.9
0	n.a.	-24.32	-17.10	-19.49
10	n.a.	-16.88*	-14.40	-21.79
25	n.a.	-13.05*	-10.91	-18.48
35	n.a.	-6.56	-12.43	-20.06
45	n.a.	-7.27	-8.95	-12.94

*Activation energy of diffusion was calculated using activation energy of diffusion calculated using data at 35 and 50 °C

6.1.7.4.2.   Pressure Decay Sorption Experiments

Sorption was also directly measured with a pressure decay at 35 °C for He, CO_2, N_2 and CH_4. **Figure 6.30** reports the concentration of each gas in the pristine materials: PPO and ZIF-8. ZIF-8 adsorbed much more that PPO, as expected. In both samples pure-gas solubility follows the same order of the critical temperature: $C_{CO_2} > C_{CH_4} > C_{N_2} > C_{He}$. PPO sorption isotherm in the figure were fitted with the Dual Mode Sorption (DMS)[84] model, while that of ZIF-8 with the Langmuir-Freundlich model:

$C = (C'_H bp^n)/(1 + bp^n)$.[85] The parameters of these models are reported in **Table 6.8** and **Table 6.9**, respectively.
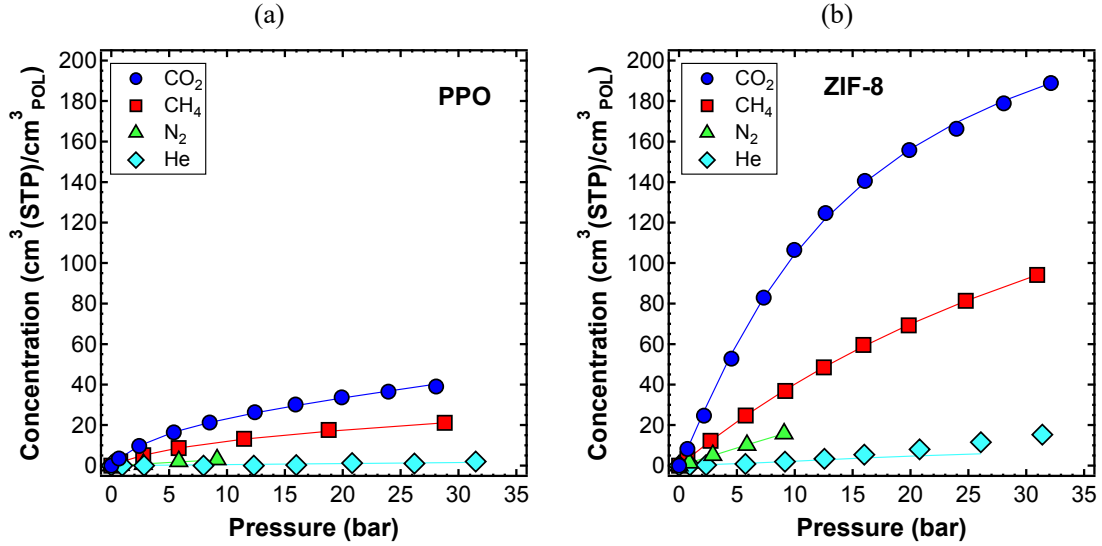
Figure 6.30: *Pure-gas sorption data in (a) PPO, and (b) ZIF-8. The y-axis are kept the same to highlight the differences between the two materials.*

Once the two materials were combined to form MMMs, sorption was enhanced. Results are reported in **Figure 6.31** and show that the isotherms have the typical shape of glassy polymers. The presence of ZIF-8 increase the solubility of the MMMs with respect to that of the pure polymer. Measuring gas sorption in MMMs, in addition to evaluating an important contribution to the permeation of gases, is also a way of probing the internal structure of the composite materials. In the MMMs, the contribution of each component to the overall solubility measured can be deconvoluted and combined based on the fraction of the filler as reported in Eq. (6.2).

$$C_{i,MMM} = \omega_{ZIF8}\, C_{i,ZIF8} + (1 - \omega_{ZIF8})\, C_{i,PPO} \qquad\qquad \text{Eq. (6.2)}$$

where $C_{i,MMM}$ is the concentration of the gas i in the MMM, $C_{i,ZIF8}$ is the concentration of the gas i in ZIF-8, and $C_{i,PPO}$ is the concentration of the gas i in PPO. All of them are evaluated at the same temperature and pressure. ω_{ZIF8} is the volume fraction (or the mass fraction, depending on the unit of the concentration) of ZIF-8 in the MMM.

A variation, even limited, of the gas solubility in composite materials from the additive rule, is an indication of the deviation of the material from the case of the ideal composite.[86,87] In particular, negative deviations may indicate that a partial occlusion of the free volume of the filler by the polymer occurred, which would lead also to a decrease in permeability. Conversely, positive deviations from additive behavior indicate that there was an increase in free volume, perhaps due to disruption of polymer chains packing or imperfect filler-polymer adhesion, and that therefore the permeability of the material would increase.[21,86] Experimental results revealed that ZIF-8/PPO MMMs follow the additive rule with high accuracy. This confirms that disruption of the polymer chain packing by the filler could also be excluded, as expected, since the dimension of the filler was too big to inhibit rigid packing of the polymer chains.[87–89] DMS parameters for MMMs are shown in **Table 6.8**.
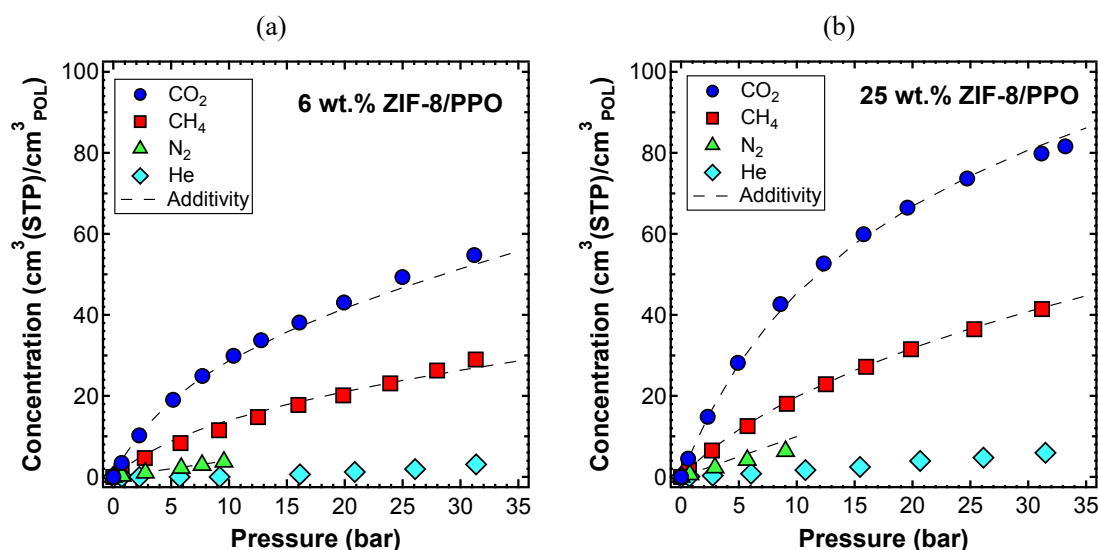
Figure 6.31: Pure-gas sorption isotherms in MMMs: (a) 6 wt.% ZIF-8/PPO, and (b) 25 wt.% ZIF-8/PPO.

Table 6.8: Dual Mode model parameters for pure PPO and MMMs sorption.

		k_d (cm³(STP) cm⁻³$_{pol}$ bar⁻¹)	C'_H (cm³(STP) cm⁻³ $_{pol}$)	b (bar⁻¹)
Pure PPO				
	N$_2$	0.31	1.21	0.01
	CH$_4$	0.29	16.27	0.13
	CO$_2$	0.72	23.42	0.22
6 wt.% ZIF-8/PPO				
	N$_2$	0.39	0.04	0.03
	CH$_4$	0.65	10.06	0.14
	CO$_2$	0.73	41.13	0.12
25 wt.% ZIF-8/PPO				
	N$_2$	0.62	1.15	0.19
	CH$_4$	0.59	35.49	0.06
	CO$_2$	0.07	115.31	0.07

Table 6.9: Langmuir-Freundlich model parameters for ZIF-8 sorption.

		n	C'_H (cm³(STP) cm⁻³ $_{pol}$)	b (bar⁻¹)
ZIF-8				
	N$_2$	1.06	155.29	0.01
	CH$_4$	1.01	251.20	0.02
	CO$_2$	1.14	266.17	0.05

The effect of the filler on the CO_2 sorption-induced hysteresis has been investigated. After reaching the maximum pressure allowed by the transducer (*i.e.*, ~33 bar), a de-sorption isotherm was measured for pure PPO and ZIF-8, as well as for the two MMMs at 6 wt.% and 25 wt.%. **Figure 6.32** shows that all the materials underwent hysteresis to some extent. Interestingly, the MMMs featuring 25% ZIF-8 seemed providing the best resistance to CO_2-induced plasticization, probably due to the higher content of ZIF-8. Another important result is that ZIF-8 presented some hysteresis as well, supporting the understanding that MOFs' cages are flexible (**Figure 6.32d**).
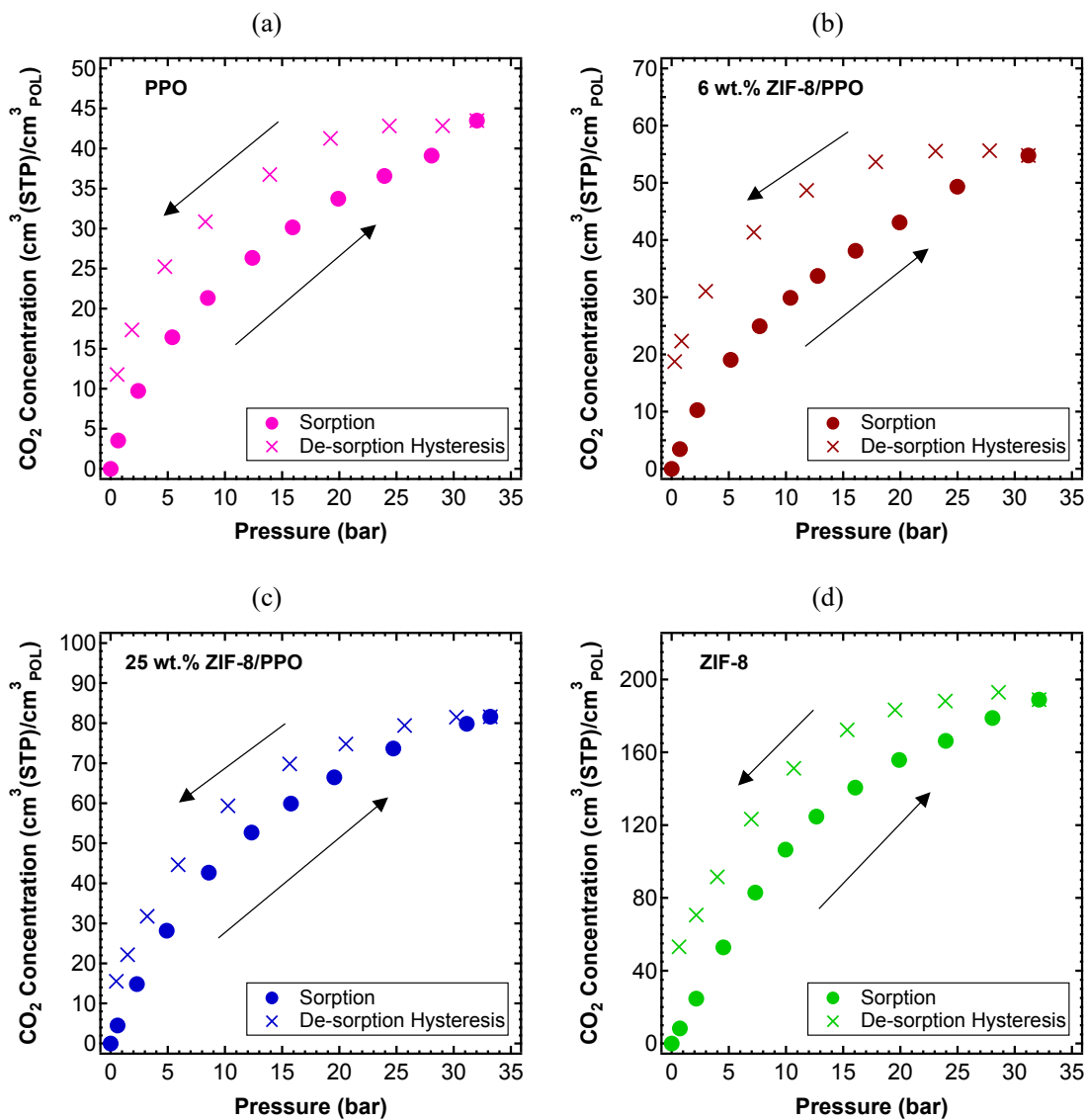
Figure 6.32: CO$_2$ sorption-induced hysteresis in, (a) PPO, (b) 6 wt.% ZIF-8/PPO, (c) 25 wt.% ZIF-8/PPO, and (d) ZIF-8.

Another evidence of the plasticization resistance provided by 25 wt.% ZIF-8/PPO, is the trend of the CO$_2$ diffusion coefficient calculated from the sorption kinetics. **Figure 6.33b** shows that the MMM has higher diffusion coefficient at the beginning, as expected from the higher permeability. However, increasing CO$_2$ pressure/concentration, PPO diffusion coefficient increases more sharply than that of the MMM, ending up having higher diffusivity from when concentration was above ~20 cm^3(STP)/cm$^3_{pol}$. This can be related to the capacity of the composite material to resist the CO$_2$-

induced swelling of the matrix. A similar trend was observed with CH_4. Although methane is not a swelling agent, its diffusivity increases much more quickly than that of the MMM, till they are about the same at an average concentration equal to ~20 $cm^3(STP)/cm^3_{pol}$.
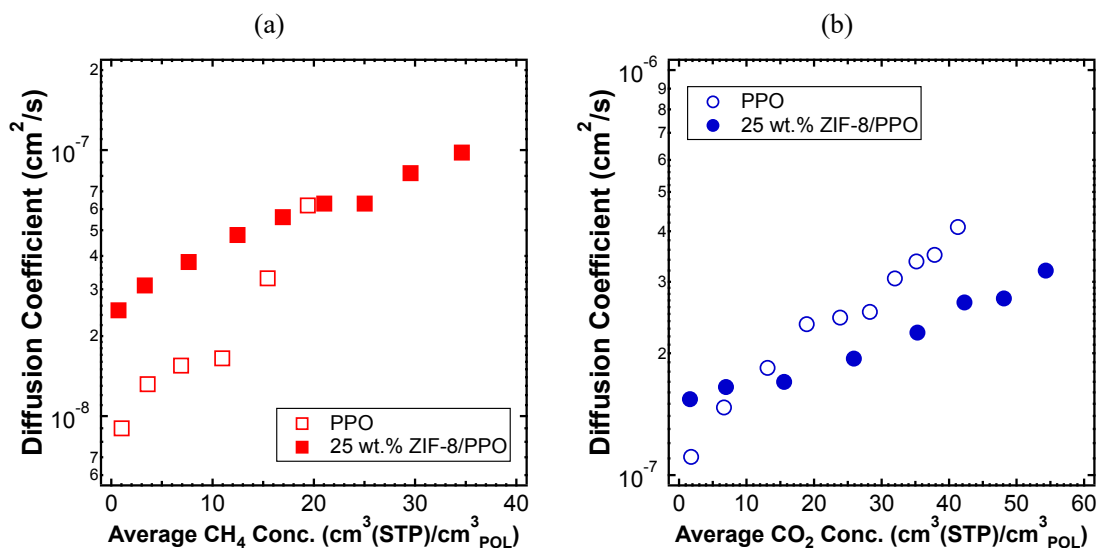
Figure 6.33: *(a) CH_4, and (b) CO_2 diffusion coefficients from sorption kinetics in PPO and 25 wt.% ZIF-8/PPO.*

6.1.7.5.   Positioning on the He/CO$_2$ Robeson Plot

The performance of the composite membranes developed in this work were plotted on the Robeson upper bound plot for He/CO$_2$ pair, featuring both 1991[6] and 2008[7] limits. Results are reported in **Figure 6.34**. The 1991 upper bound was overcame by ZIF-8/PPO MMMs at 35 and 45 wt.% at room temperature, while at 65 °C also 25 wt.% surpassed the limit. These results were achieved because MMMs were simultaneously more permeable and more selective.
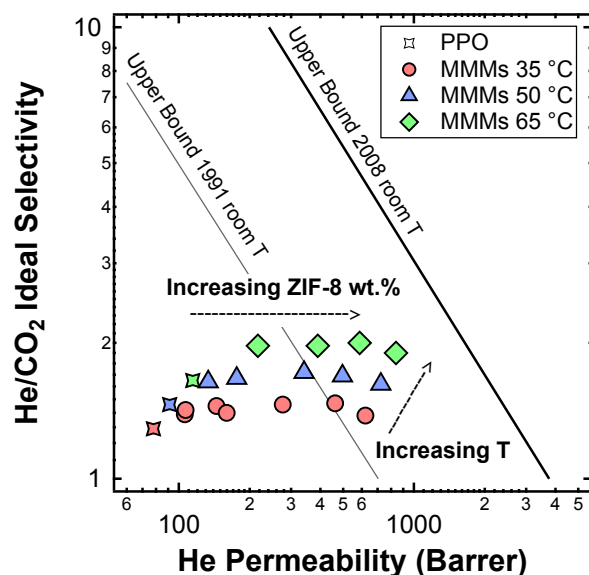
Figure 6.34: Positioning of the MMMs studies in this work in a Robeson plot for the He/CO₂ separation. Data are reported for the various filler loadings and temperatures.

6.1.7.6.   Comparison with other MMMs

In the present section results are compared in terms of relative permeability enhancement with respect to helium (or hydrogen) and selectivity enhancement with respect to He/CO_2 or H_2/CO_2 separation, obtained by adding H_2-selective fillers to glassy polymers. The data showed in **Figure 6.35** refer to mixed matrix membranes formed by Polybenzimidazole (PBI) + ZIF-7[59], Polysulfone + Zeolite 3A[57], ZIF-8 blended with different polymer matrices such as Matrimid®[45], PIM-1[64] and PPEES[63], Matrimid® + Cu-BPY-HSF[90] and PMDA-ODA + Cu₃(BTC)₂.[91] It can be seen in all cases that the addition of ZIF fillers has generally the effect on enhancing the permeability, but slightly affects the selectivity of the membrane. The best compromise was best found using PIM-1, since both He and H_2 permeability and He/CO_2 and H_2/CO_2 selectivity were improved. The permeability enhancement observed by adding ZIF-8 to PPO, as assessed in this work, is among the highest once recorded, second just to the PPEES/ZIF-8 (30 wt.%) membrane produced by Díaz *et al.*.[63] The addition of the hydrophilic Zeolite 3A, characterized by smaller pore size, on the other hand, enhances appreciably the selectivity, but increases only slightly the permeability, as observed in the case of Polysulfone. This effect is most

likely due to the fact that Zeolite 3A has a higher selectivity than ZIF-8. The data seem to indicate that, in order to have a comparable increase of permeability and selectivity, one should use a combination of different fillers.
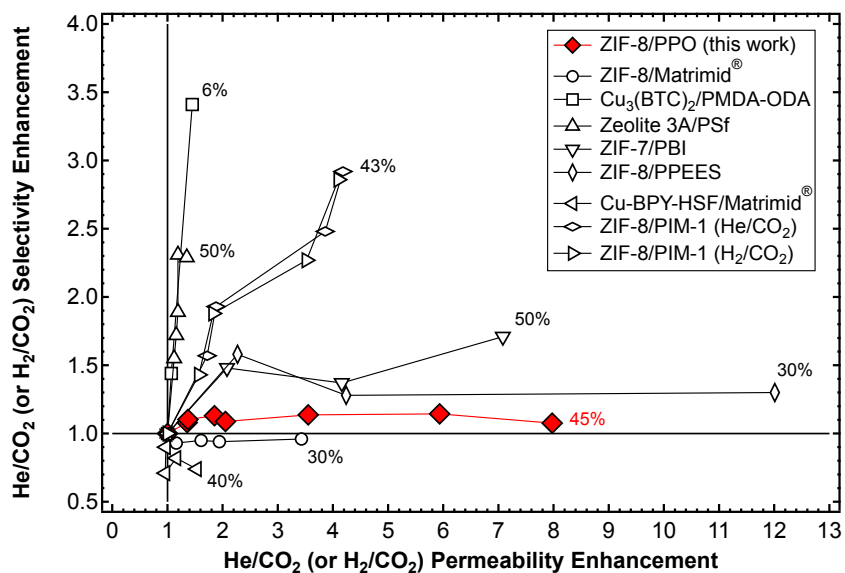
Figure 6.35*: Effect of the addition of size-selective fillers on the He(H₂) permeability and He(H₂)/CO₂ selectivity of various glassy polymers. The maximum loading reached by the MMMs is represented next to proper markers. Data from refs*[45,57,59,63,64,90,91]*.*

6.1.8. ZIF-8/PPO Section Conclusions

In this work, we fabricated MMMs based on PPO and variable amounts of ZIF-8 with the main aim of enhancing the size selectivity in view of the H_2/CO_2 separation. A preparation protocol was defined, that allowed to obtain membranes with loadings of filler as high as 45 wt.%. The samples were characterized via SEM, DSC, TGA and buoyancy tests. The SEM analysis highlighted the presence of generally well dispersed filler particles but also the formation of some aggregates at high loadings, but with a general good adhesion between polymer and filler. DSC tests showed the absence of residual solvents or moisture, the amorphous structure of the membranes, and the polymer rigidification when ZIF-8 is added, according to the linear increase of T_g with increasing filler content. Buoyancy tests allowed to estimate the density of the composite membranes and attest that the volume follows an

additive behavior, based on the pure polymer and the theoretical density of the ZIF-8 crystal, indicating that there is good adhesion between the two phases.

Permeability tests were performed on membranes containing various loadings of ZIF-8 at temperature between 35 and 65 °C on four gases: He, CO_2, N_2 and CH_4. The addition of ZIF-8 to the polymer produces a monotonous increase of permeability among all gases, with factors as high as 8. The trend is obeyed at all temperatures. The selectivity with respect to the He/CO_2 mixtures, on the other hand, increases, to a smaller extent than permeability, up to a loading of ZIF-8 of about 35%. Results of the Maxell model indicate that up to 15 wt.% the MMMs behave like ideal composite materials. At filler loadings of 25 wt.% or above, all models underestimate permeability, which lead to the conclusion that a percolation transport regime may be activated at high loadings, supported by SEM images.

The gas diffusivity estimated with the time-lag method was also a monotonous increasing function of ZIF-8 content, for all gases and at all temperatures. However, the enhancement of diffusivity alone does not justify the observed enhancement of permeability and, according to the solution diffusion-model, we were able to assess that there was also a beneficial effect of ZIF-8 addition on the solubility of the membrane. The contribution of sorption to the overall permeability increase was also investigated *via* pressure decay experiment, which results supported the previous conclusions. The MMMs obey the additive rule of sorption at various compositions, which indicates that the films behave as ideal composite materials. The evaluation of the CO_2 de-sorption hysteresis and the trend of diffusion coefficients measured from sorption kinetics in pure polymer and MMMs, allow to assess the beneficial effect of the ZIF-8 towards plasticization resistance.

The activation energy for the various transport quantities was estimated in the thermal range investigated. All the energetic contributions, and the dependence of the transport properties on temperature, decrease with increasing ZIF-8 content in the membrane. This behavior is compatible with the availability of a higher free volume for gas transport in the presence of filler.

The Robeson's plot for He/CO_2 separation indicates that the addition of ZIF-8 pushes the membranes performances above the 1991 upper bound, and close to the 2008 upper bound. The temperature increase

also yields a fast and monotonous approach to the upper bound of the latter separation, indicating that such membranes can be used for applications at higher temperature.

6.2. Zeolite 3A/PPO Composite Materials

Zeolite 3A was selected as an alternative filler to ZIF-8 to prepare MMMs. DSC, SEM, and a detailed study of transport properties highlighted relevant differences between the two systems that require to be addressed at fundamental level.

6.2.1. Properties of Zeolite 3A

Zeolites are used in many applications, from the traditional separation field (*i.e.*, hydrogen, carbon dioxide, water etc…), to more innovative applications, such as membrane reactors and functional films.[92] Zeolites are very stable materials, and can resist towards severe environmental conditions such as high temperature, and high pressures. The structure of Zeolite 3A is represented in **Figure 6.36**.[16,93] Despite of the similar topology with respect to ZIF-8, these two materials have a very different chemistry. Zeolite 3A is an aluminum-silicate, therefore, a fully inorganic material with the following composition: $K_{12}[(AlO_2)_{12}(SiO_2)_{12}] \cdot xH_2O$.[57] As many other zeolites, it is capable to perform a molecular sieve action, discriminating different molecules based of their size.[94] This effect is more marked when the distribution of the pore size is uniform. Type 3A zeolite is characterized by a single-mode distribution of the 3 Angstrom pores, which is between the kinetic diameters of H_2 and CO_2, 2.89 Å and 3.3 Å, respectively. One of the drawbacks of zeolites, however, is that only a limited number of structures and compositions are possible.[95] The properties of this Zeolite 3A, purchased by *Sigma Aldrich* (Molecular sieve 3A, Cat. 95664), are summarized in **Table 6.10**. It is worth noticing that Zeolite 3A is highly hydrophilic, given its low Si/Al ratio (*i.e.*, 1).[89,92,96,97] This is an aspect to be taken into consideration, since the syngas could contain water vapor, if not properly condensed, given the water gas shift reaction.[43,44]
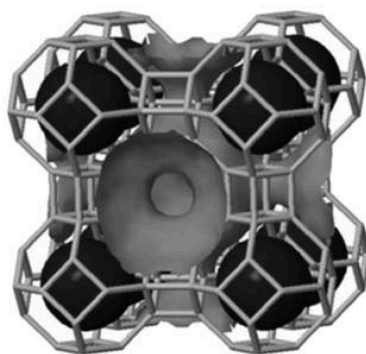
Figure 6.36: *Structure of the zeolite A type from ref.*[16].

Table 6.10: *Properties of Zeolite 3A.*

Filler	Composition[57]	Net	d_a	Surface Area (BET)	Density	Thermal Stability	Si/Al
		/	Å	m²/g	g/cm³	°C	/
Zeolite 3A	$K_{12}[(AlO_2)_{12}(SiO_2)_{12}] \cdot xH_2O$	SOD	3	558[81]	0.72ᵃ 1.27ᵇ	> 800	1[96]

ᵃ **Bulk density provided by *Sigma Aldrich*[89]**

ᵇ **Framework density[98]**

Given its nature, zeolites generally are less compatible with polymer matrices when embedded together to make a MMM. For this reason, many strategies have been tried to improve the adhesion between the filler and the polymer.[16] Probably the most common is the chemical modification of the zeolite surface, making use of silane coupling agents such as APTMS ((3-Aminopropyl)triethoxysilane) or APDEMS (3-Aminopropyl(diethoxy)methylsilane).[57,81] **Figure 6.37** shows the flowchart we followed to functionalize the surface of the zeolite.[81] This procedure is a modification of the *Plueddemann's* method.[99]

The coupling agent used was APDEMS. Chloroform was chosen as solvent, since it was the same solvent used for casting PPO, so we could not worry about residues from the modification step. The mixture of chloroform, zeolite and APDEMS was stirred for 24 h at ambient temperature and under nitrogen atmosphere. Then the solution was filtered and washed with chloroform in order to remove the non-reacted APDEMS. As last step, zeolite was dried under vacuum at 110 °C for 1 h. The removal of

the -OH group from the surface was performed to make the membrane less hydrophilic and more compatible with the polymer matrix.
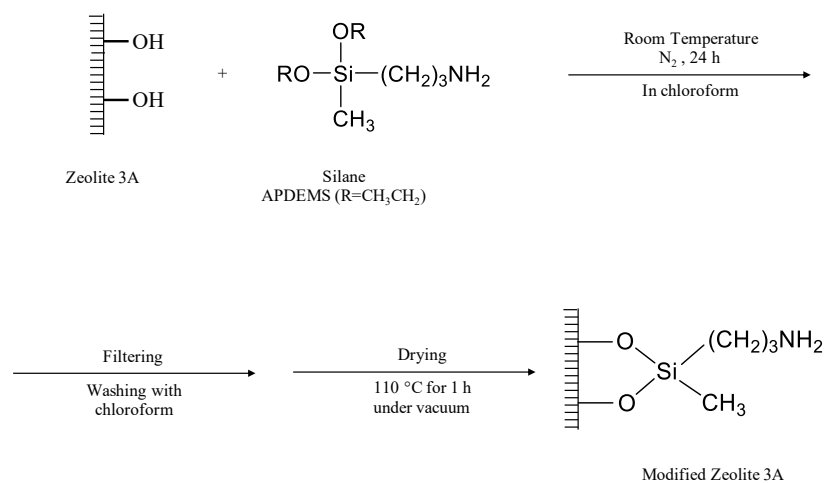
Figure 6.37: *Procedure for the chemical modification of zeolite surface. Adapted from reference*[81].

Li *et al.*[81] used toluene instead of chloroform, and another difference was that the zeolite/APDEMS mass and the APDEMS/solvent volume ratios applied were lower (*i.e.*, more dilutes solutions) than the ones we adopted in this work as reported in **Table 6.11**.

Table 6.11: *Zeolite/APDEMS and APDEMS/solvent ratios used to modify the surface of the zeolite.*

	Li *et al.*[81]	**This work**
wt.% (Zeolite/APDEMS)	12	15
ϕ % (APDEMS/solvent)	3.9	12

Starting from a volume of CHCl₃ of 80 ml, we performed the following calculations to find the quantities of zeolite and APDEMS that respect the ratios previously mentioned:

$$\frac{V_{APDEMS}}{V_{APDEMS} + V_{CHCl_3}} = 0.12 \qquad\qquad \text{Eq. (6.3)}$$

$$V_{APDEMS} = 80 \cdot \frac{0.12}{1 - 0.12} = 10.91 ml \qquad \text{Eq. (6.4)}$$

$$m_{APDEMS} = \rho_{APDEMS} \cdot V_{APDEMS} = 0.916 \cdot 10.91 = 9.99g \qquad \text{Eq. (6.5)}$$

$$\frac{m_{Zeolite}}{m_{Zeolite} + m_{APDEMS}} 100 = 15 \qquad \text{Eq. (6.6)}$$

$$m_{Zeolite} = \frac{0.15 \cdot 9.99}{(1 - 0.15)} = 1.76g \qquad \text{Eq. (6.7)}$$

6.2.2. Aspect: Membrane Formation and SEM

The protocol followed to prepare Zeolite/PPO mixed matrix membranes was the same to that illustrated for membranes with ZIF-8. The aspect of MMMs changed from when the surface of the zeolite was chemically modified and when it was not. In particular, the modified zeolite made the membrane more transparent as shown in **Figure 6.38**. The flexibility of the membrane, instead, was not affected by the functionalization.

(a)   (b)
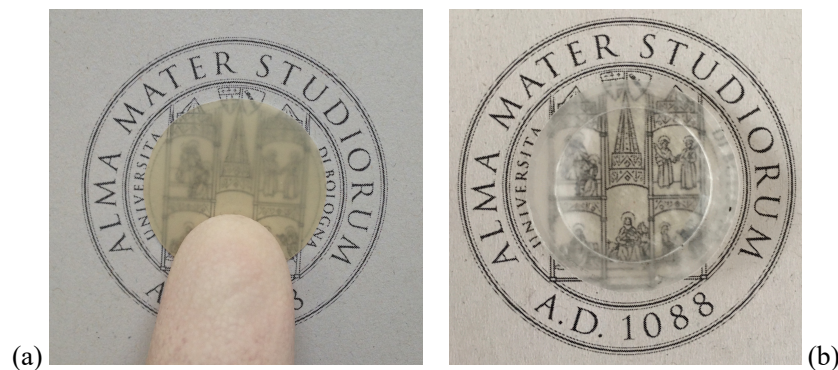
Figure 6.38: Samples of MMMs: (a) 15 wt.% Zeolite/PPO, and (b) 15 wt.% Modified Zeolite/PPO.

SEM cross-section images were taken to investigate the adhesion between the polymer matrix and the filler. Unfortunately, SEM images were not collected after the surface of the zeolite was chemically modified, which is something that will be addressed in the future. **Figure 6.39** shows non-modified zeolites in PPO. In **Figure 6.39b** the polymer seems interacting well with the zeolite (6 wt.%) wrapping

it all around. The residual traces of polymer on the surface of the inorganic filler reveled, that before breaking the membrane in liquid nitrogen, the organic matrix was in close contact with the zeolite. However, not all cases showed the same good adhesion, in fact **Figure 6.39a**, **c**, **d**, and **f**, reveals that the zeolite might also have worse compatibility. It is interesting how the morphology of the polymer matrix changes when the concentration of zeolite increases. In membranes at 6% zeolite, the polymer surface remains flat and uniform (**Figure 6.39e**), while at higher content (25%), the formation of polymer cavities was observed. However, this feature did not go with an increase of permeability, since the opposite was actually experienced, as illustrated in the next section.
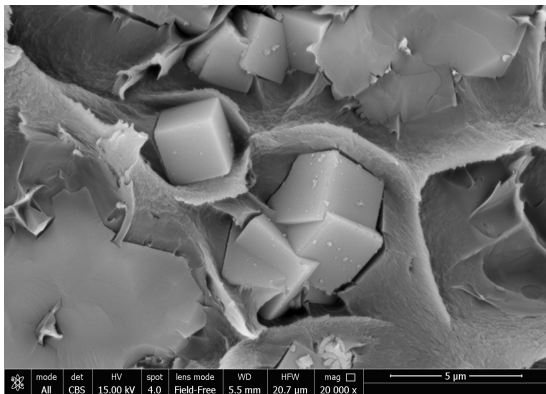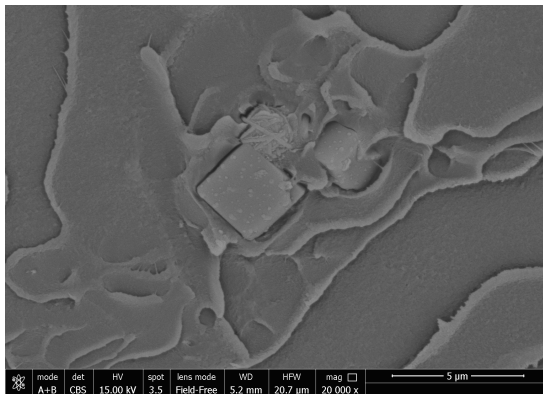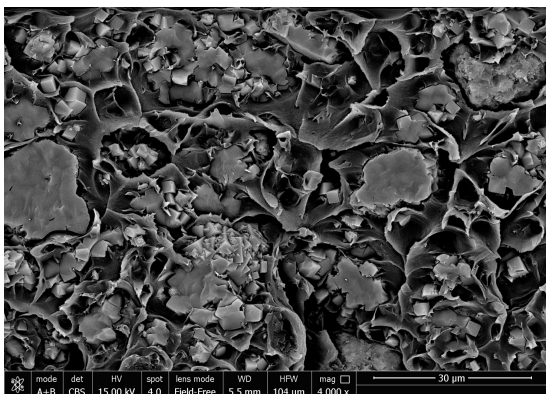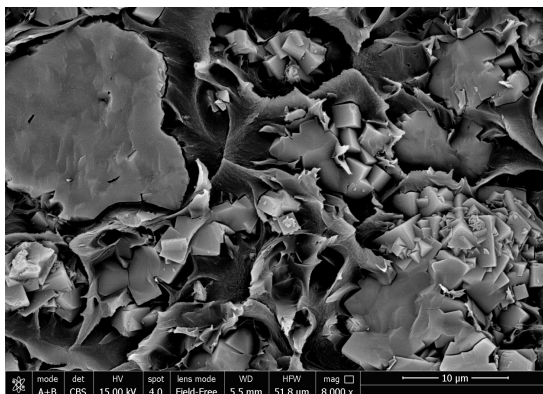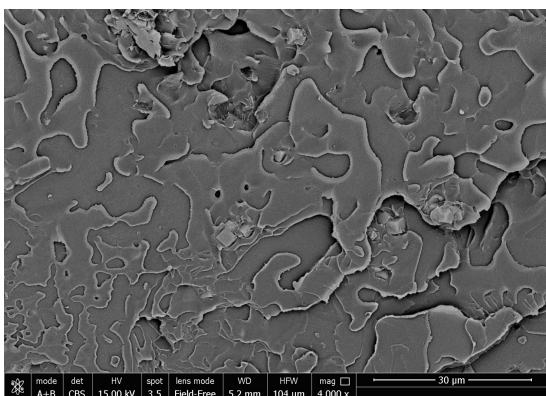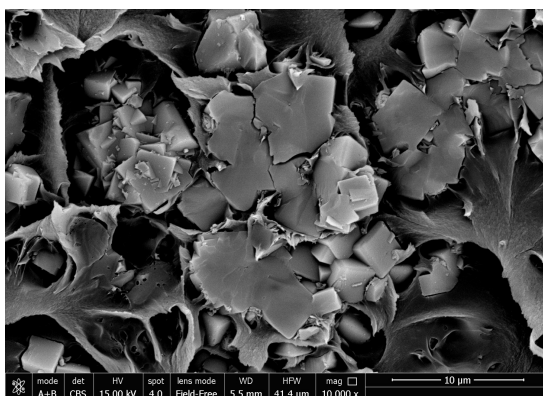
Figure 6.39: *Cross-section SEM images of Zeolite 3A/PPO systems: (a) 25% 20,000 x; (b) 6% 20,000 x; (c) 25% 4,000 x; (d) 25% 8,000 x; (e) 6% 4,000 x, and (f) 25% 10,000 x.*

In **Figure 6.40** elementary analysis of the MMMs is shown. The presence of zeolite was confirmed by the Aluminum (Al) and Silicon (Si) peaks in **Figure 6.40a**, while the polymer phase was highlighted by the reduced intensity of those peaks (**Figure 6.40b**).

(a)

(b)
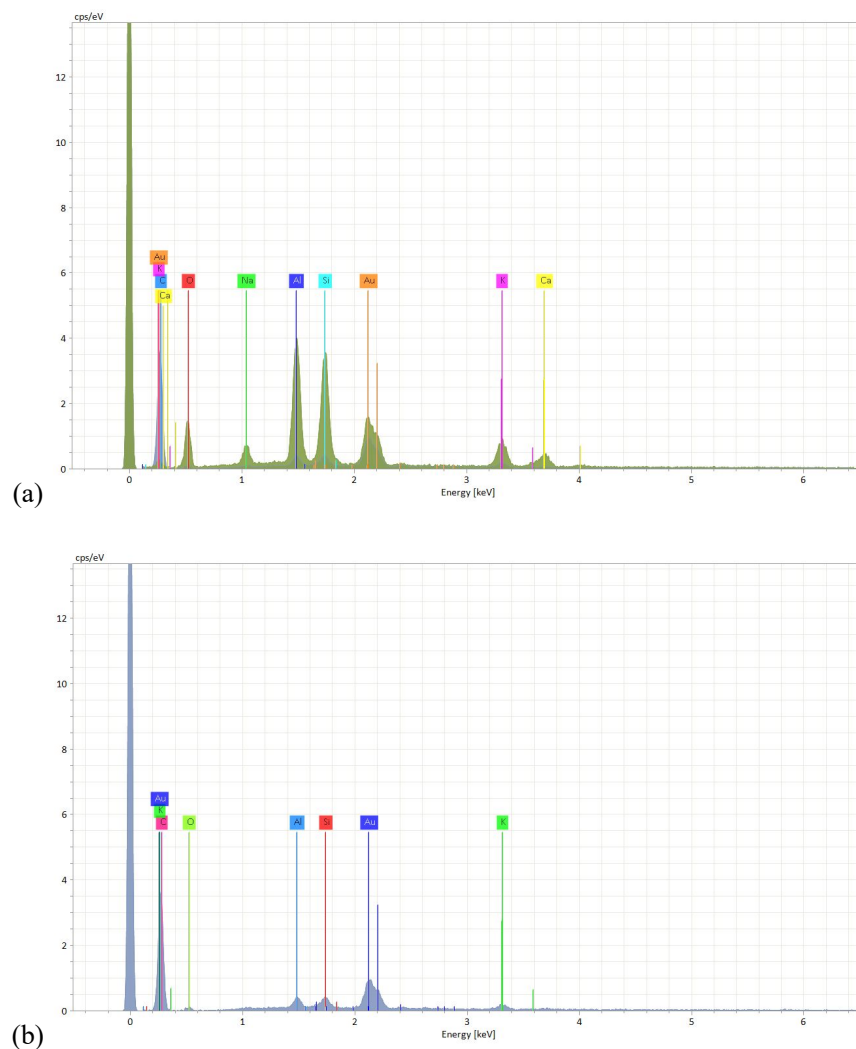
Figure 6.40: Elementary analysis of (a) zeolite particle, and (b) polymer phase, in Zeolite/PPO MMMs.

6.2.3. DSC: Relevance of a Hydrophilic Filler

The hydrophilic nature of Zeolite 3A was investigated to understand the effect it might have on the transport properties.[89] DSC tests revealed that high temperature films pre-treatments were not able to remove completely the residual humidity from the membrane. **Figure 6.41a** reports a series of first scans

spectra performed at the DSC after treating Zeolite/PPO films at different temperatures for different time. Results were almost independent from the treatments, and a big endothermic curve, which reveals water evaporation, was always observed. Interestingly, water was adsorbed very strongly to zeolites that a very high temperature (*i.e.*, 300 °C) is necessary to completely remove it. That was probably the rationale that led Khan *et al.*.[57] to dry the zeolite in a muffle furnace at 500 °C for 4 h, the same treatment we also applied. In fact, by performing a second scan on the same sample kept in the DSC, it was shown that all residuals components were gone, and the PPO glass transition temperature could be observed (**Figure 6.41b**). In conclusion, being the temperature required to remove all the residual species from the MMMs very high, membranes were tested after undergoing thermal treatment at 200 °C overnight under vacuum (optimized on PPO), being aware that the film could not be water-free after that.
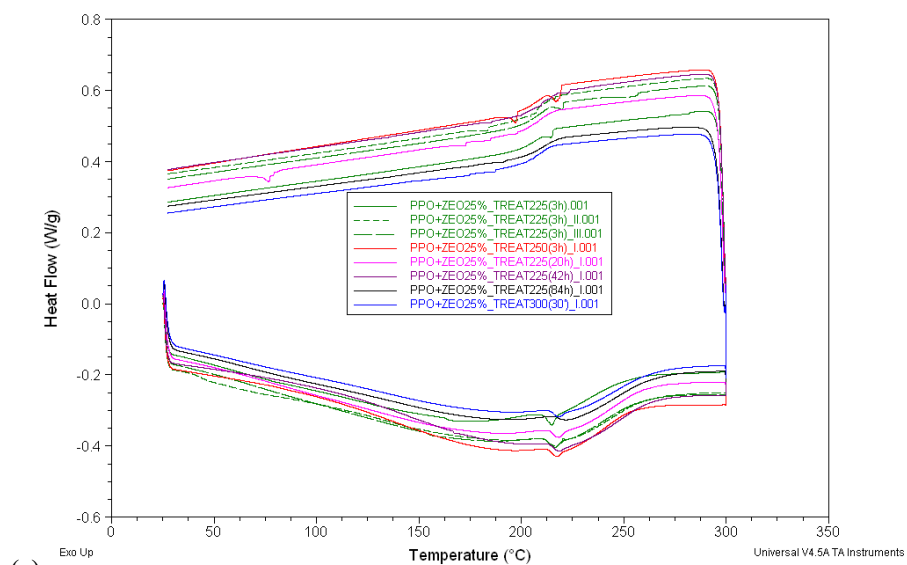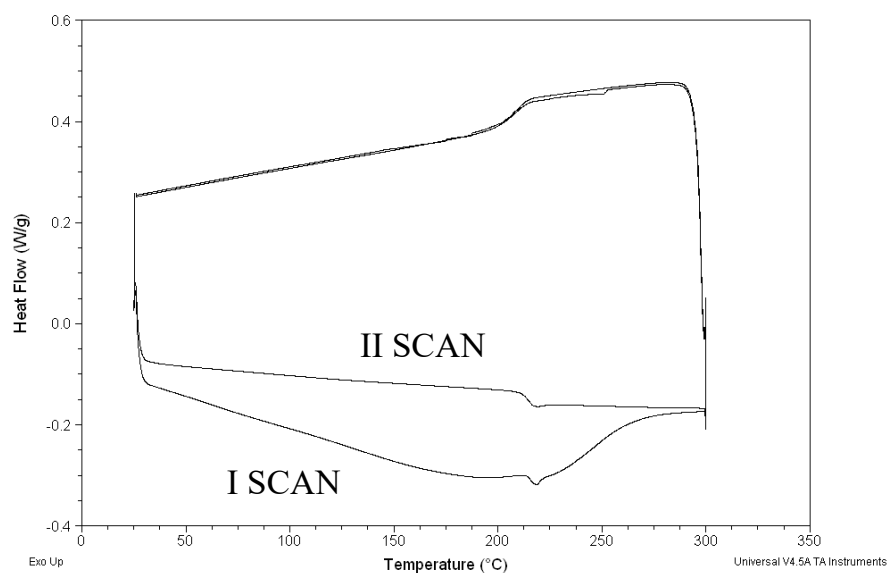
Figure 6.41: *DSC experiments of 25 wt.% Zeolite/PPO MMMs: (a) First-scan spectra of films that underwent different treatments, (b) First and second scan of a film that was exposed to 300 °C for 30 minutes prior to be tested at the DSC after brief exposition to air.*

6.2.4. Transport Properties

In the following section, transport properties of MMMs prepared with modified Zeolite 3A are compared to analogues membranes with non-modified ones.

6.2.4.1. Permeability and Diffusivity

The graph in **Figure 6.42** shows a comparison of permeability data at 35 °C measured in the various PPO membranes with 6, 15, and 25% modified zeolite and 3, 6, 10, 15, 25, and 40% non-modified Zeolite 3A. The qualitative trends indicate in both cases a depression of permeability with increasing filler loading. MMMs featuring modified zeolite showed higher permeability for helium than non-modified ones, which was the desired outcome of the surface functionalization. On the other hand, CO_2 permeability decreased as the filler content was reduced, as desired, although in a less marked way than with unmodified zeolite. The permeability of other compounds larger than the pores of zeolite, 3 Å, such as N_2 (3.64 Å) and CH_4 (3.80 Å), decreased with the increase of the zeolite fraction to a greater extent than what was observed using non-modified zeolite. However, since 40 wt.% Modified Zeolite/PPO is missing, it is hard at the moment to draw definitive conclusions on the ability of the surface functionalization to free, at least partially, the zeolite pores from the excess of adsorbed moisture, and make actively contributing to the selective transport of gases.
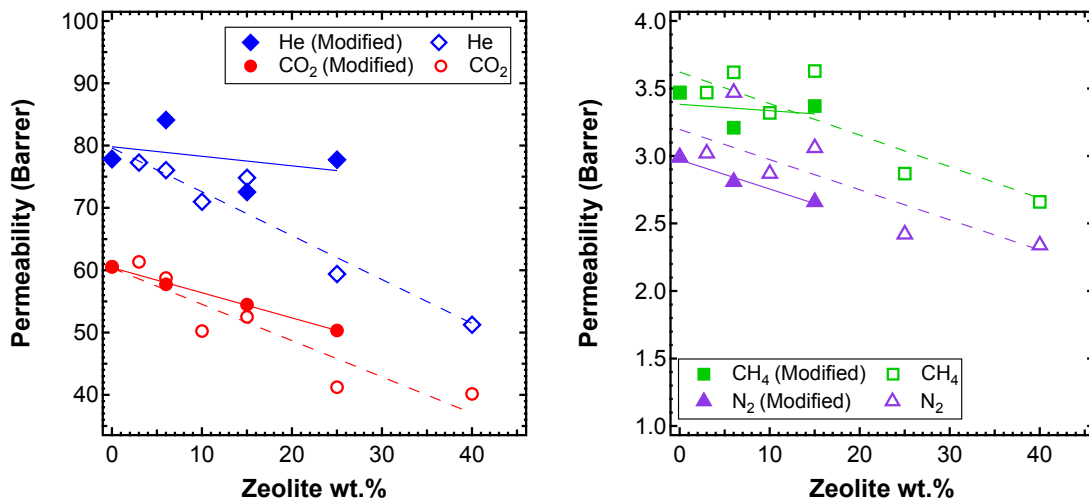
Figure 6.42*: He, CO_2, N_2, and CH_4 permeability at 35 °C in modified (filled markers) and non-modified (empty markers) Zeolite 3A/PPO MMMs.*

In **Figure 6.43**, diffusion coefficients measured from time-lag were used to compare modified and non-modified systems. The results likewise confirmed that differences are not significant. Further, gas diffusivity was not very much affected by the presence of the filler, remaining similar to that of PPO.

Considering the SEM images showed in the previous section (6.2.2), permeability and diffusivity results look surprising, and further experiments are ongoing to determine the rationale behind the experimental evidence collected so far.
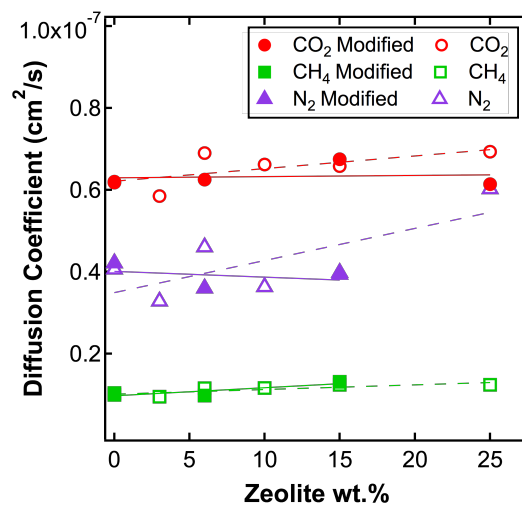
Figure 6.43: CO_2, N_2, and CH_4 diffusion coefficients measured from time-lag at 35 °C in modified (filled markers) and non-modified (empty markers) Zeolite 3A/PPO MMMs

Permselectivity was calculated at 35 °C for different gas pairs and monitored as a function of the filler loading. He/CO_2 selectivity was enhanced up to 20% more by higher content of both non-modified and modified zeolite (**Figure 6.44a**). At 40 wt.% zeolite, however, a drop in selectivity was observed, probably due to the formation to non-selective voids given the high loading of the filler. In **Figure 6.44b** the permselectivity of other gas pairs, *i.e.*, He/N_2, He/CH_4, CO_2/N_2, and CO_2/CH_4, is represented. On average MMMs featuring non-modified zeolite showed a slight decrease in selectivity for all the gas pairs. On the other hand, modified zeolite suffered less this selectivity depression and data look stable with increasing loading.
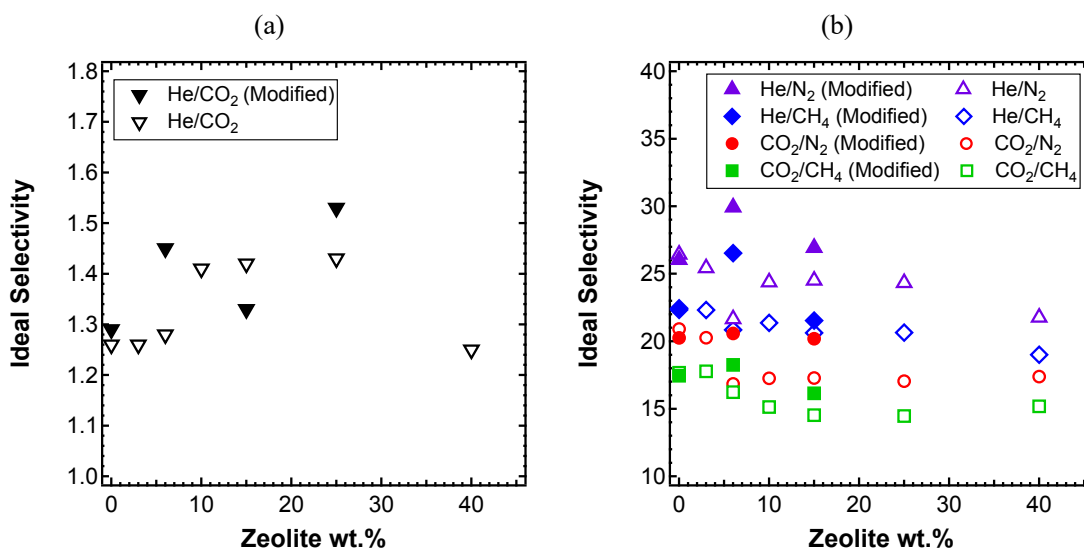
Figure 6.44: *Permselectivity for (a) He/CO₂ pair, and (b) He/N₂, He/CH₄, CO₂/N₂, and CO₂/CH₄: comparison between modified (full symbols) and non-modified (void symbols) zeolite.*

6.2.4.1.1. Effect of the Temperature

Increasing temperature enhanced gas permeability and diffusivity in each MMM. If in the previous section it was observed that at 35 °C there was not a significant difference between booth systems, higher temperature actually amplified the differences between non-modified and modified zeolite, even though similar trends were observed. **Figure 6.45** shows results for MMMs at 15 wt.% of zeolite (modified and non-modified) used as a reference. At 65 °C the modified membranes have higher permeability and diffusivity in general. Just CO_2 diffusion is higher for non-modified membranes.
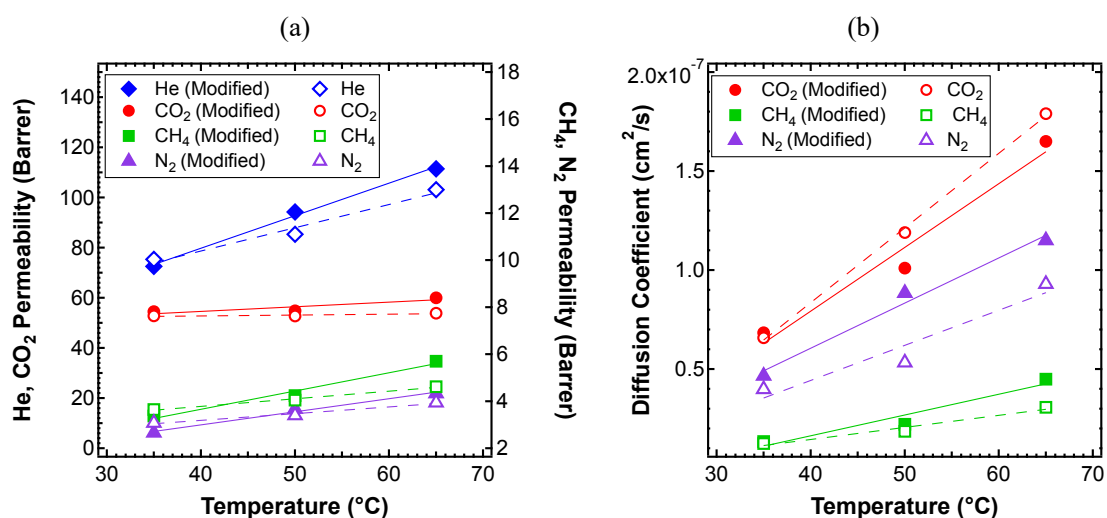
Figure 6.45: 15 wt.% zeolite/PPO (a) permeability, and (b) diffusivity for modified (full symbols) and non-modified (void symbols) zeolite as a function of temperature: 35, 50, 65 °C.

The effect of humidity in non-modified membranes can be observed in **Figure 6.46**. Helium permeability and He/CO_2 selectivity were enhanced in the composite material (25% Zeolite) at 65 °C, generating a jump towards higher values that, on the other hand, was not observed for PPO, being a hydrophobic material. Thus, high temperature can activate the transport in some of the pores provided by zeolites. However, to fully exploit the transport properties of these systems, temperature much higher than 65 °C are needed.
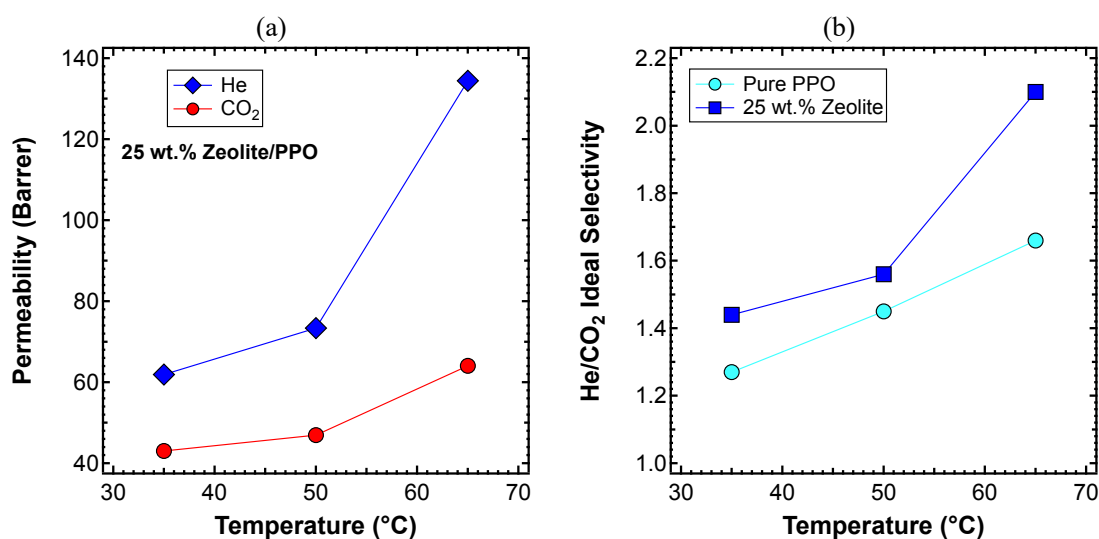
Figure 6.46: Evidence of partial removal of humidity and enhanced permeability and permselectivity in 25 wt.% Zeolite/PPO at 65 °C.

As for the case of ZIF-8/PPO MMMs, zeolite-based materials experienced similar results in terms of permselectivity when the effect of temperate was investigated. To provide an example, **Figure 6.47** shows how temperature affects He/CO_2 and CO_2/CH_4 selectivity. The trend is analogous for all the MMMs at different loadings. Temperature worked in favor of He/CO_2 separation[75], while CO_2/CH_4 selectivity was depressed. The best performance for He/CO_2 separation was achieved by 25 wt.% Modified Zeolite/PPO at 65 °C, while for CO_2/CH_4 it was basically the opposite: the lower filler loading and the lower temperature provided a better separation.
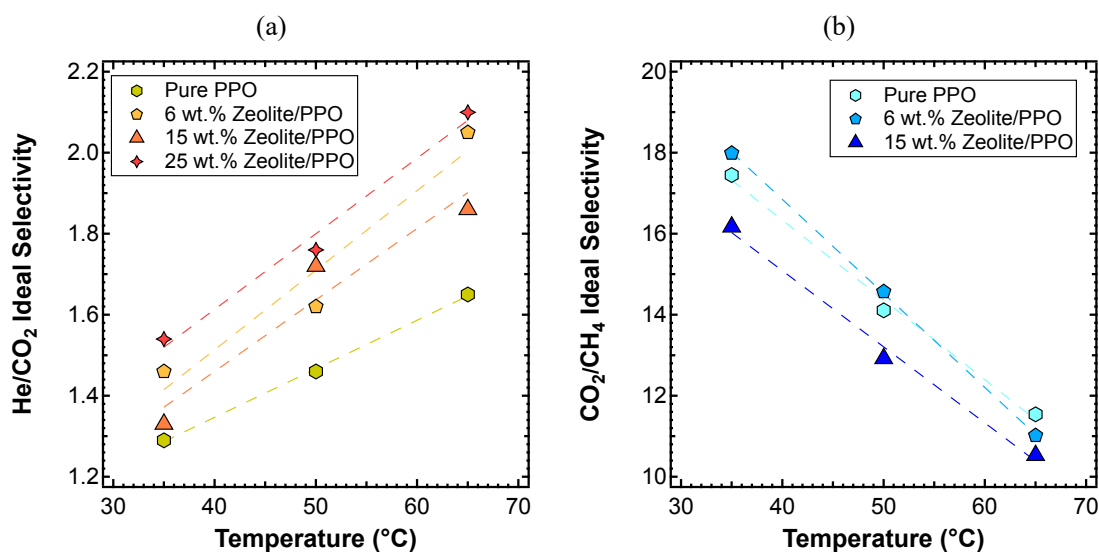
Figure 6.47: (a) He/CO_2, and (b) CO_2/CH_4 selectivity trends with temperature for modified zeolite MMMs at different loadings.

The energetics of the permeation process, E_P, were calculated by means of three permeability values measured at 35, 50, and 65 °C for all gases. **Figure 6.48** shows just data collected for modified MMMs. E_P values were barely affected by the filler content for helium, as expected by the low molecular size of He and the low interaction with the membrane material[83], while for all the other species they were slightly decreasing. The energetics of permeation follow the same order of the ZIF-8/PPO systems, thus the strongest dependence of permeability on temperature was experienced by methane.
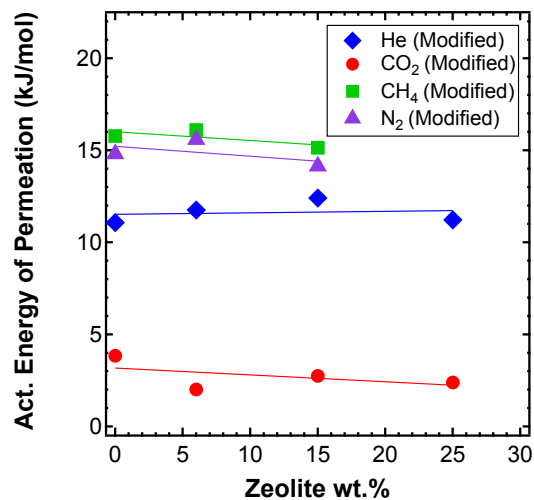
Figure 6.48: Activation energy of permeability as measured in the interval 35 – 65 °C for 4 gases in the various Modified Zeolite/PPO MMMs inspected, as a function of filler loading.

6.2.4.2. Solubility Isotherms

Solubility of He, N_2, CH_4, and CO_2 were measured in Zeolite/PPO MMMs. **Figure 6.49** shows sorption isotherms in a 25 wt.% material. The trend was the typical one expected from glassy polymers, and it was consistent with that observed for ZIF-8/PPO MMMs in the previous section.
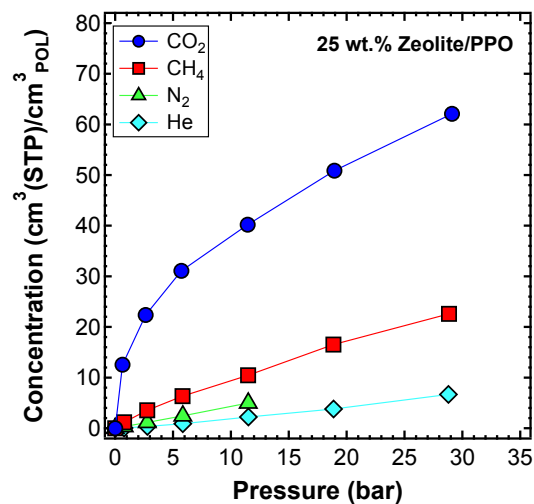
Figure 6.49: 25 wt.% Zeolite/PPO sorption isotherms: CO_2, CH_4, N_2, and He.

196

In order to better evaluate the differences between pure PPO and MMMs, solubility isotherms for membranes and for Zeolite 3A were directly compared in **Figure 6.50**. As expected, the filler adsorbs more gas than PPO and MMMs. However, it was observed that for methane and nitrogen the solubility does not significantly change between the pure PPO film and the membrane loaded with zeolite. This could be related to the interaction between PPO and zeolite, since the access to the pores of the latter may be blocked by the polymer chains. This may also be part of the reason why gas permeability decreases with increasing filler loading, as shown in **Figure 6.42**. On the other hand, in **Figure 6.50a** can be observed that 25 wt.% Zeolite/PPO adsorbs more than pure PPO, and this may be ascribed to the smaller kinetic diameter of CO_2 with respect to N_2 and CH_4, thus its faster diffusivity, as confirmed by results shown in **Figure 6.43**. This may allow CO_2 to access pores that are not available for bigger gases, providing eventually enhanced solubility in the composite material.

(c)
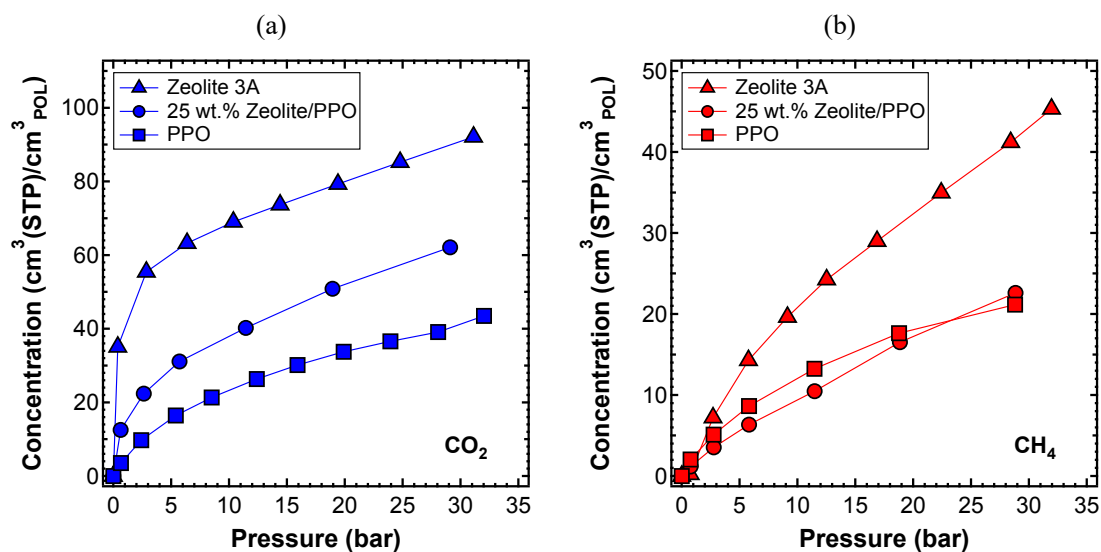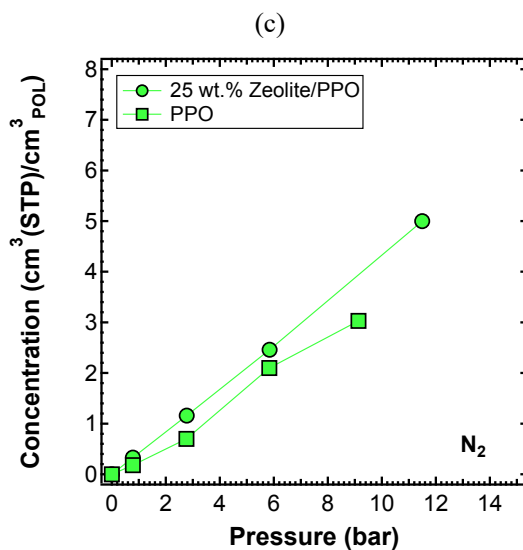
Figure 6.50: Comparison of the absorption isotherms of (a) CO_2, (b) CH_4, and (c) N_2, in PPO, 25 wt.% Zeolite/PPO (non-modified) MMMs, and Zeolite 3A.

6.2.5. Conclusions of Zeolite 3A/PPO MMMs Section

New membranes based on commercially available PPO and Zeolite 3A were manufactured with a simple and reproducible method with loadings up to 40 wt.%. The effect of the silane functionalization of Zeolite 3A surface on the gas transport properties was investigated. The modification was performed to reduce the hydrophilicity of zeolite and try to make it more compatible with the polymer, as well as more permeable at low temperatures. DSC analysis revealed that residual atmospheric moisture can be easily entrapped in non-modified MMMs after the casting procedure, and not even after thermal treatment at 200 °C. The presence of water in the filler can prevent the full exploitation of the zeolite transport properties.

The comparison of the performance at 35 °C, indicated that helium permeability was higher in the case of modified zeolite, while for the other gases the two types of membranes had in general similar performance. This was possible because of the reduction of hydrophilicity occurred after surface modification, which allowed to exploit better its transport properties. Further, selectivity was in general higher in the case of modified zeolite. At higher temperature, *i.e.*, 65 °C, differences between the two systems were amplified, and higher permeability and diffusivity was experienced with modified MMMs.

In fact, the highest He/CO_2 selectivity was measured at 65 °C in the membrane with the highest content of modified zeolite. Preliminary sorption results revealed that solubility selectivity can be enhanced by higher loadings of zeolite, because for molecules bigger that the pores of the filler (*i.e.*, CH_4 and N_2), MMMs solubility was not higher than that of PPO alone, while it was enhanced for He and CO_2.

Future development of this activity may involve testing materials at higher temperatures and performing morphological and calorimetric characterization on membranes with modified zeolite.

References

[1]   N. W. Ockwig, T. M. Nenoff, *Chem. Rev.* **2007**, *107*, 4078.

[2]   W. J. Koros, R. Mahajan, *Mahajan J Membr Sci Vol 175 p 181* **2000**, *175*, 181.

[3]   P. Bernardo, E. Drioli, G. Golemme, *Ind. Eng. Chem. Res.* **2009**, *48*, 4638.

[4]   J. M. S. Henis, M. K. Tripodi, *Sep. Sci. Technol.* **1980**, *15*, 1059.

[5]   M. Galizia, W. S. Chi, Z. P. Smith, T. C. Merkel, R. W. Baker, B. D. Freeman, *Macromolecules* **2017**, *50*, 7809.

[6]   L. M. Robeson, *J. Memb. Sci.* **1991**, *62*, 165.

[7]   L. M. Robeson, *J. Memb. Sci.* **2008**, *320*, 390.

[8]   H. W. H. Lai, F. M. Benedetti, Z. Jin, Y. C. Teo, A. X. Wu, M. G. De Angelis, Z. P. Smith, Y. Xia, *Submitt. to Macromol.* **2019**.

[9]   Y. He, F. M. Benedetti, S. Lin, C. Liu, Y. Zhao, H.-Z. Ye, T. Van Voorhis, M. G. De Angelis, T. M. Swager, Z. P. Smith, *Submitt. to Adv. Mater.* **2019**.

[10] I. Rose, C. G. Bezzu, M. Carta, B. Comesanã-Gándara, E. Lasseuguette, M. C. Ferrari, P. Bernardo, G. Clarizia, A. Fuoco, J. C. Jansen, K. E. Hart, T. P. Liyana-Arachchi, C. M. Colina, N. B. McKeown, *Nat. Mater.* **2017**, *16*, 932.

[11] M. Carta, R. Malpass-Evans, M. Croad, Y. Rogan, J. C. Jansen, P. Bernardo, F. Bazzarelli, N. B. McKeown, *Science (80-.).* **2013**, *339*, 303.

[12] P. M. Budd, E. S. Elabas, B. S. Ghanem, S. Makhseed, N. B. McKeown, K. J. Msayib, C. E. Tattershall, D. Wang, *Adv. Mater.* **2004**, *16*, 456.

[13] Z. Kang, Y. Peng, Y. Qian, D. Yuan, M. A. Addicoat, T. Heine, Z. Hu, L. Tee, Z. Guo, D. Zhao, *Chem. Mater.* **2016**, *28*, 1277.

[14] B. P. Biswal, H. D. Chaudhari, R. Banerjee, U. K. Kharul, *Chem. - A Eur. J.* **2016**, *22*, 4695.

[15] J. Dechnik, J. Gascon, C. J. Doonan, C. Janiak, C. J. Sumby, *Angew. Chemie Int. Ed.* **2017**, *56*, 9292.

[16] G. Dong, H. Li, V. Chen, *J. Mater. Chem. A* **2013**, *1*, 4610.

[17] B. Zornoza, C. Tellez, J. Coronas, J. Gascon, F. Kapteijn, *Microporous Mesoporous Mater.* **2013**, *166*, 67.

[18] T. S. Chung, L. Y. Jiang, Y. Li, S. Kulprathipanja, *Prog. Polym. Sci.* **2007**, *32*, 483.

[19] L. Olivieri, S. Ligi, M. G. De Angelis, G. Cucca, A. Pettinau, *Ind. Eng. Chem. Res.* **2015**, *54*, 11199.

[20] K. Althumayri, W. J. Harrison, Y. Shin, J. M. Gardiner, C. Casiraghi, P. M. Budd, P. Bernardo, G. Clarizia, J. C. Jansen, *Philos. Trans. R. Soc. A Math. Phys. Eng. Sci.* **2016**, *374*, 20150031.

[21] T. C. Merkel, Z. He, I. Pinnau, B. D. Freeman, P. Meakin, A. J. Hill, *Macromolecules* **2003**, *36*, 8406.

[22] G. Dong, H. Li, V. Chen, *J. Memb. Sci.* **2011**, *369*, 206.

[23] J. Li, J. Sculley, H. Zhou, *Chem. Rev.* **2012**, *112*, 869.

[24] O. M. Yaghi, M. O'Keeffe, N. W. Ockwig, H. K. Chae, M. Eddaoudi, J. Kim, *Nature* **2003**, *423*, 705.

[25] C. A. Trickett, A. Helal, B. A. Al-Maythalony, Z. H. Yamani, K. E. Cordova, O. M. Yaghi, *Nat. Rev. Mater.* **2017**, *2*, 17045.

[26] H. Yehia, T. J. Pisklak, K. J. Balkus, I. H. Musselman, in *Polym. Prepr. - Am.*, **2004**, pp. 35–36.

[27] R. Mahajan, W. J. Koros, *Ind. Eng. Chem. Res.* **2000**, *39*, 2692.

[28] R. Mahajan, W. J. Koros, *Polym. Eng. Sci.* **2002**, *42*, 1420.

[29] J. Caro, *Curr. Opin. Chem. Eng.* **2011**, *1*, 77.

[30] Z. Wang, D. Wang, S. Zhang, L. Hu, J. Jin, *Adv. Mater.* **2016**, *28*, 3399.

[31] Q. Xin, J. Ouyang, T. Liu, Z. Li, Z. Li, Y. Liu, S. Wang, H. Wu, Z. Jiang, X. Cao, *ACS Appl. Mater. Interfaces* **2015**, *7*, 1065.

[32] R. Banerjee, A. Phan, B. Wang, C. Knobler, H. Furukawa, M. O'Keeffe, O. M. Yaghi, *Science (80-.).* **2008**, *319*, 939.

[33] Y. Li, F. Liang, H. Bux, W. Yang, J. Caro, *J. Memb. Sci.* **2010**, *354*, 48.

[34] V. M. Aceituno Melgar, J. Kim, M. R. Othman, *J. Ind. Eng. Chem.* **2015**, *28*, 1.

[35] L. R. Parent, C. H. Pham, J. P. Patterson, M. S. Denny, S. M. Cohen, N. C. Gianneschi, F. Paesani, *J. Am. Chem. Soc.* **2017**, *139*, 13973.

[36] S. Hyun, J. H. Lee, G. Y. Jung, Y. K. Kim, T. K. Kim, S. Jeoung, S. K. Kwak, D. Moon, H. R. Moon, *Inorg. Chem.* **2016**, *55*, 1920.

[37] J.-J. Shieh, T. S. Chung, *J. Polym. Sci. Part B Polym. Phys.* **1999**, *37*, 2851.

[38] H. Bux, F. Liang, Y. Li, J. Cravillon, M. Wiebcke, J. Caro, *J. Am. Chem. Soc.* **2009**, *131*, 16000.

[39] M. C. McCarthy, V. Varela-Guerrero, G. V. Barnett, H. K. Jeong, *Langmuir* **2010**, *26*, 14636.

[40] H. Bux, A. Feldhoff, J. Cravillon, M. Wiebcke, Y.-S. Li, J. Caro, *Chem. Mater.* **2011**,

23, 2262.

[41] V. M. Aceituno Melgar, H. Ahn, J. Kim, M. R. Othman, *J. Ind. Eng. Chem.* **2015**, *21*, 575.

[42] N. Hara, M. Yoshimune, H. Negishi, K. Haraya, S. Hara, T. Yamaguchi, *J. Memb. Sci.* **2014**, *450*, 215.

[43] T. C. Merkel, M. Zhou, R. W. Baker, *J. Memb. Sci.* **2012**, *389*, 441.

[44] J. J. Marano, J. P. Ciferino, *Energy Procedia* **2009**, *1*, 361.

[45] M. J. C. Ordoñez, K. J. Balkus, J. P. Ferraris, I. H. Musselman, *J. Memb. Sci.* **2010**, *361*, 28.

[46] K. S. Park, Z. Ni, A. P. Cote, J. Y. Choi, R. Huang, F. J. Uribe-Romo, H. K. Chae, M. O'Keeffe, O. M. Yaghi, *Proc. Natl. Acad. Sci.* **2006**, *103*, 10186.

[47] S. Rafiq, A. Maulud, Z. Man, M. I. A. Mutalib, F. Ahmad, A. U. Khan, A. L. Khan, M. Ghauri, N. Muhammad, *Can. J. Chem. Eng.* **2015**, *93*, 88.

[48] M. Aguilar-Vega, D. R. Paul, *J. Polym. Sci. Part B Polym. Phys.* **1993**, *31*, 1577.

[49] A. Alentiev, E. Drioli, M. Gokzhaev, G. Golemme, O. Ilinich, A. Lapkin, V. Volkov, Y. Yampolskii, *J. Memb. Sci.* **1998**, *138*, 99.

[50] B. J. Story, W. J. Koros, *J. Appl. Polym. Sci.* **1991**, *42*, 2613.

[51] K. Toi, G. Morel, D. R. Paul, *J. Appl. Polym. Sci.* **1982**, *27*, 2997.

[52] Y. Huang, D. R. Paul, *J. Polym. Sci. Part B Polym. Phys.* **2007**, *45*, 1390.

[53] M. Galizia, C. Daniel, G. Fasano, G. Guerra, G. Mensitieri, *Macromolecules* **2012**, *45*, 3604.

[54] H. Fu, L. Jia, J. Xu, *J. Appl. Polym. Sci.* **1994**, *51*, 1399.

[55] J. D. Le Roux, D. R. Paul, J. Kampa, R. J. Lagow, *J. Memb. Sci.* **1994**, *90*, 21.

[56] H. Yasuda, K. Rosengren, *J. Appl. Polym. Sci.* **1970**, *14*, 2839.

[57] A. L. Khan, A. Cano-Odena, B. Gutiérrez, C. Minguillón, I. F. J. Vankelecom, *J. Memb. Sci.* **2010**, *350*, 340.

[58] Q. Song, S. K. Nataraj, M. V. Roussenova, J. C. Tan, D. J. Hughes, W. Li, P. Bourgoin, M. A. Alam, A. K. Cheetham, S. A. Al-Muhtaseb, E. Sivaniah, *Energy Environ. Sci.* **2012**, *5*, 8359.

[59] T. Yang, Y. Xiao, T.-S. Chung, *Energy Environ. Sci.* **2011**, *4*, 4171.

[60] T. Yang, T.-S. Chung, *Int. J. Hydrogen Energy* **2013**, *38*, 229.

[61] T. Yang, G. M. Shi, T.-S. Chung, *Adv. Energy Mater.* **2012**, *2*, 1358.

[62] C. Zhang, Y. Dai, J. R. Johnson, O. Karvan, W. J. Koros, *J. Memb. Sci.* **2012**, *389*, 34.

[63] K. Díaz, M. López-González, L. F. del Castillo, E. Riande, *J. Memb. Sci.* **2011**, *383*, 206.

[64] A. F. Bushell, M. P. Attfield, C. R. Mason, P. M. Budd, Y. Yampolskii, L. Starannikova, A. Rebrov, F. Bazzarelli, P. Bernardo, J. Carolus Jansen, M. Lanč, K. Friess, V. Shantarovich, V. Gustov, V. Isaeva, *J. Memb. Sci.* **2013**, *427*, 48.

[65] P. D. Sutrisna, J. Hou, H. Li, Y. Zhang, V. Chen, *J. Memb. Sci.* **2017**, *524*, 266.

[66] C. Casado-Coterillo, A. Fernández-Barquín, B. Zornoza, C. Téllez, J. Coronas, Á. Irabien, *RSC Adv.* **2015**, *5*, 102350.

[67] P. Küsgens, M. Rose, I. Senkovska, H. Fröde, A. Henschel, S. Siegle, S. Kaskel, *Microporous Mesoporous Mater.* **2009**, *120*, 325.

[68] A. U. Ortiz, A. P. Freitas, A. Boutin, A. H. Fuchs, F. X. Coudert, *Phys. Chem. Chem. Phys.* **2014**, *16*, 9940.

[69] L. Ansaloni, M. Minelli, M. Giacinti Baschetti, G. C. Sarti, *Oil Gas Sci. Technol. – Rev. d'IFP Energies Nouv.* **2015**, *70*, 367.

[70] A. C. Savoca, A. D. Surnamer, C. Tien, *Macromolecules* **1993**, *26*, 6211.

[71] Y. Huang, D. R. Paul, *Polymer (Guildf).* **2004**, *45*, 8377.

[72] Y. Huang, D. R. Paul, *Macromolecules* **2005**, *38*, 10148.

[73] M. Moaddeb, W. J. Koros, *J. Memb. Sci.* **1997**, *125*, 143.

[74] E. V. Perez, K. J. Balkus, J. P. Ferraris, I. H. Musselman, *J. Memb. Sci.* **2009**, *328*, 165.

[75] B. W. Rowe, L. M. Robeson, B. D. Freeman, D. R. Paul, *J. Memb. Sci.* **2010**, *360*, 58.

[76] J. C. Maxwell, *A Treatise on Electricity and Magnetism*, Oxford: Claredon Press, London, **1873**.

[77] D. A. G. Bruggeman, *Ann. Phys.* **1935**, *416*, 636.

[78] H. Vinh-Thang, S. Kaliaguine, *Chem. Rev.* **2013**, *113*, 4980.

[79] T. B. Lewis, L. E. Nielsen, *J. Appl. Polym. Sci.* **1970**, *14*, 1449.

[80] M. L. Lind, A. K. Ghosh, A. Jawor, X. Huang, W. Hou, Y. Yang, E. M. V. Hoek, *Langmuir* **2009**, *25*, 10139.

[81] Y. Li, H.-M. Guan, T.-S. Chung, S. Kulprathipanja, *J. Memb. Sci.* **2006**, *275*, 17.

[82] R. W. Baker, *Membrane Technology and Applications*, **2004**.

[83] C. Casado-Coterillo, T. Yokoo, T. Yoshioka, T. Tsuru, M. Asaeda, *Sep. Sci. Technol.* **2011**, *46*, 1224.

[84] G. H. Fredrickson, E. Helfand, *Macromolecules* **1985**, *18*, 2201.

[85] R. J. Umpleby, S. C. Baxter, Y. Chen, R. N. Shah, K. D. Shimizu, *Anal. Chem.* **2001**, *73*, 4584.

[86] M. C. Ferrari, M. Galizia, M. G. De Angelis, G. C. Sarti, *Ind. Eng. Chem. Res.* **2010**, *49*, 11920.

[87] T. C. Merkel, Z. He, I. Pinnau, B. D. Freeman, P. Meakin, A. J. Hill, *Macromolecules* **2003**, *36*, 6844.

[88] M. Woo, J. Choi, M. Tsapatsis, *Microporous Mesoporous Mater.* **2008**, *110*, 330.

[89] A. Fernández-Barquín, R. Rea, D. Venturi, M. Giacinti-Baschetti, M. G. De Angelis, C. Casado-Coterillo, Á. Irabien, *RSC Adv.* **2018**, *8*, 3536.

[90] Y. Zhang, I. H. Musselman, J. P. Ferraris, K. J. Balkus, *J. Memb. Sci.* **2008**, *313*, 170.

[91] J. Hu, H. Cai, H. Ren, Y. Wei, Z. Xu, H. Liu, Y. Hu, *Ind. Eng. Chem. Res.* **2010**, *49*, 12605.

[92] J. Caro, M. Noack, *Microporous Mesoporous Mater.* **2008**, *115*, 215.

[93] C. Baerlocher, L. B. McCusker, D. H. Olson, *Atlas of Zeolite Framework Types*, Elsevier, **2007**.

[94] L. D. Rollmann, E. W. Valyocsik, R. D. Shannon, **2007**, pp. 61–68.

[95] R. Adams, C. Carson, J. Ward, R. Tannenbaum, W. Koros, *Microporous Mesoporous Mater.* **2010**, *131*, 13.

[96] J. Wang, X. Zheng, H. Wu, B. Zheng, Z. Jiang, X. Hao, B. Wang, *J. Power Sources* **2008**, *178*, 9.

[97] N. Y. Chen, *J. Phys. Chem.* **1976**, *80*, 60.

[98] A. Colantuono, S. Dal Vecchio, G. Mascolo, M. Pansini, *Thermochim. Acta* **1997**, *296*, 59.

[99] E. P. Plueddemann, *Silane Coupling Agents*, Springer, New York, **1991**.

7. CO$_2$/CH$_4$ Mixed-Gas Sorption in Glassy Polymers

In this chapter the results obtained from the study of mixed-gas solubility of CO$_2$ and CH$_4$ mixtures at different compositions in a series of glassy polymers are reported. The materials investigated were:

- 3,3'-dihydroxy-4,4'-diamino-biphenyl (HAB) 2,2'-bis-(3,4-dicarboxyphenyl) hexafluoropropane dianhydride (6FDA) polyimide, and its thermally rearranged (TR) derivative TR450;

- Polymer of Intrinsic Microporosity-ethanoanthracene-Tröger's base (PIM-EA-TB), and

Parts of this chapter have been adapted from the following references: 1) E. Ricci, F.M. Benedetti, M. E. Dose, M.G. De Angelis, B.D. Freeman, D.R. Paul; *Experimental Characterization and Modelling of Mixed-Gas Sorption of CO$_2$/CH$_4$ in HAB-6FDA polyimide and its Thermally Rearranged derivative*, to be submitted; 2) F.M. Benedetti, E. Ricci, M. Carta, M.G. De Angelis, N. McKeown; *Sorption of CO$_2$, CH$_4$ and their mixtures in PIM-EA-TB: Experimental and Modelling*, to be submitted.

7.1. Introduction and Motivations

Despite the continuing effort in the synthesis and characterization of countless high-performance new materials[1–10], traditional ones (*e.g.* cellulose acetate[11,12] and polysulfone[13]) still hold their position very firmly in the industry, with only few innovations having been adopted over the years.[14] The very first reason for this lack of success of promising materials in penetrating the market, listed by Baker at al.[15] in their review, is that pure-gas measurements do not provide an accurate prediction of the performance of the membrane in realistic industrial conditions. In fact, tests were performed to screen the properties of these new materials at laboratory-scale, usually involving single gas tests, while, in real applications mixtures can be very complex[16–18], and temperature and pressure far from the operating conditions adopted in laboratory experiments.

A necessary step forward to address the needs industry has, is performing experiments with mixtures instead of pure-gases to assess deviations from the ideal behavior as well as to account for competitive effects among gases. Both mixed-gas permeability[19–25] and mixed-gas sorption[26–28] tests are available options. As mentioned, this section will be focusing on the results obtain performing mixed-gas sorption experiments involving CO_2/CH_4 mixtures. CO_2/CH_4 is a relevant gas pair since it can be found in different applications such as natural gas upgrading and CO_2-enhanced oil recovery, for which it has been shown that the permselectivity in mixed-gas conditions can be markedly different from the single-gas one, sometimes improved[25,29], other times decreased.[12,16,30–33] Depending on the mixture composition, the deviations from the ideal behavior can vary and affect one gas more than the other.

Recently, experimental techniques for the direct determination of gas diffusivity in multicomponent conditions were reported. Garrido et al.[34] used a combination of ^{13}C NMR spectroscopy and pulsed-field gradient NMR, to determine the solubility and diffusion coefficients of gas mixtures, including CO_2/CH_4, in 6FDA-TMPDA polyimide. Fraga et al.[35] recently developed a time-lag technique to measure diffusivity in mixed-gas conditions, based on mass spectroscopy analysis of permeate composition during the permeation transient, and applied it to study the behavior of a CO_2/CH_4 mixture in PIM-EA-TB. In both works multicomponent diffusivity-selectivity values lower than the corresponding pure-gas ones were measured. One of the goals that we have tried to develop upon this PhD, was to couple multicomponent sorption and permeation measurements, according to the solution-diffusion model, and evaluate indirectly the multicomponent diffusivity-selectivity. This method could be of great interest to deconvolute the sorption and diffusion contributions to permeability, and assess their relative weight to the overall performance of a material operating in real conditions. This would help determine if, in multicomponent conditions, the separation is driven by sorption or diffusion and whether or not that would be the same conclusion one could draw from pure-gas considerations. A consequence of this approach is that also the selectivity could be evaluated separating the contributions of solubility-diffusivity and diffusivity-selectivity. This knowledge would eventually drive the design of new material and more suitable processes for the applications of membrane-based technologies.

Mixed-gas sorption tests are significantly more delicate and time-consuming than pure-gas tests, especially when materials exhibit low diffusion coefficients. Therefore, there is a great potential advantage in the use of modelling tools capable of predicting the mixed-gas behavior, using pure-gas experimental information only. If model predictions proved to be reliable, meaningful information about multicomponent behavior could be obtained directly from the pure-gas tests already extensively available in the literature. In fact, the experimental results obtained during this doctoral degree support the modelling activity performed by colleagues in the research group in Bologna.

As a general comment on the topic, mixed-gas sorption calculations can be performed using the well-established Dual Mode Sorption (DMS) model[36–39], which was extended and applied to the multicomponent case by Koros *et al.*[22,40,41]. Alternatively, thermodynamics-based models suitable to the prediction of sorption equilibria in glassy polymers, such as the Non-Equilibrium Thermodynamics for Glassy Polymers approach (NET-GP)[42–46], can be used. The latter approach provides an extension of Equations of State theory to nonequilibrium materials and has been successfully applied to the calculation of sorption of gases and vapors in glassy polymers, as described in more detail in the theoretical background chapter.[46–51] Both the multicomponent DMS model and the NET-GP approach can perform mixed-gas sorption calculations predictively, since only pure-gas sorption data are needed for their parametrization.

7.2. Materials

7.2.1. HAB-6FDA Polyimide and its TR Derivative

Aromatic polyimides such as HAB-6FDA have already found commercial application in CO_2/CH_4 membrane separation. On average, they are characterized by low permeability but high ideal selectivity, by virtue of high chain stiffness and low free volume, which enhance the difference in the mobility of the penetrants inside the matrix. Moreover, these materials exhibit an excellent thermal, mechanical and chemical stability.[32,52]

On the other hand, thermally rearranged polymers were first discovered by Park *et al.* almost ten years ago.[53] They discovered that by performing post-fabrication polymer-modifying reactions at high temperature (350 – 450 °C), completely aromatic, insoluble and thermally resistant materials could be prepared from highly soluble precursors. The strategy was then to cast soluble and processable polymers into films, and then, through this irreversible molecular rearrangement, obtain membranes that otherwise we would never be able to get, precisely because they are not soluble, and they could not be casted. From that first finding, a new family of materials called Thermally Rearranged (TR) polymers was developed.[54,55] They comprised polybenzoxazoles (PBO) and polybenzothiazoles (PBT) that have recently received increasing attention[4,56–61], because they showed high permeability values without compromised selectivity. These features make them interesting candidates for gas separation, especially for CO_2/CH_4 and CO_2/N_2 separations, for which they were often located above the 2008 Robeson upper bound.[62,63] In addition, these materials show an excellent thermal and chemical stability. Positron annihilation lifetime spectroscopy (PALS) measurements and molecular modelling revealed that, during the rearrangement process, a favorable free volume distribution for gas separation was created. This can be schematized as hourglass-shaped, thus having a large average cavity size, which favors high permeability, coupled with a narrow cavity size distribution and small bottlenecks connecting the cavities, which confer sieving properties and higher ideal selectivity compared to other materials with a similar fractional free volume.[53,54,64,65] The rigid backbone structure of PBOs, made up of interconnected heterocyclic rings having very high rotational barriers, makes the microstructure of the materials rather stable towards ageing and plasticization, evidenced by low hysteresis in repeated pressurization-depressurization cycles.[53,66–68] This is a critical when CO_2, water or more condensable species such as heavy hydrocarbons are present.

HAB-6FDA polyimide was synthesized from 3,3'-dihydroxy-4,4'-diamino-biphenyl (HAB) and 2,2'-bis- (3,4-dicarboxyphenyl) hexafluoropropane dianhydride (6FDA) *via* two-step polycondensation method with chemical imidization.[69,70] The rearrangement reaction can be performed at temperatures ranging from 350 to 450 °C, as indicated in the reaction scheme showed in **Figure 7.1**. The mass loss during the process was used to estimate the conversion of the polyimide precursor to the final

polybenzoxazole (PBO) TR structure obtained. This carries the assumption that all mass loss should be due to thermal rearrangement, and not thermal degradation. The percent conversion of the polyimide precursor to TR polymer used in this work was 70.8%. Both HAB-6FDA and TR450 were provided by the colleagues at the *University of Texas at Austin*. Thermal rearrangement was performed by heating the polyimide, initially at ambient conditions, at a ramp rate of 5 °C/min to 300 °C, where the sample was held isothermally for 1 h to ensure complete imidization. Then, temperature was increased at 5 °C/min to the target thermal rearrangement temperature (450 °C), where the sample was held for the desired amount of time (30 minutes). The furnace was then cooled to ambient conditions at a rate no greater than 10 °C/min. This heating protocol was used to expose the samples to thermal histories similar to those reported in previous studies of TR polymers and ensures minimal thermal degradation.[25,53,54,69,70]
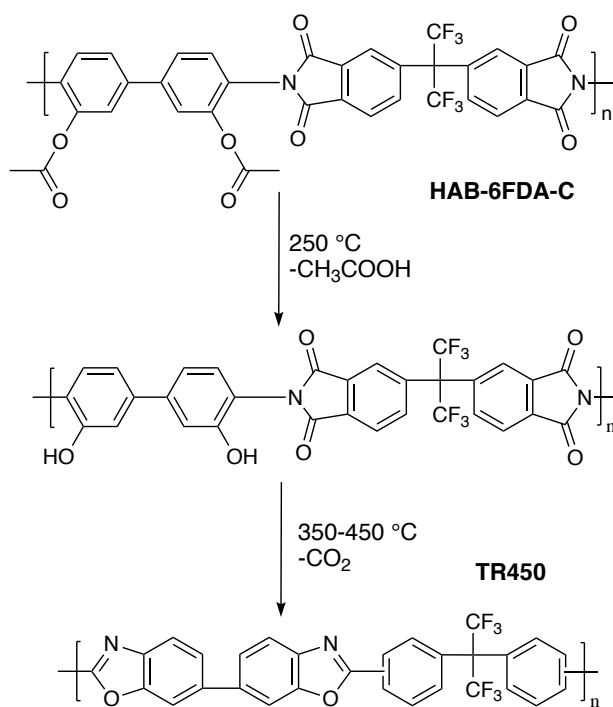
Figure 7.1: *Conversion of HAB-F6DA-C in TR450 through thermal rearrangement. Reaction scheme rearranged from Sanders et al.*[69]*.*

HAB-6FDA and its TR derivatives were intensively characterized over the past few years. Pure-gas sorption[70], pure-gas permeation[69] and mixed-gas permeation of CO_2 and CH_4[25], also as a function of temperature[71], were determined. With this study, we expanded the characterization by performing mixed-gas sorption experiments of a CO_2/CH_4 mixture. The characteristics of the two films investigated are reported in **Table 7.1**.

Table 7.1: Properties of the samples used for pure- and mixed-gas sorption: HAB-6FDA and TR450.

	Thickness (μm)	Mass (g)	Density (g/cm³)	FFV (%)[69]	Conversion (%)
HAB-6FDA	55 ± 3.8	0.35	1.407	15.0	/
TR450	43 ± 1.3	0.35	1.340	19.6	70.8

7.2.2. PIM-EA-TB

The remarkable properties of Polymers of Intrinsic Microporosity (PIMs) have been often presented and described across the dissertation so far (*i.e.*, 3.1, 4.2.1, 4.3.3, 5.1.3 and 6.1.7.6), as well as in the following chapter 10.[72] In this section of chapter 7, the PIM that was selected to investigate CO_2/CH_4 mixtures was PIM-EA-TB.[10] PIM-EA-TB is an outstanding polymer because it initiated the use of Tröger's Base as a constituent of ladder polymers, providing enhanced rigidity and molecular sieve capability (*i.e.*, higher diffusivity-selectivity). The sample was provided in powder form by the colleagues at *University of Edinburgh* and *Swansea University*.
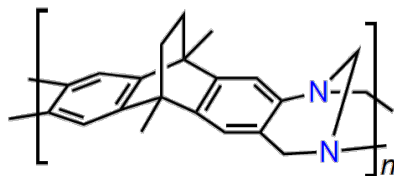
Figure 7.2: Chemical structure of PIM-EA-TB.[1]

The polymer was dissolved in chloroform (1.5 wt.%) and left under magnetic stirring for 1 hour to ensure all the powder was properly dissolved. The solution was then casted onto a 7 cm glass Petri dish placed on a flat and levelled surface. The Petri dish was covered to allow for a slow solvent evaporation. After 4 days the cover was removed and the film was easily detached from the casting support. The film was then soaked for 2 days in methanol, to remove the residual chloroform from the film. Methanol was periodically replaced to guarantee a complete extraction of the casting solvent. The membrane was then dried under vacuum at 100 °C for 5 days. This thermal treatment was performed to remove the methanol and to stabilize the transport properties of the polymer over time, accelerating ageing. The methanol treatment makes the transport properties strongly time-dependent, because it swells the polymer matrix, that eventually becomes denser when the alcohol is removed.[72] Since the measurements of single gas and mixed-gas sorption take about 30 days to be performed, variations of the polymer structure during this time frame needed to be avoided.

All the experiments were performed on the same sample, whose characteristic are reported in **Table 7.2**. The measurement of the polymer density with the buoyancy method in liquid water and n-dodecane did not yield reliable results, due to high absorption of those liquids into the polymer sample. Therefore, the density of the polymer was assumed to be 1.08 g/cm^3, according to Tocci *et al.*.[73]

Table 7.2: Properties of the samples used for pure- and mixed-gas sorption: PIM-EA-TB.

	Thickness (µm)	Mass (g)	Density (g/cm^3)[73]	FFV (%)[73]
PIM-EA-TB	111 ± 10	0.512	1.08	27.6

7.3. Pure- and Mixed-Gas Sorption Isotherms

HAB-6FDA & TR450

At first, pure CO_2 and CH_4 sorption isotherms in HAB-6FDA at 35 °C were measured, to verify consistency with literature data.[70,71] The comparison showed good agreement between the two data sets and is reported in **Figure 7.3**.
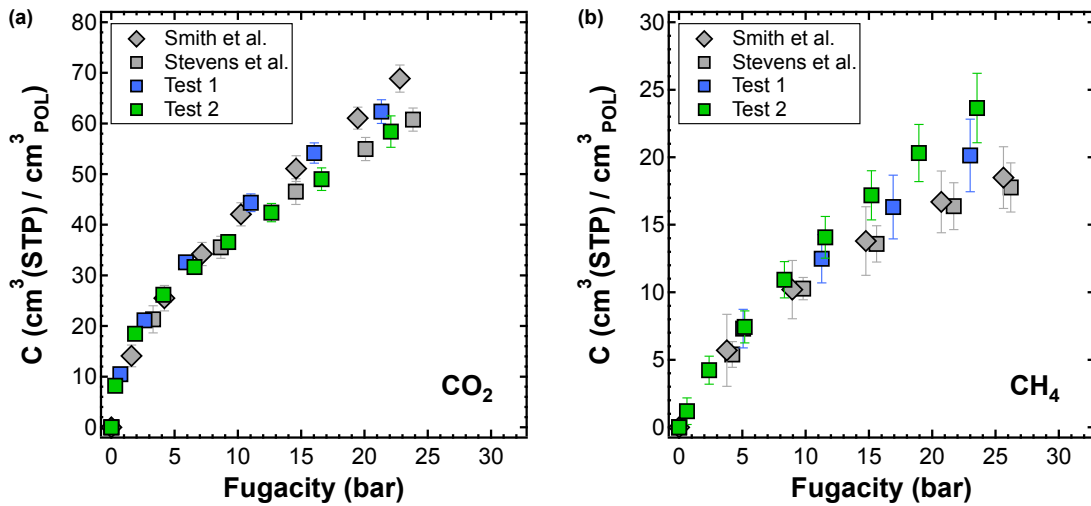
Figure 7.3: *Pure-gas sorption isotherms at 35 °C of (a) CO_2 and (b) CH_4 in HAB-6FDA polyimide compared to literature data.* Green *and* blue *symbols are data from this work collected in two different in-house equipment, grey markers are from Smith et al.*[70] *and Stevens et al..*[71]

In addition, diffusion coefficients of CO_2 and CH_4 in HAB-6FDA were calculated from the analysis of sorption kinetics, and the results compared with the ones obtained with the time-lag method by Sanders *et al.*.[69] Pure-gas diffusion coefficients as a function of gas concentration are shown in **Figure 7.4**.
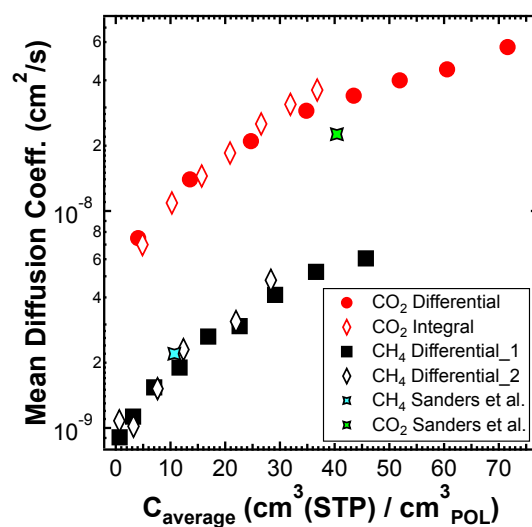
Figure 7.4: Pure-gas diffusion coefficients of CO_2 and CH_4 in HAB-6FDA from sorption kinetics. Comparison with data from Sanders et al..[69]

The mixed-gas sorption test was performed right after pure-gas measurements. **Figure 7.5** shows the experimental sorption data of a CO_2/CH_4 mixture in HAB-6FDA and TR450 at 35 °C. The average final composition of the gas mixture in equilibrium with the polymer was 28.8 mol.% CO_2 in the case of HAB-6FDA and 29.5 mol.% CO_2 in the case of TR450. The error bars were calculated by means of the propagation of the error method[74] by considering the uncertainty on the volume calibration, composition, and pressure. Pure-gas sorption isotherms from the literature[71] were added to the plot for comparison. The typical behavior observed for multicomponent sorption in glassy polymers[26–28] was observed also for HAB-6FDA and TR450. The presence of around 70 mol.% CH_4 had little effect on CO_2 sorption, while CH_4 was markedly affected by the presence of the second gas, especially in the TR polymer. This result highlights the competitive nature of multicomponent sorption in glassy polymers, with the less condensable gas being more excluded from the polymer, even though it is the most abundant in the gas phase.
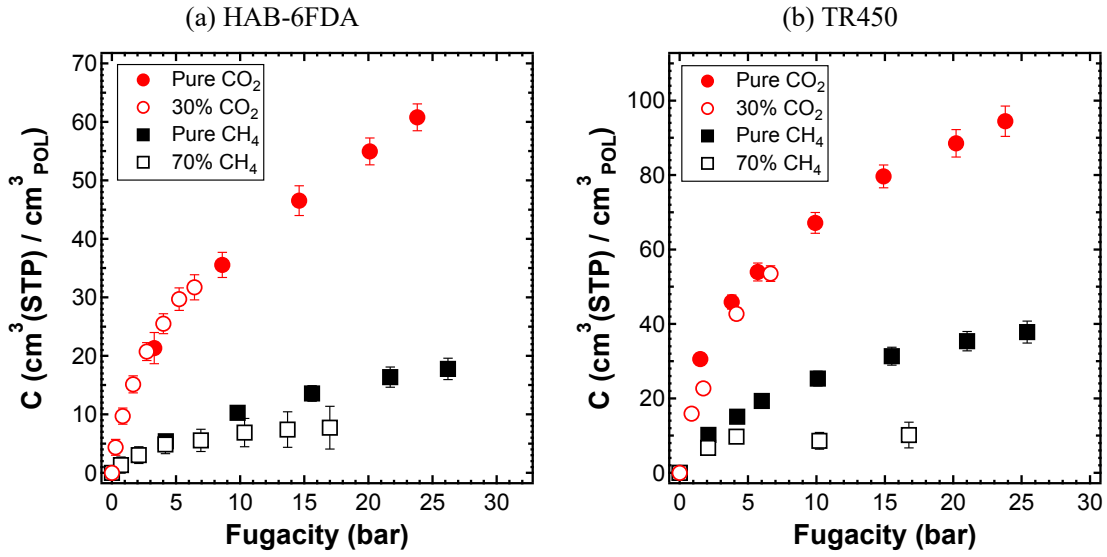
(a) HAB-6FDA

(b) TR450

Figure 7.5*: Empty symbols: Mixed-gas sorption isotherms of CO_2 (red) and CH_4 (black) at 35 °C (~30 mol.% CO_2 composition) in (a) HAB-6FDA and (b) TR450. Filled symbols: literature[71] pure-gas CO_2 (red) and CH_4 (black) sorption isotherms added for comparison.*

In **Figure 7.6** the differences between the pure-gas measurements and the mixed-gas results are highlighted. Further, the fittings of the DMS model in the pure- and in the mixed-gas case are reported. A description of the DMS model is provided in the theoretical background chapter of this dissertation, and the extension to the mixtures is simply given by Eq. (7.1). The parameters retrieved from the pure-gas sorption isotherms and collected in **Table 7.3** can be directly applied to the mixed-gas case.

$$C_i = k_{D,i}f_i + \frac{C'_{H,i}b_if_i}{1 + b_if_i + b_jf_j}$$

Eq. (7.1)

f_i is the fugacity of component i, while f_j is the fugacity of component j of the mixture. The fugacity was calculated by means of Peng-Robinson Equation of State.[75] All the other parameters were defined in the theoretical background chapter 4.3.2. Consistently with the fact that more condensable gases tend to have larger affinity constants, the values for the b parameter associated with CO_2 sorption were larger than those retrieved for CH_4. Also, the capacity constants, C'_H, of both gases were higher for TR450 than HAB-6FDA, which mirrors the difference in the free volume between the two materials, 19.6% and 15.0% respectively (**Table 7.1**).[69]

Table 7.3: *Dual Mode sorption model fugacity-based parameters for CO_2 and CH_4 sorption in HAB-6FDA and TR-450 at 35 °C.*

	Gas	k_D $\left(\dfrac{cm^3_{STP}}{cm^3_{pol}bar}\right)$	C'_H $\left(\dfrac{cm^3_{STP}}{cm^3_{pol}}\right)$	b (bar^{-1})
HAB-6FDA	CO_2	1.33	32.62	0.33
	CH_4	0.36	10.99	0.15
TR-450	CO_2	1.68	59.44	0.56
	CH_4	0.38	35.75	0.15

(a) HAB-6FDA
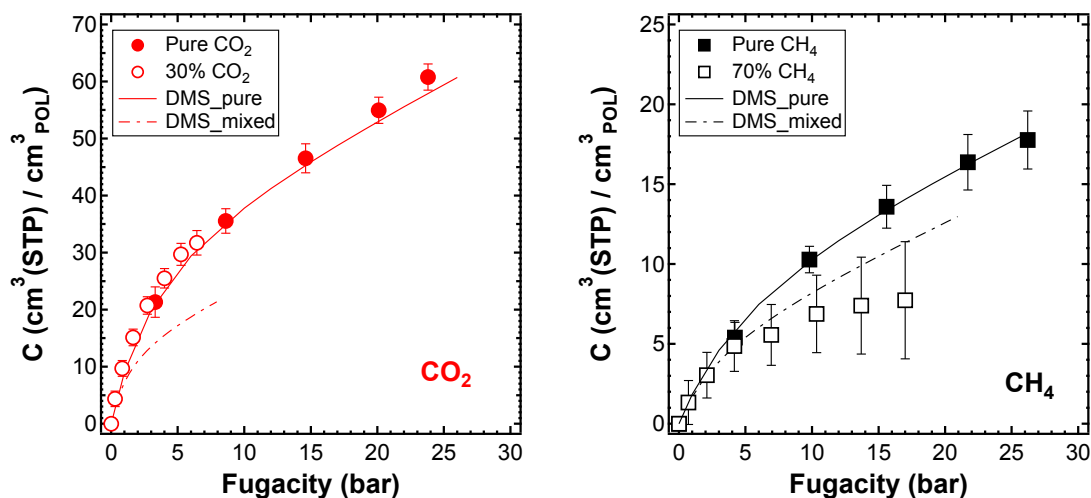
(b) TR450
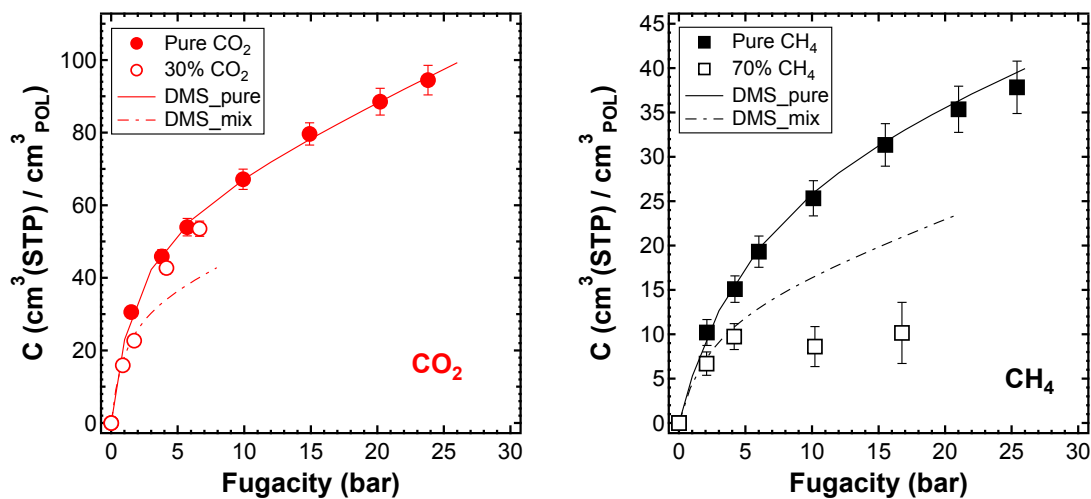
Figure 7.6: *Experimental data of pure- and mixed-gas (30 mol.% CO_2) sorption isotherms of CO_2 and CH_4 in (a) HAB-6FDA and (b) TR450 at 35 °C. Solid line: pure-gas fitting performed with DMS model. Dashed line: mixed-gas predictions obtained with the multicomponent DMS model.*

The DMS model captured the competitive nature of multicomponent sorption qualitatively, predicting a reduction in the solubility of both gases in both materials. However, the competitive effect is significantly overestimated in the case of CO_2 and underestimated in the case of CH_4, especially at high pressure, where deviations as high as ~50% were recorded. Explanations for the deviation of the multicomponent DMS predictions from the experimental data were identified originally by Koros[40] as the possible presence of non-negligible penetrant-penetrant specific interactions, or as the consequence of swelling and plasticization effects, which were not accounted for in the model and that would make the parameters concentration-dependent. The first assumption, related to the CO_2-CH_4 negligible interaction, was also an assumption of the NELF model, which however provided much better agreement with the experimental mixed-gas data as reported by Ricci *et al.*.[76] As a consequence, the most relevant difference could be due to the fact that DMS model does not account for CO_2-induced swelling, which was instead considered in the NELF model. Further to what hypothesized by Koros, a sensitivity analysis of multicomponent DMS model calculations[77], showed that poor results in mixed-gas predictions with this model can be ascribed to parametrization issues. Due to the strong coupling between the parameters C_H' and b, several different parameter sets were found that provided an equally satisfactory representation of the sorption isotherms, within the experimental error. However, even though these different parameter sets gave an equivalent representation of pure-gas data, their prediction of multicomponent sorption was either really accurate or really poor, therefore, in the absence of experimental data to validate the results of the calculations, their accuracy cannot be assured. Gleason *et al.*[25] reported similar issues in their analysis of DMS parameters for mixed-gas permeation of CO_2/CH_4 in HAB-6FDA and TR-PBOs, resolving to include the mixed-gas data into the parametrization. In this way a superior representation was achieved, but the procedure was no longer predictive. As pointed out by Smith *et al.*[70] that characterized sorption isotherms in HAB-6FDA and TR-PBOs, DMS parameters did not exhibit systematic trends with penetrant condensability or degree of conversion of the TR polymers. What they did was to constrain k_D and b to increase exponentially with critical temperature of each gas tested, with a slope assigned from the analysis of the solubility

coefficients measured at 10 atm plotted against T_c. Although it was not used in the present dissertation, this strategy could be implemented in future works to enhance accuracy of the mixed-gas sorption predictions.

PIM-EA-TB

CO_2 and CH_4 pure- and mixed-gas sorption experiment were performed by testing PIM-EA-TB polymer films at 35 °C up to about 30 bar by means of the pressure decay technique, as described in the experimental methods chapter (section 5.7). The apparatus used to carry out pure-gas experiments was the same as the one adopted for mixed-gas sorption, because the equipment allows to perform both types of measurement. CH_4 was tested before CO_2, to reduce the conditioning of the sample due to the exposition to carbon dioxide at high pressure. The nominal composition selected for mixed-gas experiments was 30 mol.%, while the actual experimental curve at equilibrium revealed to be at an average of 28.6 mol.% of CO_2.

The two sorption isotherms obtained by means of *differential* experiments at 35 °C for the pure-gases are shown in **Figure 7.7**, versus respective gas fugacity. As expected, CO_2 was more soluble than CH_4, due to the lower condensability of the latter gas.
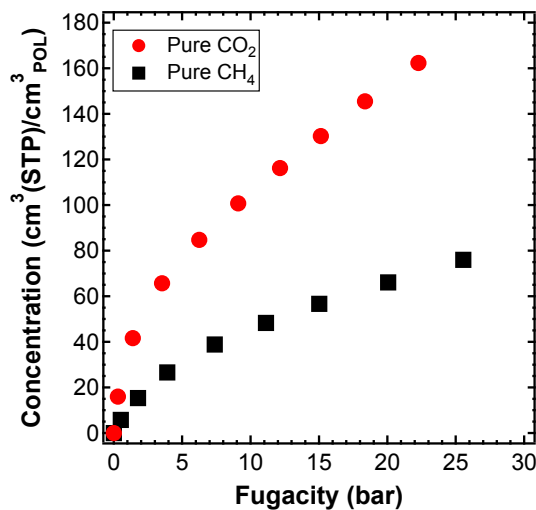
Figure 7.7*: Pure-gas sorption isotherms in PIM-EA-TB at 35 °C. Red circles CO_2, black squares CH_4.*

Table 7.4 contains the fugacity-based DMS parameters for PIM-EA-TB sorption data. As mentioned above, they could be used directly to provide an interpretation of the pure-gas data and predict the solubility isotherms in case of mixtures.

Table 7.4: Fugacity-based Dual Mode parameters for CO_2 and CH_4 pure-gas sorption at 35°C in PIM-EA-TB. Maximum pressure 32 bar.

	Gas	k_D $\left(\dfrac{cm^3_{STP}}{cm^3_{pol}bar}\right)$	C'_H $\left(\dfrac{cm^3_{STP}}{cm^3_{pol}}\right)$	b (bar^{-1})
PIM-EA-TB	CO_2	4.72	64.61	0.90
	CH_4	1.51	43.55	0.24

As it can be observed in **Figure 7.8**, results were very similar to those observed for HAB-6FDA polyimide and its TR derivative TR450. The solubility of both species in mixed-gas conditions was lower than that of the pure-gases at the same fugacity. However, the more condensable gas (*i.e.*, CO_2) was barely altered by the presence of a 70 mol.% of CH_4, while the latter was markedly affected by the presence of the more soluble gas. The competitive effect is still the framework in which these results can be explained. Further, **Figure 7.8** shows the multicomponent prediction of the DMS model. Again, the model can describe qualitatively the results obtained, since it predicted that the concentration in the mixed-gas case would have been lower for both species. Hoverer, as for the previous case, CO_2 exclusion was overestimated, while that of CH_4 underestimated. The NELF model provides a better description of the multicomponent sorption isotherms, as reported in the literature.[78] The reasons why the DMS model may have failed in this prediction, especially at high pressure, are reported in the previous session and apply also to the case of PIM-EA-TB.
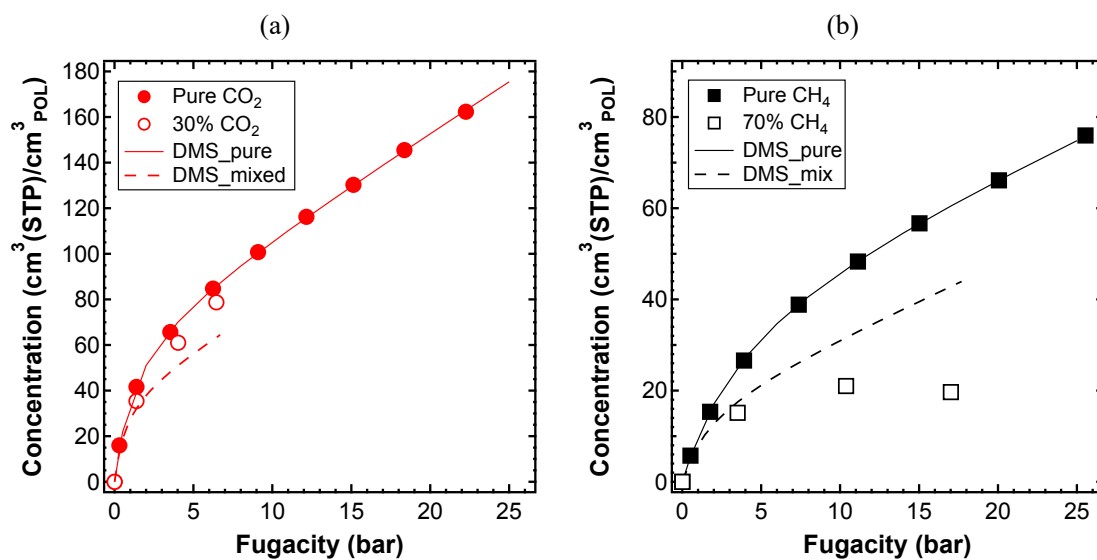
Figure 7.8*: Pure-gas sorption isotherms (filled symbols) and mixed-gas isotherms at 30 mol.% CO_2 (empty symbols) in PIM-EA-TB at 35 °C. (a) CO_2 and (b) CH_4.*

A comparison was carried out between the behavior of PIM-EA-TB and PIM-1, for which mixed-gas sorption data in the same conditions of temperature (35 °C) and composition (30 mol.% CO_2) were available.[27] As shown in **Figure 7.9**, the two materials exhibited a remarkably similar behavior, both for pure- and mixed-gas sorption.
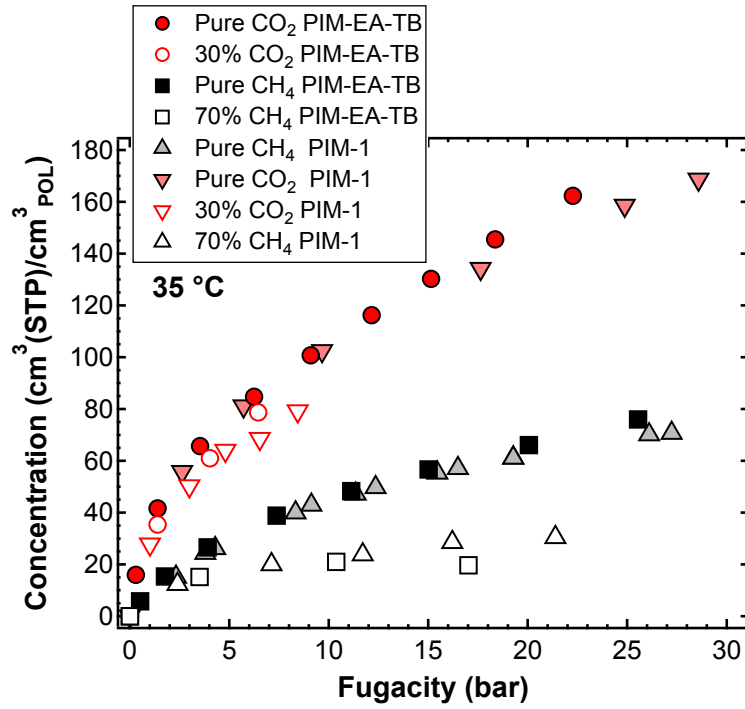
Figure 7.9*: Comparison of pure- and mixed-gas sorption (30 mol.% CO₂) isotherms of PIM-EA-TB (this work), and PIM-1 from Vopička et al.[27].*

7.3.1.1. Solubility-Selectivity

The multicomponent solubility-selectivity of the penetrant i over penetrant j, $\alpha_{i,j}^{S}$, was calculated solving

Eq. (7.2) with the mixed-gas sorption data showed above, and was compared with the ideal one obtained

from pure-gas sorption data.

$$\alpha_{i.j}^{S} = \frac{S_i}{S_j} = \frac{C_i/f_i}{C_j/f_j}$$

Eq. (7.2)

HAB-6FDA & TR450

Pure-gas solubility-selectivity was calculated from pure-gas sorption data reported in the literature[71]

and is reported in **Figure 7.10**. The DMS model predictions are featured in the graphs as well.

Multicomponent values were significantly different from the ideal ones. In particular, they were up to three times higher than the ideal ones, which means that competitive sorption had a positive impact on the separation performance, enhancing the selectivity. Moreover, the mixed-gas solubility-selectivity in these conditions was increasing as the total pressure increased, while the ideal values would indicate the opposite trend. These discrepancies between the multicomponent and ideal results for α^S emphasize the need to take multicomponent effects into account when designing the separation operation. The DMS model cannot predict the increase in solubility-selectivity, and it would also indicate the opposite dependence with pressure (decreasing trend). Instead, the NELF model indicated the same trend with pressure, but with a weaker dependence on the latter, thus the α^S was underestimated also by the non-equilibrium model.[76]
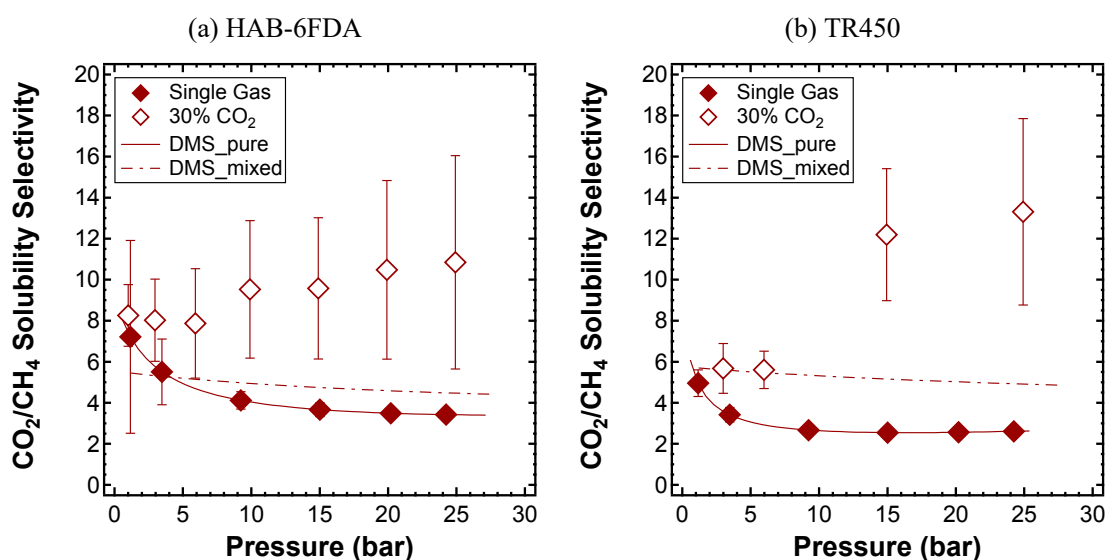
(a) HAB-6FDA   (b) TR450

Figure 7.10: Experimental solubility-selectivity for CO₂/CH₄ in (A) HAB-6FDA and (b) TR-450. Full diamonds are ideal values calculated with literature data from Stevens et al..[71] Void diamonds represent multicomponent values calculated from data measured in this work. Lines represent the DMS model results.

PIM-EA-TB

Both pure-gas and mixed-gas solubility-selectivity were calculated from experiments performed on the same sample by means of Eq. (7.2). **Figure 7.11** reports the trends obtained. $\alpha^S_{CO_2/CH_4}$ in

multicomponent conditions was higher than the ideal value calculated from pure-gas sorption data, and increases with the total equilibrium pressure, as it was for HAB-6FDA and TR450.
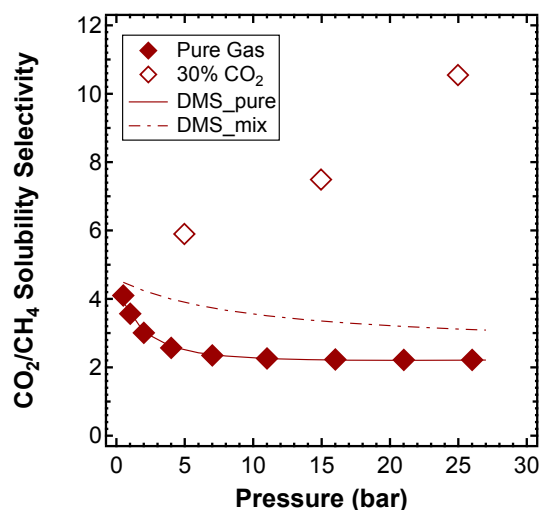
Figure 7.11: *Experimental solubility-selectivity for CO_2/CH_4 in PIM-EA-TB at 35 °C. Full diamonds are pure-gas values, while void diamonds refer to a 30 mol.% of CO_2 mixture.*

7.3.1.2. The Dominant Role of Solubility-Selectivity in Multicomponent Performance

Pure-gas measurements revealed that the main factor behind the higher permeability of the TR polymers compared to their polyimide precursor was an order of magnitude increase in gas diffusivity. This is consistent with the difference in fractional free volume between the materials analyzed, which increased after the thermal rearrangement process (**Table 7.1**). On the other hand, solubility increased only by approximately a factor two after the TR process, providing a modest contribution to the overall increase in permeability. The differences in gas solubility and diffusivity between HAB-6FDA and TR450 were proportionally higher for CH_4 than CO_2, therefore TR450 displayed lower permselectivity compared to HAB-6FDA.[69,70]

As mentioned above, Gleason *et al.*[25] measured pure CO_2 and CH_4 permeability and mixed-gas permeability of a 50% CO_2/CH_4 mixture in HAB-6FDA and TR450 at 35 °C. By applying the solution-diffusion model to the permselectivity reported in their work, and the and solubility-selectivity values

calculated with the NELF model by Ricci *et al.*[76], it was possible to evaluate both pure-gas and mixed-gas diffusivity-selectivity of the two materials. This approach was validated and reported by Ricci *et al.*[79] also for other materials and mixtures at different compositions.

Figure 7.12 shows the result of this decomposition for the case of pure-gas measurements. Ideal permselectivity as a function of gas fugacity can be read on the y-axis as the total height of the bars. Ideal solubility-selectivity and ideal diffusivity-selectivity are plotted for each bar of the histogram to highlight the contribution of each term to the overall permselectivity measured. It can be observed that the ideal diffusivity-selectivity was the highest factor for both materials, and it was approximately two to four times higher than the ideal solubility-selectivity in the pressure range inspected. Even though the absolute value of diffusivity-selectivity was slightly higher for HAB-6FDA especially at low pressures (*i.e.*, 8.4 to 13.1 for the polyimide against 7.7 to 8.6 for the TR), in proportion, the diffusivity-selectivity has a greater weight in the case of TR450 (**Figure 7.12c**). At higher pressures the trend observed was the opposite, since α^D for HAB-6FDA became more relevant than for TR450, as represented in **Figure 7.12c**. However, despite the fact that both types of selectivity decreased after the thermal rearrangement, the sieving effect was less compromised than the solubility-selectivity.
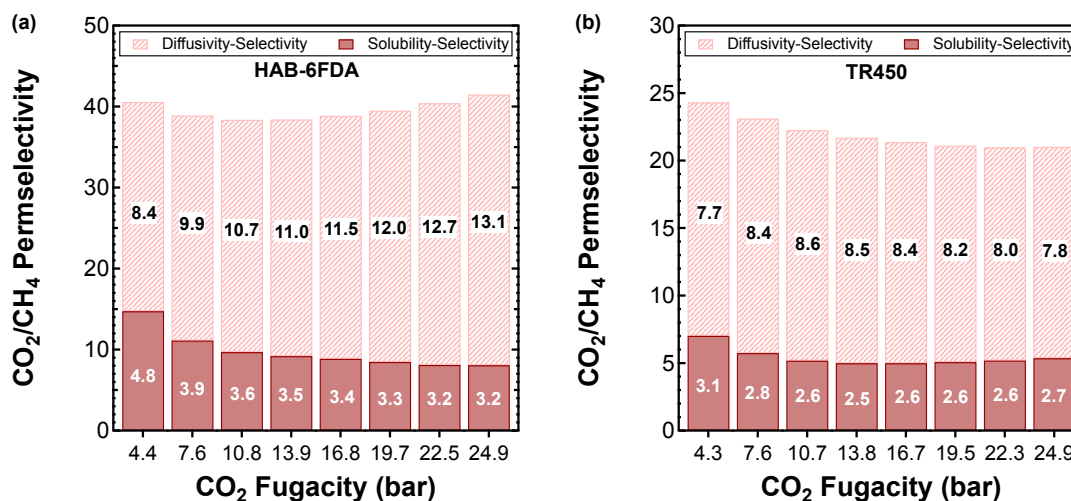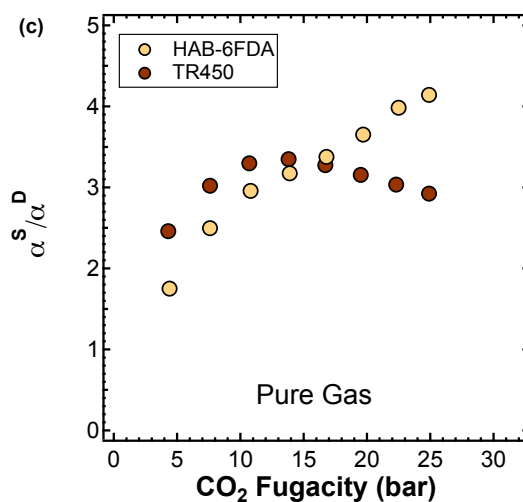
Figure 7.12: Ideal CO_2/CH_4 permselectivity[25] of (a) HAB-6FDA and (b) TR-450 split into its solubility-selectivity, as reported by Ricci et al.[76], and diffusivity-selectivity, obtained invoking the solution-diffusion model. (c) Solubility-selectivity over diffusivity-selectivity as a function of CO_2 fugacity for HAB-6FDA (yellow diamonds) and TR450 (brown circles). All data at 35 °C and 50:50 mixture of CO_2 and CH_4.

The effect of CO_2 acting as a swelling agent and its consequences in terms of mixed-gas selectivity loss has been explained in the theoretical background chapter.[21–24] However, this was not true for HAB-6FDA and TR450, which showed a slightly higher permselectivity in the mixed-gas test.[25] To analyze this interesting behavior, we performed the same deconvolution into solubility- and diffusivity-selectivity for the mixed-gas case and the results are shown in Figure 7.13a, and b. Unlike the pure-gas case, in multicomponent conditions the biggest contribution to the selectivity came from sorption. As highlighted in **Figure 7.13**, the increase in solubility-selectivity outweighed the decrease in diffusivity-selectivity, and was indeed responsible for the higher permselectivity in multicomponent conditions, confirming the hypothesis of Gleason *et al.*.[25] The loss in diffusivity-selectivity was higher for the TR-polymer (*i.e.*, from -61% at around 4 bar to -74% at about 22 bar), while the polyimide was capable of maintaining a greater sieving capability in the multicomponent case over the whole range of pressure (*i.e.*, from -36% at around 4 bar to -68% at about 22 bar). As indicated in **Figure 7.13c**, the higher the fugacity, the more important the contribution of solubility-selectivity over diffusivity-selectivity to the overall permselectivity, which however decreases monotonously with CO_2 fugacity[25] as shown by **Figure 7.13a** and **b**. TR450 shows much higher values of α^S/α^D with respect

to the precursor polyimide, which remarks that the thermally rearranged polymer can exploit the competitive effect occurring between CO_2 and CH_4 to a higher extent.
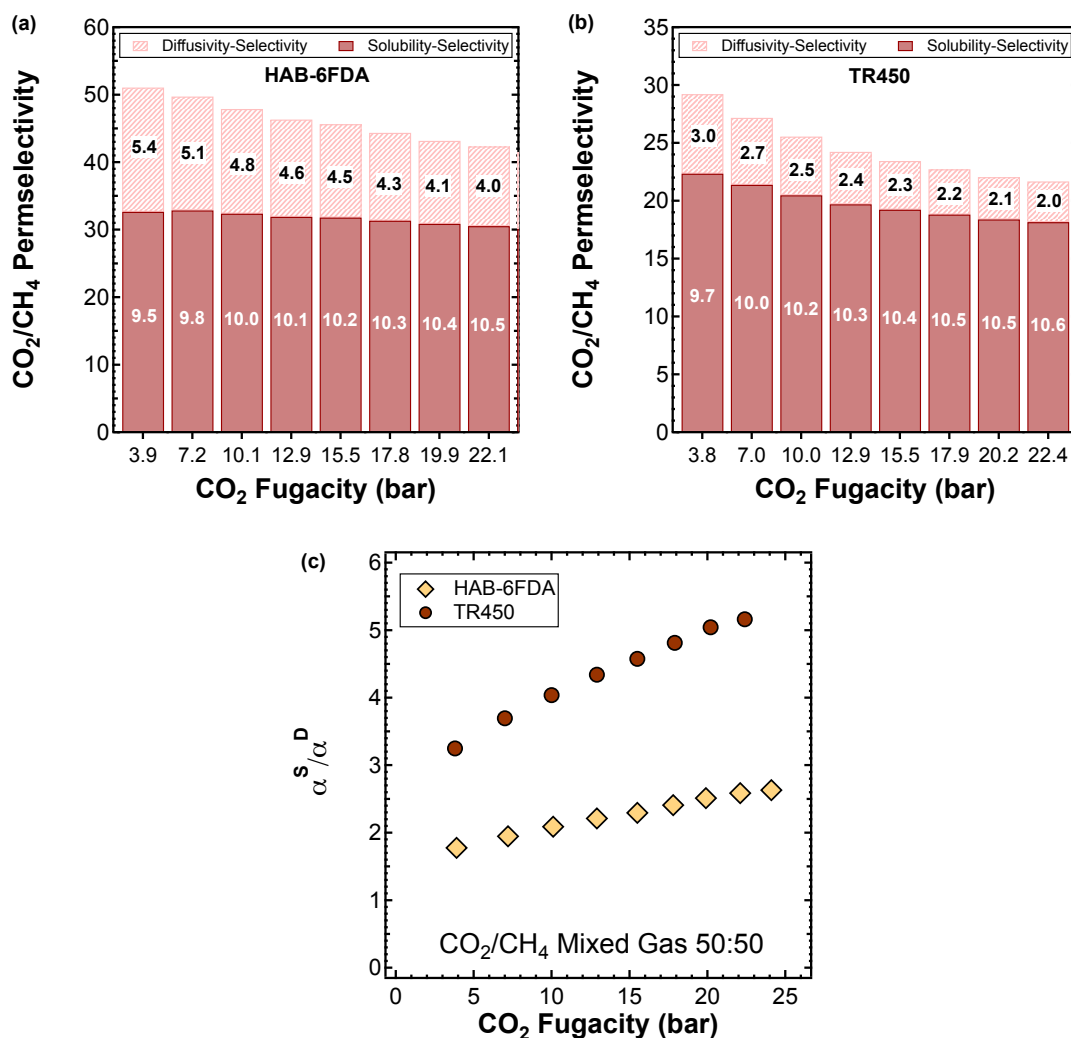
Figure 7.13: *Multicomponent CO_2/CH_4 permselectivity[25] of (a) HAB-6FDA and (b) TR-450 split into its solubility-selectivity, as reported by Ricci et al.[76], and diffusivity-selectivity, obtained invoking the solution-diffusion model. (c) Solubility-selectivity over diffusivity-selectivity as a function of CO_2 fugacity for HAB-6FDA (yellow diamonds) and TR450 (brown circles). All data at 35 °C and 50:50 mixture of CO_2 and CH_4.*

7.4. Overall Comparison

The following considerations come from an analysis performed by Ricci *et al.*[76] and here reported just for the polymers tested in the framework of this dissertation, plus Matrimid® from the literature[80]. **Figure 7.14** reports the diffusivity-selectivity as a function of solubility-selectivity, in the mixed-gas

case as well as in the pure-gas case. It can be observed that it is a common feature, among the different polymers studied, that from pure-gas experiments one would conclude that diffusivity-selectivity provides the most important contribution to the overall permselectivity, since it is larger than solubility-selectivity in all the polymers reported. However, plotting the same quantity evaluated in the case of mixed-gas sorption, therefore accounting for the competitive effect, which cannot be assessed in pure-gas experiments, the result is the opposite. In the multicomponent case solubility-selectivity outweighs the diffusivity contribution to selectivity, determining how remarkable it is to take into account this phenomenon while designing new materials for real industrial applications.
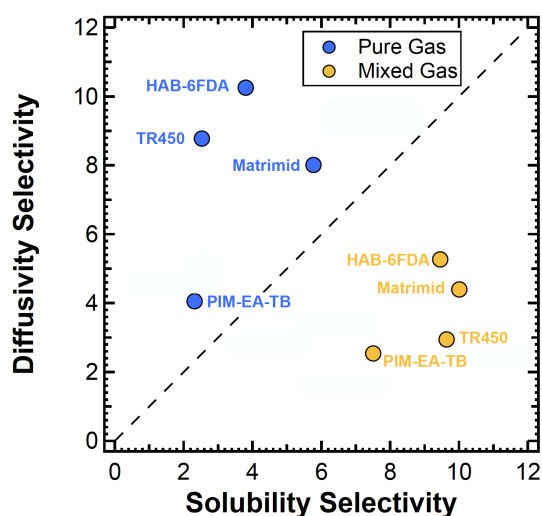
Figure 7.14: *Diffusivity-selectivity versus solubility-selectivity in pure- (blue) and mixed-gas (yellow) case for the polymers presented in this chapter, PIM-EA-TB, HAB-6FDA, and TR450, plus Matrimid® obtained from computational analysis from the literature.*[80]

In **Figure 7.15** it is can be assessed that diffusivity-selectivity is always higher in the ideal case then in the multicomponent case, while solubility-selectivity is always higher in the mixed-gas case. The overall contribution to permeability, however, cannot be determined *a priori*, because it depends on the depression or enhancement that $\alpha^{\mathcal{D}}$ and $\alpha^{\mathcal{S}}$ would respectively experience in mixed-gas experiments compared to their ideal values.
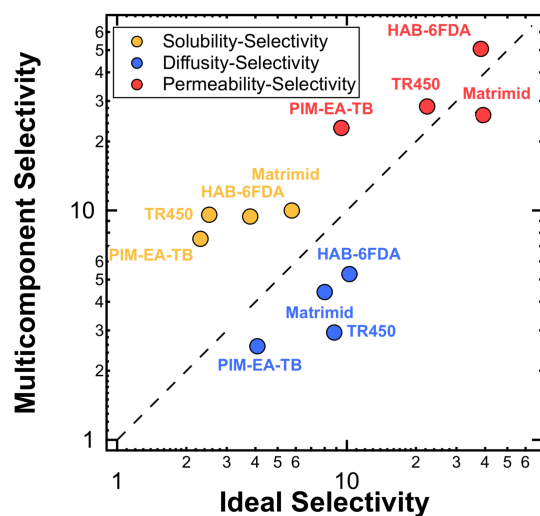
Figure 7.15*: Ideal selectivity versus multicomponent selectivity for solubility (yellow), diffusivity (blue), and permeability (red). Comparison among polymers presented in this chapter, PIM-EA-TB, HAB-6FDA, and TR450, plus Matrimid® obtained from computational analysis from the literature.*[80]

7.5. Conclusions for Mixed-Gas Sorption

In all the glassy polymers studied, CO_2/CH_4 mixed-gas sorption measurements revealed that the solubility in multicomponent conditions was always lower than the pure-gas one, for both species, due to competition between CO_2 and CH_4. Because CO_2 is more soluble than CH_4, its solubility is only weakly affected by the presence of methane in a wide range of mixture compositions, whereas the opposite happens to CH_4. In fact, methane solubility was significantly lowered by the presence of even a small fraction of CO_2, often leading to a substantial increase in the solubility-selectivity. This was consistent with what already observed for other glassy materials such as PIM-1 and PTMSP. The DMS model could describe qualitatively the reduction in the solubility of both gases in all the materials, but overestimated significantly the reduction of CO_2 sorption while underestimating that of CH_4. As a consequence, solubility-selectivity was also underestimated by the model in the mixed-gas case. Furthermore, the trend predicted was not increasing with pressure, while solubility-selectivity in the multicomponent case has always been found to increase monotonously with equilibrium pressure. By combining mixed-gas permeation data from the literature with in-house measured mixed-gas sorption data, it was possible to determine that, contrarily to the pure-gas case, solubility-selectivity controls the

overall permselectivity experienced in the mixed-gas case. The presence of a swelling agent, such as CO_2, had a compromising effect on the diffusivity-selectivity of the materials, but its ability to exclude the less condensable gas, such as CH_4, compensated this loss with an increase of solubility differences. For HAB-6FDA and TR450 this led to an increase of permselectivity from the ideal case to the multicomponent case. Further development of this analysis can lead to gather important information to design better-performing membranes whose separation performances are favored by the competitive effect occurring in real conditions.

References

[1]   I. Rose, C. G. Bezzu, M. Carta, B. Comesanã-Gándara, E. Lasseuguette, M. C. Ferrari, P. Bernardo, G. Clarizia, A. Fuoco, J. C. Jansen, K. E. Hart, T. P. Liyana-Arachchi, C. M. Colina, N. B. McKeown, *Nat. Mater.* **2017**, *16*, 932.

[2]   B. S. Ghanem, R. Swaidan, E. Litwiller, I. Pinnau, *Adv. Mater.* **2014**, *26*, 3688.

[3]   B. S. Ghanem, R. Swaidan, X. Ma, E. Litwiller, I. Pinnau, *Adv. Mater.* **2014**, *26*, 6696.

[4]   S. Luo, Q. Zhang, L. Zhu, H. Lin, B. A. Kazanowska, C. M. Doherty, A. J. Hill, P. Gao, R. Guo, *Chem. Mater.* **2018**, *30*, 5322.

[5]   Y. C. Teo, H. W. H. Lai, Y. Xia, *Chem. - A Eur. J.* **2017**, *23*, 14101.

[6]   W. J. Koros, C. Zhang, *Nat. Mater.* **2017**, *16*, 289.

[7]   C. Li, S. M. Meckler, Z. P. Smith, J. E. Bachman, L. Maserati, J. R. Long, B. A. Helms, *Adv. Mater.* **2018**, *30*, DOI 10.1002/adma.201704953.

[8]   S. Kim, Y. M. Lee, *Prog. Polym. Sci.* **2015**, *43*, 1.

[9]   W. Kim, S. Nair, *Chem. Eng. Sci.* **2013**, *104*, 908.

[10]   M. Carta, R. Malpass-Evans, M. Croad, Y. Rogan, J. C. Jansen, P. Bernardo, F. Bazzarelli, N. B. McKeown, *Science (80-.).* **2013**, *339*, 303.

[11]   H. Strathmann, P. Scheible, R. W. Baker, *J. Appl. Polym. Sci.* **1971**, *15*, 811.

[12]   M. D. Donohue, B. S. Minhas, S. Y. Lee, *J. Memb. Sci.* **1989**, *42*, 197.

[13]   A. J. Erb, D. R. Paul, *J. Memb. Sci.* **1981**, *8*, 11.

[14]   M. Galizia, W. S. Chi, Z. P. Smith, T. C. Merkel, R. W. Baker, B. D. Freeman, *Macromolecules* **2017**, *50*, 7809.

[15]   R. W. Baker, B. T. Low, *Macromolecules* **2014**, *47*, 6999.

[16] R. W. Baker, K. Lokhandwala, *Ind. Eng. Chem. Res.* **2008**, *47*, 2109.

[17] Q. Liu, M. Galizia, K. L. Gleason, C. A. Scholes, D. R. Paul, B. D. Freeman, *J. Memb. Sci.* **2016**, *514*, 282.

[18] L. Olivieri, R. Trichkov, D. Pizzi, L. Merlo, M. G. Baschetti, *J. Memb. Sci.* **2018**, *566*, 96.

[19] S. Thomas, I. Pinnau, N. Du, M. D. Guiver, *J. Memb. Sci.* **2009**, *333*, 125.

[20] R. Swaidan, B. S. Ghanem, E. Litwiller, I. Pinnau, *J. Memb. Sci.* **2014**, *457*, 95.

[21] A. Bos, I. G. M. Pünt, M. Wessling, H. Strathmann, *Sep. Purif. Technol.* **1998**, *14*, 27.

[22] B. J. Story, W. J. Koros, *J. Appl. Polym. Sci.* **1991**, *42*, 2613.

[23] T. A. Barbari, W. J. Koros, D. R. Paul, *J. Memb. Sci.* **1989**, *42*, 69.

[24] S. M. Jordan, W. J. Koros, G. K. Fleming, *J. Memb. Sci.* **1987**, *30*, 191.

[25] K. L. Gleason, Z. P. Smith, Q. Liu, D. R. Paul, B. D. Freeman, *J. Memb. Sci.* **2015**, *475*, 204.

[26] O. Vopička, M. G. De Angelis, G. C. Sarti, *J. Memb. Sci.* **2014**, *449*, 97.

[27] O. Vopička, M. G. De Angelis, N. Du, N. Li, M. D. Guiver, G. C. Sarti, *J. Memb. Sci.* **2014**, *459*, 264.

[28] A. E. Gemeda, M. G. De Angelis, N. Du, N. Li, M. D. Guiver, G. C. Sarti, *J. Memb. Sci.* **2017**, *524*, 746.

[29] N. Du, H. B. Park, G. P. Robertson, M. M. Dal-Cin, T. Visser, L. Scoles, M. D. Guiver, *Nat. Mater.* **2011**, *10*, 372.

[30] S. Basu, A. Cano-Odena, I. F. J. Vankelecom, *Sep. Purif. Technol.* **2011**, *81*, 31.

[31] R. Swaidan, B. S. Ghanem, E. Litwiller, I. Pinnau, *J. Memb. Sci.* **2014**, *457*, 95.

[32] J. D. Wind, D. R. Paul, W. J. Koros, *J. Memb. Sci.* **2004**, *228*, 227.

[33] A. Fernández-Barquín, C. Casado-Coterillo, M. Palomino, S. Valencia, A. Irabien, *Sep. Purif. Technol.* **2016**, *157*, 102.

[34] L. Garrido, C. García, M. López-González, B. Comesaña-Gándara, Á. E. Lozano, J. Guzmán, *Macromolecules* **2017**, *50*, 3590.

[35] S. C. Fraga, M. Monteleone, M. Lanč, E. Esposito, A. Fuoco, L. Giorno, K. Pilnáček, K. Friess, M. Carta, N. B. McKeown, P. Izák, Z. Petrusová, J. G. Crespo, C. Brazinha, J. C. Jansen, *J. Memb. Sci.* **2018**, *561*, 39.

[36] W. J. Koros, D. R. Paul, A. A. Rocha, *J. Polym. Sci.* **1976**, *14*, 687.

[37] W. R. Vieth, J. M. Howell, J. H. Hsieh, *J. Memb. Sci.* **1976**, *1*, 177.

[38] D. R. Paul, W. J. Koros, *J. Polym. Sci. Polym. Phys. Ed.* **1976**, *14*, 675.

[39] G. H. Fredrickson, E. Helfand, *Macromolecules* **1985**, *18*, 2201.

[40] W. J. Koros, *J. Polym. Sci. Polym. Phys. Ed.* **1980**, *18*, 981.

[41] W. J. Koros, E. S. Sanders, *J. Polym. Sci. Polym. Symp.* **1985**, 141.

[42] F. Doghieri, G. C. Sarti, *Macromolecules* **1996**, *29*, 7885.

[43] G. C. Sarti, F. Doghieri, *Chem. Eng. Sci.* **1998**, *53*, 3435.

[44] F. Doghieri, G. C. Sarti, *J. Memb. Sci.* **1998**, *147*, 73.

[45] F. Doghieri, M. Quinzi, D. G. Rethwisch, G. C. Sarti, **2004**, pp. 74–90.

[46] M. G. De Angelis, G. C. Sarti, *Annu. Rev. Chem. Biomol. Eng.* **2011**, *2*, 97.

[47] F. Doghieri, M. Minelli, C. J. Durning, S. Kumar, *Fluid Phase Equilib.* **2016**, *417*, 144.

[48] M. Minelli, G. Cocchi, L. Ansaloni, M. G. Baschetti, M. G. De Angelis, F. Doghieri, *Ind. Eng. Chem. Res.* **2013**, *52*, 8936.

[49] F. Doghieri, M. G. De Angelis, M. G. Baschetti, G. C. Sarti, *Fluid Phase Equilib.* **2006**, *241*, 300.

[50] M. G. De Angelis, G. C. Sarti, F. Doghieri, *J. Memb. Sci.* **2007**, *289*, 106.

[51] M. Minelli, M. G. De Angelis, *Fluid Phase Equilib.* **2014**, *367*, 173.

[52] D. F. Sanders, Z. P. Smith, R. Guo, L. M. Robeson, J. E. Mcgrath, D. R. Paul, B. D. Freeman, **2013**, *54*, 4729.

[53] H. B. Park, C. H. Jung, Y. M. Lee, A. J. Hill, S. J. Pas, S. T. Mudie, E. Van Wagner, B. D. Freeman, D. J. Cookson, *Science (80-.).* **2007**, *318*, 254.

[54] H. B. Park, S. H. Han, C. H. Jung, Y. M. Lee, A. J. Hill, *J. Memb. Sci.* **2010**, *359*, 11.

[55] S. H. Han, H. J. Kwon, K. Y. Kim, J. G. Seong, C. H. Park, S. Kim, C. M. Doherty, A. W. Thornton, A. J. Hill, Á. E. Lozano, K. A. Berchtold, Y. M. Lee, *Phys. Chem. Chem. Phys.* **2012**, *14*, 4365.

[56] C. Aguilar-Lugo, C. Álvarez, Y. M. Lee, J. G. de la Campa, Á. E. Lozano, *Macromolecules* **2018**, *51*, 1605.

[57] C. A. Scholes, B. D. Freeman, *J. Memb. Sci.* **2018**, *563*, 676.

[58] S. Luo, Q. Zhang, T. K. Bear, T. E. Curtis, R. K. Roeder, C. M. Doherty, A. J. Hill, R. Guo, *J. Memb. Sci.* **2018**, *551*, 305.

[59] S. M. Meckler, J. E. Bachman, B. P. Robertson, C. Zhu, J. R. Long, B. A. Helms, *Angew. Chemie Int. Ed.* **2018**, *57*, 4912.

[60] Q. Liu, D. R. Paul, B. D. Freeman, *Polym. (United Kingdom)* **2016**, *82*, 378.

[61] S. Li, H. J. Jo, S. H. Han, C. H. Park, S. Kim, P. M. Budd, Y. M. Lee, *J. Memb. Sci.* **2013**, *434*, 137.

[62] L. M. Robeson, *J. Memb. Sci.* **1991**, *62*, 165.

[63] L. M. Robeson, *J. Memb. Sci.* **2008**, *320*, 390.

[64] M. Calle, A. E. Lozano, Y. M. Lee, *Eur. Polym. J.* **2012**, *48*, 1313.

[65] L. M. Robeson, M. E. Dose, B. D. Freeman, D. R. Paul, *J. Memb. Sci.* **2017**, *525*, 18.

[66] A. Brunetti, M. Cersosimo, J. S. Kim, G. Dong, E. Fontananova, Y. M. Lee, E. Drioli, G. Barbieri, *Int. J. Greenh. Gas Control* **2017**, *61*, 16.

[67] C. A. Scholes, B. D. Freeman, S. E. Kentish, *J. Memb. Sci.* **2014**, *470*, 132.

[68] Z. P. Smith, G. Hernández, K. L. Gleason, A. Anand, C. M. Doherty, K. Konstas, C. Alvarez, A. J. Hill, A. E. Lozano, D. R. Paul, B. D. Freeman, *J. Memb. Sci.* **2015**, *493*,

766.

[69]   D. F. Sanders, Z. P. Smith, C. P. Ribeiro, R. Guo, J. E. McGrath, D. R. Paul, B. D. Freeman, *J. Memb. Sci.* **2012**, *409–410*, 232.

[70]   Z. P. Smith, D. F. Sanders, C. P. Ribeiro, R. Guo, B. D. Freeman, D. R. Paul, J. E. McGrath, S. Swinnea, *J. Memb. Sci.* **2012**, *415–416*, 558.

[71]   K. A. Stevens, Z. P. Smith, K. L. Gleason, M. Galizia, D. R. Paul, B. D. Freeman, *J. Memb. Sci.* **2017**, *533*, 75.

[72]   Z.-X. Low, P. M. Budd, N. B. McKeown, D. A. Patterson, *Chem. Rev.* **2018**, *118*, 5871.

[73]   E. Tocci, L. De Lorenzo, P. Bernardo, G. Clarizia, F. Bazzarelli, N. B. McKeown, M. Carta, R. Malpass-Evans, K. Friess, K. Pilnáček, M. Lanč, Y. P. Yampolskii, L. Strarannikova, V. Shantarovich, M. Mauri, J. C. Jansen, *Macromolecules* **2014**, *47*, 7900.

[74]   P. R. Bevington, D. K. Robinson, *Error Data Reduction and Error Analysis for the Physical Sciences*, **1992**.

[75]   D.-Y. Peng, D. B. Robinson, *Ind. Eng. Chem. Fundam.* **1976**, *15*, 59.

[76]   E. Ricci, F. M. Benedetti, M. E. Dose, M. G. De Angelis, B. D. Freeman, D. R. Paul, *To be Submitt.* **n.d.**

[77]   E. Ricci, M. De Angelis, *Membranes (Basel).* **2019**, *9*, 8.

[78]   F. M. Benedetti, E. Ricci, M. Carta, M. G. De Angelis, N. B. McKeown, *To be Submitt.* **n.d.**

[79]   E. Ricci, A. E. Gemeda, N. Du, N. Li, M. G. De Angelis, M. D. Guiver, G. C. Sarti, *J. Memb. Sci.* **2019**.

[80]   E. Ricci, M. Minelli, M. G. De Angelis, *J. Memb. Sci.* **2017**, *539*, 88.

8. Fundamental Study of the Plasticization Phenomena in Glassy Matrimid®

8.1. Introduction and Motivations

In glassy polymeric membranes, gas permeability shows different trends as upstream pressure increases, including a monotonous decline, a monotonous increase, as well as an initial reduction followed by a subsequent increase after a minimum permeability value is reached.[1] The minimum value, whenever present, occurs at a pressure conventionally indicated as the plasticization pressure.[2] Qualitatively, this phenomenon is related to large amounts of low molecular weight penetrants (*e.g.*, vapors, liquids, gases) absorbed in the polymer matrix.[2,3] Among gases, CO_2 is considerably more soluble then He, H_2, N_2 and CH_4, and plasticization becomes very relevant when operating with high pressure feed streams (*e.g.* in the case of natural gas upgrade or CO_2-enhanced oil recovery).[3,4] Plasticization of glassy membranes is typically recognized through an increase in gas permeability as the upstream pressure increases[1,3] and associated to an enhancement of polymer chain mobility with consequent increase in penetrant diffusivity, starting from a certain relatively high upstream pressure below which such effects do not occur.[1,5–7] The increased mobility affects the transport properties of the plasticizing agent as well as that of the other gases possibly present in the feed, leading to appreciable reductions of the membrane mixed-gas selectivity.[8–11] Plasticization of glassy membranes also involves important volume dilation of the polymer matrix, reduced mechanical rigidity and depression of the glass transition temperature.[3,12,13]

A quantitative description of gas permeability and, possibly, the prediction of its dependence on operating pressure is thus relevant for a better understanding of the phenomenon and for the selection of the most suitable operating conditions for gas separation applications. It is currently accepted that permeability behavior can be conveniently well described by a transport model only below plasticization

233

pressure, while, above that value, the presumed onset of additional phenomena at higher pressures is responsible of the observed increase in permeability and decrease in selectivity. With this contribution, we seek to demonstrate plasticization is not a state of the system, and it is not associated to the occurrence of any additional peculiar phenomenon, and consequently the gas transport behavior can be fully described in the solution-diffusion model framework.

8.1.1. Plasticization in the Solution-Diffusion Model Framework

As introduced in the theoretical background, chapter 4.1, the solution-diffusion is currently recognized as the most widely accepted framework to describe gas transport in dense polymeric membranes.[14,15] The penetrant molecules first dissolve into the polymer matrix at the high concentration (*i.e.*, high chemical potential face) of the membrane, then they diffuse through the film down a gradient of chemical potential and finally desorb at the downstream side of the polymeric film (*i.e.*, the face at low penetrant concentration and lower chemical potential). In this framework, the relation $\mathcal{P} = \mathcal{D} \cdot \mathcal{S}$ holds, in which $\mathcal{P}$ is the permeability, $\mathcal{D}$ is the average diffusion coefficient and $\mathcal{S}$ is the average solubility coefficient. It was important to recall the equation again to visualize that permeability is given by the contribution of diffusivity and solubility. For a glassy polymer, diffusivity and solubility coefficient show opposite dependence with respect to upstream pressure, as $\mathcal{D}$ often increases at increasing gas concentration in the polymer, while $\mathcal{S}$ is a decreasing function of penetrant pressure for glassy systems (**Figure 8.1**). Therefore, their combination does not exclude any possible trend of the resulting permeability (**Figure 8.2**).
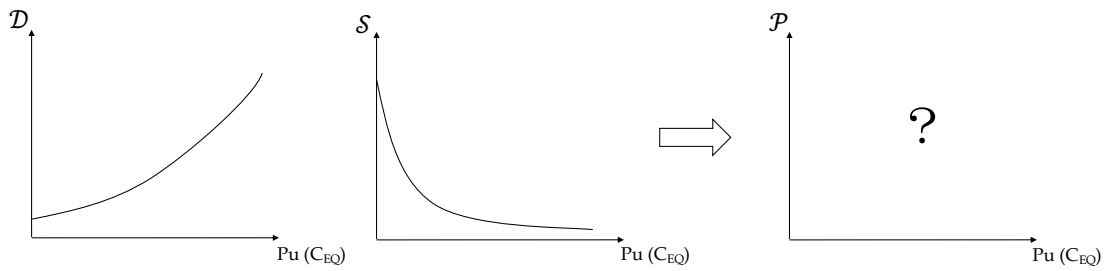
Figure 8.1:*Typical qualitative trend of diffusivity and solubility coefficient in glassy polymers, and impossibility to determine a priori the trend of permeability in the framework of the solution-diffusion model. p_u is the upstream pressure, while C_{EQ} the concentration at equilibrium.*
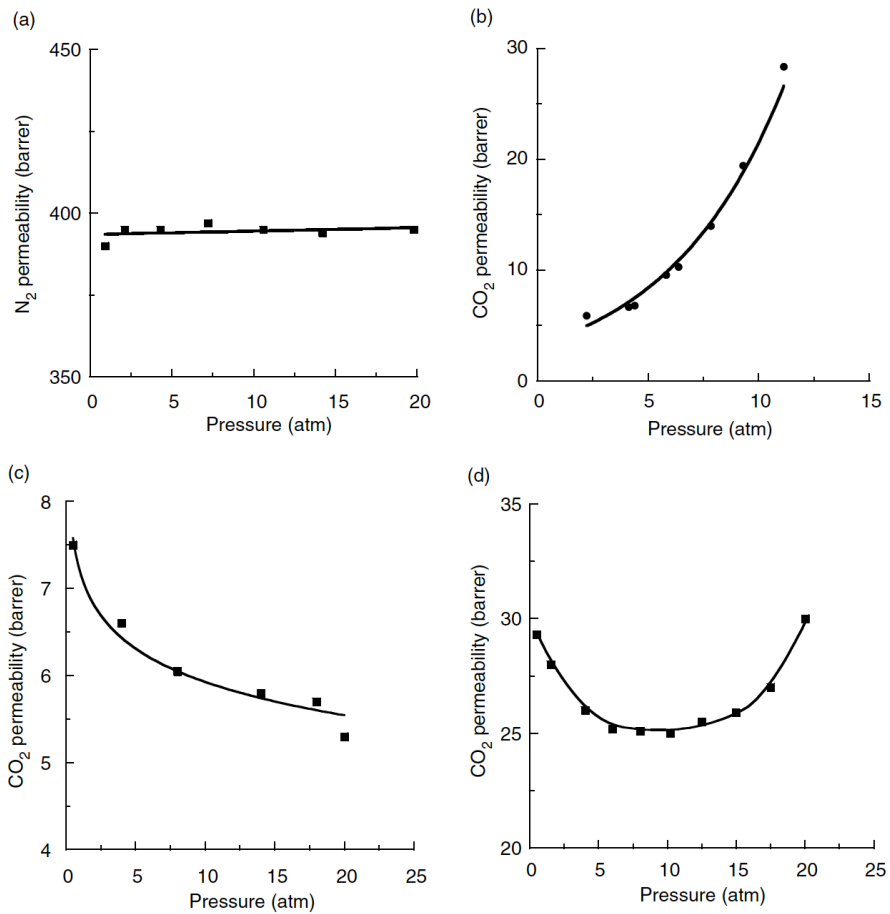
Figure 8.2: *Possible trends for permeability as a function of upstream pressure. (a) light gasses with low solubility in rubbery polymers, (b) condensable gases and vapors in rubbery polymers, (c) low molecular weight gases in glassy polymers, and (d) condensable gases or vapors in glassy polymers. Figure from reference* [1].

Penetrant solubility in glassy polymers is often described by the Dual Mode Sorption model.[6,16,17] Both DMS model equations to calculate the concentration and the solubility coefficient in the explicit forms were defined in section 4.3.2. According to Koros and Paul[6], an expression for permeability can be derived in the framework of the dual mode description of solubility and transport in glassy polymers. The assumptions were that only the gas sorbed by Henry's mode is free to diffuse, while that sorbed by Langmuir's contribution is completely or partially immobilized. In view of this, a value of $\mathcal{D}_D$ of the diffusion coefficient was attributed to the gas population sorbing in Henry's mode, while a value of $\mathcal{D}_H$ to the Langmuir population. In this framework, $\mathcal{F} = \mathcal{D}_H/\mathcal{D}_D$ was equal to zero when the gas was totally immobilized, and equal to one when there was no immobilization. The expression for the permeability obtained under these hypothesis is the following:

$$P = k_D \mathcal{D}_D + \frac{C_H' b \mathcal{F} \mathcal{D}_D}{1 + bp} \qquad \text{Eq. (8.1)}$$

where k_D is the Henry coefficient, C_H' is the Langmuir capacity, b is the affinity constant, and p is pressure. By defining a quantity that contains all the DMS model parameters, $\mathcal{K} = C_H' b/k_D$, Eq. (8.1) can be rewritten as follows[6]:

$$P = k_D \mathcal{D}_D \left(1 + \frac{\mathcal{F}\mathcal{K}}{1 + bp_u} \right) \qquad \text{Eq. (8.2)}$$

Nevertheless, the resulting transport equation is able to describe only decreasing permeability behaviors with penetrant pressure, and non-monotonous trends are clearly out of reach. In the past few decades considerate was customary to attribute an increase in permeability with increasing pressure to a different phenomenon, that was not accounted for in the dual sorption-partial immobilization theory: the plasticization phenomenon. Such interpretation led to define the so-called *plasticization pressure* as the pressure at which the minimum value of permeability was measured in a curve like the one represented in **Figure 8.2d**. Bos *et al.*[2] studied CO_2-induced plasticization in a series of glassy polymers and discovered that plasticization pressures vary from one polymer to another, but that all materials show this minimum at a critical concentration of $38 \pm 7 \text{ cm}^3(\text{STP})/\text{cm}^3_{\text{pol}}$ (**Table 8.1**). Further, in

correspondence to this concentration value, the local diffusion coefficient showed a significant increase with increasing concentration once overcame that threshold.

Table 8.1:Plasticization pressure (p_{pl}) and concentration at plasticization pressure (C) measured for some of the most diffused commercial polymers. Table from reference [2].

	Polymer name	p_{pl} (bar)	$P(p_{pl})$ (Barrer)	$P(p=0)$ (Barrer)	C at $p=pl$ (cm^3(STP)/cm^3)	Experimental temperature (°C)
1	PSF	34	3.6	5.0	47	23
2	PES	27	2.6	3.7	43	21
3	PEI	28	0.84	1.1	37	21
4	BPA–PC	31	4.7	7.5	33	25
5	BPZ–PC	24	1.0	1.4	32	23
6	TMBPA–PC	13	13	16	36	25
7	PPO	14	82	99	34	25
8	Matrimid	12	4.8	5.7	47	22
9	P84	22	0.92	1.1	48	23
10	CA	11	6.0	6.7	31	27
11	CTA	10	7.3	9	31	24

The idea that all polymers need the same amount of CO_2 to induce plasticization was based on the physical picture that glassy polymers experience similar internal swelling stress when they have similar characteristics.[18] However, there are cases such as 6FDA-6FpDA[19] in which plasticization pressure was reached at a concentration of 60 cm^3(STP)/cm$^3_{pol}$. More recently, CO_2-induced plasticization pressure of a 119 μm thick film of PIM-1 was found to be at ~27.5 bar[20], which corresponds to a concentration of 135 ± 15 cm^3(STP)/cm$^3_{pol}$, depending on the source from which sorption isotherms are retrieved.[21–23] Thickness also plays a role, and if a 30 μm thick film of PIM-1 is considered, plasticization pressure drops at ~8 bar.[24] The fact that plasticization pressure depends on the thickness of the membrane is supported also by Horn and Paul that intensively studied the phenomenon.[25,26] This undermines the idea that plasticization represents an intrinsic property of a material or a state of the system.

All this information suggests that the phenomenology of plasticization is not fully clear, and there is a need for a physical and mathematical description, in particular for mixed-gases applications. A quantitative description of gas permeability has been provided by Minelli & Sarti[27] using the Non-Equilibrium Lattice Fluid (NELF) model[28], but the prediction of its dependence on operating pressure is a relevant development that needs to be addressed for a better understanding of the plasticization phenomenon and for the selection of suitable operating conditions.

8.2. Material: Matrimid® Polyimide

A commercial polyimide, Matrimid® 5218 (3,3'-4,4'-benzophenone tetracarboxylic dianhydide (BTDA) and diaminophenylindane (DAPI)), was chosen to investigate the plasticization phenomenon. The material was supplied by *Huntsman Advanced Materials* in powder form and used as received. Matrimid®, **Figure 8.3**, is a thermoplastic soluble glassy polymer which exhibits excellent mechanical properties, can be used at high temperature and is suitable for CO_2/CH_4 separation, showing an ideal selectivity towards CO_2 greater than 40 at 35°C.[29–31] Some of the relevant physical properties of this material, such as density (ρ), glass transition temperature (T_g) and Fractional Free Volume (FFV), are presented in **Table 8.2**. Several studies have shown that Matrimid® undergoes significant CO_2-induced plasticization[2,25,26,32], and many authors investigated how to reduce the impact of this phenomenon.[8,33]
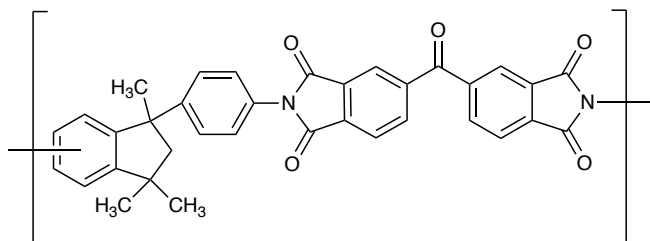
Figure 8.3: Chemical structure of Matrimid® polyimide.

Table 8.2: Matrimid® 5218 bulk physical properties.

ρ (27 °C)[30]	T_g[34]	FFV(%)[30]	Polydispersity index[35]	Refractive index[25]	Average Molecular Weight[34]
g/cm³	°C	/	/	/	g/mol
1.238	320	14.4	4.5	1.648	80,000

A solvent casting technique was used to obtain self-standing Matrimid® films with controlled thickness of about 45 μm. A similar methodology to the one developed by Ansaloni *et al.*[30] was applied. Membranes were casted starting from a 2 wt.% solution of the polyimide in dichloromethane (DCM)

provided by *Sigma Aldrich* (purity $\geq$ 99.8%). To obtain a controlled thickness, a known quantity of solution was poured in a Petri dish with a diameter of 10 cm, to avoid any edge effect on the center of the membrane. The dish was covered to induce a slow solvent evaporation, necessaire to obtain a homogeneous and defect-free film and placed in the fume hood at room temperature for 48 hours. The sample was then detached from the Petri and treated under vacuum overnight at 200 °C to make residual solvent evaporate. The temperature was chosen accordingly to the physical aging results obtained by Ansaloni *et al.*[30] after treating membranes at different temperatures. The increase of the temperature at which the thermal treatment was performed, led to a densification (*i.e.*, a reduction of the FFV). With a temperature of 200 °C, it was shown that the permeability of Matrimid® was stable over time, for at least six months, after the treatment. Since the time required to build a plasticization curve is of the order of a few days, it is important to operate in such a way that is possible to assume that permeability variations of Matrimid® films cannot be attributed to aging effects.

8.3. Experimental Setup

Permeability was evaluated at 35 °C at different downstream pressures, p_d: 0, 2, 5 and 10 bar, by varying the upstream pressure, p_u, up to 25 bar. For each p_d a brand new Matrimid® film has been used. After reaching the maximum p_u (*i.e.*, 25 bar), without changing the sample, the film permeability was also measured decreasing p_u up to a minimum Δp ($\Delta p = p_u - p_d$) of 2 bar, to evaluate the hysteresis effect on the transport properties, going down the same path in the opposite direction. For each combination of p_d and p_u, the experiment was repeated twice. The so-called *plasticization pressure*, p_{pl}, was then evaluated as a function of p_d while increasing p_u.

To perform the experiments, the manometric technique previously described in the experimental methods session, was slightly modified to allow each membrane to equilibrate at p_d before each permeability measurement. The layout of the equipment is shown in **Figure 8.4**. The thick red lines were always kept at high pressure (up to 25 bar), while the dashed red lines were always kept at the

downstream pressure (*i.e.*, 0, 2, 5 or 10 bar), to exclude any leak from V06 to be responsible of anomalous behaviors.
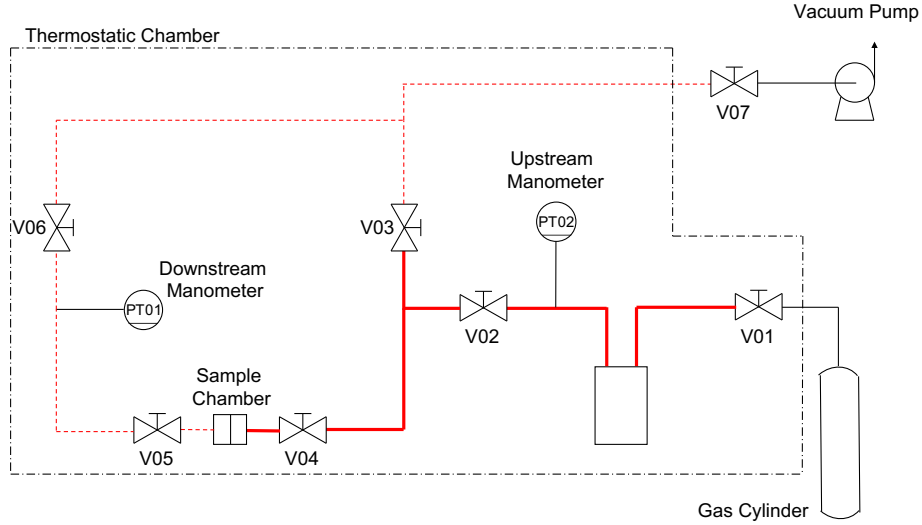
Figure 8.4: Layout of a permeation equipment. The outer black dashed line indicates the volume in which temperature is controlled. The inner red dashed line indicates the branches of the apparatus in which $p=p_d$ and the thick red solid line indicates the volume in which $p=p_u$.

To work with high-pressure in the downstream side, it was necessary to use a transducer with higher full-scale. The increase of the downstream pressure in the calibrated closed volume, V_d, between the sample holder and V06 is monitored by a capacitance manometer (PT01 - *Edwards Barocel®*) with a sensitivity of 1 Torr and an accuracy of 0.15% of the reading. Permeability was evaluated at the steady by introducing the compressibility factor, $Z(p_d)$, in the equation already derived in the experimental section:

$$\mathcal{P} = \frac{1}{Z(p_d)} \frac{V_d}{RT} \frac{l}{A} \frac{1}{(p_u - \bar{p}_d)} \left(\frac{dp_d}{dt}\right)_{t \to \infty} \qquad \text{Eq. (8.3)}$$

in which R is the gas constant, T is the operative temperature, l is the membrane thickness and $\bar{p}_{CO_2,d}$ is the average downstream pressure of CO_2. The compressibility factor, $Z(p_d)$, was introduced to take into account the fact that p_d in some experiments was higher that the vacuum (*i.e.*, 2, 5, and 10 bar), and the

non-ideal behavior of CO_2 must be evaluated (**Figure 8.5**). The Peng-Robinson equation of state was used for this purpose.[36]
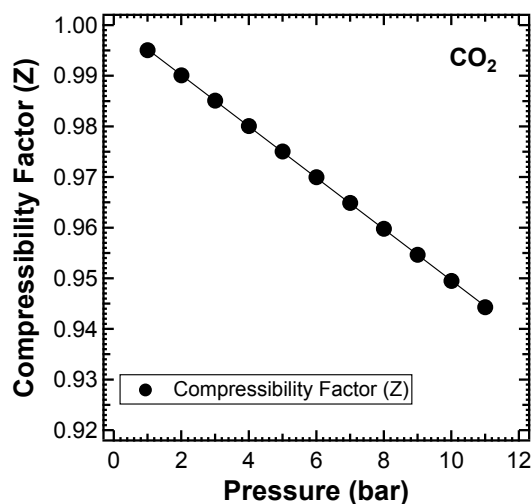
Figure 8.5: Evaluation of the compressibility factor with the Peng Robinson EoS for CO_2.

8.4. Transport Properties

The following section describes the results obtained investigating the CO_2-induced plasticization in Matrimid® polyimide. Permeability and solubility experiments were performed, and diffusivity was calculated by means of three different techniques: sorption kinetics, time-lag, and as permeability divided by solubility in the framework of the solution-diffusion model.

8.4.1. Permeability: Plasticization Curves

The first plasticization curve measured was the one in which the downstream pressure was kept at full vacuum while the upstream pressure was increasing step by step and shown in **Figure 8.6**. This is the setup usually adopted in the literature, in fact various authors performed similar experiments in their works.[2,25,26] The expected trend was obtained, indeed pressure initially decreased, reached a minimum, and eventually increased again while p_u was gradually increased up to 25 bar. The minimum, the plasticization pressure (p_{pl}), was reached when p_u was equal to 11.60 bar, in good agreement with the

results already reported in the literature for films of comparable thickness (*i.e.*, 12 bar[2], and 16 atm[25]). Other important information to compare different studies are reported in **Table 8.3**. The differences may be due to the fact that plasticization is a time-dependent measurement. The longer the time the film is in contact with CO_2, the more severe is the induced relaxation of the matrix. The time Horn *et al.*[25] spent on each intermediate step for a 20 μm thick film was 10 minutes. In our case the film was thicker, 44 μm, and the duration of each step was between 2 and 3 hours, depending on the upstream pressure (the lower, the longer the experiment). This was necessary to ensure that the pseudo-steady state was reached, since the time-lag was found to be about 5 to 20 minutes, depending on the upstream pressure (the higher the pressure the shorter the time-lag). The thickness itself can play a role, but an increase of p_{pl} is generally expected when the thickness increases.[26]
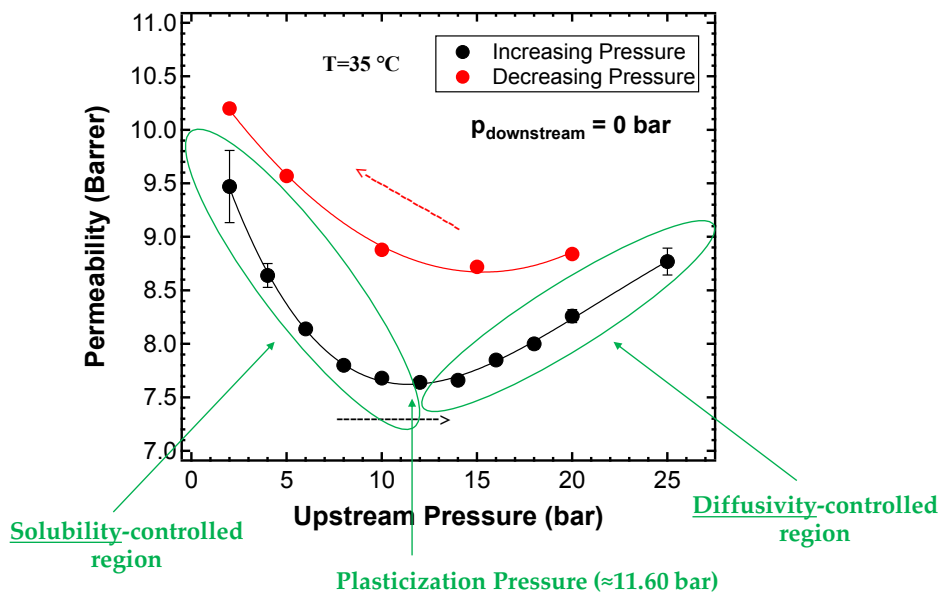
Figure 8.6: *CO_2 plasticization curve and hysteresis at p_d = 0 bar. Data collected increasing the upstream pressure (black dots), data collected decreasing upstream pressure (red dots).*

Table 8.3: *Comparison of relevant quantities determined performing CO_2-induced plasticization curve experiments in Matrimid® films: plasticization pressure (p_{pl}), CO_2 permeability at plasticization pressure, initial permeability of the film before exposing to higher CO_2 pressure, CO_2 concentration in the film at p_{pl}.*

	p_{pl} (bar)	$\mathcal{P}(p_{pl})$ (Barrer)	$\mathcal{P}(p = 2\ bar)$ (Barrer)	$C_{CO2}(p = p_{pl})$ ($cm^3(STP)/cm^3_{pol}$)	T (°C)	
	11.6	7.6	9.5	46.3	35	This Work
Matrimid®	12.0	4.8	5.7	47.0	22	[8]
	16.0	4.9	8.3	/	35	[25]

As represented in **Figure 8.6**, and based on the sketch provided in **Figure 8.1**, the plasticization phenomena can be qualitatively described in the framework of the solution-diffusion model. The initial part of the curve, low CO_2 pressure, followed the same trend that the solubility coefficient follows in glassy polymers. The increase in CO_2 concentration in the polymer matrix starts inducing relaxation[5] of the polymer chain, leading to a consequent increase of the diffusion coefficient (consistent with **Figure 8.1**). In the case of polymers such as Matrimid®, PPO, CA, that cannot prevent this dilation to happen, the result is that the increase of diffusion coefficient outweighs the decrease of solubility coefficient, and the overall permeability increases at increasing upstream pressure. The point in which the minimum permeability is recorded depends on the behavior of each of the two contributions and can be evaluated, for instance, with the NELF model.[27]

The conditioning induced by exposing the film to 25 bar of CO_2 pressure was quantified by measuring the hysteresis curve of permeability while decreasing p_u back to the minimum Δp investigated, *i.e.*, 2 bar (red dots in **Figure 8.6**). As expected, permeability was higher than that measured while the pressure was increasing (black dots in **Figure 8.6**).

Analogous experiments were performed at different downstream pressure: 2, 5, and 10 bar, as it can be observed in **Figure 8.7**. The fresh polymer featuring the same thickness ± 1 μm was first equilibrated at the desired p_d until no pressure change could be observed in the system. Permeation tests were run in the same way as for the previous case, but between one intermediate point and another, the vacuum was not pulled to allow for desorption, and pressure was equilibrated again at p_d instead. Similar trends were observed, in fact all the plasticization curves represented by black filled circles revealed a minimum

value of permeability at a certain pressure. Permeability hysteresis showed a similar behavior among all cases as well.
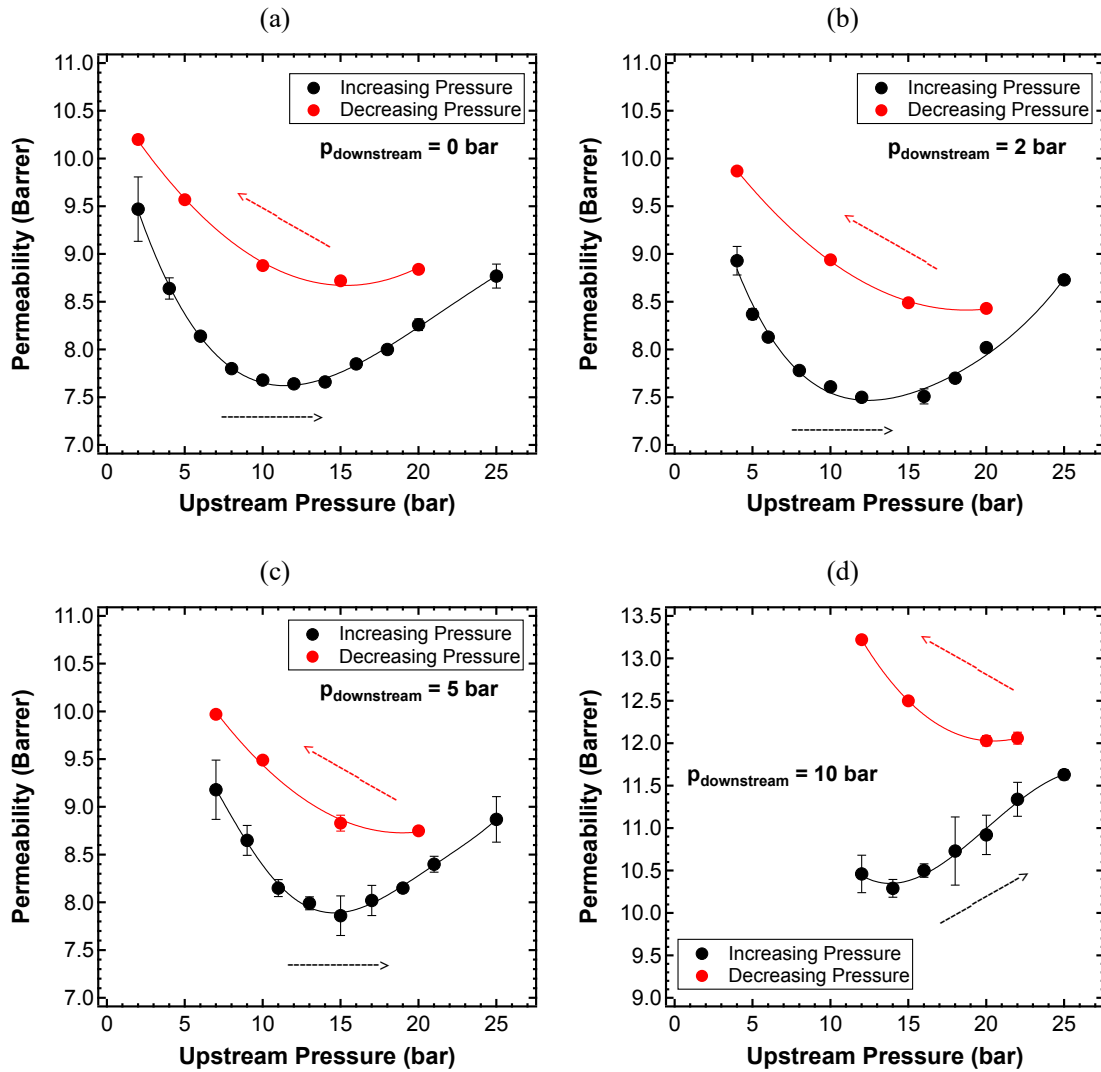
Figure 8.7: CO$_2$ plasticization curve and hysteresis different cases: (a) $p_d = 0$ bar, (b) $p_d = 2$ bar, (c) $p_d = 5$ bar, and (d) $p_d = 10$ bar.

What was very interesting to quantify was how p_{pl} evolved with p_d, namely at different boundary conditions. The results are represented in **Figure 8.8**, where the increase of plasticization pressure with the downstream pressure is shown. This remarkable finding provided important information about the plasticization phenomenon, confirming the intuition that the minimum does not indicate a state of the system, and that there is no onset of new phenomena which take place at the minimum. These samples

all underwent the same treatment and featured about the same thickness, so all differences are just related to the way solubility and diffusivity combine to generate the plasticization curves obtained.
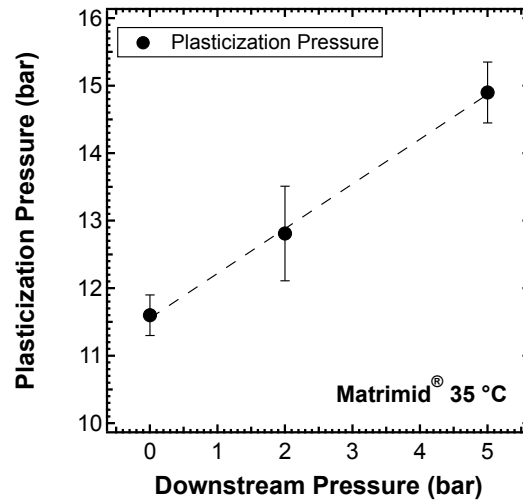
Figure 8.8: Plasticization pressure as a function of the downstream pressure at which permeation experiments were performed.

Figure 8.9 compares two curves obtained performing the same plasticization experiment with downstream pressure equal to 2 bar. The difference was in the rate at which CO_2 upstream pressure was increased. By normalizing permeability on the first value obtained at 4 bar upstream (*i.e.*, $\Delta p = 2$ bar), the two curves obtained at increasing pressure lay very close to one another, providing a similar result in terms of plasticization pressure. This may be related to the characteristic relaxation time of Matrimid[®] chains, which may be higher than the duration of each experiment, both in the setup adopted for the results reported in **Figure 8.7** and in the faster version. In fact, anticipating results from the evaluation of diffusivity, sorption kinetics revealed that deviation from the Fickian law of diffusion started to occur after $3 - 4$ hours from the exposure to CO_2 at pressure higher than that of the previous step (**Figure 8.12**).
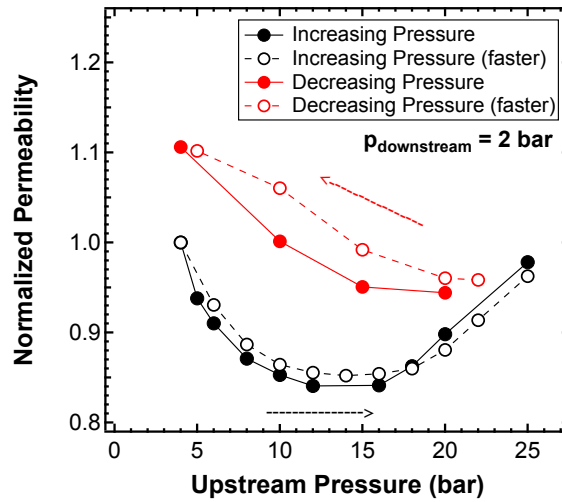
Figure 8.9: Comparison between two tests performed at downstream pressure equal to 2 bar: filled circles represent a slower rate of CO_2 upstream pressure increase, crosses represent faster rate of increase.

8.4.2. Solubility

Solubility is one of the fundamental contributions to the overall plasticization curves observed, and it is relevant to determine it independently. The CO_2 sorption isotherm at 35 °C is reported in **Figure 8.10**, as well as its hysteresis curve Data were compared to literature results, revealing good agreement.[26] A similar degree of hysteresis, induced by the exposure of the sample to a CO_2 pressure higher than 30 bar, was observed also by Visser *et al.*.[5] In-house made data were interpreted with the DMS model and fitting coefficients are reported in **Table 8.4**. By repeating the sorption isotherm twice on the same sample, a slightly higher sorption was reported in the second run, as shown in **Figure 8.11**, which is another evidence of the conditioning induced by CO_2 in the polyimide.
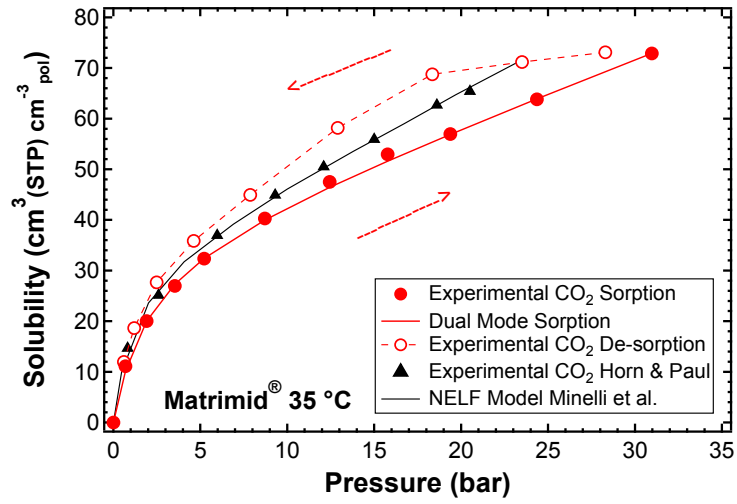
***Figure 8.10**:Matrimid® sorption isotherm (filled circles) and de-sorption isotherm (empty circles). Triangles are data from Horn and Paul[26], and they were modelled by Minelli et al.[27] with the NELF model.*

***Table 8.4**: Dual Mode Sorption parameters for Matrimid® polyimide at 35 °C.*

		k_d (cm³(STP) cm⁻³_pol bar⁻¹)	C'_H (cm³(STP) cm⁻³ _pol)	b (bar⁻¹)
Matrimid®				
	CO₂	1.33	34.10	0.56
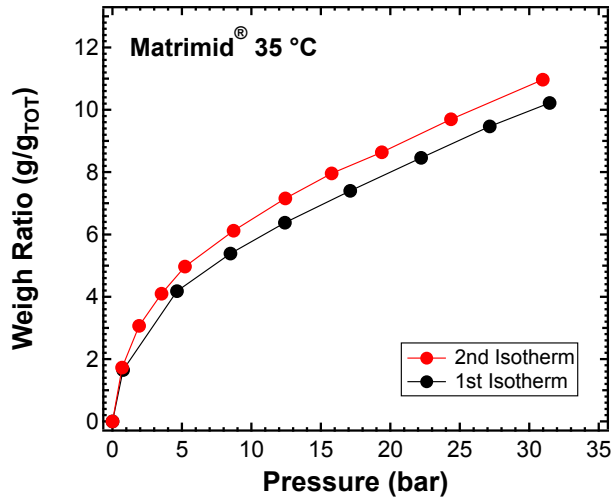
***Figure 8.11**: CO₂ conditioning effect of a Matrimid® sample which sorption isotherm was measured twice in a row.*

8.4.2.1.   Diffusivity from Sorption Kinetics: Deviations from Fick's Law

From the sorption isotherms, diffusion coefficients can be calculated with the method described in the experimental section 5.7.1.1 of this dissertation. Measuring $\mathcal{D}$ allowed to deconvolute the contribution of diffusion to the final permeability experienced. To make results accurate, it was very important to cast a film with a very homogeneous thickness (44 µm ± 0.89). Some of the curves from which sorption kinetics were retrieved are reported in **Figure 8.12** and the fitting of the Fick's law of diffusion on the experimental data measured is showed. In the case at low pressure, **Figure 8.12a**, the kinetic is Fickian and the diffusivity can be directly calculated. When pressure increased, the polymer matrix experienced dilation and relaxational non-Fickian transport. However, the Fickian diffusion can still be evaluated as shown in **Figure 8.12b**, **c**, and **d** by selecting whether relaxation starts occurring. In this framework, $M(\infty)$ represents the mass of CO_2 the polymer could sorb at equilibrium if relaxation did not occur. $M(t)/M(\infty)$ was equal to 1 when the pre-relaxation saturation was achieved. The intensity of the relaxation was evaluated at various pressures (*i.e.*, different concentrations in the polymer). It gradually increased with increasing concentration of CO_2, and the most relevant result was that it occurred to a non-negligible extent also at concentrations lower than the one reached at the plasticization pressure (*i.e.*, 46.32 cm^3(STP)/cm$^3_{pol}$). This provided another evidence that no transition occurred from below to above plasticization pressure, rather the relaxation was a gradual phenomenon. This supports mixed-gas sorption results that showed a gradual decrease of mixed-gas selectivity while CO_2 partial pressure increased, and not a sudden decrease after reaching p_{pl}.[8–11,37]
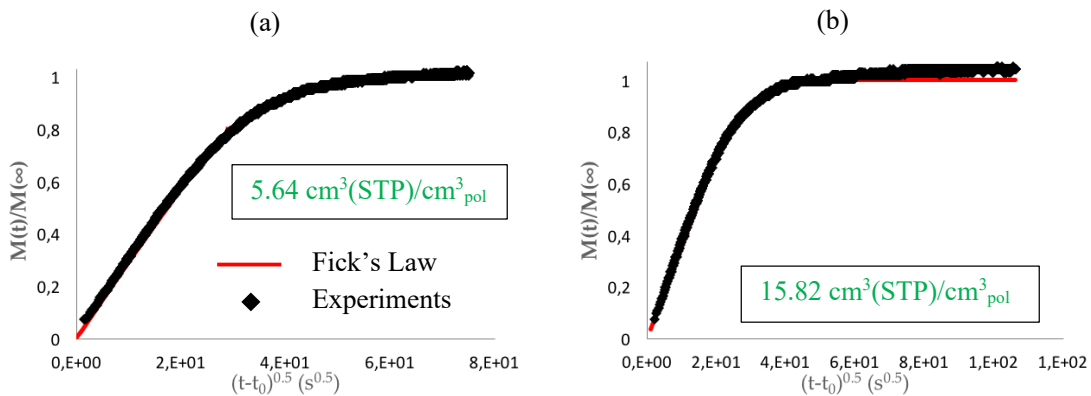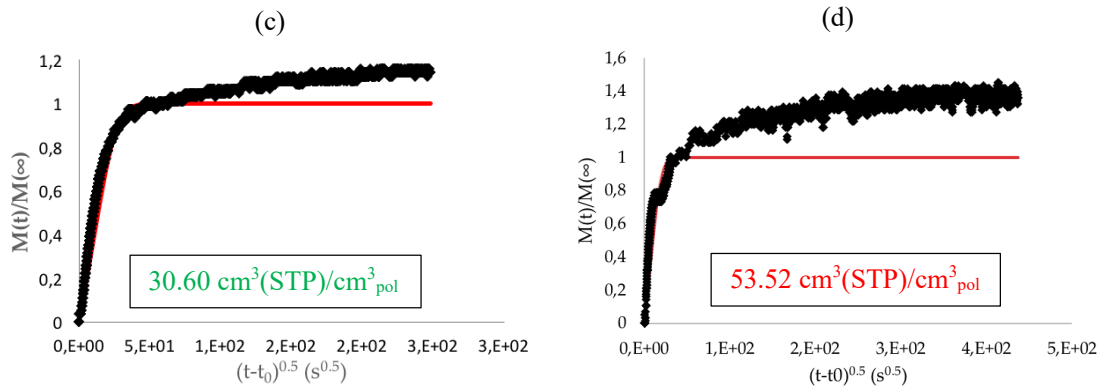
Figure 8.12: *Sorption kinetics from differential CO_2 sorption steps performed on Matrimid® at 35 °C. (a), (b), and (c) concentration values lower than the plasticization concentration (i.e., 46.32 $cm^3(STP)/cm^3_{pol}$), while (d) concentration of CO_2 higher than that measured at the plasticization pressure. Red curve: Fick's law of diffusion, Black diamonds, experimental data.*

Diffusion coefficients were also determined by means of the time-lag technique from permeation experiments performed at a downstream pressure of 0 bar. This was possible because Matrimid® film was always degassed between one experiment and the following one. Results are reported in **Figure 8.13**. To further validate the solution-diffusion model, diffusivity was also calculated dividing permeability, $\mathcal{P}$, and solubility coefficient, $\mathcal{S}$. The solubility coefficient was evaluated with the DMS interpolation at the same pressure than that applied on the upstream side of the membrane in the permeation experiment. The results obtained using the three methods are reported in **Figure 8.13** and further compared with data obtained by Visser *et al.*.[5] Given that the three methods revealed comparable results and each of them appears reliable, it may be possible to use sorption isotherms to evaluate the diffusion coefficient from the sorption kinetics, and combine solubility and diffusivity in the framework of the solution-diffusion model to determine whether a plasticization pressure would be reached or not in a certain pressure range.
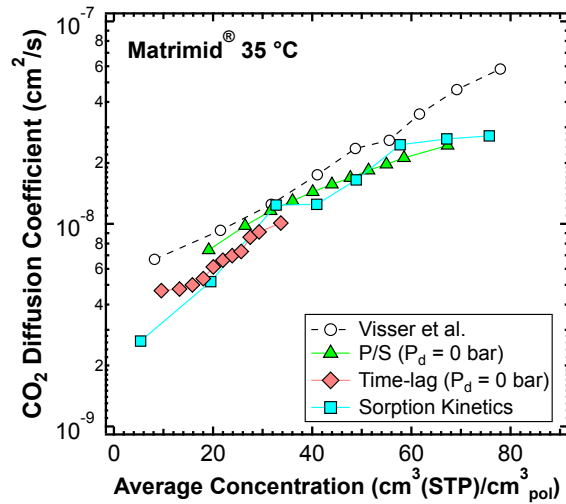
Figure 8.13: *CO₂ diffusion coefficient in Matrimid® measured with different methods: time-lag method (red diamonds), sorption kinetics (blue squares), and permeability divided solubility in the framework of the solution-diffusion model (green triangles). Open circles are data from the literature measured by Visser et al..*[5]

8.5. Conclusions and Future Works

At constant downstream pressure, permeability was found to vary with the upstream pressure, and a minimum value was observed at the so-called *plasticization pressure*. Plasticization pressure varied while increasing downstream pressure up to 5 bar, following an increasing trend. When increasing the CO_2 concentration inside of the polymer matrix, a progressive and regular relaxation of the polymer chains was observed. All these results led to the conclusion that plasticization does not indicate a state of the system. It is indeed a gradual effect, proportional to the upstream pressure to which the polymer is exposed, thus to the penetrant concentration in the polymer matrix, due to the combination of diffusivity and solubility contributions. No specific discontinuity and/or transition could be observed when crossing the plasticization pressure. Therefore, the solution-diffusion model should be sufficient to describe gas permeability as a function of the upstream pressure also in the presence of non-monotonous trends.

Future works on this topic will include measurements of the glass transition temperature of Matrimid® thick films equilibrated at high CO_2 pressure (up to 25 bar). To predict the dependence of plasticization

pressure on operating pressure, a modelling activity will be carried out by using the NELF model for solubility combined with a transport model.

References

[1] S. Matteucci, Y. Yampolskii, B. D. Freeman, I. Pinnau, *Mater. Sci. Membr. Gas Vap. Sep.* **2006**, 1.

[2] A. Bos, I. G. M. Pünt, M. Wessling, H. Strathmann, *J. Memb. Sci.* **1999**, *155*, 67.

[3] J. S. Chiou, J. W. Barlow, D. R. Paul, *J. Appl. Polym. Sci.* **1985**, *30*, 2633.

[4] P. Bernardo, E. Drioli, G. Golemme, *Ind. Eng. Chem. Res.* **2009**, *48*, 4638.

[5] T. Visser, M. Wessling, *Macromolecules* **2007**, *40*, 4992.

[6] W. J. Koros, D. R. Paul, A. A. Rocha, *J. Polym. Sci.* **1976**, *14*, 687.

[7] C. A. Scholes, G. Q. Chen, G. W. Stevens, S. E. Kentish, *J. Memb. Sci.* **2010**, *346*, 208.

[8] A. Bos, I. G. M. Pünt, M. Wessling, H. Strathmann, *Sep. Purif. Technol.* **1998**, *14*, 27.

[9] B. J. Story, W. J. Koros, *J. Appl. Polym. Sci.* **1991**, *42*, 2613.

[10] T. A. Barbari, W. J. Koros, D. R. Paul, *J. Memb. Sci.* **1989**, *42*, 69.

[11] S. M. Jordan, W. J. Koros, G. K. Fleming, *J. Memb. Sci.* **1987**, *30*, 191.

[12] Y. P. Handa, S. Lampron, M. L. O'neill, *J. Polym. Sci. Part B Polym. Phys.* **1994**, *32*, 2549.

[13] Z. Zhang, Y. P. Handa, *J. Polym. Sci. Part B Polym. Phys.* **1998**, *36*, 977.

[14] J. G. Wijmans, R. W. Baker, *J. Memb. Sci.* **1995**, *107*, 1.

[15] D. R. Paul, *Sep. Purif. Methods* **1976**, *5*, 33.

[16] D. R. Paul, *J. Polym. Sci. Part A-2 Polym. Phys.* **1969**, *7*, 1811.

[17] W. R. Vieth, J. M. Howell, J. H. Hsieh, *J. Memb. Sci.* **1976**, *1*, 177.

[18] M. Wessling, I. Huisman, T. v. d. Boomgaard, C. A. Smolders, *J. Polym. Sci. Part B Polym. Phys.* **1995**, *33*, 1371.

[19] J. D. Wind, C. Staudt-Bickel, D. R. Paul, W. J. Koros, *Ind. Eng. Chem. Res.* **2002**, *41*, 6139.

[20] Y. He, F. M. Benedetti, S. Lin, C. Liu, Y. Zhao, H.-Z. Ye, T. Van Voorhis, M. G. De Angelis, T. M. Swager, Z. P. Smith, *Submitt. to Adv. Mater.* **2019**.

[21] O. Vopička, M. G. De Angelis, N. Du, N. Li, M. D. Guiver, G. C. Sarti, *J. Memb. Sci.* **2014**, *459*, 264.

[22] O. Hölck, M. Böhning, M. Heuchel, M. R. Siegert, D. Hofmann, *J. Memb. Sci.* **2013**, *428*, 523.

[23] P. Li, T. S. Chung, D. R. Paul, *J. Memb. Sci.* **2014**, *450*, 380.

[24] R. R. Tiwari, J. Jin, B. D. Freeman, D. R. Paul, *J. Memb. Sci.* **2017**, *537*, 362.

[25] N. R. Horn, D. R. Paul, *Polymer (Guildf).* **2011**, *52*, 1619.

[26] N. R. Horn, D. R. Paul, *Polymer (Guildf).* **2011**, *52*, 5587.

[27] M. Minelli, G. C. Sarti, *J. Memb. Sci.* **2013**, *435*, 176.

[28] F. Doghieri, G. C. Sarti, *Macromolecules* **1996**, *29*, 7885.

[29] M. J. C. Ordoñez, K. J. Balkus, J. P. Ferraris, I. H. Musselman, *J. Memb. Sci.* **2010**, *361*, 28.

[30] L. Ansaloni, M. Minelli, M. Giacinti Baschetti, G. C. Sarti, *Oil Gas Sci. Technol. – Rev. d'IFP Energies Nouv.* **2015**, *70*, 367.

[31] S. Shishatskiy, C. Nistor, M. Popa, S. P. Nunes, K. V. Peinemann, *Adv. Eng. Mater.* **2006**, *8*, 390.

[32] G. Dong, H. Li, V. Chen, *J. Memb. Sci.* **2011**, *369*, 206.

[33] J. D. Wind, C. Staudt-Bickel, D. R. Paul, W. J. Koros, *Macromolecules* **2003**, *36*, 1882.

[34] G. C. Kapantaidakis, G. H. Koops, *J. Memb. Sci.* **2002**, *204*, 153.

[35] M. Kiyono, Carbon Molecular Sieve Membranes for Natural Gas Separations, Georgia Institute of Technology, **2010**.

[36] D.-Y. Peng, D. B. Robinson, *Ind. Eng. Chem. Fundam.* **1976**, *15*, 59.

[37] K. L. Gleason, Z. P. Smith, Q. Liu, D. R. Paul, B. D. Freeman, *J. Memb. Sci.* **2015**, *475*, 204.

9. New CANAL Ladder Polymers for Gas Separation

9.1. Introduction and Motivations

As described in the introductory chapter 1 of this dissertation, ladder polymers like PIMs[1–6] represent probably the most recent and significant advance in the field of polymer materials for gas separation applications. Films made from such polymers generally combine high gas permeability and moderate permselectivity for some of the most important gas pairs (*e.g.*, CO_2/N_2, CO_2/CH_4, O_2/N_2, and H_2/CH_4).[7] These features are related to the characteristic ladder-type architecture which provides them with rigid polymer chains which restrict efficient packing in the solid state. This leads to exceptionally higher fractional free volumes (FFVs) with respect to traditional single-stranded polymers. However, just few types of microporous ladder polymers have been developed and widely investigated due to the demanding chemistry for efficient and selective molecular ladder formation, as well as relatively low solubility of rigid ladder polymers in common organic solvents.[8] Therefore, the expansion of the structural diversity of microporous ladder polymers, which are capable of forming films and separating small gas molecules, is of significant importance

In this chapter, a new approach to the synthesis of ladder polymers which relies on the Catalytic Arene-Norbornene Annulation (CANAL) polymerization, developed by Professor Yan Xia and coworkers[8–12] at *Stanford University*, is presented. The focus is on the analysis of three norbornyl benzocyclobutene (NBC) ladder polymers which differ to one another because of the alkyl side-chain substitutions. The goal was to study how subtle changes in the molecular structure of the polymer chains would affect the transport properties of the different materials.

9.2. Effect of Alkyl Substitution

Part of this chapter was adapted from the following reference: H.W.H. Lai, F.M. Benedetti, Z. Jin, Y.C. Teo, A. Wu, M.G. De Angelis, Z.P. Smith, Y. Xia; *Tuning the Molecular Weights, Chain Packing, and Gas Transport Properties of CANAL Ladder Polymers via Alkyl Substitutions;* to be submitted to Macromolecules.

Developing fundamental understanding of how the molecular structure of polymers affects chain packing and the resulting porosity is very important to rationally tune the transport properties of CANAL ladder polymers. The unique purely hydrocarbon and nonpolar rigid backbone of NBC ladder polymers, make CANALs an exceptional model system for fundamental investigations of the structure-transport-property relationships of ladder polymers. Indeed, by excluding variables such as polar gas-polymer or polymer-polymer interactions, differences arise just according to the way polymer chains rearrange in space. The effect of alkyl substitution on the chain packing and transport properties of CANAL ladder polymers was investigated by pure-gas permeation and sorption experiments, as well as wide-angle X-ray scattering.

9.2.1. Materials

9.2.1.1.   Chemical Structure and Film Formation

The synthesis of NBC ladder polymers has been described in the experimental methods section 5.8.1. High-molecular-weight ladder polymers are necessary to obtain materials which are able to form a film. Indeed, for step growth condensation reactions like the CANAL polymerization, the conversion of the reaction needs to be remarkably high to achieve high molecular weight (M_W). The selective and efficient polymerization was optimized by Holden W. L. Lai in Professor Yan Xia lab. This enabled the formation of ultra-high molecular weight CANAL ladder polymers. The M_W was increased up to 750 kDa from

previously reported values often below 50 kDa.[9] From each batch, 150 mg to 200 mg of off-white powder were obtained. Different attempts were made to change the R_1 and R_2 substituents on both reagents (*i.e.*, dibromobenzenes and dinorbornenes), which were used in the general reaction scheme presented in the experimental methods section (5.8.1) to obtain different materials. **Table 9.1** summarizes the results in terms of R_1 and R_2 combinations, solubility of the product, and molecular weight of each polymer obtained.

Table 9.1: *Summary of the different combination attempted to synthesize CANAL ladder polymer with different functionalities (R_1, R_2) on the backbone.*

Polymer	R_1	R_2	Solubility	M_W (kDa)
CANAL-Me	Methyl	Methyl	Insoluble	/
CANAL-Me*	Methyl	Methyl	Soluble	< 80
CANAL-Et	Ethyl	Ethyl	Soluble	634
CANAL-Et**	Ethyl	Ethyl	Soluble	> 200
CANAL-iPr	Isopropyl	Isopropyl	Soluble	< 80
CANAL-Me-iPr	Methyl	Isopropyl	Soluble	450
CANAL-Me-Et	Methyl	Ethyl	Insoluble	/
CANAL-Et-iPr	Ethyl	Isopropyl	Soluble	757
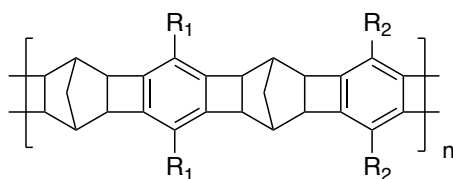
*Using a different synthesis approach: 1,4-dibromo-2,5-dimethylbenzene and norbornadiene as reagent set.
**Using a different synthesis approach: 1,4-dibromo-2,5-diethylbenzene and norbornadiene as reagent set

It was found that the R_2 substituents on the dinorbornene reagents, do not affect significantly the reactivity of the solution. On the other hand, the R_1 functionalities on the dibromobenzenes determines the outcome of the reaction. In particular, bulkier groups slow down the reaction due to steric congestion, preventing the achievement of high conversions.[10] For instance, CANAL-iPr, for which both R_1 and R_2 are isopropyl groups, provided systematic lower molecular weight than other NBC ladder polymers.

This result was attributed to the slower polymerization as a consequence of the increased steric hindrance imposed by isopropyl groups. However, CANAL-iPr was soluble in chloroform and tetrahydrofuran (THF). Alkyl substituents played an important role in solubilizing CANAL polymers. While CANAL-Et, CANAL-Et-iPr, and CANAL-Me-iPr are soluble in common solvents, CANAL-Me and CANAL-Me-Et formed insoluble aggregates. A hypothesis is that when R_1 is the smallest substituent, $i.e.$, methyl, and R_2 one of the two smaller ones used, either methyl and ethyl, the reaction is very effective and the extremely high molecular weight reached prevents the polymer to solubilize. Eventually, the polymers that presented the best compromise in terms of molecular weight and solubility were CANAL-Et, CANAL-Et-iPr, and CANAL-Me-iPr, and are represented in **Figure 9.1a**, **b**, and **c**, respectively. Interestingly, using rigorously dry THF as the solvent, which was obtained by storing it over molecular sieves for at least 3 days, yielded CANAL polymers with $M_W < 80$ kDa. The presence of water has been shown to prevent the formation of palladium black[13], eventually prolonging the lifetime of the catalyst. Thus, it was hypothesized that using THF that was not rigorously dry would stabilize more the catalyst enabling higher molecular weights.

(a)

(b) (c)
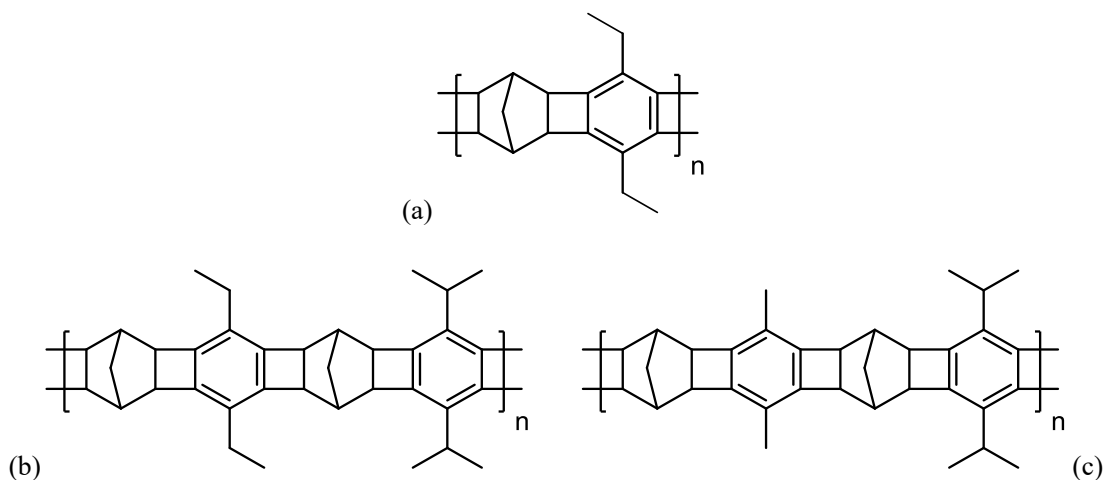
Figure 9.1: *Chemical Structure of (a) CANAL-Et, (b) CANAL-Et-iPr, and (c) CANAL-Me-iPr.*

^{1}H NMR spectra for the polymers represented in **Figure 9.1**, collected as described in the experimental session 5.10 of this dissertation, are reported in **Figure 9.2**. Some relevant properties of CANALs such as density and FFV are summarized in **Table 9.2**.

(a)

(b)

(c)
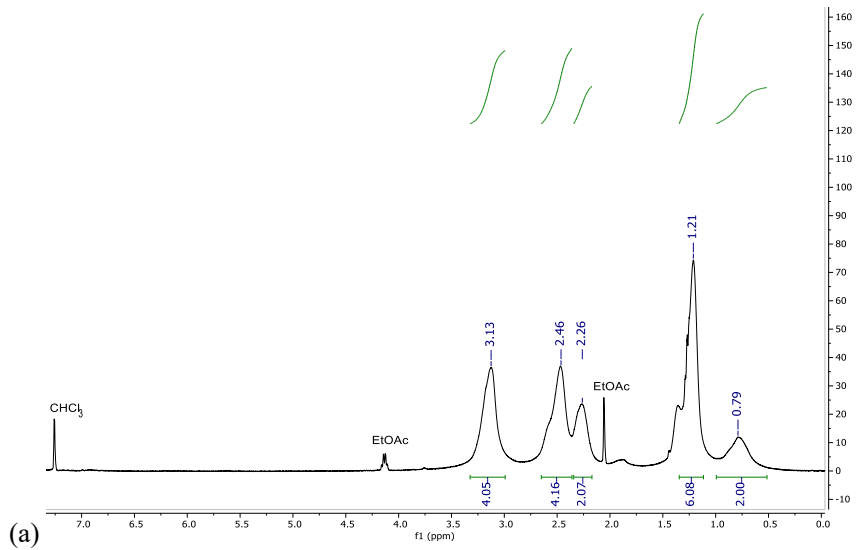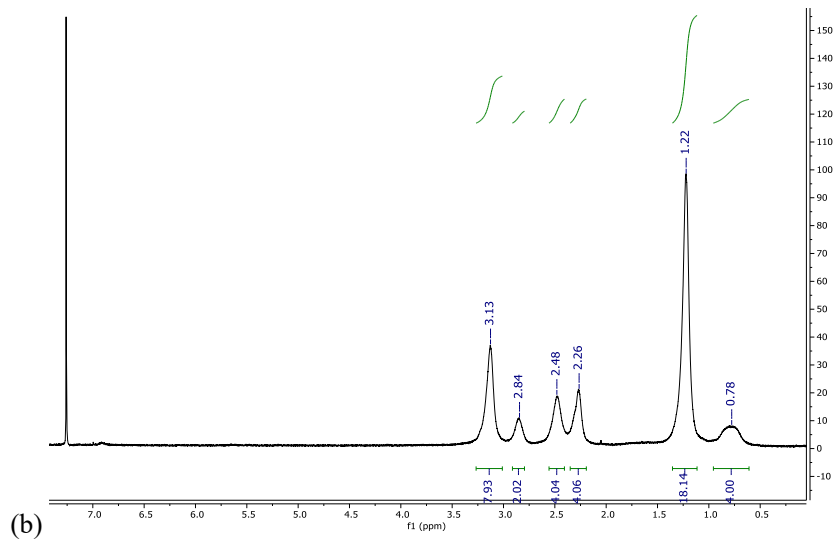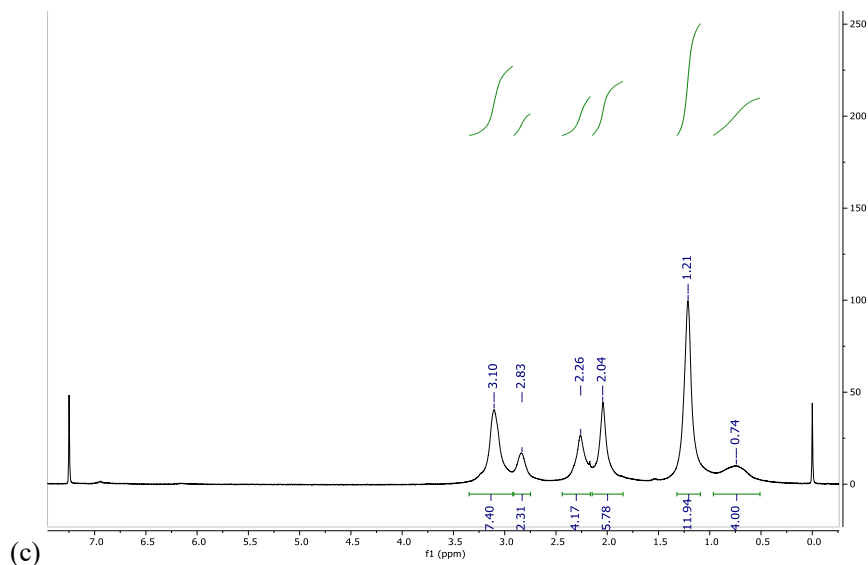
Figure 9.2: *¹H NMR spectra of (a) CANAL-Et, (b) CANAL-Et-iPr, and (c) CANAL-Me-iPr.*

Table 9.2: *Properties of NBC CANAL ladder polymers.*

Polymer	Density (g cm⁻³)[a]	FFV[b]
CANAL-Et	1.00	0.23
CANAL-Et-iPr	0.97	0.26
CANAL-Me-iPr	0.97	0.27

[a] Determined using a density kit (*analytical balance Mettler Toledo*, *Columbus OH*)
[b] Calculated using Bondi's group contribution method[14]

The samples were dissolved in chloroform, which was selected because it is effective on all the CANAL polymers and because there is evidence in the PIMs literature that it maximizes the performance for microporous polymers such as PIM-1.[15] The polymers were casted following the procedure described in section 5.1.2 of the experimental methods. Films are showed in **Figure 9.3**. As explained in 5.1.2, films were 1-2 cm, thus 20% to 40%, smaller than the diameter of the Petri dish. This is due to the shrinkage of polymer films during solvent evaporation till the formation of a glassy membrane.
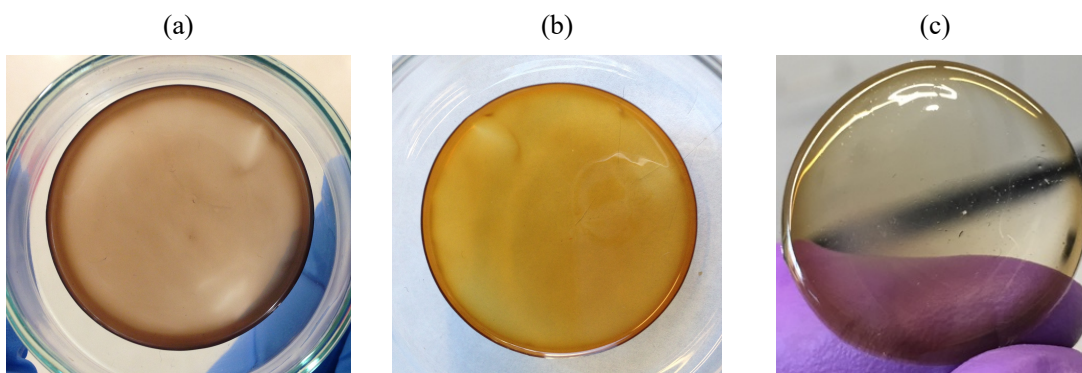
Figure 9.3: Film of (a) CANAL-Et, (b) CANAL-Me-iPr, and (c) CANAL-Et-iPr.

The polymer films were heated at 120 °C under vacuum for 24 h, treated with 200 mbar to 300 mbar of vapor methanol at 35 °C for 8 h to erase the casting history. This was performed because CANALs are glassy materials, thus not at their thermodynamic equilibrium. Eventually the materials were heated again at 100 °C under vacuum for 12 h to ensure the removal of residual methanol. However, given the non-polar nature of hydrocarbon-based NBC CANAL ladder polymers and the low activity of methanol to which the films were exposed, experiments indicated that vapor methanol treatment had no effect on transport properties and namely was not conditioning the samples. Further will be discussed in section 9.2.2. For this reason, experiments performed at variable-temperature to investigate the energetics contributions of gas diffusion and permeation, were run with films treated at 120 °C under vacuum for 24 h.

9.2.1.2.   WAXS

Wide-Angle X-ray Scattering (WAXS) was performed on CANAL ladder polymers to investigate the chain packing. Patterns are represented in **Figure 9.4**. It can be observed that all the three polymers showed a broad peak at $q \cong 0.8$ Å^{-1}, which means a chain spacing of $d \cong 8$ Å. The highest d-spacing was observed for CANAL-Et-iPr, *i.e.* 8 Å, which is consistent with the fact that it features the bulkier groups: ethyl and isopropyl. CANAL-Me-iPr showed smaller d-spacing, 7.7 Å, while CANAL-Et had

the smallest spacing, 7.6 Å. These features will be further related to diffusivity data evaluated with the time-lag method, which will be discussed in the following section 9.2.2.
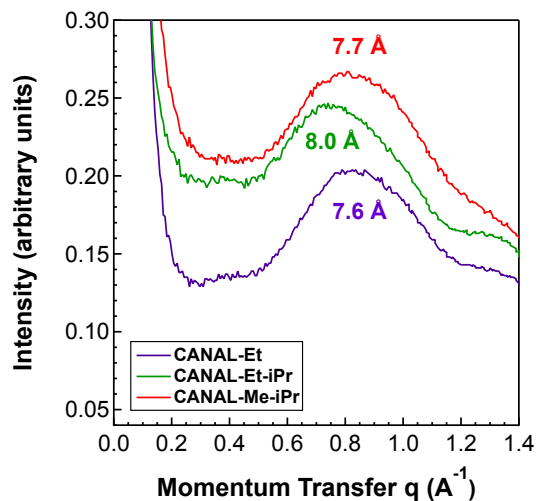
Figure 9.4*:Wide-Angle X-ray Scattering patterns of norbornyl benzocyclobutene CANAL ladder polymers.*

9.2.1.3.   TGA

Thermogravimetric analysis was performed on the films according to the method described in the experimental section 5.2. **Figure 9.5** shows that films were free of any residual solvent after the thermal treatment performed at 120 °C under vacuum for 24 h. The materials feature good thermal stability and decomposition temperatures above 400 °C.
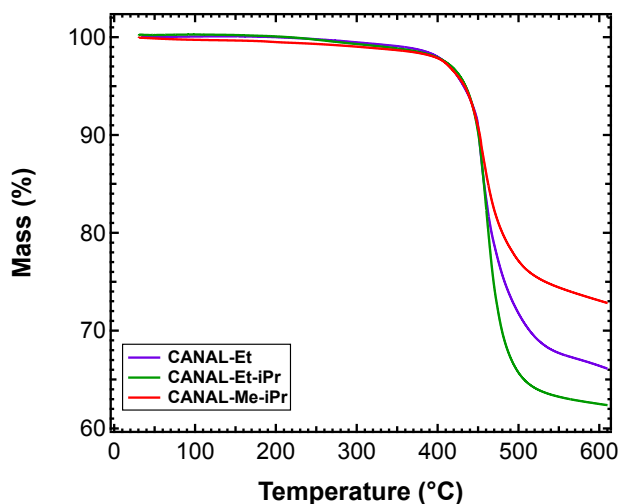
Figure 9.5: *TGA trace of NBC CANAL ladder polymer films after they were heated in the vacuum oven at 120 °C for 24 h.*

9.2.2. Pure-Gas Permeation

Permeability and ideal selectivity results obtained for the three NBC CANAL ladder polymers are summarized in **Figure 9.6**. These values refer to films investigated right after the post-casting treatment, namely at the beginning of the aging process. Among the CANAL ladder polymers, CANAL-Me-iPr revealed to have the highest permeability for all gases, followed by CANAL-Et-iPr, and CANAL-Et (**Figure 9.6a**). These results indicate that subtle variations on the alkyl substituents on the ladder backbone, can lead to significantly different values of permeability. However, despite the latter result, permselectivity was very similar for all three NBC CANAL polymers, as illustrated in **Figure 9.6b**. Considering all the gases tested, permeability increased by up to 80% going from CANAL-Et to CANAL-Me-iPr.
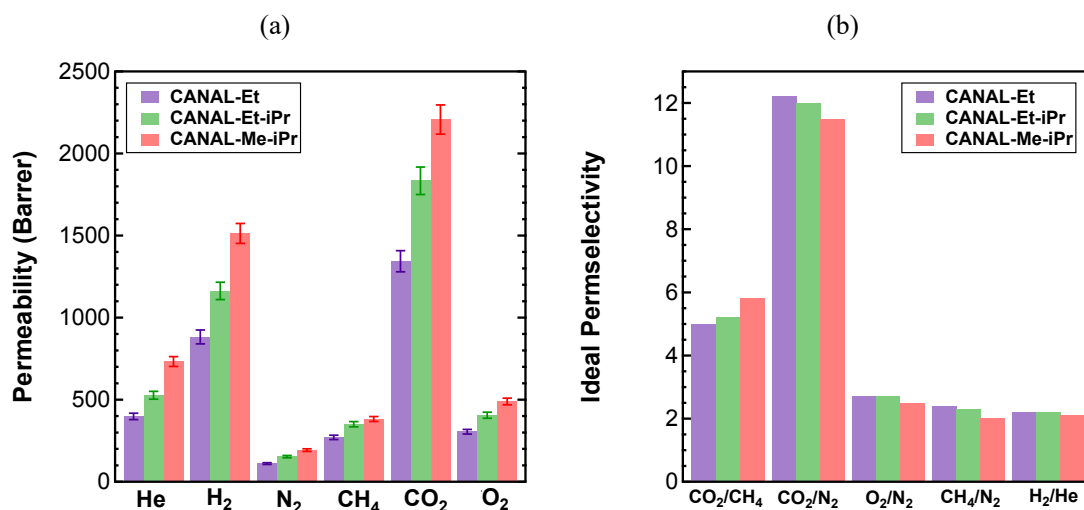
Figure 9.6: Pure-gas permeability (a) and ideal permselectivity (b) for CANAL-Et, CANAL-Et-iPr and CANAL-Me-iPr.

In the framework of the solution diffusion model (*i.e.*, $\mathcal{P} = \mathcal{DS}$), both diffusivity, $\mathcal{D}$, and solubility coefficients, $\mathcal{S}$, contribute to the overall permeability, $\mathcal{P}$, which was measured. The diffusion coefficients were determined by using the time-lag method. It allowed to assess that the main reason why CANAL-Et-iPr had higher permeability than CANAL-Et, was explained by the faster diffusion occurring in CANAL-Et-iPr (**Figure 9.7a**). This is consistent with the WAXS results illustrated in **Figure 9.4**, which show that CANAL-Et-iPr had the highest chain spacing. On the other hand, solubility coefficients calculated from $\mathcal{S} = \mathcal{P}/\mathcal{D}$ reported in **Figure 9.7b**, revealed very similar results for the two materials, within the error bars. The same graph shows that CANAL-Me-iPr had larger solubility coefficients than the other two CANAL polymers. The larger solubility coefficients of CANAL-Me-iPr were explained because of the lack of flexible ethyl groups. Indeed, rotatable and long alkyl chains have previously been found to reduce free volumes in polymers, thus reducing the Langmuir sorption capacity of the materials.[16] Overall, CANAL-Me-iPr had the highest permeability for all gases tested. This means that the higher solubility of CANAL-Me-iPr outweighs its lower diffusivity compared to CANAL-Et-iPr. Another information we can gather from **Figure 9.7** is that the slope of the best-fit lines in both figures was very similar, thus all the CANALs present similar diffusivity-selectivity and solubility-selectivity, which is consistent with what observed in **Figure 9.7b**.
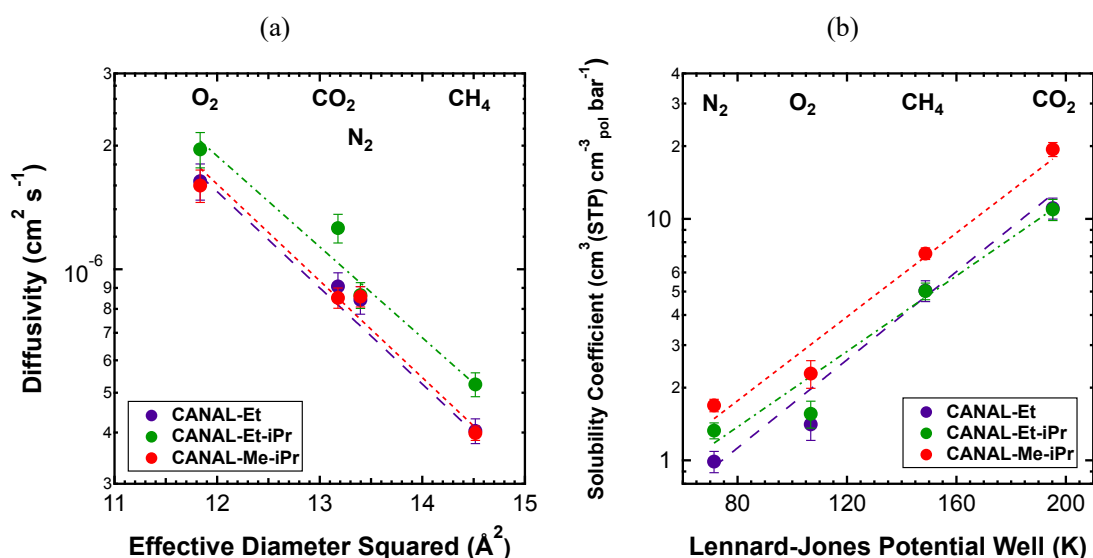
Figure 9.7: *(a) Diffusion coefficients as a function of the effective diameter of gases[17], and (b) correlation of solubility coefficients calculated using the solution-diffusion model, with Lennard-Jones potential wells of gases[18]. He and H_2 values were not reported because the time-lag was often too short for accurate calculations.*

As mentioned in section 9.2.1.1, vapor methanol treatment had no effect on transport properties. In the following **Table 9.3**, **Table 9.4**, and **Table 9.5**, results will be provided to support this statement. *Treatment A* indicates that membranes have been heated at 120 °C under vacuum for 24 h, treated with 200 mbar to 300 mbar of vapor methanol at 35 °C for 8 h, and heated at 100 °C under vacuum for 12 h. *Treatment B* indicates that membranes have been heated at 120 °C under vacuum for 24 h.

Table 9.3: *Permeability coefficients of gases in CANAL ladder polymers under film treatment A (white background) and treatment B (grey background). Temperature = 35 °C, upstream pressure = 15 psia.*

Polymer (thickness)	Permeability (Barrer)[a]					
	He	H_2	N_2	CH_4	CO_2	O_2
CANAL-Et (112.9 ± 3.8 μm)	399 ± 23	883 ± 51	111 ± 6.4	271 ± 16	1,344 ± 78	305 ± 18
CANAL-Et (85.3 ± 3.9 μm)[b]	410 ± 25	858 ± 52	95 ± 5.8	204 ± 12	1,192 ± 72	270 ± 16
CANAL-Et-iPr (114.9 ± 4.0 μm)	527 ± 24	1,163 ± 53	153 ± 7.0	351 ± 16	1,834 ± 84	406 ± 19
CANAL-Et-iPr (92.4 ± 5.2 μm)	578 ± 40	1,228 ± 84	153 ± 11	355 ± 24	1,858 ± 128	423 ± 29

Polymer (thickness)						
CANAL-Me-iPr (107.3 ± 1.9 μm)	733 ± 30	1,513 ± 61	193 ± 7.8	383 ± 16	2,207 ± 89	489 ± 20
CANAL-Me-iPr (177.3 ± 0.4 μm)	699 ± 24	1,549 ± 54	181 ± 6.3	386 ± 14	2,341 ± 82	501 ± 18

[a]Barrer=10^{-10} cm$^3_{STP}$ cm cm^{-2} s^{-1} cmHg^{-1}

[b]Film was aged 3 days

Table 9.4: *Diffusion coefficients of gases in CANAL ladder polymers under film treatment A (white background) and treatment B (grey background). Temperature = 35 °C, upstream pressure = 15 psia.*

Polymer (thickness)	Diffusion Coefficient (10^{-7} cm^{-2} s^{-1})					
	He	H$_2$	N$_2$	CH$_4$	CO$_2$	O$_2$
CANAL-Et (112.9 ± 3.8 μm)	320 ± 470	160 ± 130	8.42 ± 0.65	4.02 ± 0.28	9.09 ± 0.72	16.2 ± 0.2
CANAL-Et (85.3 ± 3.9 μm)[b]	340 ± 950	250 ± 500	8.70 ± 1.0	4.41 ± 0.43	9.90 ± 1.2	18.5 ± 3.3
CANAL-Et-iPr (114.9 ± 4.0 μm)	220 ± 180	200 ± 150	8.65 ± 0.62	5.24 ± 0.35	12.6 ± 1.0	19.6 ± 1.9
CANAL-Et-iPr (92.4 ± 5.2 μm)	250 ± 450	160 ± 180	13.4 ± 2.0	6.20 ± 0.75	13.0 ± 1.9	24.0 ± 4.9
CANAL-Me-iPr (107.3 ± 1.9 μm)	210 ± 230	127 ± 84	8.58 ± 0.49	4.00 ± 0.16	8.53 ± 0.48	16.1 ± 1.5
CANAL-Me-iPr (177.3 ± 0.4 μm)	280 ± 150	190 ± 71	7.78 ± 0.12	4.14 ± 0.04	10.0 ± 0.20	17.6 ± 0.6

[b]Film was aged 3 days

Table 9.5: *Solubility coefficients of gases in CANAL ladder polymers under film treatment A (white background) and treatment B (grey background). Temperature = 35 °C, upstream pressure = 15 psia.*

Polymer (thickness)	Solubility Coefficient (cm$^{-3}_{STP}$ cm$^{-3}_{pol}$ bar^{-1})					
	He	H$_2$	N$_2$	CH$_4$	CO$_2$	O$_2$
CANAL-Et (112.9 ± 3.8 μm)	0.09 ± 0.14	0.40 ± 0.31	0.99 ± 0.10	5.05 ± 0.46	11.1 ± 1.1	1.40 ± 0.16
CANAL-Et (85.3 ± 3.9 μm)[b]	0.09 ± 0.25	0.26 ± 0.53	0.82 ± 0.11	3.47 ± 0.40	9.1 ± 1.2	1.09 ± 0.21
CANAL-Et-iPr (114.9 ± 4.0 μm)	0.18 ± 0.15	0.44 ± 0.34	1.33 ± 0.11	5.03 ± 0.41	11.0 ± 1.0	1.56 ± 0.17
CANAL-Et-iPr (92.4 ± 5.2 μm)	0.17 ± 0.31	0.58 ± 0.65	0.85 ± 0.14	4.29 ± .60	10.7 ± 1.7	1.32 ± 0.28
CANAL-Me-iPr (107.3 ± 1.9 μm)	0.26 ± 0.29	0.90 ± 0.66	1.69 ± 0.12	7.19 ± 0.41	19.4 ± 1.4	2.29 ± 0.83

CANAL-Me-iPr (177.3 ± 0.4 μm)	0.19 ± 0.10	0.60 ± 0.22	1.74 ± 0.07	7.00 ± 0.25	17.5 ± 0.7	2.13 ± 0.10

[b]Film was aged 3 days

9.2.2.1.   Variable Temperature Permeation

To deepen the understanding on the transport mechanisms in CANAL ladder polymers, variable-temperature pure-gas permeation experiments were performed to calculate the activation energy of gas transport using the Arrhenius and van't Hoff approach described in section 4.1.1. NBC CANALs are rigid microporous materials, and present both features of dense polymers and porous materials. Indeed, CANALs revealed to have also high BET internal surface area[9,11], comparable to that of PIMs[1,19], as calculated from N_2 sorption isotherms at 77 K.[20] For these experiments, CANAL-Me-iPr was selected as a model polymer. A thick film (125 μm) was treated at 120 °C under vacuum for 24 h and then aged for two weeks at ambient conditions before running the experiments to ensure sufficient stability of the polymer film's properties over the course of the experiments, which took three days. Experiments were performed at 35, 45, 55, and 65 °C at 15 psia for N_2, CH_4, O_2 and CO_2. **Figure 9.8** shows the trends of permeability, diffusivity and solubility versus $1/T$. **Table 9.6** summarizes the energetics contributions related to gas permeation, sorption and diffusion processes in CANAL-Me-iPr. For O_2, N_2, and CH_4, positive values of energy of permeation, E_P, were recorded, thus activation energy of diffusion, E_D, was larger than the absolute value of the enthalpy of sorption, ΔH_S ($E_D > |\Delta H_S|$). On the other hand, for CO_2 a negative value of E_p was calculated ($E_D < |\Delta H_S|$). This indicated that the transport of CO_2 in the CANAL polymer may be consistent with the surface diffusion model[21], suggesting that the transport mechanism in CANAL-Me-iPr resemble that of materials that are traditionally thought of as porous.
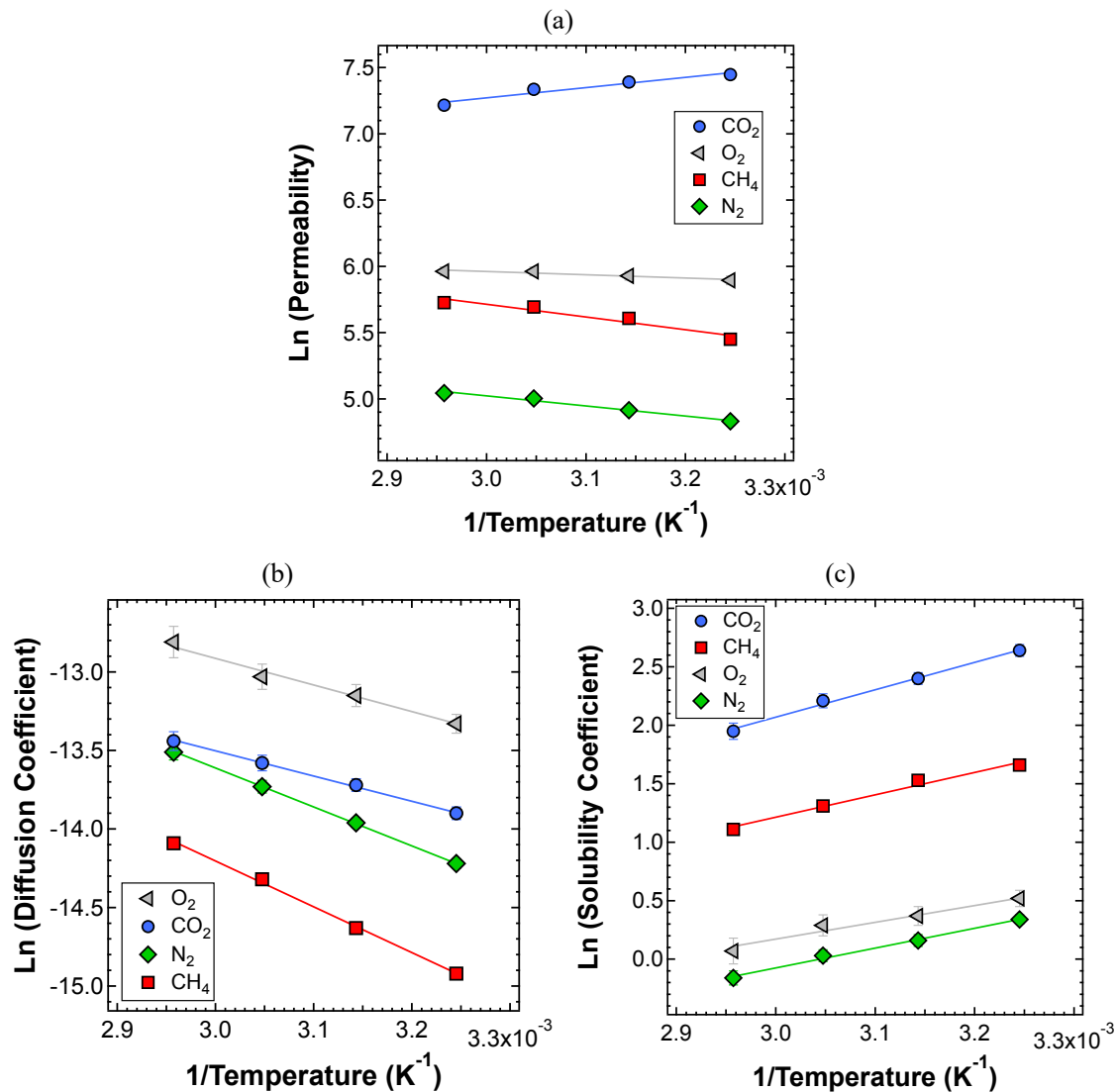
Figure 9.8*: Arrhenius plots of permeability (a) and diffusivity (b), and van't Hoff plot of solubility (c), of CANAL-Me-iPr for CO_2, O_2, CH_4, and N_2. Permeation was measured at an upstream pressure of 15 psia at 35, 45, 55, and 65 °C. Diffusion coefficients were evaluated with the time-lag method. Solubility coefficients were calculated in the framework of the solution-diffusion model.*

Table 9.6*: Energetics of permeation in CANAL-Me-iPr for N_2, CH_4, CO_2, and O_2.*

	N_2	CH_4	CO_2	O_2
E_P (kJ mol^{-1})	6.51 ± 0.71	8.3 ± 1.5	-6.13 ± 0.92	2.2 ± 2.0
E_D (kJ mol^{-1})	20.61 ± 0.30	24.24 ± 0.57	13.32 ± 0.48	14.1 ± 1.2
ΔH_S (kJ mol^{-1})	-14.1 ± 0.64	-15.9 ± 1.4	-19.45 ± 0.84	-11.9 ± 1.6

To further investigate the behavior of CO_2, experiments were performed on CANAL-Me-iPr also at 5, 10 and 15 psia for each of the four temperatures (*i.e.*, 35, 45, 55, and 65 °C). Sub-atmospheric upstream pressures were selected to avoid any significant plasticization of the film. At steady-state, the absolute value of ΔH_S was determined to be decreasing with increasing pressure, namely the energetics associated to the sorption process were more negative at lower pressure. This is consistent with the most favorable sorption sites being occupied first, leading to lower average ΔH_S at higher pressure as the remaining less favorable sorption sites are progressively occupied. At the same time, E_D was found to be decreasing with increasing pressure. Results are shown in **Figure 9.9a**. The inverse correlation between E_D and ΔH_S suggests that desorption of CO_2 from the pore walls of CANAL polymers is relevant to the rate of diffusion. Furthermore, we determined the $E_D/|\Delta H_S|$ ratios to be 0.68, 0.75, and 0.79 at upstream pressures of 5, 10, and 15 psi, respectively. These $E_D/|\Delta H_S|$ ratios are close to the values of < 1 previously determined for surface diffusion on solid surfaces such as porous carbon and glass.[21,22] Similar $E_D/|\Delta H_S|$ ratios have been observed for the transport of some gases in polymeric materials with substantially high FFV and gas permeability, such as PTMSP[23,24] and PIM-1[15,25,26].

In 1999, Freeman[27] developed the theoretical basis for the permeability/selectivity tradeoff relation of polymeric gas separation membranes known as the Robeson upper bound[28,29]. The theory includes an equation that correlates the kinetic diameter of the penetrant (d_k) with E_D as follows:

$$E_D = cd_k^2 - f \qquad \text{Eq. (9.1)}$$

where c and f are fitting parameters. Parameter c is a measure of the polymer's size selectivity, and $\sqrt{f/c}$ is the kinetic diameter of the largest hypothetical molecule that can diffuse through the polymer with zero activation energy. Thereby, $\sqrt{f/c}$ can be interpreted as the average distance between polymer chains.[23,27] Eq. (9.1) is based on Brandt's model for molecular diffusion in polymers.[30] **Figure 9.9b** shows the remarkably linear relationship between E_D and d_k^2 for CANAL-Me-iPr, which is typical for dense polymers. Comparison of the slope and intercept of **Figure 9.9b** indicates that CANAL-Me-iPr is very similar to rigid and glassy polymers, such as 6FDA-2,6-DAT (poly[2,6-toluene-2,2-bis(3,4-

dicarboxylphenyl)hexafluoropropane diimide]) polyimide[31], PIM-1[15], as well as PIM-TMN-Trip and

PIM-BTrip which contain extended triptycene motifs.[32,33]
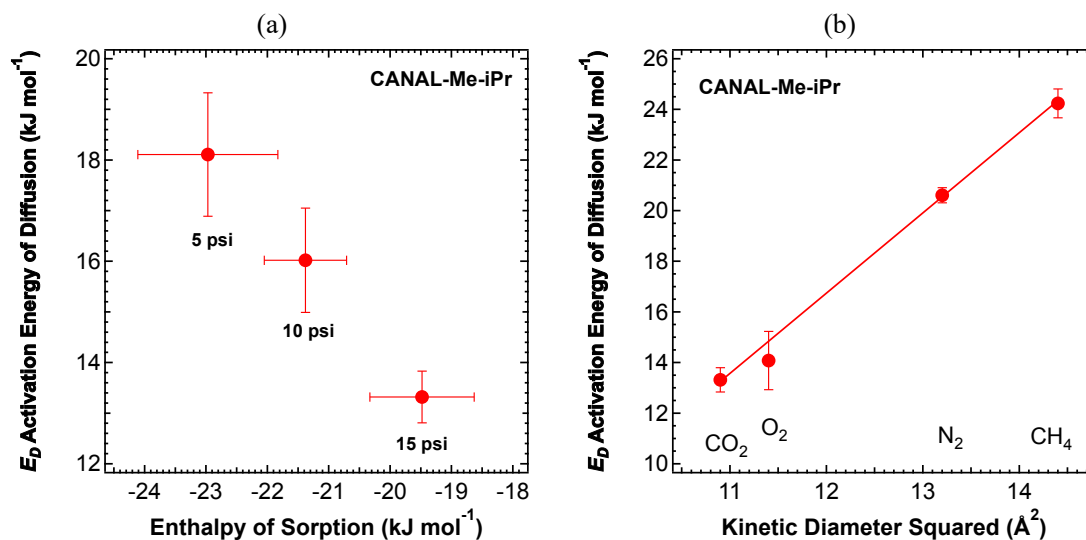
Figure 9.9: (a) Correlation between activation energy of diffusion and enthalpy of sorption of CO_2 in CANAL-Me-iPr. Upstream pressures are noted below each data point. (b) Activation energy of diffusion for CO_2, O_2, N_2, and CH_4 as a function of kinetic diameter squared in CANAL-Me-iPr..

9.2.3. Pure-Gas Sorption

Pure-gas sorption experiments were performed with N_2, O_2, CH_4, and CO_2 on the three NBC CANAL

ladder polymers and are reported in **Figure 9.10**. CANAL-Me-iPr revealed to have overall the highest

sorption capacity, consistently with the results obtained from the solution-diffusion model analysis in

section 9.2.2. On the other hand, CANAL-Et and CANAL-Et-iPr had very similar sorption capacity.

Interestingly, the three materials seem to have nearly identical O_2 sorption isotherms, which is observed

in **Figure 9.10d**. This result requires to be further investigated to find a rational explanation.
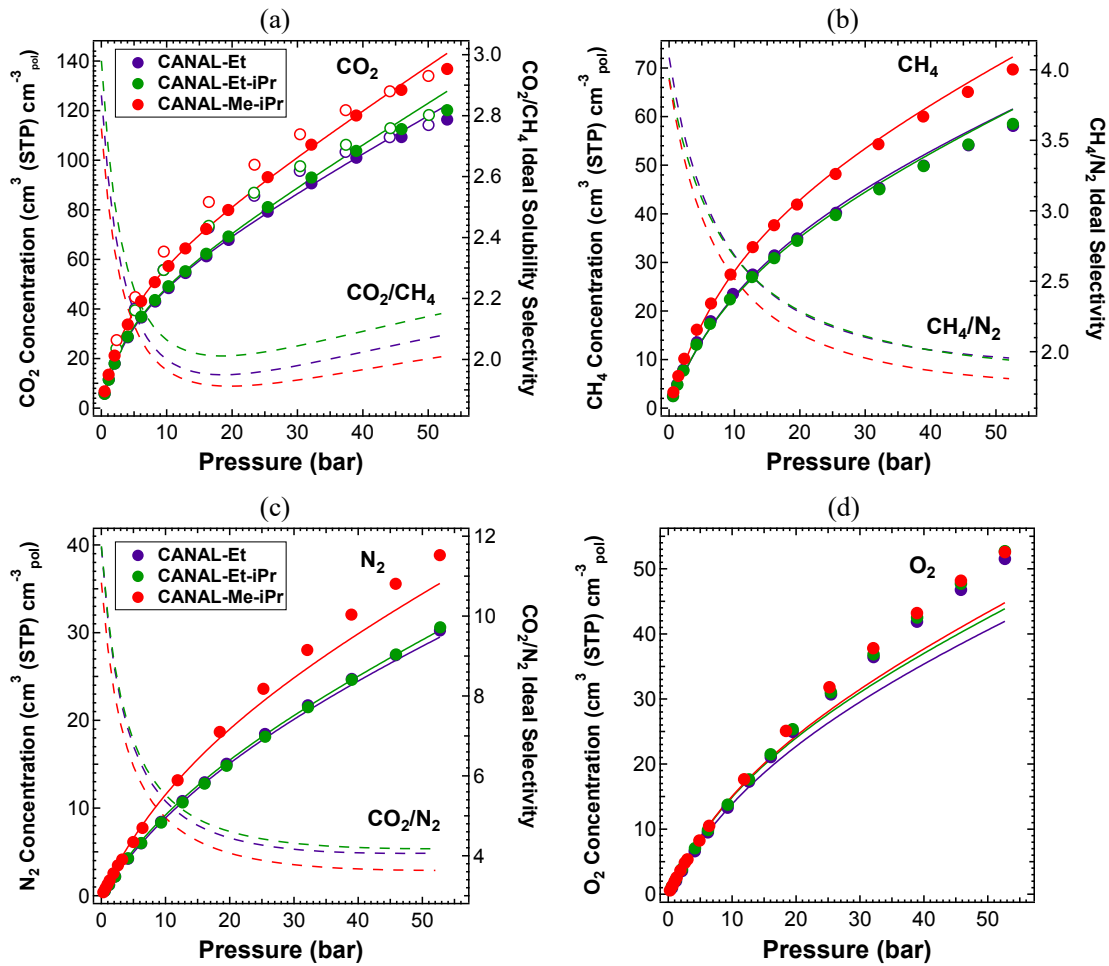
Figure 9.10: *Sorption (solid circles, left axis) and desorption (open circles, left axis) isotherms of CANAL ladder polymers at 35 °C for (a) CO_2, (b) CH_4, (c) N_2, and (d) O_2. Ideal sorption selectivity (dashed lines, right axis) is shown for (a) CO_2/CH_4, (b) CH_4/N_2, and (c) CO_2/N_2. DMS fittings (solid lines, left axis) were done constraining k_D and b to increase exponentially with the same slope from the trend of S vs T_C both at 10 bar as described by Smith et al.[34].*

Figure 9.10 also features ideal sorption selectivity for three industrial relevant gas pairs: CO_2/CH_4, CO_2/N_2, and CH_4/N_2 as a function of pressure. These $\alpha_{i,j}^S$ were evaluated by using the best-fit curves of the sorption isotherms. As often observed in glassy polymers, ideal sorption selectivity decreased monotonically as pressure increased for CH_4/N_2. However, for CO_2/CH_4 and CO_2/N_2, ideal sorption selectivity first decreased rapidly and then increased in the case of CO_2/CH_4 and plateaued in the case of CO_2/N_2. Similar results were previously reported in literature for PIM-1[35], as shown in **Figure 9.11** for the case CO_2/CH_4. This can be attributed to the plasticization of the polymer chains as the concentration of CO_2 in the film increases, leading to higher uptake of CO_2. Because CH_4 and N_2 are

non-plasticizing gases, the apparent ideal sorption selectivity for CO_2/CH_4 and CO_2/N_2 is higher than expected at high pressure. Plasticization of the films during CO_2 sorption was further confirmed by hysteresis in the CO_2 desorption isotherm (**Figure 9.10a**). After being exposed to > 50 bar of CO_2, desorption points at a given pressure were slightly but consistently higher than sorption points, indicating that high concentration CO_2 led to swelling of the polymer chains and thus increased the sorption capacity of the film for CO_2. Notably, the extent of hysteresis observed in the CO_2 sorption and desorption isotherms of CANAL polymers was much less than the previously reported for other glassy polymers such as polycarbonate[36,37] (**Figure 9.12**), or Matrimid®, as reported in section 8.4.2 of this dissertation. The sorption deviation in **Figure 9.12** was simply calculated as $100 * (C_{des} - C_{sor})/C_{sor}$, were C_{sor} is the concentration of CO_2 in the sorption curve and C_{des} is the concentration of CO_2 in the desorption curve, both evaluated at the same pressure.
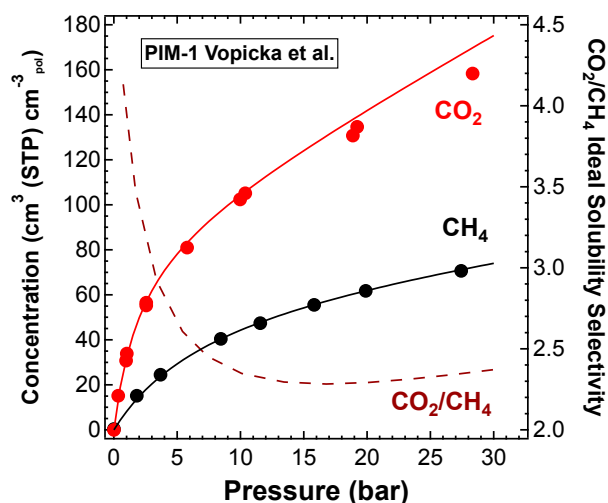

Figure 9.11: Sorption isotherms (solid circles, left axis) and DMS fittings (solid lines, left axis) of CANAL ladder polymers at 35 °C for CO_2 and CH_4. Ideal sorption selectivity (dashed lines, right axis) is shown for (a) CO_2/CH_4. Data from Vopička et al.[35].
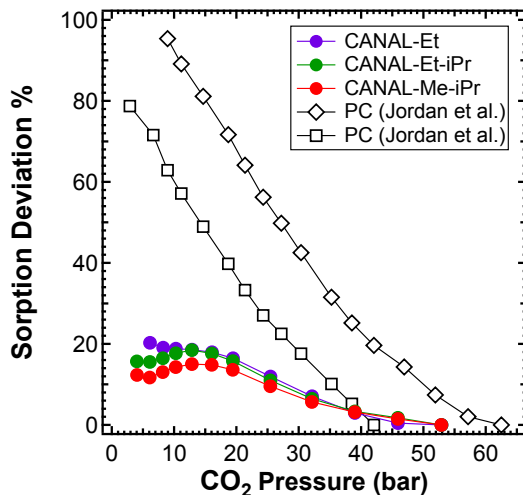
Figure 9.12*: Hysteresis induced by sorption of CO_2 up to around 52 bar for CANAL-Et, CANAL-Et-iPr, and CANAL-Me-iPr. Polycarbonate (PC) data is from Jordan et al.[36]. PC was exposed up to 42 bar (open squares) and 62 bar (open diamonds). The percentage sorption deviation was evaluated from the difference between sorption and desorption curves.*

Another information extracted from sorption experiments was how alkyl substituents can affect solubility selectivity ($\alpha_{i,j}^{S}$) at high pressure. This is a crucial information since industrial gas separations are often performed at > 20 bar, depending on the specific application.[38] Further, it was not possible to retrieve this information from permeation experiments since they were performed at lower upstream pressure. While at low pressure $\alpha_{i,j}^{S}$ of the three polymers was found to be remarkably similar for each gas pair (**Figure 9.10a**, **b**, **c**), at higher pressure (*i.e.*, > 10 bar), the ideal solubility-selectivity for CH_4/N_2, CO_2/N_2, and CO_2/CH_4 was higher for CANAL-Et-iPr and CANAL-Et than CANAL-Me-iPr. Given that all three polymers consist of completely nonpolar hydrocarbons, specific polymer-gas interactions are expected to be very similar among these polymers. Therefore, the difference in ideal sorption selectivity at high pressure can be attributed to difference in chain packing and pore structure as a result of alkyl substitutions.

A Dual Mode Sorption (DMS) analysis has been reported in **Figure 9.10** along with the sorption isotherms. Ricci *et al.*[39] recently reported that different sets of DMS parameters describe the same pure-gas sorption isotherm with similar goodness of fit. However, parameters obtained through a least-squares method for individual gas-polymer isotherms often do not follow systematic trends of the

intrinsic property of penetrants (*i.e.*, critical temperature), and therefore have no physical significance. To obtain systematic and meaningful parameters, DMS fitting was performed with k_D and b constrained to increase exponentially with the same slope calculated from the trend of solubility coefficient vs critical temperature at 10 bar, as described by Smith *et al.*.[34] Simultaneously, c'_H was determined as an adjustable parameter. **Figure 9.13a** and **b** show how c'_H varies with FFV and T_C, respectively. Although there was no constrain on the parameter related to the Langmuir capacity, it increased with T_C for each CANAL polymer, consistently with its physical meaning explained in section 4.3.2. CANAL-Me-iPr revealed to have the highest values of c'_H, as expected from its higher sorption capacity and its higher FFV. The results observed in **Figure 9.10d** for O_2 sorption, were confirmed by the modeling results. Indeed, the value of c'_H for CANAL-Me-iPr does not increase with respect to the other two polymers, opposed to the values of c'_H for all the other gases that are systematically higher. Values for k_D and b are shown in **Figure 9.13c** and **d**, and follow the trends imposed by the constrains. CANAL-Me-iPr also reported the highest values of the Henry coefficient parameter.
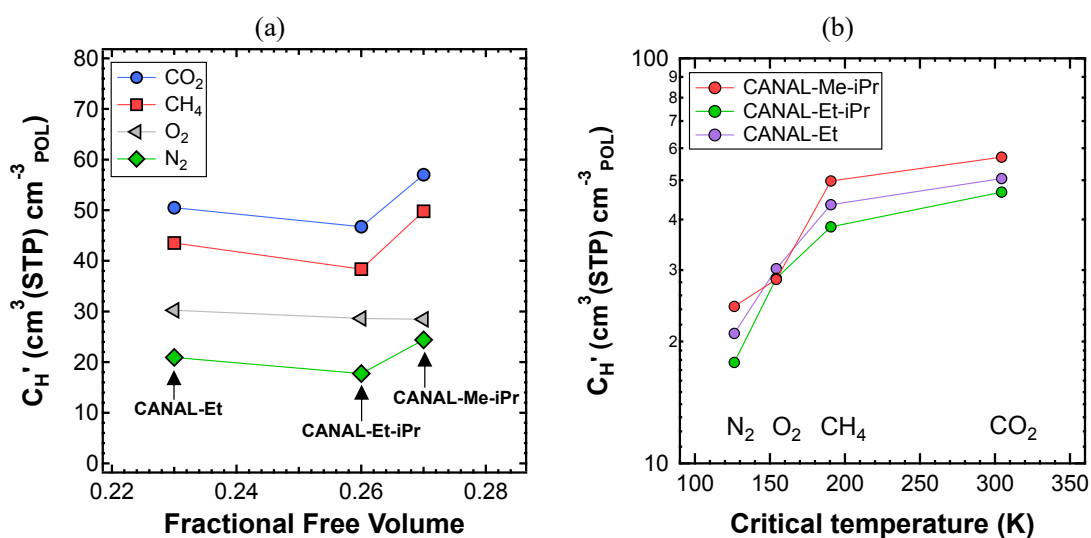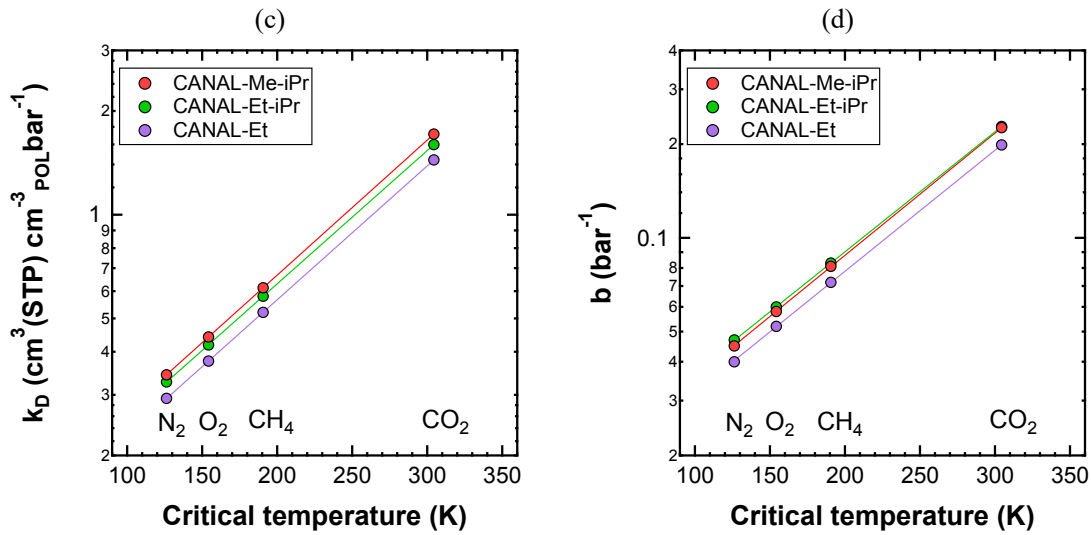
*Figure 9.13: Pressure-based DMS parameters calculated by applying constraints on k_D and b as described by Smith et al.[34].
c'_H trends against (a) FFV, and (b) Tc. Trends of (c) k_D and (d) b plotted against critical temperature.*

It was found that the slope S vs T_C decreased at increasing pressure (**Figure 9.14**). Since the DMS modeling results depend on the value of the slope, it was performed a sensitivity analysis on the parametrization to evaluate the extent of the variability. Pressure-based DMS parameters were also calculated constraining k_D and b to increase with the slope S against T_C determined at 50 bar. Results are reported in **Table 9.7** along with those calculated from the approach at 10 bar previously described, for comparison. As expected, DMS parameters are significantly different, but the sorption isotherms they generate are very similar to one another, as shown in **Figure 9.15**. These results emphasize the importance of using a consistent set of parameters retrieved by applying proper constrains. Following this approach, it was possible to extract further information from the parameters to support the considerations discussed above.
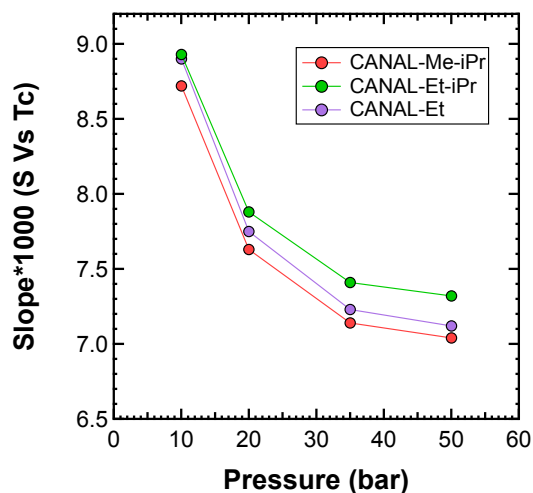
Figure 9.14*: Variability of the slope calculated from S vs Tc as a function of pressure at which S was calculated.*

Table 9.7*: Pressure-based DMS parameters obtained constraining k_D and b to increase exponentially with the same slope from the trend of S vs T_C both at 10 bar[34] (solid lines) and 50 bar (dashed lines).*

polymer	gas	k_D (cm³(STP) cm⁻³ pol bar⁻¹)		c'_H (cm³(STP) cm⁻³ pol)		b (bar⁻¹)	
		10 bar*	50 bar*	10 bar*	50 bar*	10 bar*	50 bar*
CANAL-Et	N₂	0.29	0.40	20.9	12.7	0.04	0.06
	O₂	0.38	0.50	30.3	21.2	0.05	0.08
	CH₄	0.52	0.65	43.5	34.3	0.07	0.10
	CO₂	1.44	1.54	50.5	46.3	0.20	0.23
CANAL-Et-iPr	N₂	0.33	0.41	17.8	12.7	0.05	0.06
	O₂	0.42	0.50	28.6	22.3	0.06	0.07
	CH₄	0.58	0.66	38.4	33.7	0.08	0.10
	CO₂	1.60	1.56	46.8	47.2	0.23	0.23
CANAL-Me-iPr	N₂	0.34	0.46	24.4	16.6	0.05	0.06
	O₂	0.44	0.57	28.5	20.8	0.06	0.07
	CH₄	0.61	0.76	49.8	42.1	0.08	0.10
	CO₂	1.71	1.80	57.0	54.8	0.23	0.24

*Pressure at which the slope S vs T_C was calculated
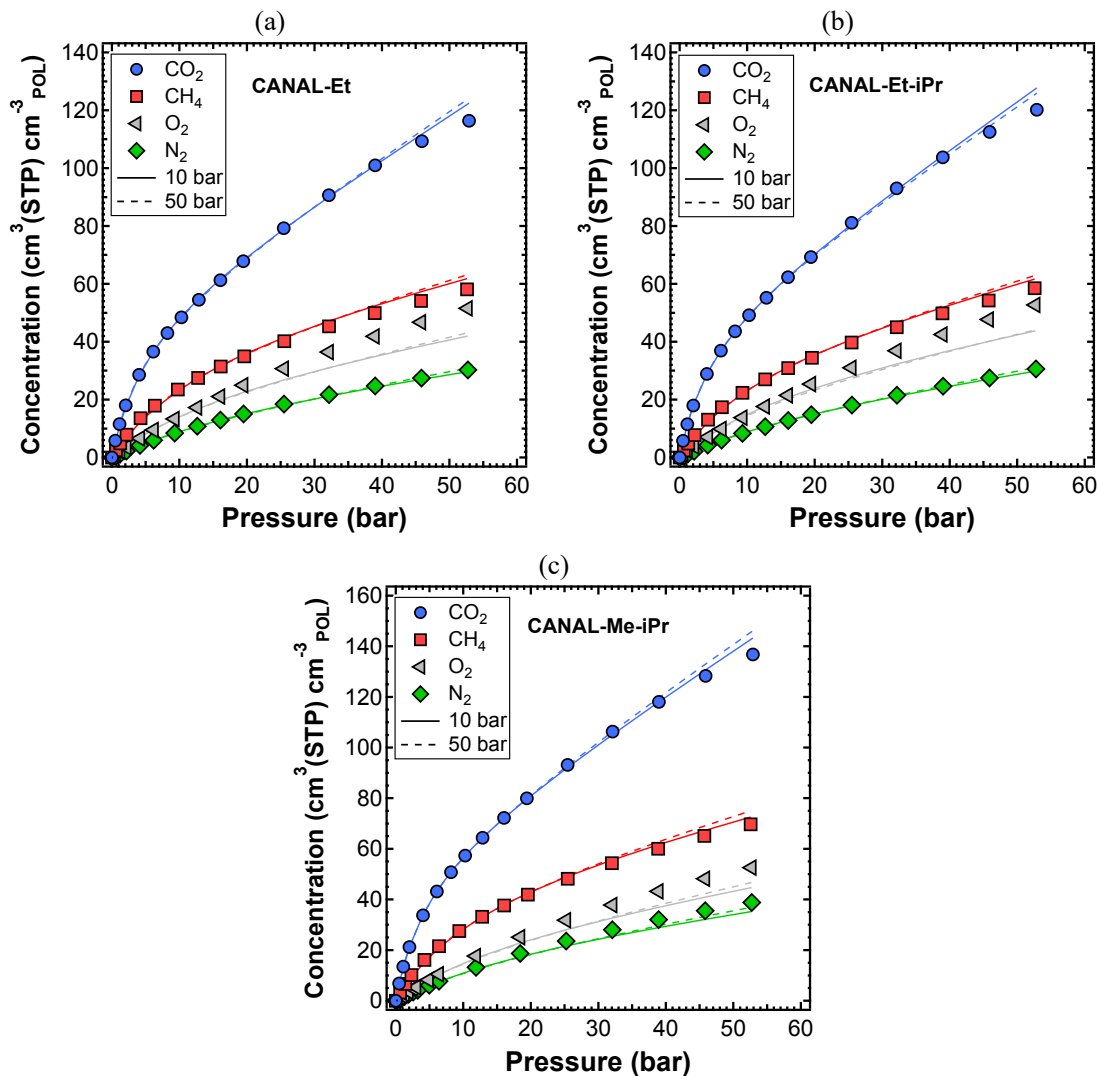
Figure 9.15: Pressure-based gas sorption isotherms (a) CANAL-Et, (b) CANAL-Et-iPr, and (c) CANAL-Me-iPr. DMS fittings were done constraining k_D and b to increase exponentially with the same slope calculated from the trend of S vs T_C both at 10 bar (solid lines) and 50 bar (dashed lines).

9.3. Conclusions on CANAL Ladder Polymers

The development of highly efficient and selective catalytic arene-norbornene annulation (CANAL) reaction enabled the synthesis of very high M_w ladder polymers. A compromise between molecular weight and solubility had to be achieved to make polymers which were soluble in common solvents such as THF and chloroform, while keeping the ability to be casted into films. Short alkyl substituents are key to maintain the good solubility of these high M_w (up to 750 kDa), ladder polymers. Three

species, CANAL-Et, CANAL-Et-iPr, and CANAL-Me-iPr, featured the required characteristics and formed self-standing films, allowing us to evaluate gas separation properties for these purely hydrocarbon and nonpolar rigid ladder polymers never applied before to this field. The alkyl substituents were found to have a dramatic effect on polymers' permeability, but a minimal effect on the polymers' permselectivity. CANAL-Me-iPr with methyl and isopropyl substituents had the highest permeability (up to 80% more than CANAL-Et for helium) because of its high solubility for gases and high FFV (27%). The high FFV in CANAL-Me-iPr was also confirmed by the polymer's high Langmuir capacity determined from a dual-mode sorption analysis performed on high-pressure sorption data. Permselectivity was not compromised by the higher permeability. Indeed, CANAL-Me-iPr revealed to have also the highest CO_2/CH_4 permselectivity, while solubility-selectivity was slightly lower at high pressure for the same gas pair. Between CANAL-Et and CANAL-Et-iPr, higher permeability was observed in CANAL-Et-iPr because of its generally greater diffusion coefficients compared to CANAL-Et. The greater diffusion coefficients are consistent with the larger intersegmental distance observed by WAXS experiments. Manipulating short alkyl substitution on ladder polymers, therefore, represents an effective strategy to increase the permeability of polymer films without compromising permselectivity. Similar extent of hysteresis was observed among all three polymers while performing high-pressure CO_2 sorption and desorption experiments, suggesting that the polymer backbone, rather than the alkyl substituents, may play a more important role in the moderate plasticization reported by CANALs. From variable-temperature pure-gas permeation experiments, CANALs show to have features of both dense polymers and porous materials. In particular, similar linear trends of E_D with d_k for the CANAL ladder polymers, rigid polyimide 6FDA-2,6-DAT, and PIMs suggest a similar mechanism for gas diffusion in these glassy polymers. Results also indicate that the transport mechanism for the most condensable gas tested, CO_2, in CANAL-Me-iPr is consistent with the surface diffusion model, while the other tested gases are not.

References

[1]   P. M. Budd, E. S. Elabas, B. S. Ghanem, S. Makhseed, N. B. McKeown, K. J. Msayib, C. E. Tattershall, D. Wang, *Adv. Mater.* **2004**, *16*, 456.

[2]   M. Carta, R. Malpass-Evans, M. Croad, Y. Rogan, J. C. Jansen, P. Bernardo, F. Bazzarelli, N. B. McKeown, *Science (80-.).* **2013**, *339*, 303.

[3]   B. S. Ghanem, R. Swaidan, X. Ma, E. Litwiller, I. Pinnau, *Adv. Mater.* **2014**, *26*, 6696.

[4]   N. Du, H. B. Park, G. P. Robertson, M. M. Dal-Cin, T. Visser, L. Scoles, M. D. Guiver, *Nat. Mater.* **2011**, *10*, 372.

[5]   I. Rose, C. G. Bezzu, M. Carta, B. Comesanã-Gándara, E. Lasseuguette, M. C. Ferrari, P. Bernardo, G. Clarizia, A. Fuoco, J. C. Jansen, K. E. Hart, T. P. Liyana-Arachchi, C. M. Colina, N. B. McKeown, *Nat. Mater.* **2017**, *16*, 932.

[6]   M. Carta, M. Croad, R. Malpass-Evans, J. C. Jansen, P. Bernardo, G. Clarizia, K. Friess, M. Lanč, N. B. McKeown, *Adv. Mater.* **2014**, *26*, 3526.

[7]   N. B. McKeown, P. M. Budd, *Chem. Soc. Rev.* **2006**, *35*, 675.

[8]   Y. C. Teo, H. W. H. Lai, Y. Xia, *Chem. - A Eur. J.* **2017**, *23*, 14101.

[9]   S. Liu, Z. Jin, Y. C. Teo, Y. Xia, *J. Am. Chem. Soc.* **2014**, *136*, 17434.

[10]   H. W. H. Lai, Y. C. Teo, Y. Xia, *ACS Macro Lett.* **2017**, *6*, 1357.

[11]   H. W. H. Lai, S. Liu, Y. Xia, *J. Polym. Sci. Part A Polym. Chem.* **2017**, *55*, 3075.

[12]   M. A. Abdulhamid, H. W. H. Lai, Y. Wang, Z. Jin, Y. C. Teo, X. Ma, I. Pinnau, Y. Xia, *Chem. Mater.* **2019**, acs. chemmater.8b05359.

[13]   D. I. Chai, P. Thansandote, M. Lautens, *Chem. - A Eur. J.* **2011**, *17*, 8175.

[14]   A. Bondi, *J. Phys. Chem.* **1964**, *68*, 441.

[15]   P. Li, T. S. Chung, D. R. Paul, *J. Memb. Sci.* **2014**, *450*, 380.

[16]   R. Swaidan, M. Al-Saeedi, B. Ghanem, E. Litwiller, I. Pinnau, *Macromolecules* **2014**, *47*, 5104.

[17]   L. M. Robeson, M. E. Dose, B. D. Freeman, D. R. Paul, *J. Memb. Sci.* **2017**, *525*, 18.

[18]   B. E. Poling, J. M. Prausnitz, J. P. O'Connell, *The Properties of Gases and Liquids*, McGraw-Hill, **1987**.

[19]   M. L. Jue, C. S. McKay, B. A. McCool, M. G. Finn, R. P. Lively, *Macromolecules* **2015**, *48*, 5780.

[20]   S. Brunauer, P. H. Emmett, E. Teller, *J. Am. Chem. Soc.* **1938**, *60*, 309.

[21]   E. R. Gilliland, R. F. Baddour, G. P. Perkinson, K. J. Sladek, *Ind. Eng. Chem. Fundam.* **1974**, *13*, 95.

[22]   A. J. Robell, E. V. Ballou, M. Boudart, *J. Phys. Chem.* **1964**, *68*, 2748.

[23]   R. Srinivasan, S. R. Auvil, P. M. Burban, *J. Memb. Sci.* **1994**, *86*, 67.

[24]   T. Masuda, Y. Iguchi, B.-Z. Tang, T. Higashimura, *Polymer (Guildf).* **1988**, *29*, 2041.

[25]   P. M. Budd, N. B. McKeown, B. S. Ghanem, K. J. Msayib, D. Fritsch, L. Starannikova,

N. Belov, O. Sanfirova, Y. Yampolskii, V. Shantarovich, *J. Memb. Sci.* **2008**, *325*, 851.

[26]   S. Thomas, I. Pinnau, N. Du, M. D. Guiver, *J. Memb. Sci.* **2009**, *333*, 125.

[27]   B. D. Freeman, *Macromolecules* **1999**, *32*, 375.

[28]   L. M. Robeson, *J. Memb. Sci.* **1991**, *62*, 165.

[29]   L. M. Robeson, *J. Memb. Sci.* **2008**, *320*, 390.

[30]   W. W. Brandt, *J. Phys. Chem.* **1968**, *63*, 1080.

[31]   T.-S. Chung, C. Cao, R. Wang, *J. Polym. Sci. Part B Polym. Phys.* **2004**, *42*, 354.

[32]   A. Fuoco, B. Comesaña-Gándara, M. Longo, E. Esposito, M. Monteleone, I. Rose, C. G. Bezzu, M. Carta, N. B. McKeown, J. C. Jansen, *ACS Appl. Mater. Interfaces* **2018**, *10*, 36475.

[33]   P. M. Budd, K. J. Msayib, C. E. Tattershall, B. S. Ghanem, K. J. Reynolds, N. B. McKeown, D. Fritsch, *J. Memb. Sci.* **2005**, *251*, 263.

[34]   Z. P. Smith, D. F. Sanders, C. P. Ribeiro, R. Guo, B. D. Freeman, D. R. Paul, J. E. McGrath, S. Swinnea, *J. Memb. Sci.* **2012**, *415–416*, 558.

[35]   O. Vopička, M. G. De Angelis, N. Du, N. Li, M. D. Guiver, G. C. Sarti, *J. Memb. Sci.* **2014**, *459*, 264.

[36]   S. M. Jordan, G. K. Fleming, W. J. Koros, *J. Polym. Sci. Part B Polym. Phys.* **1990**, *28*, 2305.

[37]   G. K. Fleming, W. J. Koros, *Macromolecules* **1986**, *19*, 2285.

[38]   M. Galizia, W. S. Chi, Z. P. Smith, T. C. Merkel, R. W. Baker, B. D. Freeman, *Macromolecules* **2017**, *50*, 7809.

[39]   E. Ricci, M. De Angelis, *Membranes (Basel).* **2019**, *9*, 8.

10. New ROMP Polymers with Tailored Properties and High CO$_2$ Plasticization Resistance

This chapter has been partially adapted from the following reference: Y. He†, F.M. Benedetti†, S. Lin, C. Liu, Y. Zhao, H.-Z. Ye, T. van Voorhis, M.G. De Angelis, T.M. Swager, Z.P. Smith; *Polymers with Side Chain Porosity for Ultrapermeable and Plasticization Resistant Materials for Gas Separations*; submitted to Advanced Materials.

As discussed in the introduction of this dissertation, polymer membranes with ultrahigh CO$_2$ permeability and high plasticization resistance are essential to provide membrane technology with commercially interesting properties to be applied at industrial level. This may increase the energy efficiency and mitigate environmental problems, especially in natural gas purification and post-combustion carbon capture applications. In the framework of this PhD, a novel class of porous polymers obtained via Ring Opening Metathesis Polymerization (ROMP) was studied for the first time to investigate the gas separation performance. This new family of materials has a flexible backbone with rigid side chains and can be easily tuned by changing functionalities attached to the side chains. These polymers could cover a wide range of gas separation performance, from ultrahigh CO$_2$ permeability (*i.e.*, > 21000 Barrer) and moderate selectivity, to high selectivity towards different gas pairs (*i.e.*, CO$_2$/CH$_4$ selectivity ≈12) and lower permeability. In all cases, they were featuring an exceptional plasticization resistance, and CO$_2$-induced plasticization pressure was always recorded to be > 51 bar. Compared to other polymers of intrinsic microporosity (PIMs) reported, the rate of physical aging was also slower in some cases, especially for gases with smaller effective diameters (*i.e.* He, H$_2$, and O$_2$).

In the following sections, the focus will be on CF$_3$-ROMP, the most permeable polymer that was synthesized and characterized among the ROMP polymers studied. It will be compared with an analogous non-fluorinated polymer, OMe-ROMP, and PIM-1 as a benchmark.

10.1.   Introduction and Motivations

Highly energy-efficient separations can be achieved using polymer membranes as they do not require thermal regeneration, phase change, or moving parts.[1,2] Increasing the permeability of polymer membranes used for gas separation is essential in enhancing productivity and reducing membrane size required for large-scale gas and vapor separations.[3] These applications include natural gas upgrade, hydrogen purification, air separation, and CO$_2$ capture from flue gas, as discussed in chapter 3 of this dissertation.[4] Despite the advance in backbone rigidity of polymer chains[5–9] whose benefits were discussed in chapter 9, a relatively unexplored design strategy to create porous polymers is to attach rigid side chains to a flexible backbone to form so-called "bottlebrush" polymers. Recently, Zhao and He *et al.*[10] have discovered that these polymers can be highly porous due to inefficient packing between rigid, non-compliant side chains. The resulting polymers revealed to be highly soluble in common organic solvents such as chloroform, and possess Brunauer−Emmett−Teller (BET) internal surface areas as high as 780 m^2/g. In addition, since rigid macromonomers containing polymerizable units were made first before polymerization, it was easier to incorporate different functionalities into this class of polymer compared to PIMs, which mainly relies on post-polymerization functionalization.[11,12]

It is well-known that the fluorination of polymers introduces many remarkable properties such as thermal stability and non-wettability, of wide interest in commercial applications.[13] In terms of gas separation, previous studies have shown that the introduction of fluorinated moieties in aromatic polyimides increased dramatically the gas permeability with little impact on the selectivity.[14–16] In poly(organosiloxanes), it was found that CO$_2$ permeability and CO$_2$/CH$_4$ selectivity increased simultaneously by incorporating fluorine-containing groups.[17] These effects can be rationalized by quadruple-dipole interaction between CO$_2$ and fluorinated moieties as well as the large polarizability of

CO$_2$, which lead to increased solubility of CO$_2$ in fluorine-rich phases.[18,19] Given the synthetic versatility of porous polymers containing flexible backbone and rigid side chains, it makes sense to investigate how the introduction of fluorinated moieties affects their gas transport properties compared to the hydrocarbon analogs.

10.2. Materials: CF$_3$-ROMP and OMe-ROMP

10.2.1. Chemical Structure

As above mentioned, the synthetic procedures for CF$_3$-ROMP and OMe-ROMP have been previously reported by Zhao and He *et al.*, and other details were reported in chapter 5.8 of this dissertation.[10] All solvents, including methanol and ethanol, were of ACS reagent grade or higher.

Ring-Opening Metathesis Polymerization (ROMP) is a chain-growth living/controlled polymerization where cyclic olefins are converted to polymeric materials.[20] ROMP polymers are characterized by high molecular weight, an important feature to cast polymers into films, and low poly-dispersity (*i.e.*, PDI close to 1).[20] To synthesize ROMP polymers, monomer **(1)** was polymerized to make an oligomer **(2)**, which eventually underwent a polymerization where the norbornene cycle was opened and the typical "bottlebrush" structure was formed, as illustrated in **Figure 10.1**. The "*X*" on the polymer chain states for a generic functionality that can be chosen based on the desired properties that want to be achieved. This is a remarkable feature that makes this novel approach very flexible and tunable.
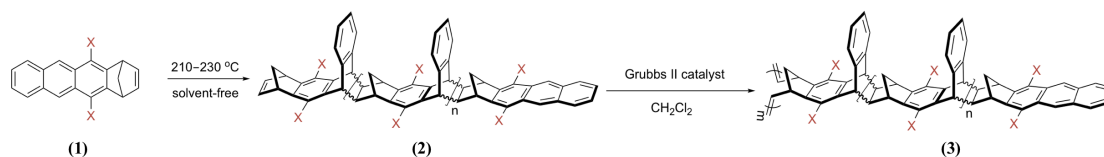

Figure 10.1: *Reaction scheme used to synthesize porous polymers through ROMP.*[10]

The two structures that will be discussed in this section of the chapter feature –CF$_3$ and –OMe functionalities to form CF$_3$-ROMP and OMe-ROMP, respectively, and are reported in **Figure 10.2**.
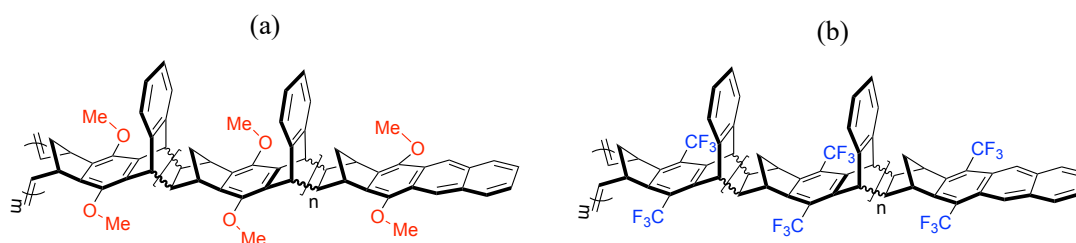

Figure 10.2: Molecular structure of (a) OMe-ROMP and (b) CF$_3$-ROMP.

The molecular structure of these polymers was geometrically optimized through molecular mechanics simulations by the colleagues in Professor van Voorhis at MIT using the MMFF94 force field[21–23] implemented in *Avogadro*.[24] **Figure 10.3** reports results for a CF$_3$-ROMP main flexible chain with 5 side chains (*i.e.*, five repeating units), whose length and stereochemistry were selected randomly. Results revealed important information on how the polymer chain rearrange in space and could help explaining the transport properties measured in this work.
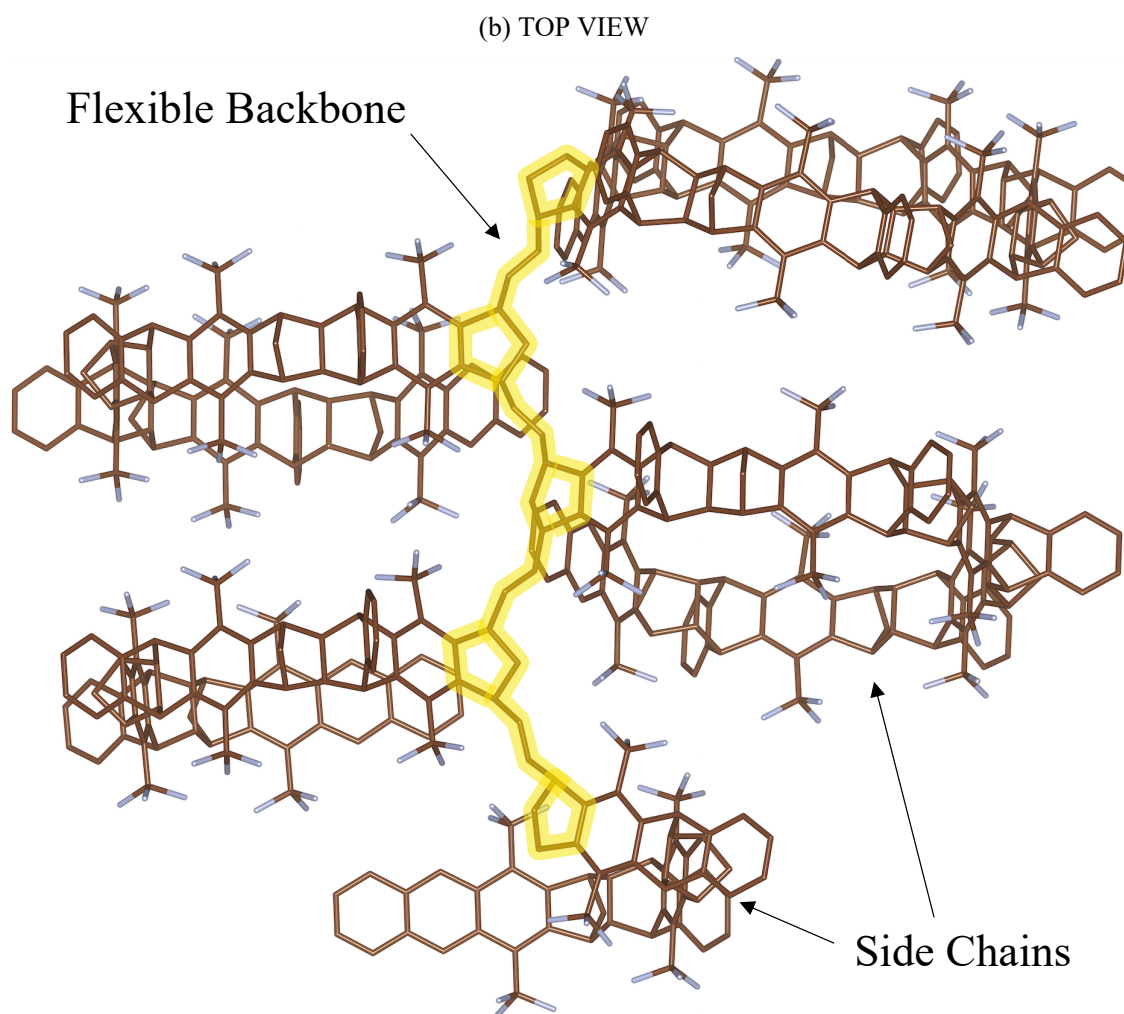
(a) SIDE VIEW

Side Chains
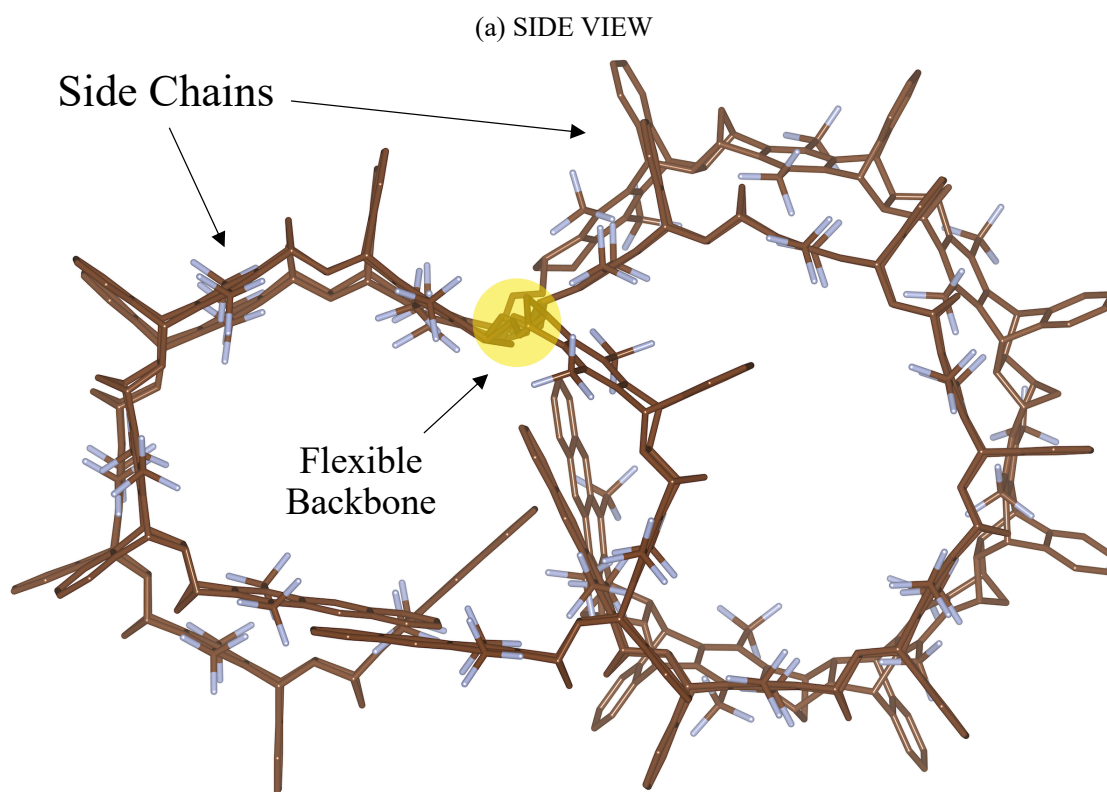
Flexible
Backbone

Figure 10.3: Geometrically optimized structure of CF₃-ROMP: (a) side view, and (b) top view. Rigid side chains and flexible backbone is highlighted.

PIM-1 was kindly provided by Dr. Helms group at Lawrence Berkeley National Laboratory and was synthesized according to previously published procedures.[25–27] It was used as a benchmark for this new class of polymers and the chemical structure is represented in **Figure 10.4**. To be properly compared, all the polymers underwent the same treatments so that they have a similar history.
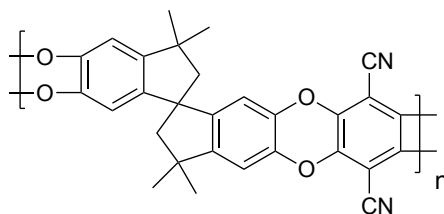
Figure 10.4: *Chemical structure of the archetypal polymer of intrinsic microporosity: PIM-1, used as a benchmark for ROMP polymers.*

10.2.2. ^{1}H NMR and GPC Results

^{1}H NMR spectra for all compounds were acquired in CDCl$_3$ on equipment and with methods described in the experimental methods chapter. Chemical shifts (δ) are reported in parts per million (ppm) and referenced with TMS. Details on the GPC experiments are reported in the dedicated section of the experimental methods chapter.

The NMR and GPC for CF$_3$-ROMP (**Figure 10.5**), OMe-ROMP (**Figure 10.6**), and PIM-1 (**Figure 10.7**) used in membrane fabrication are shown below:
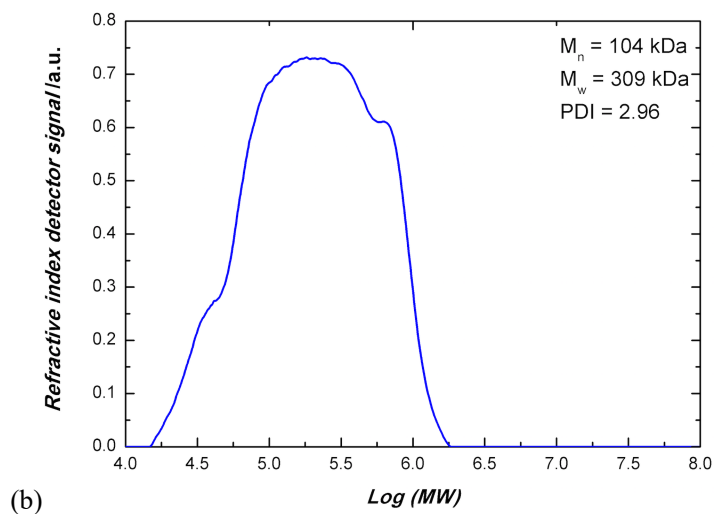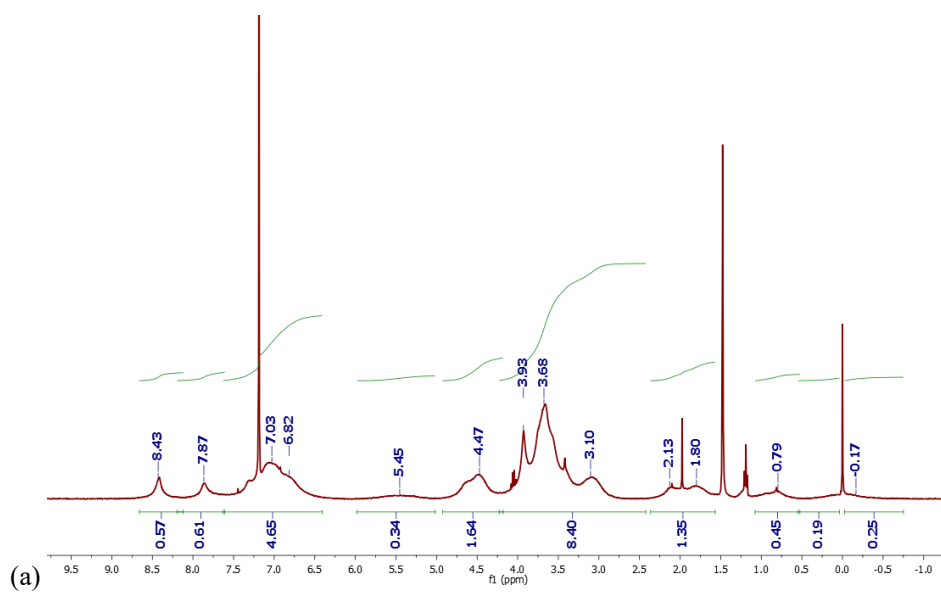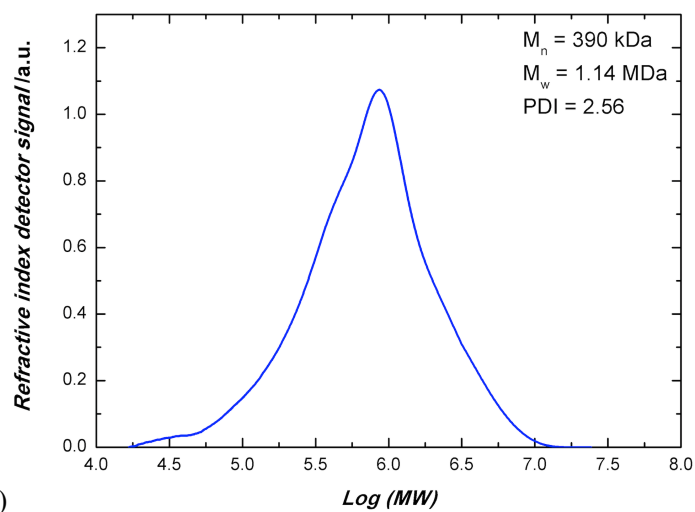

(a)
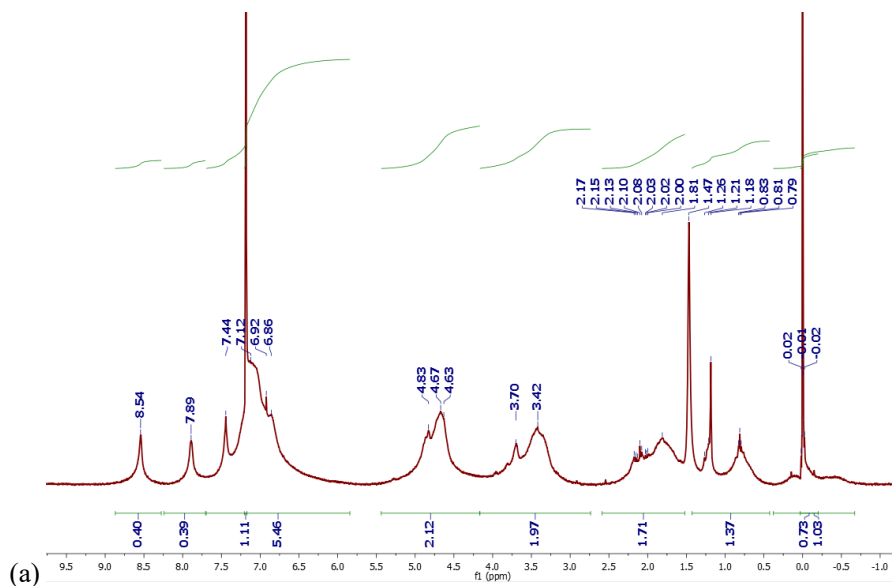
Figure 10.5: *(a) ^{1}H-NMR and (b) GPC for CF$_3$-ROMP.*

Figure 10.6: *(a)* ^{1}*H-NMR and (b) GPC for OMe-ROMP.*
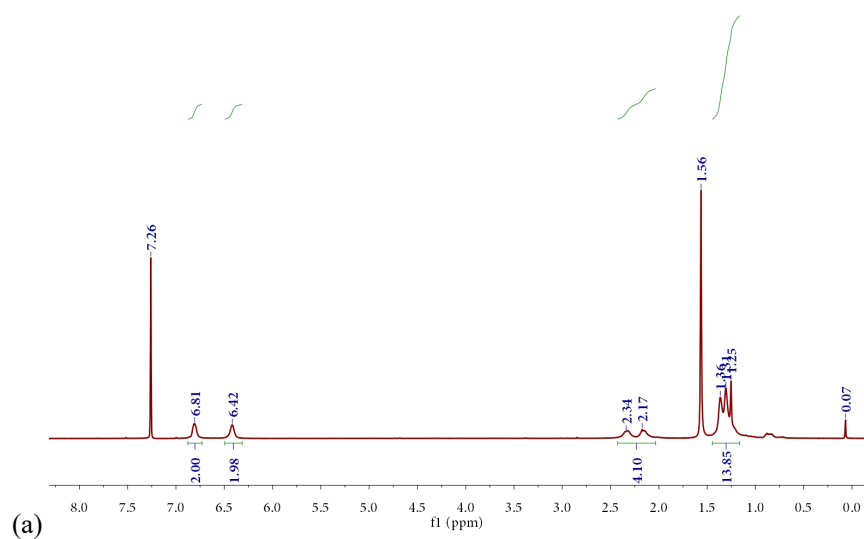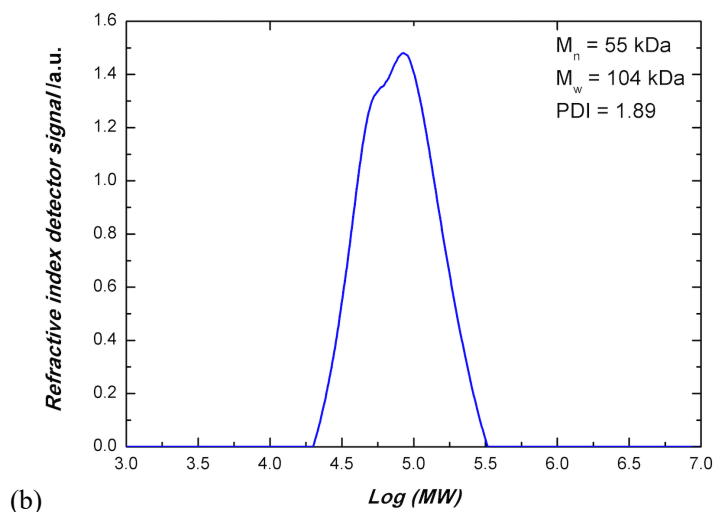
Figure 10.7: (a) ^{1}H-NMR and (b) GPC for PIM-1.

10.2.3. BET and Pore Size Distribution

The porosity of CF$_3$-ROMP, OMe-ROMP, and PIM-1 in powder form was measured using cryogenic nitrogen adsorption isotherm at 77 K with a saturation pressure of $p_0 = 1$ bar. CF$_3$-ROMP, OMe-ROMP, and PIM-1 have a Brunauer–Emmett–Teller (BET)[28] internal surface area of 700 m^2 g^{-1}, 146 m^2 g^{-1}, and 800 m^2 g^{-1}, respectively. Pore-size distributions were analyzed using the nonlocal density functional theory (NLDFT)[29] based on carbon slit pore geometry.
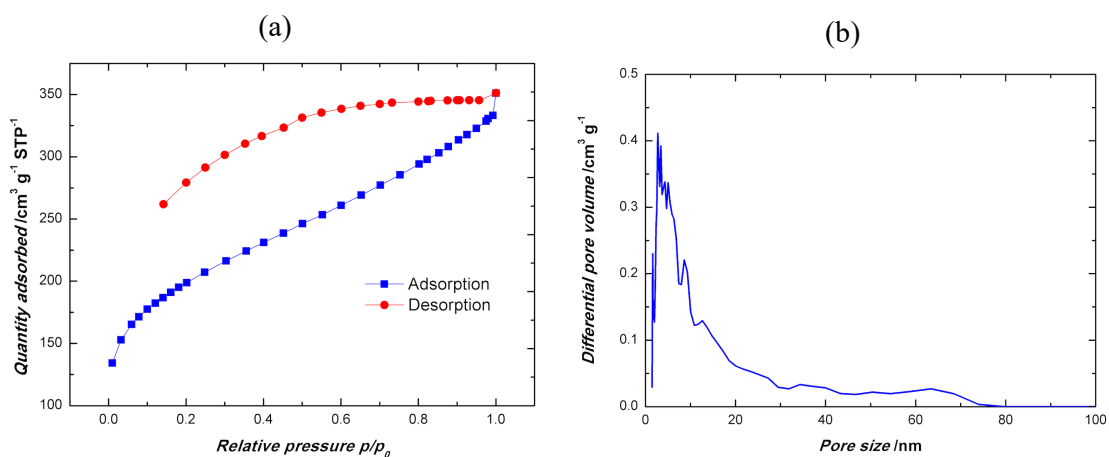
Figure 10.8: (a) BET and (b) Pore size distribution for CF$_3$-ROMP.
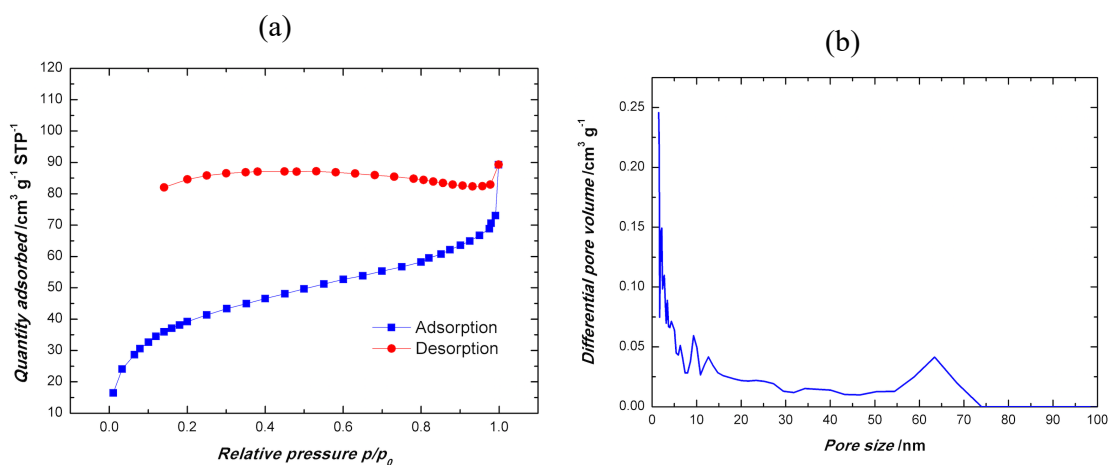
Figure 10.9: *(a) BET and (b) Pore size distribution for OMe-ROMP.*
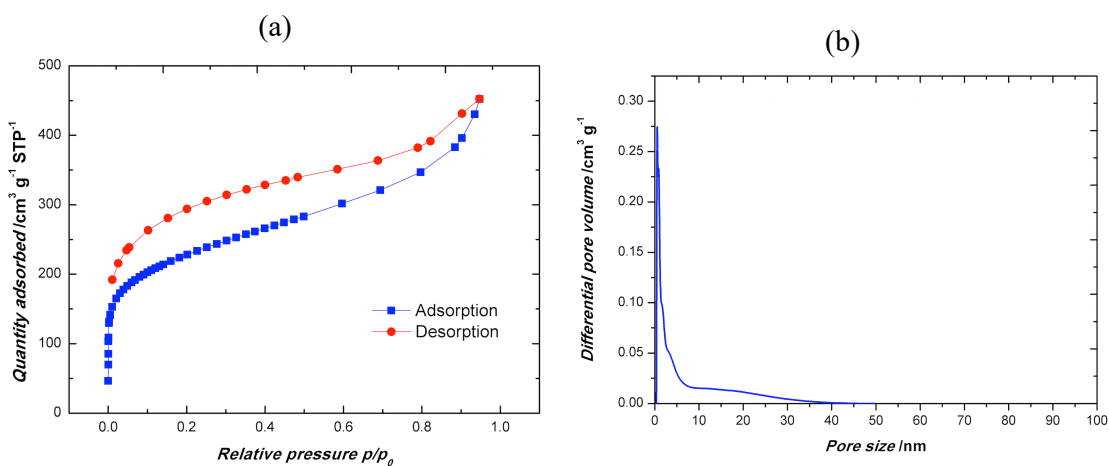
Figure 10.10: *(a) BET and (b) Pore size distribution for PIM-1.*

10.2.4. Membrane Fabrication and Treatments

Self-standing films with thickness ranging from 75 to 180 μm were obtained via drop casting technique from 3 wt.% solutions of ROMP polymers and chloroform, following the procedure described chapter in 5.1.2 of this dissertation. Pictures of films are reported in **Figure 10.11**. Films of PIM-1 were obtained following the same approach.
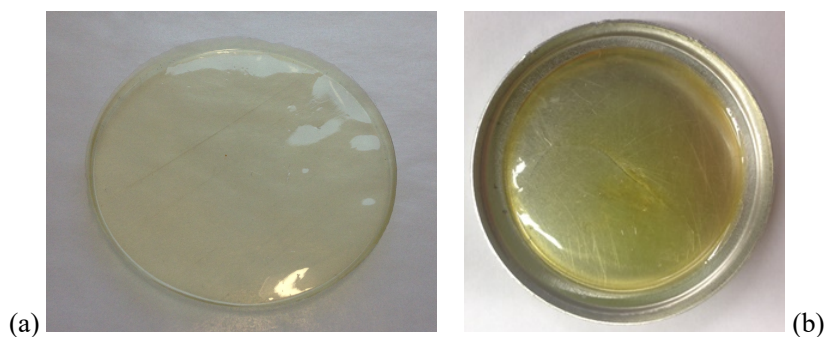
Figure 10.11: (a) CF₃-ROMP and b) OMe-ROMP films as casted from chloroform solutions.

After 4 days of slow solvent evaporation, films were ready for post-casting treatment. Different treatments, which are described below, were performed on the membranes to investigate their effects on the transport properties:

(A) Soaking in liquid ethanol for 48 h, air-drying for 24 h, and applying dynamic vacuum at 35 °C for 4 h;

(B) Soaking in liquid ethanol for 48 h, air-drying for 24 h, and applying dynamic vacuum at 35 °C for 8 h;

(C) Thermal treatment at 120 °C for 24 h under dynamic vacuum, vapor methanol treatment at 180 mbar (partial pressure of methanol) for 12 h, and applying dynamic vacuum at 100 °C for 16 h;

(D) Thermal treatment at 120 °C for 24 h under dynamic vacuum, vapor methanol treatment at 160 mbar to 200 mbar (partial pressure of methanol) for 12 h, and applying dynamic vacuum at 70 °C overnight;

(E) Thermal treatment at 120 °C for 24 h and applying dynamic vacuum;

The dynamic vacuum provided by the *Welch DuoSeal 1405* vacuum pumps was < 0.01 torr. Different batches of the same polymer revealed to have different BET internal surface area. Interestingly, it was found that BET values can be related to molecular number (M_n) values, which in turn affected the film formation. In particular, as shown in **Figure 10.12**, below a certain threshold value of M_n, values of the internal surface area were almost constant (*i.e.*, ~590 m^2 g^{-1} in the case of OMe-ROMP). For molecular numbers higher than 250 kDa, the internal surface area decreased. However, this had another implication

on the material properties, because films can be obtained just reaching high M_n values as shown in **Figure 10.12**. Transport properties of the two batches with the highest molecular number that could form a film were investigated. The first sample had a BET internal surface area of about 146 m^2 g^{-1} and a M_n equal to 390 kDa, while the other one had a BET of about 305 m^2 g^{-1} and M_n of 309 kDa. Despite of the remarkable difference in the internal surface area, permeability of the two samples were comparable. The permeability of smaller gases such as H_2, O_2 and CO_2 differed less than 1%, while that of N_2 and CH_4 revealed to be ~10 and ~20% higher, respectively, for the sample with higher BET surface area. More results are reported in **Table 10.1**. However, the relationship between surface area and transport properties is still under investigation, and these data represent just preliminary results.
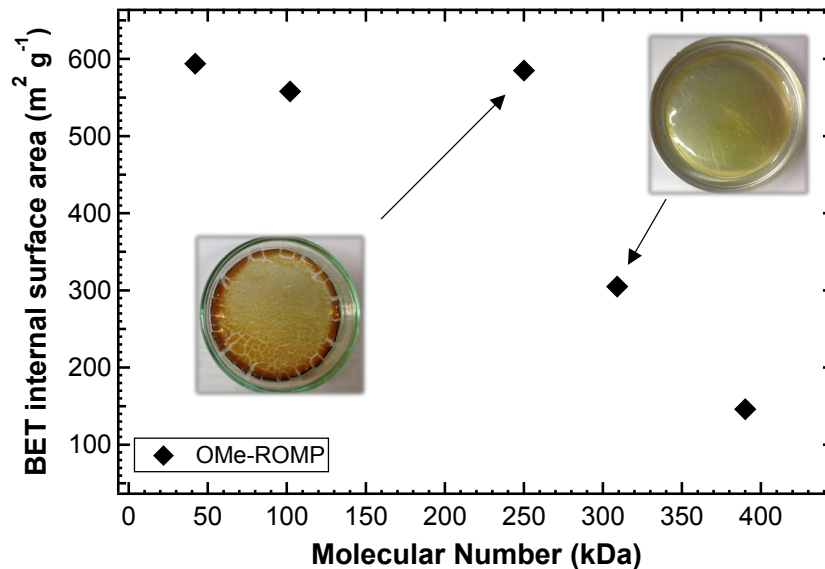
Figure 10.12: BET surface area against Molecular Number for different batches of OMe-ROMP.

10.2.5. Thermal Stability

Thermogravimetric analysis (TGA) was used to assess the thermal stability of ROMP polymers/PIM-1 and verify that all the casting solvent (chloroform) and the non-solvent used in the post-casting treatment (ethanol or methanol), were completely removed from the films before performing gas permeation experiments, to ensure that all the transport properties evaluated can be attributed to gas/polymer couple. **Figure 10.13a** shows three curves for CF_3-ROMP, OMe-ROMP, and PIM-1 that all underwent the same

treatment, (B).[30] These were samples used to perform aging experiments. There was no mass loss up to 350 °C for each polymer, which indicated that neither chloroform nor ethanol were present in any films at the end of the post-casting treatment (**Figure 10.13a**). Furthermore, both ROMP polymers showed excellent thermal stability. CF_3-ROMP degradation started at ~380 °C, while OMe-ROMP degradation started at ~350 °C. This is a feature that meets the requirement of many industrial applications which operate at high temperatures.

Different treatments, described in section 10.2.4 of this chapter, were applied to membranes made from new ROMP polymers to investigate how transport properties changed as a function of the post-casting treatment as reported in **Table 10.1**. Among those treatments, TGA was performed on samples that underwent treatment (B), (D), and (E) and curves are shown in **Figure 10.13b** and **Figure 10.13c**. Within experimental error, all the curves essentially overlapped, indicating that all the treatments led to membranes free of casting solvent and swelling agents.
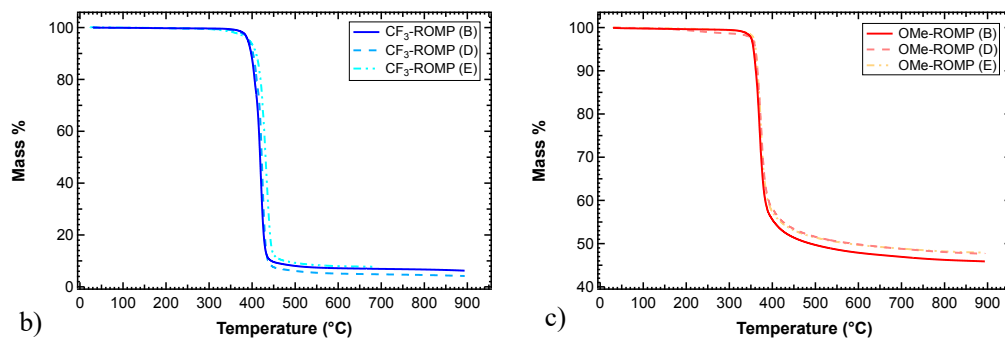

a)
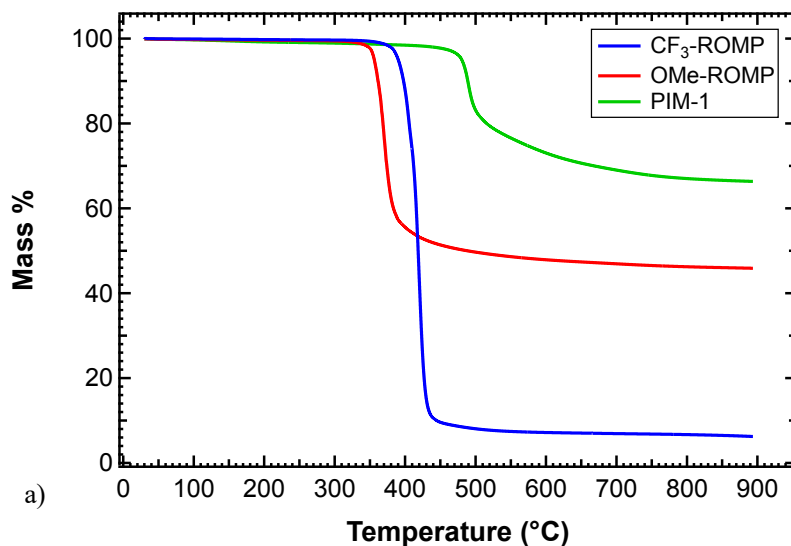
Figure 10.13: *a) TGA comparison between CF₃-ROMP, OMe-ROMP, and PIM-1 samples that underwent treatment **(B)** b), c) TGA of different CF₃-ROMP and OMe-ROMP samples, respectively, treated following different procedures: **(B)**, **(D)**, and **(E)**.*

10.3.   Gas Transport Properties

10.3.1. Effect of the Post-Casting Treatment

To characterize novel ROMP polymers, permeability and diffusivity were measured for six light gases (He, H_2, CH_4, N_2, O_2, and CO_2) at 35 °C and ~1 bar. It is known that for glassy polymers, including PIMs, transport properties depend on film history and aging time, which can lead to a wide distribution of values for permeability and diffusivity.[8,31] For this reason, different post-casting treatments and aging times were carefully tracked while performing experiments to monitor to which extent they could affect performance. Results obtained are summarized in **Table 10.1**. Permeability was measured on the automated variable-pressure closed-volume *Maxwell Robotics* permeation system described in section 5.6.1. Diffusivity was calculated with the time-lag technique, elucidated in the theoretical chapter. Since the permeability of ROMP polymers and PIM-1 tested was remarkably high in some cases, time-lag values obtained were often close to 1-2 seconds, which is close to the resolution of the acquisition time of the permeation system. For this reason, diffusion coefficients were not reported in **Table 10.1** when θ was too small, typically for He, H_2, and sometimes O_2 and CO_2.

Table 10.1: *Gas permeability and diffusivity values for CF$_3$-ROMP, OMe-ROMP, and PIM-1 measured from films with different history:* **(A)** *Soaking in liquid ethanol for 48 h, air-drying for 24 h, and applying dynamic vacuum at 35 °C for 4 h,* **(B)** *Soaking in liquid ethanol for 48 h, air-drying for 24 h, and applying dynamic vacuum at 35 °C for 8 h,* **(C)** *Thermal treatment at 120 °C for 24 h under dynamic vacuum, vapor methanol treatment at 180 mbar (partial pressure of methanol) for 12 h, and applying dynamic vacuum at 100 °C for 16 h,* **(D)** *Thermal treatment at 120 °C for 24 h under dynamic vacuum, vapor methanol treatment at 160 mbar to 200 mbar (partial pressure of methanol) for 12 h, and applying dynamic vacuum at 70 °C overnight,* **(E)** *Thermal treatment at 120 °C for 24 h and applying dynamic vacuum.*

*(*)Two OMe-ROMP samples with similar history (treatment (**D**)) OMe-ROMP sample with thickness equal to 157 μm had a BET internal surface area of 146 m^2 g^{-1} and a Molecular Number (M$_n$) equal to 390 kDa, while the one with sample thickness equal to 144 μm had a BET of about 305 m^2 g^{-1} while M$_n$ revealed to be 309 kDa.*

Permeability (P$_X$) in Barrer (10^{-10} cm^3(STP) cm cm^{-2} s^{-1} cmHg^{-1}), Diffusion Coefficient (D$_X$) in (10^{-8} cm^2 s^{-1}). All data was calculated at 35 °C and upstream pressure ~1 bar.

Polymer	Treatment	Aging (h)	Thickness (μm)	$\mathcal{P}_{He}$ ($\mathcal{D}_{He}$)	$\mathcal{P}_{H_2}$ ($\mathcal{D}_{H_2}$)	$\mathcal{P}_{CH_4}$ ($\mathcal{D}_{CH_4}$)	$\mathcal{P}_{N_2}$ ($\mathcal{D}_{N_2}$)	$\mathcal{P}_{O_2}$ ($\mathcal{D}_{O_2}$)	$\mathcal{P}_{CO_2}$ ($\mathcal{D}_{CO_2}$)
CF$_3$-ROMP	A	1	148	4296 (/)	8303 (/)	3970 (319)	2367 (570)	4354 (995)	21266 (633)
	"	830	"	/ (/)	6816 (/)	2942 (263)	1825 (493)	/ (/)	16148 (/)
	B	1	119	4372 (/)	8327 (/)	3053 (245)	1992 (509)	4035 (888)	18490 (513)
	"	1000	"	3993 (/)	7285 (/)	1995 (154)	1464 (366)	3326 (632)	15104 (418)
	C	1	80	/ (/)	4535 (/)	/ (/)	980 (287)	2072 (/)	/ (/)
	"	500	"	2685 (/)	4736 (/)	/ (/)	935 (209)	2088 (/)	9919 (/)
	D	80	109	/ (/)	4864 (/)	1778 (188)	1195 (460)	2346 (/)	11144 (461)
	"	100	"	/ (/)	4844 (/)	1718 (173)	/ (/)	/ (/)	10910 (514)
	"	300	110	/ (/)	4719 (/)	1648 (225)	1098 (/)	2285 (/)	10815 (429)
	"	310	"	/ (/)	4708 (/)	1598 (214)	/ (/)	/ (/)	/ (/)
	"	600	"	/ (/)	4679 (/)	1501 (202)	1039 (/)	2220 (/)	10490 (436)
	"	610	"	/ (/)	4677 (/)	/ (/)	/ (/)	2258 (640)	/ (/)
	"	1100	"	/ (/)	4661 (/)	1419 (134)	1008 (410)	2187 (/)	10324 (443)
	E	120	141	/ (/)	3048 (2820)	703 (81.9)	523 (211)	1244 (429)	6361 (257)

OMe-ROMP	B	1	160	664 (/)	1409 (2679)	270 (25.8)	153 (73.6)	414 (153)	2900 (91.4)
"		1000	"	563 (/)	1127 (1955)	178 (18.0)	112 (60.6)	313 (134)	2154 (74.3)
	C	1	74	/ (/)	535 (/)	/ (/)	46 (21.1)	141 (78.4)	/ (/)
"		500	"	/ (/)	535 (/)	/ (/)	42 (19.4)	131 (63.8)	/ (/)
	D	100	157 (*)	/ (/)	698 (2038)	101 (15.6)	58 (45.4)	181 (120)	1357 (97.4)
"		110	"	/ (/)	697 (1844)	/ (/)	/ (/)	/ (/)	1319 (94.8)
"		150	144 (*)	/ (/)	696 (1697)	119 (16.4)	69 (41.3)	182 (95.2)	1343 (61.7)
	E	48	180	/ (/)	587 (1501)	85 (7.81)	52 (25.7)	150 (54.5)	1072 (36.0)
"		60	"	/ (/)	578 (924)	83 (7.45)	51 (30.5)	/ (/)	1053 (38.5)
PIM-1	B	1	119	2176 (/)	5251 (/)	1297 (81.9)	777 (189)	2177 (517)	12318 (268)
"		1000	"	1882 (/)	4437 (/)	896 (58.7)	576 (155)	1736 (450)	10005 (293)
	C	1	126	/ (/)	3293 (/)	/ (/)	444 (191)	1258 (/)	/ (/)
"		500	"	1481 (/)	3325 (/)	/ (/)	417 (153)	1213 (/)	/ (/)

The highest values of permeability were obtained for the films freshly soaked in liquid ethanol. In particular, CF$_3$-ROMP and OMe-ROMP achieved CO$_2$ permeability of ~21,300 Barrer and 2,900 Barrer, and a H$_2$ permeability of ~8,300 Barrer and ~1,400 Barrer, respectively. CF$_3$-ROMP gas permeabilities were about 60 to 200% higher than the non-aged PIM-1 film under the same ethanol treatment and testing conditions, which makes CF$_3$-ROMP among the most permeable polymers reported so far, second just to PIM-TMN-Trip[8], PIM-SBF[32], and PTMSP.[33,34] In contrast, OMe-ROMP exhibited significantly lower gas permeabilities compared to CF$_3$-ROMP and PIM-1 but higher permselectivity.

Figure 10.14 visually reveals the performance differences among the polymers investigated. Data reported refer to samples that underwent treatment **(B)** with identical aging history. Standard deviations were calculated using the error propagation approach.[35] By looking at the diffusivity and solubility contribution to permeability, **Figure 10.14b** shows that high diffusion coefficient values of each gas for CF$_3$-ROMP were the main reason behind high permeability values. **Figure 10.14c** illustrates that while PIM-1 solubility exceeded that of both ROMPs for CO$_2$ and CH$_4$, PIM-1 and CF$_3$-ROMP had similar solubility for N$_2$ and O$_2$. Selectivity followed the opposite trend among the three materials if compared to permeability, as expected from the trade-off usually observed in glassy polymers. **Figure 10.14d** shows that OMe-ROMP is the most selective polymer for almost all the gas pairs besides O$_2$/N$_2$ for which Tröge's base- and dioxane-based PIMs have shown excellent properties in the last 5 years.[7,9,36]
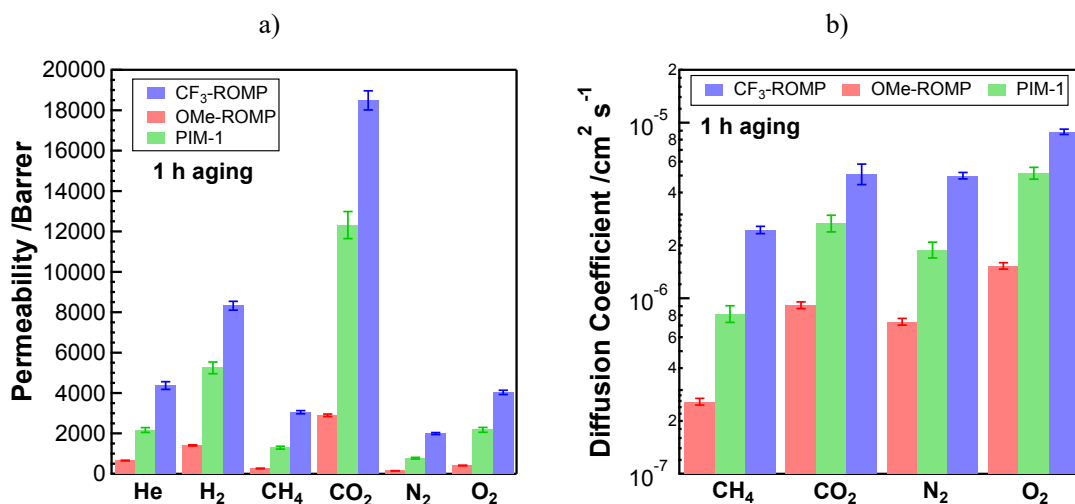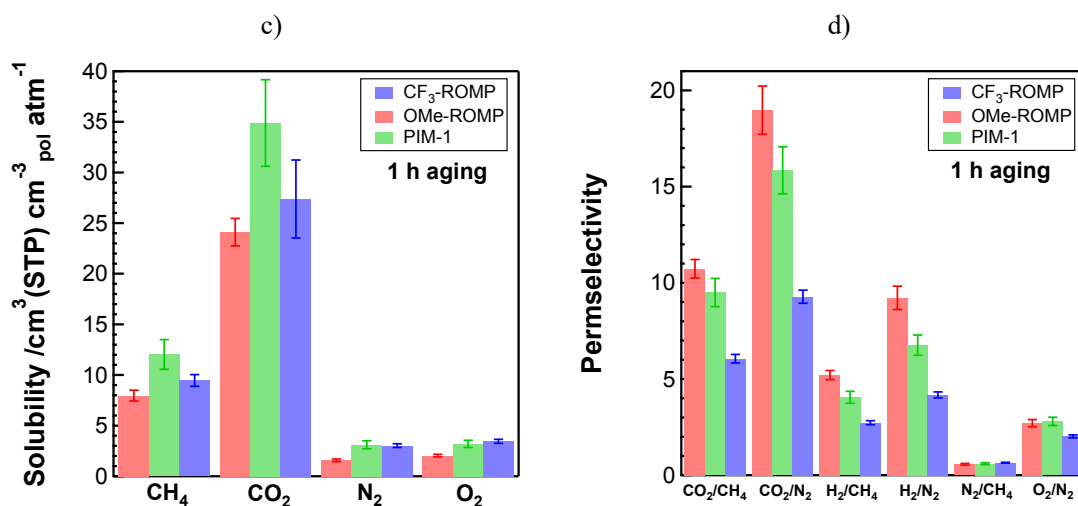
Figure 10.14*: Transport properties of ROMP polymers and PIM-1 at 35 °C and 1 bar upstream pressure that underwent treatment (B) after 1 h aging: a) permeability, b) diffusion coefficient, c) solubility coefficient, and d) permselectivity.*

The remarkably different gas transport behavior between CF_3-ROMP and OMe-ROMP is very interesting because they are structurally very similar. This can be rationalized by the higher BET surface area of CF_3-ROMP and favorable interaction between -CF_3 groups and gas molecules. The pendant -CF_3 group is bulkier and stiffer than -OMe, which hinders interchain packing and reduces intrachain rotational freedom, thus leading to higher porosity and higher diffusivity. Fluorine-containing moieties are also known to have high solubility for many light, non-polar gases such as CO_2 and O_2[37–39], in fact CF_3-ROMP solubility is higher than the non-fluorinated analogous. It may be the combination of both effects that led to the significant increase in gas permeabilities. These results were consistent with the effect of fluorination on other porous polymer systems such as polyimides and polycarbonates.[40] Because molecular mechanics simulation suggested side chain bending into "pocket-shape" to be one of the thermodynamically-stable conformers, it was also hypothesized that the pendant -CF_3 groups on the side chain may form fluorine-rich "nano-pocket" due to the curvature of side chain in 3D (**Figure 10.3**).

Compared to PIM-1, CF_3-ROMP exhibited lower permselectivity for all the gas pairs. The selectivity of gas pairs was dependent on both diffusivity-selectivity and solubility-selectivity. **Figure 10.15a**, and

b report mean values of diffusion coefficient and solubility coefficient data, averaged over 2,000 h of aging test to give a sense of the mean performance and not that measured at a specific aging time. **Figure 10.15c** plots the diffusion coefficient against the effective diameter squared. The slope of each curve is related to the molecular sieving capability. The steeper the more diffusivity-selective, thus -OMe > PIM-1 > -CF$_3$. **Figure 10.15d** represent the solubility as a function of critical temperature. According to **Figure 10.15b** and **d**, solubility-selectivity of CF$_3$-ROMP was close to PIM-1 for gas pairs such as CO$_2$/CH$_4$ and O$_2$/N$_2$, whereas its diffusivity-selectivity fell behind for all the gas pairs (**Figure 10.15a**, and **c**). Considering the difference in pore-size distribution between two polymers (**Figure 10.8b**, and **Figure 10.10b**), we hypothesize that the lower diffusivity-selectivity of CF$_3$-ROMP was most likely caused by polydispersity in length of the side chains, because microporosity was generated via inefficient packing between them. According to this hypothesis, diffusivity-selectivity may be improved by homogenizing the length of side chains and this effort is currently in progress.
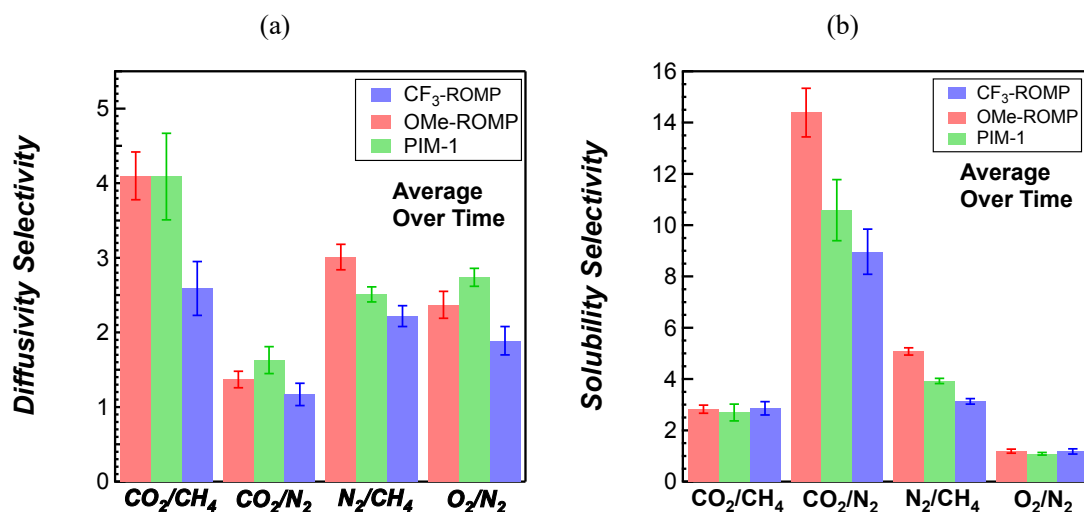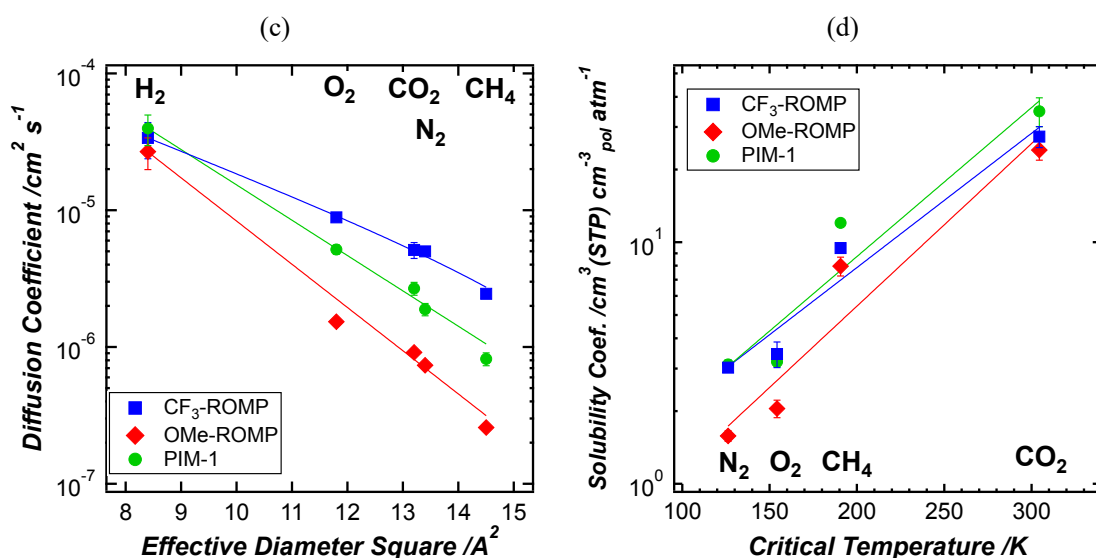
Figure 10.15*: (a) Diffusivity-selectivity averaged on the first 2,000 h aging, (b) Solubility-selectivity averaged on the first 2,000 h aging, (c) Diffusion coefficient plotted against effective diameter squared for CF$_3$-ROMP, OMe-ROMP, and PIM-1 at 1 h aging, right after liquid ethanol soaking for 48 h, air-drying for 24 h and full vacuum for 8 h at 35 °C, (d) Solubility of N$_2$, O$_2$, CH$_4$, and CO$_2$ in polymers as a function of critical temperature.*

It was shown that membranes that underwent aging for a certain amount of time, or films that were not soaked in ethanol, showed lower values of CO$_2$ permeability. In particular, CO$_2$ permeability was in the range of 6-21·10^3 Barrer for CF$_3$-ROMP and in the range of 1-3·10^3 Barrer for OMe-ROMP. Vapor methanol treatment was designed to provide a less invasive alternative to erase history from films. Partial pressures of 160 mbar to 200 mbar of methanol were reached after thermally treating the membranes at 120 °C for 24 h under vacuum. This approach led to considerably different results with respect to the traditional treatment procedure involving liquid alcohols. The permeability of ROMP polymers that underwent the vapor methanol treatment was approximately halved with respect to that obtained from films that were treated in liquid ethanol, while selectivity was generally higher. For example, CO$_2$/N$_2$ selectivity increased from 18.9 to 23.4 for OMe-ROMP.

All the data presented in this section were positioned on Robeson upper bound plots[41,42] in **Figure 10.16**, so that the results were compared with some of the most permselective polymers in the literature at present. Just the high-permeability areas of the graphs were considered to make the figures. CF$_3$-

ROMP surpassed the 2008 Robeson upper bound for H_2/CH_4 and was above the 1991 Robeson upper bound for all the other gas pairs investigated.
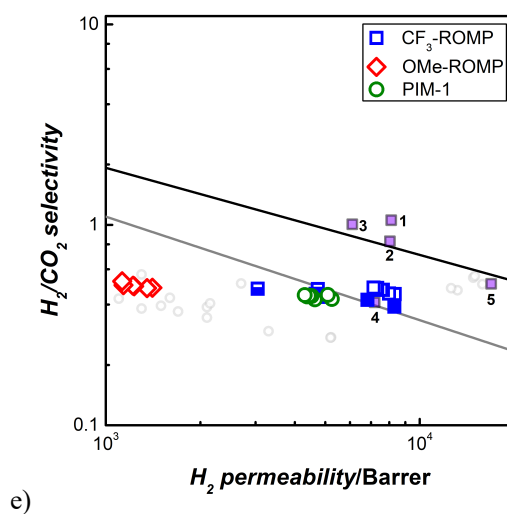

a)

b)

c)

d)

e)
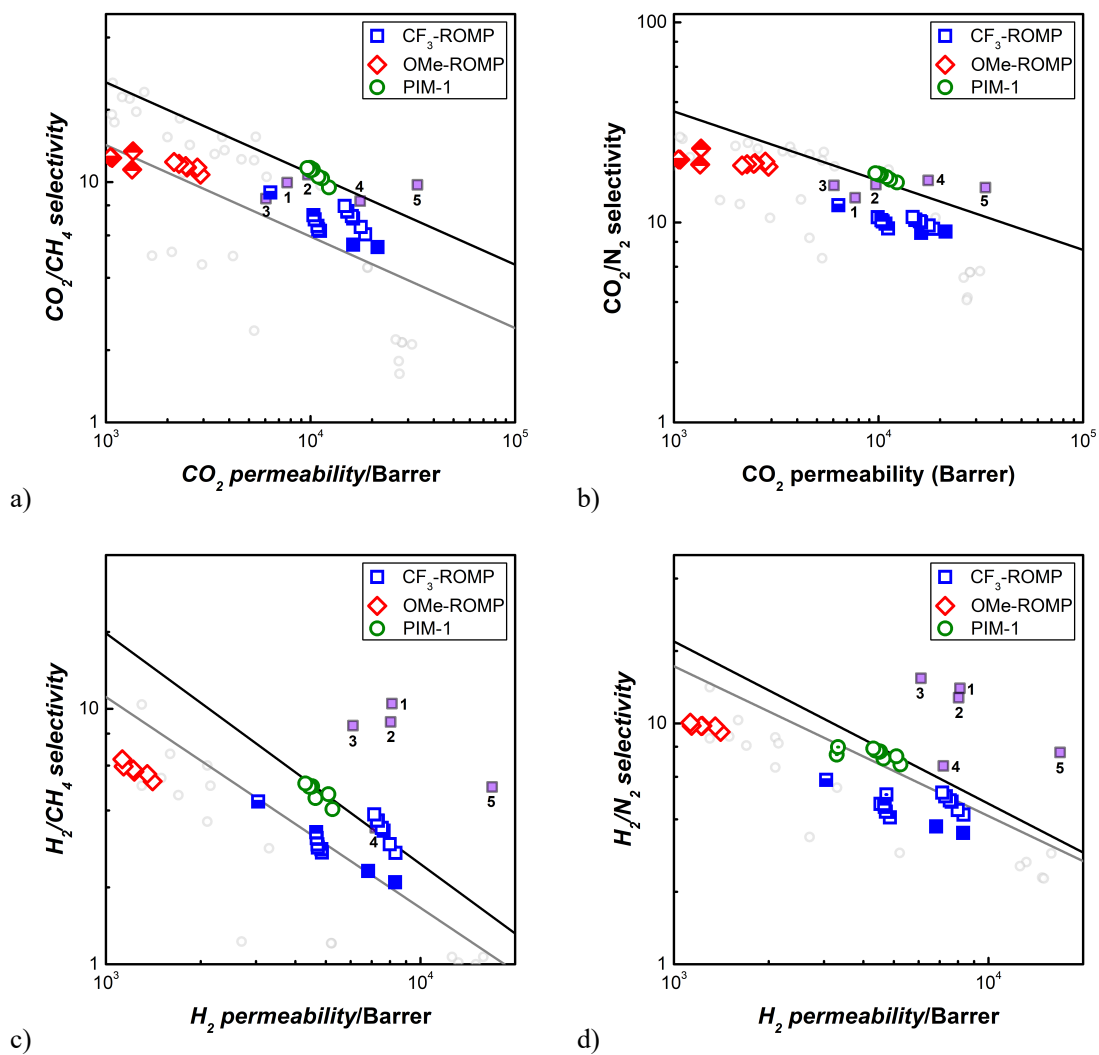
Figure 10.16: Permeability trade-off in Robeson plots a) CO_2/CH_4 b) CO_2/N_2, c) H_2/CH_4, d) H_2/N_2, and e) H_2/CO_2. Different treatments: Filled marks **(A)**, Outline with white fill **(B)**, Dot in center **(C)**, Top half filled **(D)**, and Bottom half filled **(E)**. 1) PIM-EA-TB[36], 2) PIM-Trip-TB[36], 3) PIM-TMN-SBI[8], 4) PIM-TMN-Trip-TB[8], and 5) PIM-TMN-Trip[8]. Grey dots are data from the Robeson database.[41,42]

Similar plots can be developed for diffusion (**Figure 10.17**) and solubility (**Figure 10.18**). We compared diffusivity and solubility results for ROMPs and PIM-1 on Robeson-like plots with a large database of data from literature for a series of gas pairs.[43] As with Robeson upper bound plots for permeability, ideal materials should be located in the upper right corner of the graph.

Diffusivity can change over orders of magnitude among polymers and gases, while solubility generally experiences narrower variations. Additionally, permeability upper bound selectivity values are mostly determined by diffusivity-selectivity over solubility-selectivity.[44] This is true if we base our observation on results coming from pure-gas transport properties, while it was recently formulated by Ricci *et al.*[45] that in mixed-gas conditions the solubility-selectivity actually outweighs the diffusivity contribution and controls the separation performance. Therefore, mixed-gas permeation and sorption experiments are already planned for future studies. However, as anticipated in **Figure 10.14b**, CF$_3$-ROMP has exceptionally high diffusivity. In fact, blue markers representing CF$_3$-ROMP can be observed to be on the extreme right of the following graphs, while most of the other polymers from this work and literature are distributed on the left side. For gas pairs like CO_2/CH_4, CO_2/N_2, N_2/CH_4, O_2/N_2, O_2/CH_4, and O_2/CO_2, high values of diffusivity were accompanied by good diffusivity-selectivity,

placing CF_3-ROMP on the upper limit with respect to the "clouds" formed by other polymers (**Figure 10.17**). This might be further enhanced by working on the uniformity of the length of the side ladder chains.

Exceptional results can be obtained if high diffusivity-selectivity is coupled with very high gas solubility.[46] Robeson-like solubility plots in **Figure 10.18** reveal how the solubility of CO_2 was relatively low in ROMPs. The improvement of solubility would lead this new class of polymers to be even more competitive in the vast world of polymers for gas separation. This would be particularly beneficial towards compounds like CO_2 as observed in **Figure 10.18**.
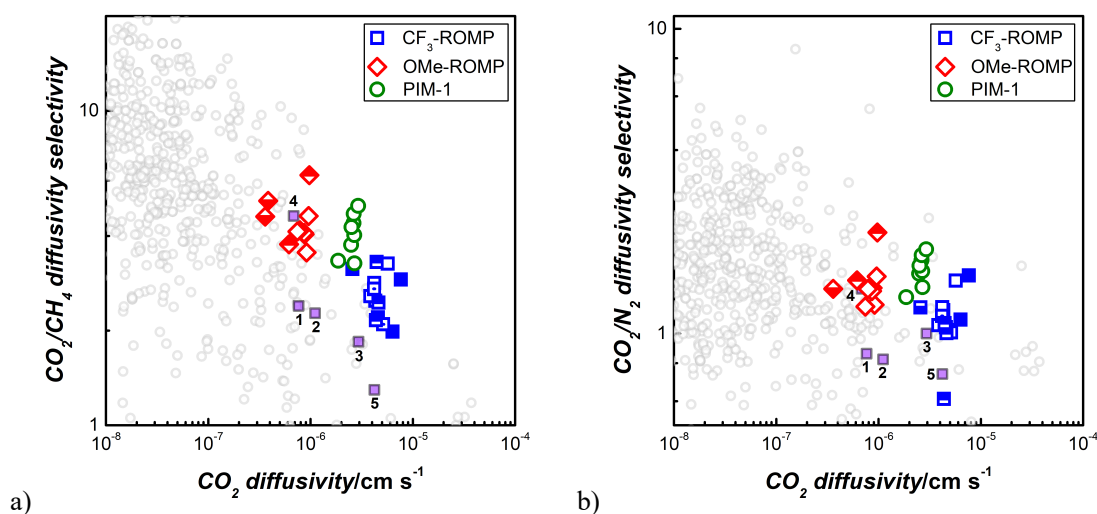

Figure 10.17: *Diffusivity trade-off in Robeson-like plots a) CO_2/CH_4 b) CO_2/N_2. Different treatments: Filled marks (**A**), Outline with white fill (**B**), Dot in center (**C**), Top half filled (**D**), and Bottom half filled (**E**). 1) PIM-EA-TB[36], 2) PIM-Trip-TB[36], 3) PIM-TMN-SBI[8], 4) PIM-TMN-Trip-TB[8], and 5) PIM-TMN-Trip[8]. Grey dots are data from the Robeson database[41,42], rearranged to determine diffusivity and diffusivity-selectivity.*
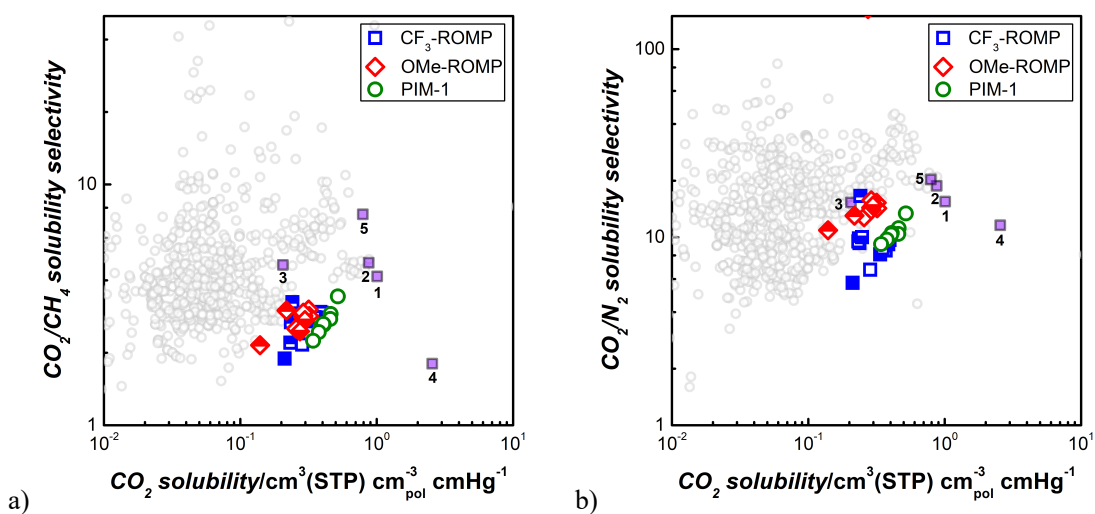
Figure 10.18: Solubility trade-off in Robeson-like plots a) CO_2/CH_4 b) CO_2/N_2. Different treatments: Filled marks (A), Outline with white fill (B), Dot in center (C), Top half filled (D), and Bottom half filled (E). 1) PIM-EA-TB[36], 2) PIM-Trip-TB[36], 3) PIM-TMN-SBI[8], 4) PIM-TMN-Trip-TB[8], and 5) PIM-TMN-Trip[8]. Grey dots are data from the Robeson database[41,42], rearranged to determine solubility and solubility-selectivity.

10.3.2. Physical Aging Study

10.3.2.1. Permeability Approach

Physical aging is a phenomenon that typically occurs in glassy polymers such as ROMPs and PIMs since they are not in thermodynamic equilibrium at temperatures below their glass transition.[47] A deeper explanation of the phenomenon can be found in the dedicated section of the theoretical background. Despite different treatments performed, herein we report results obtained using polymers that underwent treatment (B). A decrease in permeability was experienced over time for each gas tested for ROMPs and PIM-1. As shown in **Figure 10.19**, an approximately linear trend was observed in double logarithmic charts in which permeability was plotted as a function of the aging time. Similar linear behaviors were observed by other authors.[48,49] The decrease in permeability was accompanied by an increase in permselectivity for some of the most relevant gas pairs, *i.e.* CO_2/N_2, CO_2/CH_4, H_2/N_2, H_2/CH_4, O_2/N_2, and N_2/CH_4 (**Figure 10.20**). This relates to the trade-off between permeability and selectivity described by Robeson.[41] Notably, CF_3-ROMP reached the highest permeability for each gas, while OMe-ROMP was the most selective for all gas pairs.
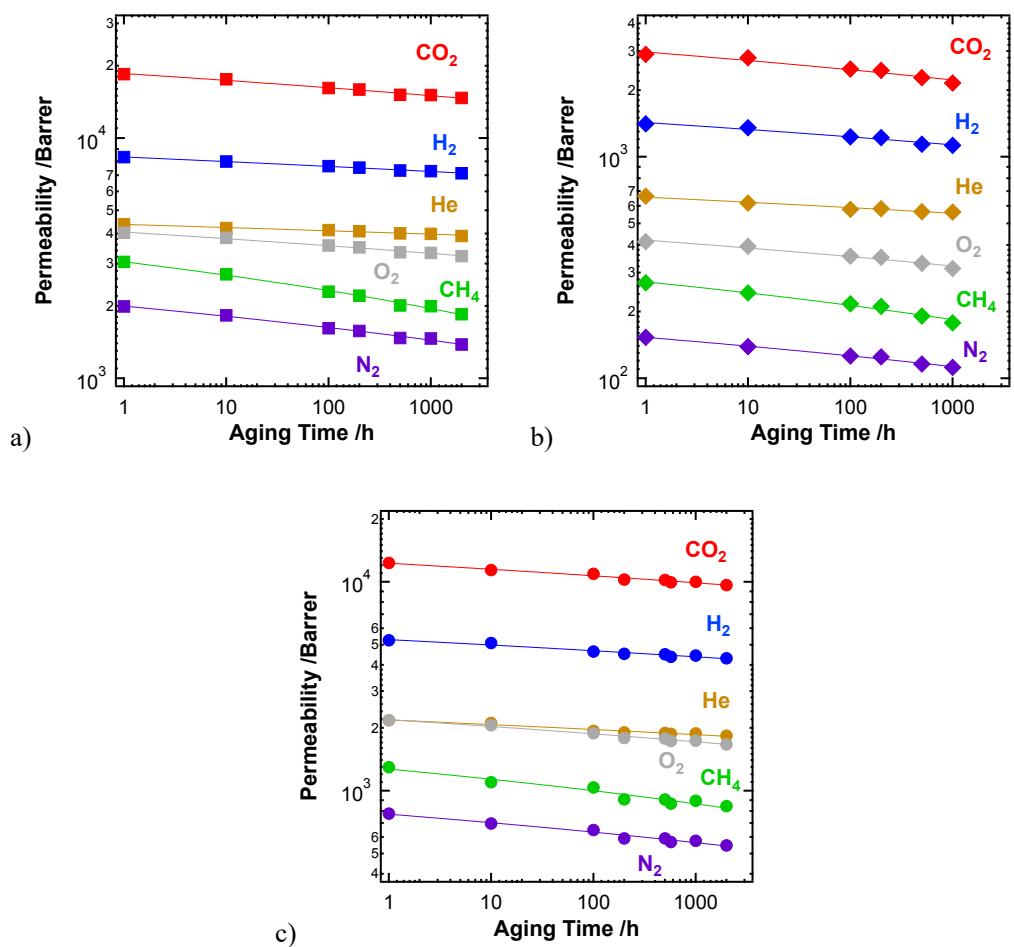
Figure 10.19*: Permeability as a function of time. Data were collected at 35 °C and 1 bar upstream pressure for a) CF$_3$-ROMP, b) OMe-ROMP, and c) PIM-1.*
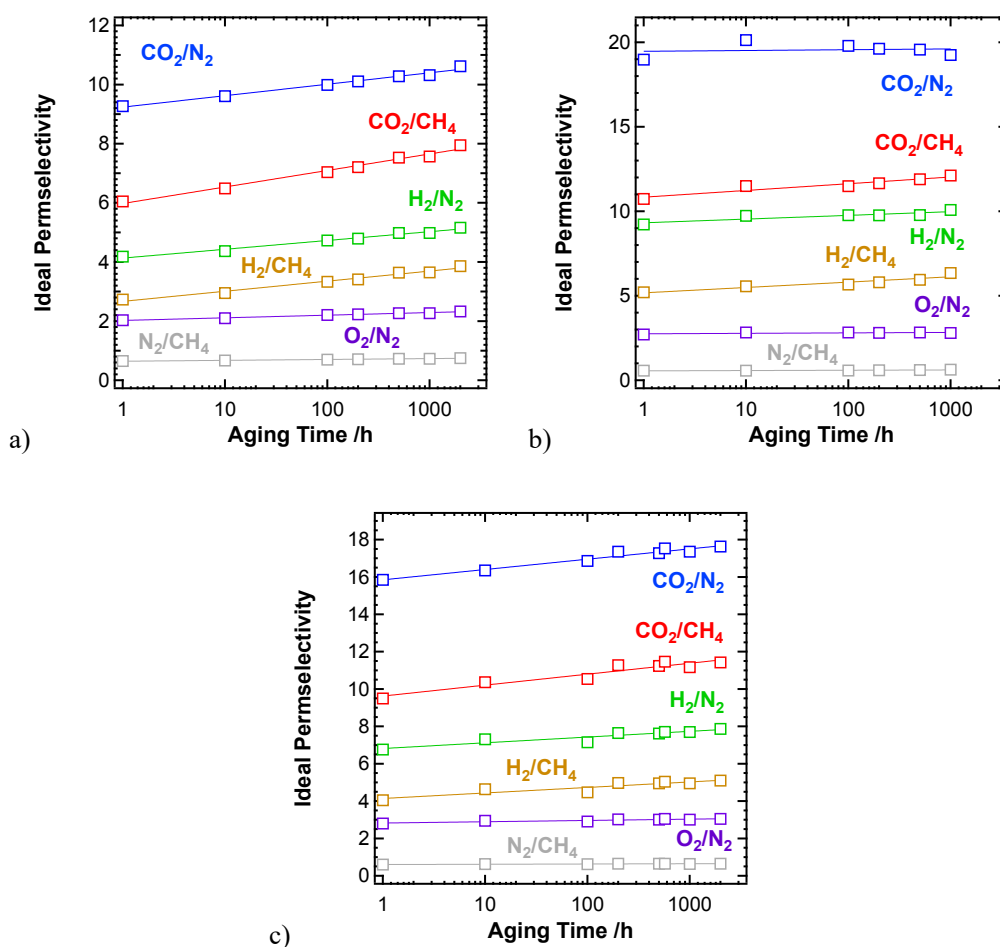
Figure 10.20: Permeability ideal selectivity as a function of time. Data were collected at 35 °C and 1 bar upstream pressure for a) CF₃-ROMP, b) OMe-ROMP, and c) PIM-1.

From **Figure 10.21a**, in which helium permeability is reported as a function of the time, we can observe that CF₃-ROMP, OMe-ROMP, and PIM-1 aged at different rates. For smaller gases like He, H₂, and O₂, CF₃-ROMP aged the slowest among three polymers, while OMe-ROMP aged the fastest with PIM-1 in between (**Figure 10.21a-f**). Notably, the aging of CF₃-ROMP for smaller gases is significantly slower compared to state-of-the-art PIMs, although the alcohol treatment is slight different (ethanol vs. methanol).[7,8] For instance, helium permeability decreased by ~45% after 1,000 h aging for PIM-TMN-Trip, whereas CF₃-ROMP only dropped by ~10%. CF₃-ROMP film was also thinner than PIM-TMN-Trip (119 μm vs. 192 μm), and physical aging is known to occur faster in thinner films.[48] For larger molecules like CO₂, N₂, and CH₄, there was no significant difference in aging rates between three

polymers compared in this work (**Figure 10.21d-f**). Previous studies have shown that the introduction of fluorinated moieties can greatly suppress physical aging in aromatic polyimides.[50,51] In this case, despite its larger surface area and fractional free volume, CF$_3$-ROMP aged considerably slower compared to OMe-ROMP for gases with smaller effective diameters.

The graphs in **Figure 10.21a-f** reveal that the permeabilities of larger gases decreased more than those of smaller gases as the materials aged. Furthermore, aging rates for each gas followed the same order of the effective diameter (He < H$_2$ < O$_2$ < CO$_2$ < N$_2$ < CH$_4$), as shown in **Figure 10.21b** for CF$_3$-ROMP were normalized permeability data are reported. The permeability loss that each gas experienced over time was plotted as a function of kinetic diameter squared, and the slope of this line can be calculated for each set of experiments at each time. **Figure 10.21c** shows that this slope increased over time. Interestingly, the rate by which it evolved was very different among the three materials, and this is related to the way polymer chains pack over time. In other words, it gave us information about the evolution of the fractional free volume of the polymer in the journey towards equilibrium. CF$_3$-ROMP showed the highest values of the slopes, and this was because small gases (*i.e.* He, H$_2$, O$_2$) experienced a smaller permeability drop over time compared to OMe-ROMP and PIM-1, while for larger gases (*i.e.*, CO$_2$, N$_2$, CH$_4$) the drop in permeability was comparable (**Figure 10.21a**). This reflects on the fact that H$_2$/X and He/X permselectivity (X = generic other gas), increased remarkably over time without compromising H$_2$ and He permeability, often surpassing the Robeson Upper Bounds.[41,42] This result was further supported by evidence from WAXS experiments that will be provided in the following section.
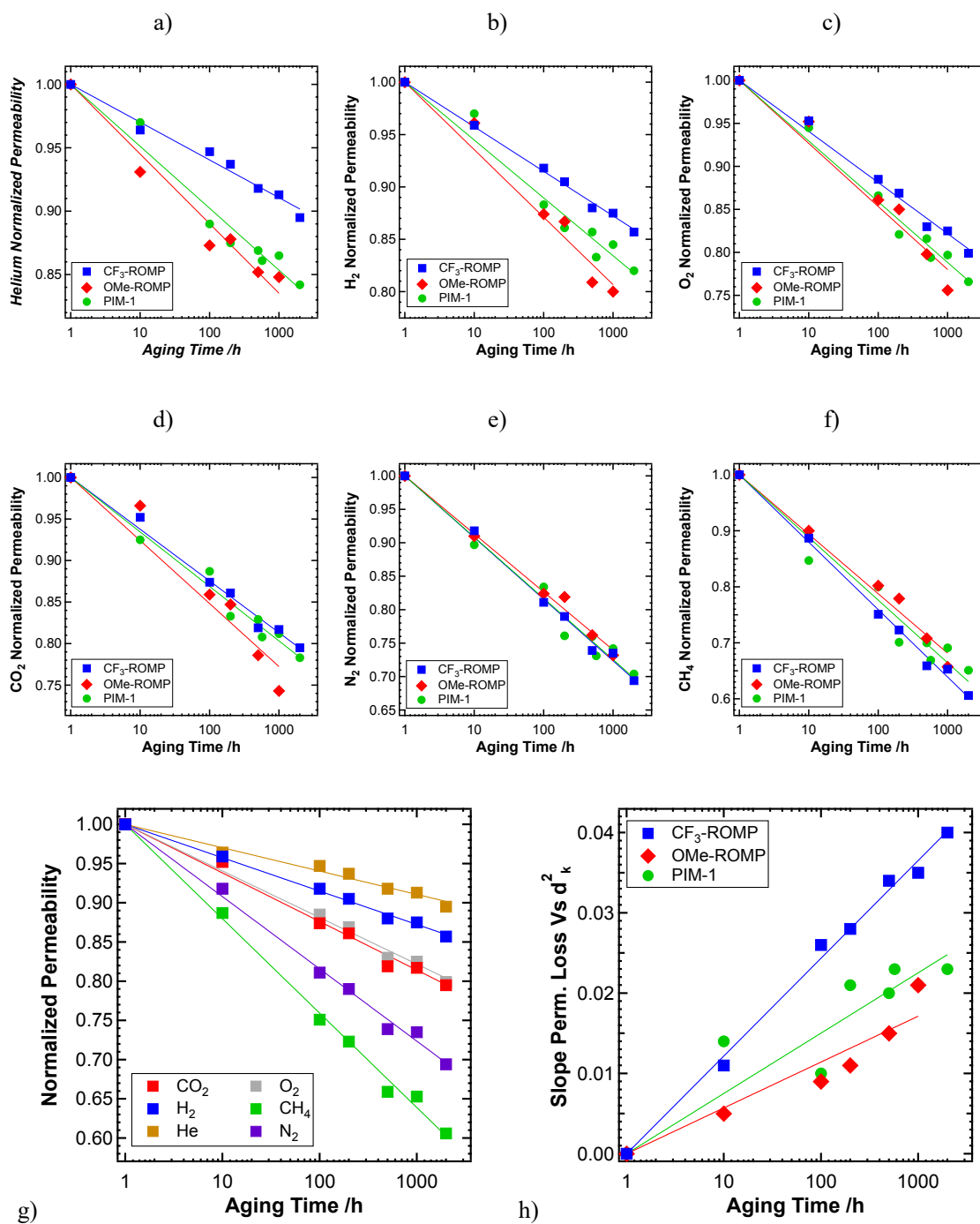
Figure 10.21*: Physical aging data. a)-f) CF₃-ROMP, OMe-ROMP, and PIM-1 comparison of normalized permeability against aging time for He, H₂, O₂, CO₂, N₂, and CH₄, g) CF₃-ROMP aging data and h) Data calculated evaluating the slope of permeability loss against kinetic diameter squared at each time (1, 10, 100, 200, 500, 1000, and 2000 h), and plotted against aging time.*

Diffusivity coefficients were monitored while films aged over time and results are shown in **Figure 10.22**. He and H_2 values were not represented in the figures because time-lag was too short for accurate calculations. Diffusion coefficients decreased according to what expected from aging experiments and contributed to the overall decrease in permeability. For ROMP polymers, the magnitude of diffusivity values, followed the inverse order of the effective diameter: (3.44 Å) O_2 < (3.63 Å) CO_2 < (3.66 Å) N_2 < (3.81 Å) CH_4. Diffusivity-selectivity increased over time, as shown in **Figure 10.23**, and this was the biggest contribution to the increase in permselectivity that allowed these ROMPs to overcome the upper bound for some gas pairs. OMe-ROMP showed diffusivity-selectivity higher than PIM-1 for CO_2/CH_4 and N_2/CH_4 separation.
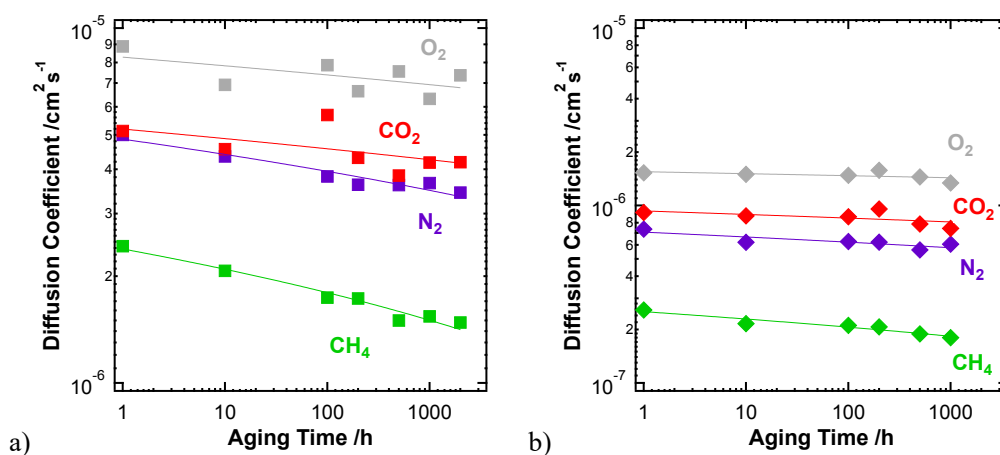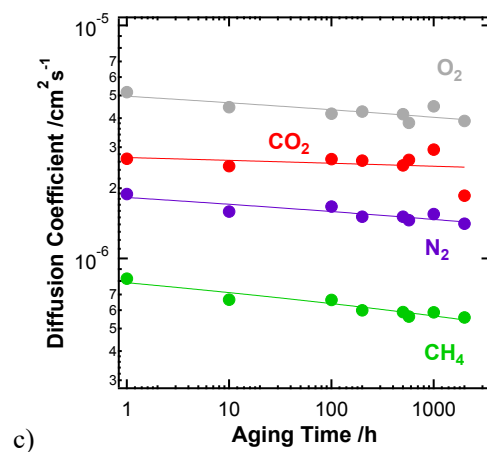
Figure 10.22: Diffusion coefficient as a function of time. Data were collected at 35 °C and 1 bar upstream pressure for a) CF_3-ROMP, b) OMe-ROMP, and c) PIM-1. He and H_2 data were not plotted because time lag was smaller than 1-2 s.
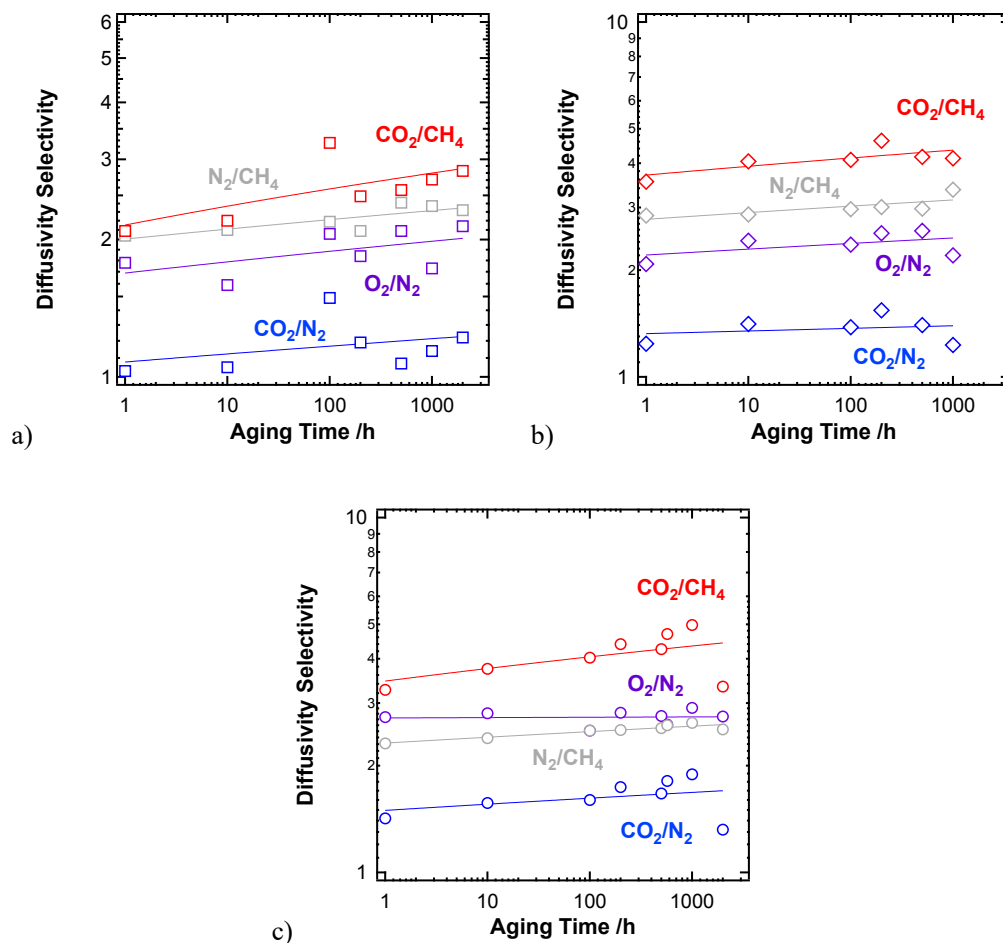

Figure 10.23: Diffusivity-selectivity as a function of time. Data were collected at 35 °C and 1 bar upstream pressure for a) CF_3-ROMP, b) OMe-ROMP, and c) PIM-1. He/X and H_2/X data were not plotted because time lag was smaller than 1-2 s.

Solubility and solubility-selectivity were also calculated in the framework of the solution-diffusion method to evaluate their trend over time. Solubility and solubility-selectivity values appear to oscillate around an average value over time, as seen in **Figure 10.24** and **Figure 10.25**, respectively. CF_3-ROMP and PIM-1 showed similar results for solubility-selectivity, while OMe-ROMP recorded higher values of CO_2/N_2 and CH_4/N_2.
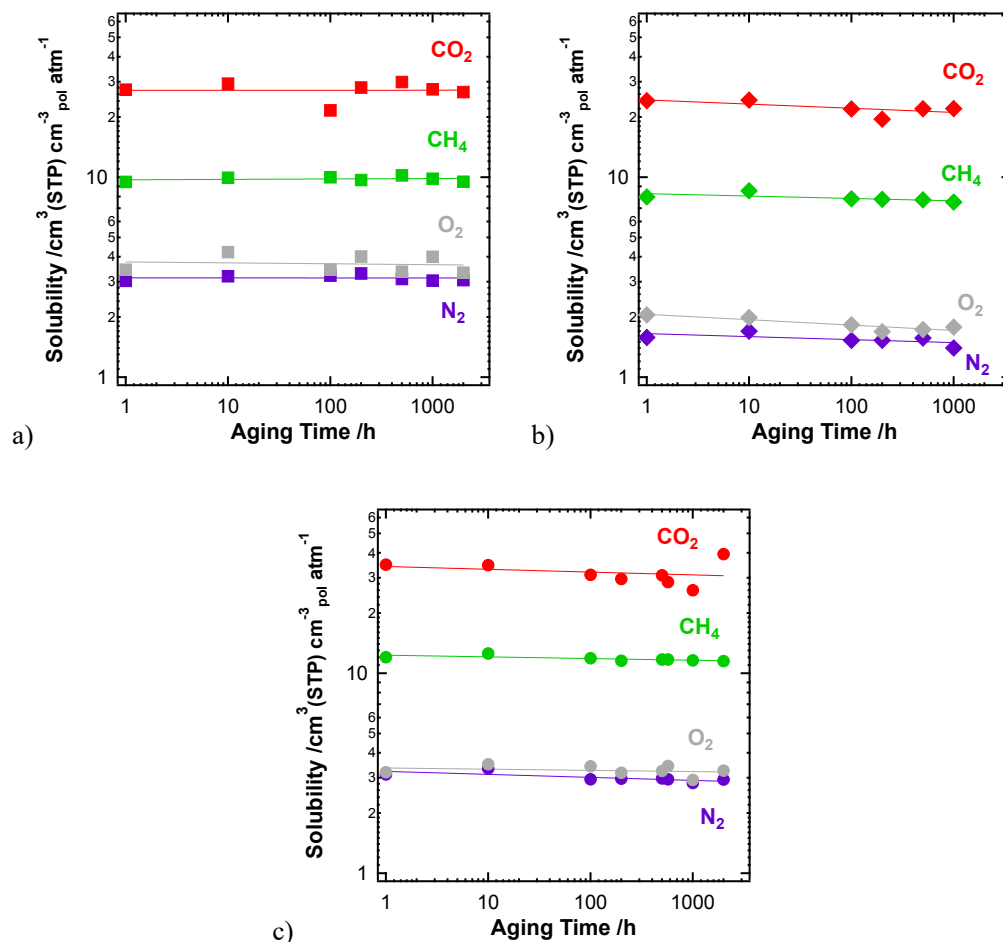

Figure 10.24*: Solubility coefficient as a function of time. Data were collected at 35 °C and 1 bar upstream pressure for a) CF_3-ROMP, b) OMe-ROMP, and c) PIM-1. He and H_2 data were not plotted because time lag was smaller than 1-2 s and the calculation of S depends on D.*
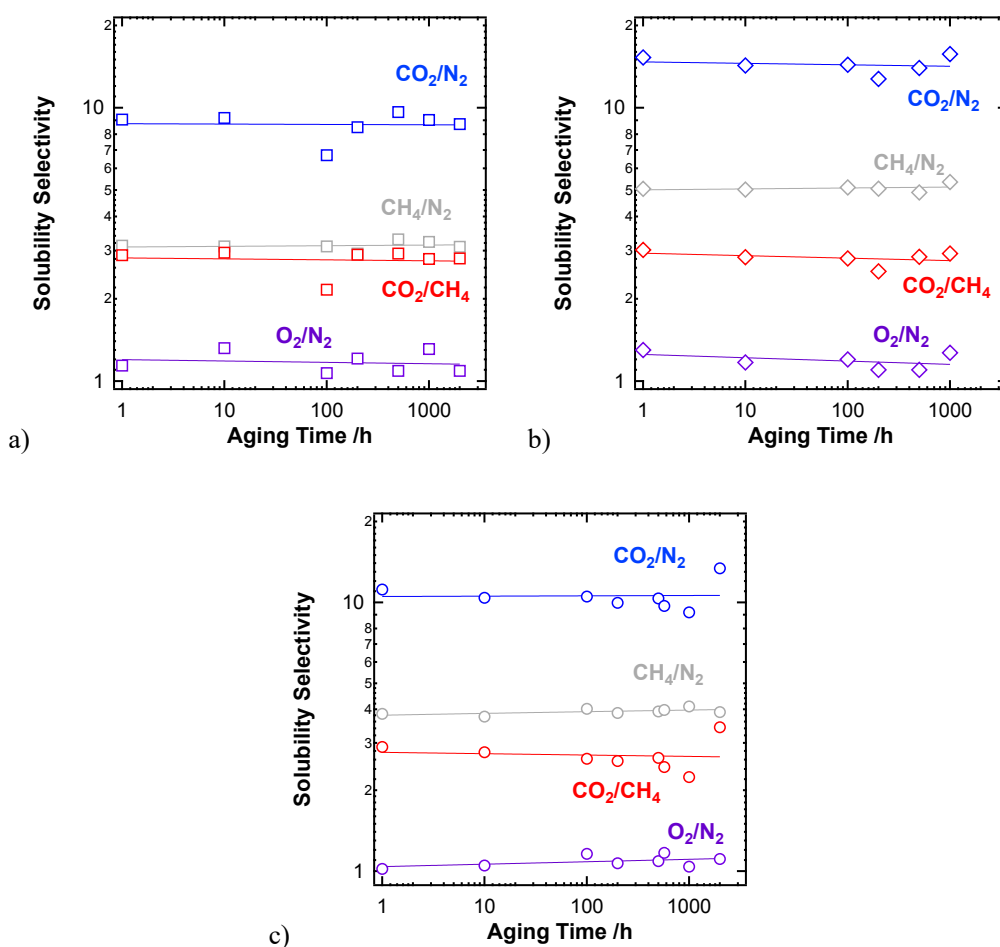
Figure 10.25: Solubility-selectivity as a function of time. Data were collected at 35 °C and 1 bar upstream pressure for a) CF$_3$-ROMP, b) OMe-ROMP, and c) PIM-1. He/X and H$_2$/X data were not plotted because time lag was smaller than 1-2 s and the calculation of S depends on D.

10.3.2.2. Wide-Angle X-ray Scattering Approach

Physical aging was also monitored by Wide-angle X-ray scattering. X-ray scattering methods are suitable for studying internal structural changes of CF$_3$-ROMP, OMe-ROMP, and PIM-1 because of their high fractional free volume and relevant pore-size distribution.[52] It is important to note that these WAXS experiments were performed in conjunction with gas permeation experiments during the course of 2,000 h on samples from the same film, so the aging history was identical and results could be directly correlated. The same sample was used for WAXS throughout the entire 2,000 h so the scattering intensity can be compared on a relative-basis. **Figure 10.26** shows that CF$_3$-ROMP *(a)* is the polymer

that experienced less aging in internal free volume, especially in the range where q is larger than 1 Å^{-1} (d-spacing < 3.14 Å), which means smaller pores were preserved over time after soaking in liquid ethanol. This is consistent with the fact that smaller gases (*e.g.*, He and H$_2$) showed slower physical aging (**Figure 10.21a-f**) and correlates with the different rates in permeability drop (**Figure 10.21g-h**). Conversely, OMe-ROMP *(b)* and PIM-1 *(c)* showed a larger decrease in the absolute scattering intensity across all ranges of pore size (0.1 Å^{-1} < q < 2 Å^{-1}), which explains their faster aging rates in small gases (*e.g.* He and H$_2$) and similar aging rates for larger gases (*e.g.* N$_2$ and CH$_4$) compared to CF$_3$-ROMP, because the shrinking of larger pores has a much larger impact on the transport of larger gas molecules compared to smaller ones.
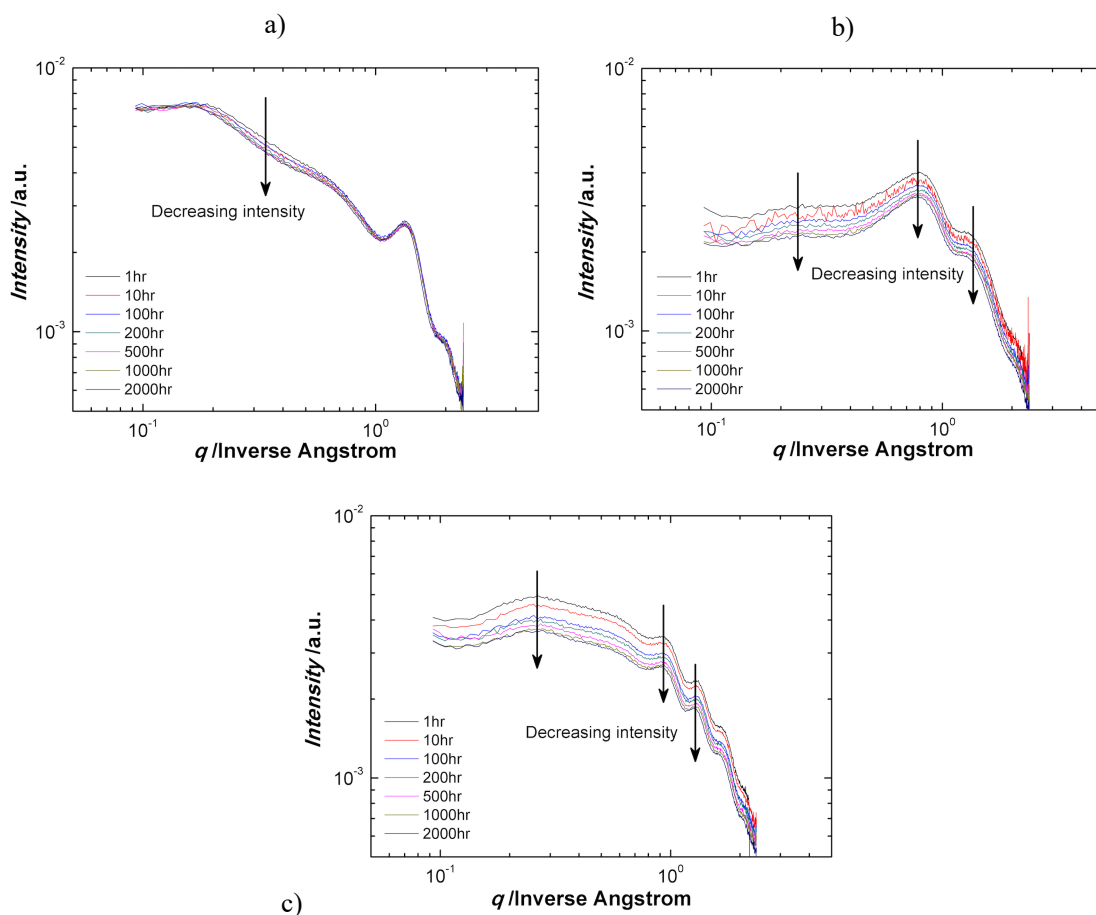

Figure 10.26: WAXS patterns for a) CF$_3$-ROMP, b) OMe-ROMP, and c) PIM-1 as a function of time up to 2,000 h, for film soaked in liquid ethanol for 48 h, then air-dried for 24 h and kept under full vacuum for 8 h before testing and starting aging time.

10.3.3. CO₂-induced Plasticization

As discussed in the theoretical background chapter in section 4.3.3, plasticization is a largely investigated phenomenon in the field of membrane science.[53–55] It is important to determine to which extent materials can resist plasticization to guarantee steady and reliable performance even when plasticizing agents are present in high concentrations. For this reason, permeation experiments were performed with CO_2 pressures up to 17, 20.5, 25, and 51 bar. ROMPs and PIM-1 plasticization performance can be compared with results previously obtained in literature at different conditions. Since plasticization pressure depends on the thickness[56], on the crosslinking degree[56,57], and on the duration of each acquisition, a direct comparison can be made just among uncrosslinked thick films. A comprehensive review on plasticization data can be found in **Table 4.1** of this dissertation, section 4.3.3.

In **Figure 10.27** the plasticization pressure of polymers investigated in this section are compared with literature data. Different thicknesses were reported, from hundreds of nanometers to hundreds of microns, but uncrosslinked polymers were left out of the chart. Among the most remarkable results, we point out that for a crosslinked Matrimid® film (treated at 350 °C for 30 minutes), permeability plateaued at 3.5 Barrer at 44 bar.[57] For non-crosslinked polymers, polysulfone (PSf) and polycarbonate (PC) had the highest plasticization pressure, p_{pl}. For PSf thick films p_{pl} was ~34 bar[54] and for thin films ~24 bar[58], while for PC thick film it was ~34 bar[55].
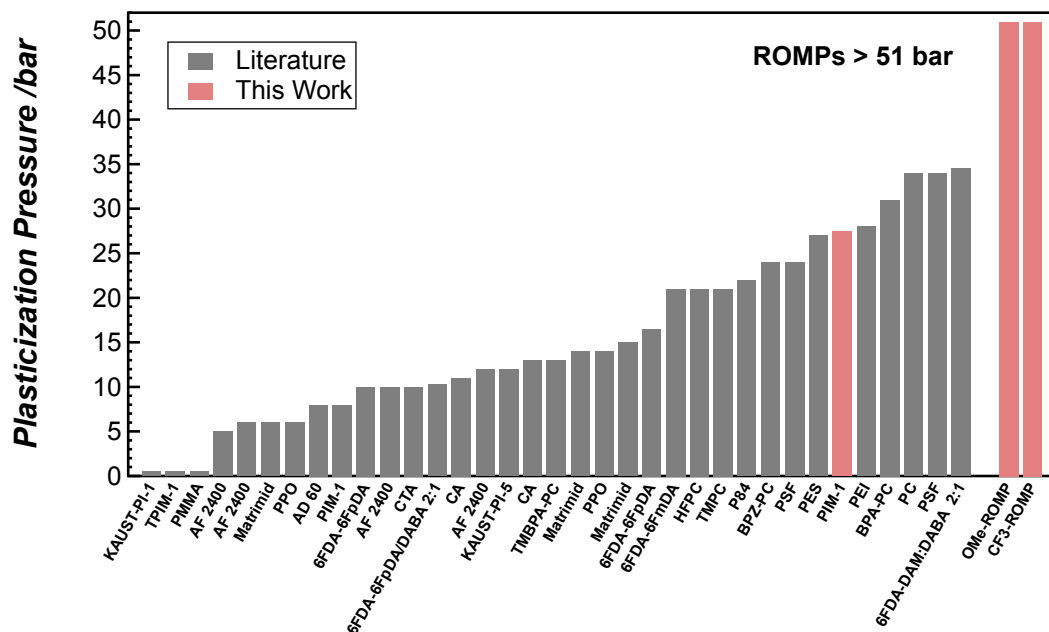
Figure 10.27: *Collection of CO_2-induced plasticization pressure results obtained for uncrosslinked polymers in pure-gas conditions from the literature (grey bars), and comparison with polymers investigated in this study (red bars).*[11,54–56,58–61]

For ROMP polymers and PIM-1 studied in this work, plasticization experiments were performed on an automated permeation system, to accurately control the feeding pressure and the duration of each experiment. The duration of each experiment was 12 minutes in the increasing pressure stage (filled markers) and 18 minutes in the decreasing pressure stage (hysteresis), to ensure that pseudo-steady state was reached to calculate permeability. To the best of our knowledge, CF_3-ROMP and OMe-ROMP were the only polymers whose permeability has been proven to still be decreasing after reaching 51 bar of CO_2, as shown in **Figure 10.28a**. Moreover, when CO_2 feed pressure was gradually released, the hysteresis induced by the conditioning of the films at 51 bar was only up to ~35% for CF_3-ROMP and up to ~52% for OMe-ROMP of the original CO_2 permeability. On the other hand, the plasticization pressure of PIM-1 was ~27 bar and showed a significantly bigger hysteresis (up to 95%) when CO_2 feed pressure was released (**Figure 10.28b**). These results indicated that the interchain cohesive energy for ROMP polymers was much stronger than that of PIM-1, which may originate from both fluorophilic interaction between fluorinated moieties and greater interchain rigidity due to "physical interlocking"

between side chains. This is in agreement with what Swaidan *et al.*[11,61] reported, in which interchain rigidity facilitated by intrachain mobility contributed to CO_2 plasticization resistance.
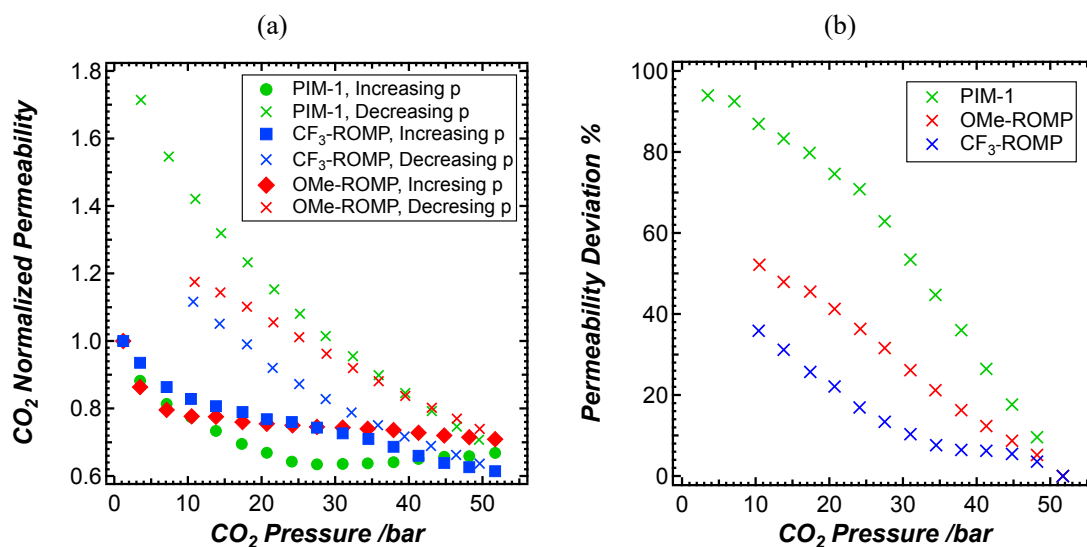

(a)   (b)

Figure 10.28: *CO_2 plasticization study (a) and hysteresis (b) induced by conditioning of the film at 51 bar of CO_2 for CF_3-ROMP, OMe-ROMP and PIM-1. Data were collected ~2000 h after film casting for CF_3-ROMP and PIM-1, and after 300 h for OMe-ROMP.*

To provide a clearer representation of the data reported in **Figure 10.28a**, and without normalizing the permeability values, **Figure 10.29** is shown.
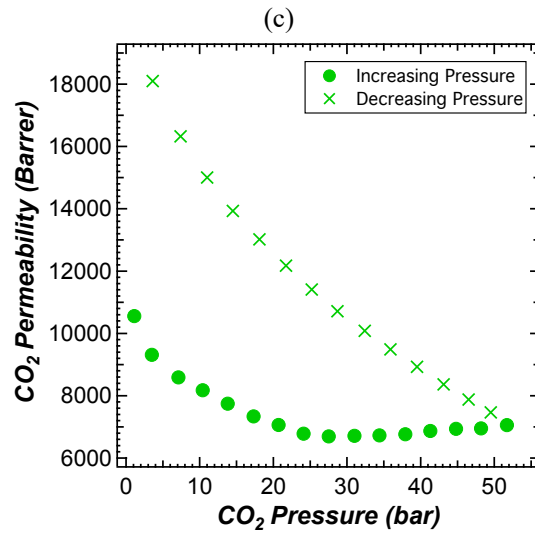

(a)   (b)
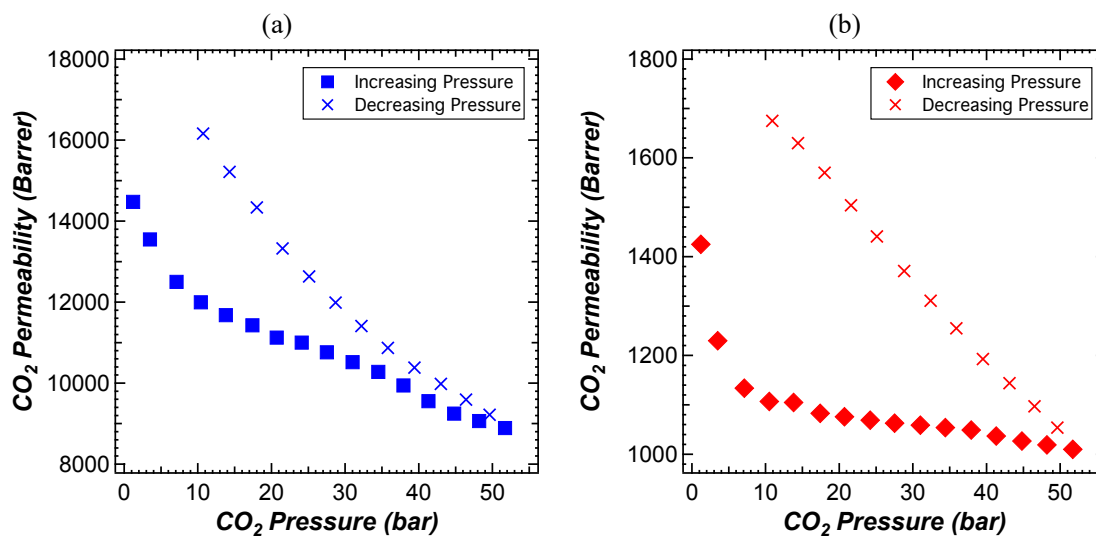
Figure 10.29: *Pressure-based CO$_2$ plasticization curves for liquid ethanol treated samples: a) CF$_3$-ROMP aged 2100 h, b) OMe-ROMP aged 300 h, and c) PIM-1 aged 2000 h.*

Considering the high upstream pressures reached during CO$_2$-induced plasticization experiments, it is important to correct for the non-ideal behavior of CO$_2$. Permeability can be calculated modifying Eq. (5.5) by using fugacity, f, instead of pressure, as indicated in Eq. (10.1):

$$\mathcal{P}' = \frac{V}{RT}\frac{l}{A}\frac{1}{(f_u - \bar{f}_d)}\left(\frac{df_d}{dt}\right)$$

Eq. (10.1)

The fugacity was calculated by means of Peng-Robinson Equation of State.[62] **Figure 10.30** shows the results reported in **Figure 10.29**, recalculated on a fugacity-based fashion. The permeability of CF$_3$-ROMP revealed to be decreasing with fugacity for the whole range investigated, while OMe-ROMP showed a minimum at ~10 bar that was not experienced when permeability was calculated based on pressure instead of fugacity. PIM-1 results, instead, confirmed that a minimum value of permeability was obtained at a fugacity of ~21 bar.
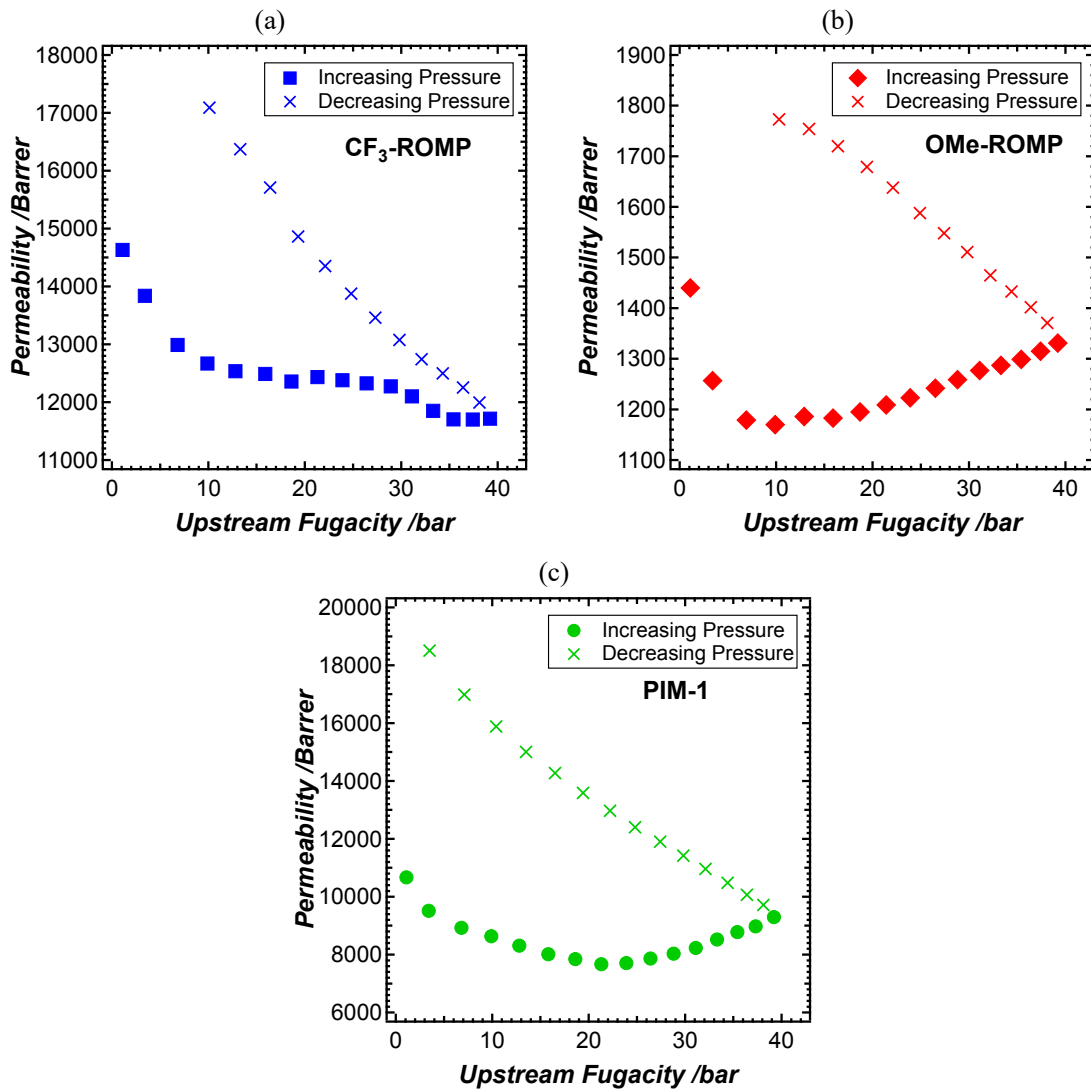
Figure 10.30: Fugacity-based CO₂ plasticization curves for liquid ethanol treated samples: a) CF₃-ROMP aged 2100 h, b) OMe-ROMP aged 300 h, and c) PIM-1 aged 2000 h.

Also CF₃-ROMP and OMe-ROMP that underwent vapor methanol treatment were tested up to ~21-25 bar and results are reported in **Figure 10.31**.
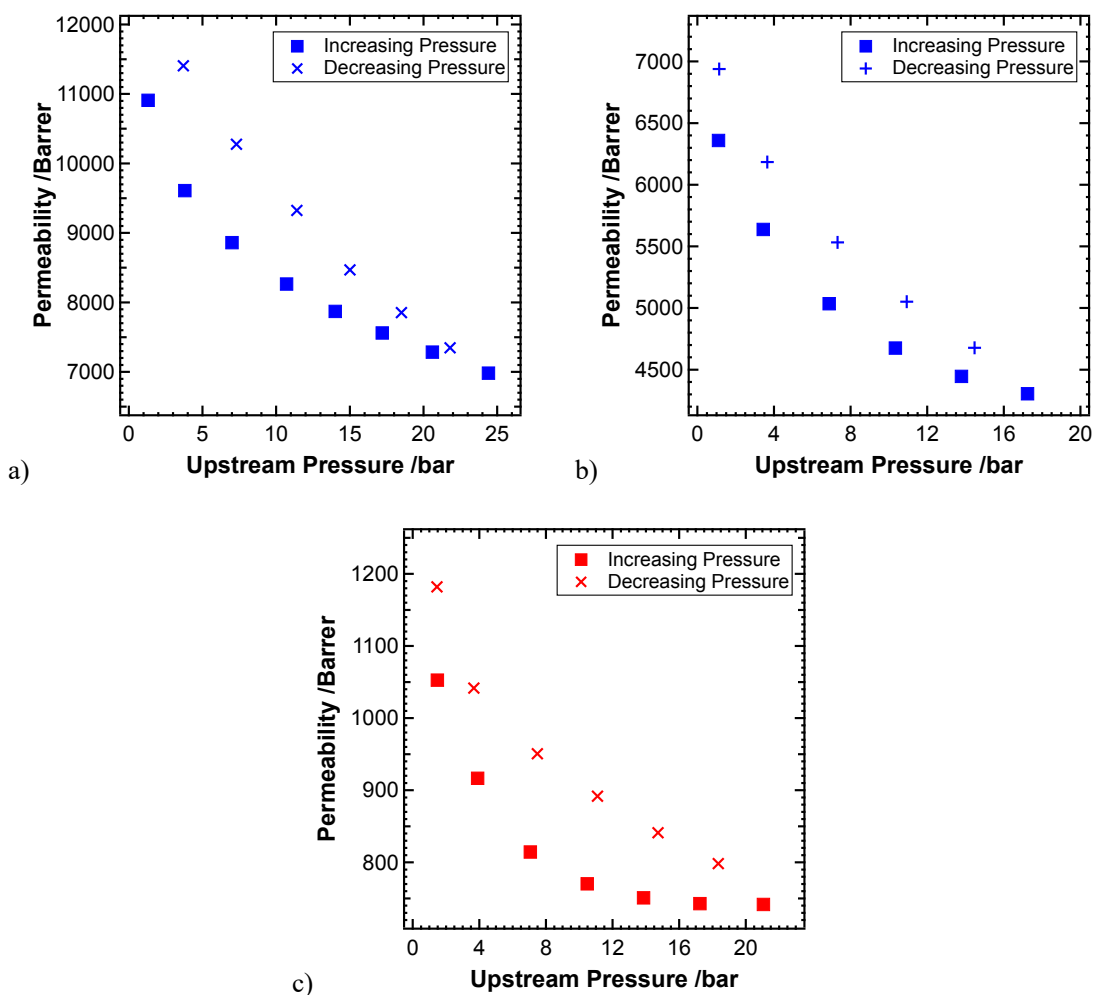
Figure 10.31: *CO₂ plasticization study a) CF3-ROMP, 24 h under vacuum 120 °C, vapor methanol treatment at 160 mbar (p$_{CH3OH}$) 12 h, drying under vacuum 70 °C overnight, 24 bar reached, 90 h aged, b) CF$_3$-ROMP, 24 h under vacuum 120 °C, 17 bar reached, 48 h aged, c) OMe-ROMP, 24 h under vacuum 120 °C, 20.5 bar reached, 60 h aged.*

10.4.   Conclusions and Future Directions on the ROMP polymers

This chapter reports the significant role of pendent -CF$_3$ groups in enhancing gas permeability and reducing physical aging in a porous ROMP polymer system. The different performance as a function of pendant groups on the side chain, reveals that these features can be used to tailor the gas separation performance. Outstanding plasticization resistance is a common property to all the ROMP polymers presented, suggesting that this new structural polymer design may offer new approaches to

systematically address the plasticization issue. The results presented suggest that the generation of porous polymers based on flexible main chains and rigid free-volume-promoting sidechains represents a promising new platform or materials. We are optimistic that continued investigations of structure-property relationships can be used to achieve additional important advances in membrane-based gas separations.

A long series of experiments are underway at the moment. Mixed-gas sorption and permeation tests with CO_2/CH_4 mixtures will indicate whether the plasticization resistance of these material can improve mixed-gas performance preventing the loss in diffusivity-selectivity which CO_2-induced plasticization is responsible for. A more controlled chemistry on length of the side chains may lead to enhanced diffusivity-selectivity, fixing the biggest issue materials such as CF_3-ROMP have. Pure-gas sorption isotherms will also be performed to evaluate the role of solubility at more fundamental level.

References

[1] M. Galizia, W. S. Chi, Z. P. Smith, T. C. Merkel, R. W. Baker, B. D. Freeman, *Macromolecules* **2017**, *50*, 7809.

[2] P. Bernardo, E. Drioli, G. Golemme, *Ind. Eng. Chem. Res.* **2009**, *48*, 4638.

[3] Y. Yampolskii, *Macromolecules* **2012**, *45*, 3298.

[4] C. G. Bezzu, M. Carta, A. Tonkins, J. C. Jansen, P. Bernardo, F. Bazzarelli, N. B. McKeown, *Adv. Mater.* **2012**, *24*, 5930.

[5] N. B. McKeown, P. M. Budd, *Chem. Soc. Rev.* **2006**, *35*, 675.

[6] Z.-X. Low, P. M. Budd, N. B. McKeown, D. A. Patterson, *Chem. Rev.* **2018**, *118*, 5871.

[7] M. Carta, R. Malpass-Evans, M. Croad, Y. Rogan, J. C. Jansen, P. Bernardo, F. Bazzarelli, N. B. McKeown, *Science (80-.).* **2013**, *339*, 303.

[8] I. Rose, C. G. Bezzu, M. Carta, B. Comesañã-Gándara, E. Lasseuguette, M. C. Ferrari, P. Bernardo, G. Clarizia, A. Fuoco, J. C. Jansen, K. E. Hart, T. P. Liyana-Arachchi, C. M. Colina, N. B. McKeown, *Nat. Mater.* **2017**, *16*, 932.

[9] B. S. Ghanem, R. Swaidan, X. Ma, E. Litwiller, I. Pinnau, *Adv. Mater.* **2014**, *26*, 6696.

[10] Y. Zhao, Y. He, T. M. Swager, *ACS Macro Lett.* **2018**, *7*, 300.

[11] R. Swaidan, B. Ghanem, M. Al-Saeedi, E. Litwiller, I. Pinnau, *Macromolecules* **2014**,

47, 7453.

[12]   N. Du, H. B. Park, G. P. Robertson, M. M. Dal-Cin, T. Visser, L. Scoles, M. D. Guiver, *Nat. Mater.* **2011**, *10*, 372.

[13]   M. G. Dhara, S. Banerjee, *Prog. Polym. Sci.* **2010**, *35*, 1022.

[14]   T. H. Kim, W. J. Koros, G. R. Husk, K. C. O'Brien, *J. Memb. Sci.* **1988**, *37*, 45.

[15]   K. Tanaka, H. Kita, M. Okano, K. ichi Okamoto, *Polymer (Guildf).* **1992**, *33*, 585.

[16]   J. R. Wiegand, Z. P. Smith, Q. Liu, C. T. Patterson, B. D. Freeman, R. Guo, *J. Mater. Chem. A* **2014**, *2*, 13309.

[17]   S. Alexander Stern, *J. Memb. Sci.* **1994**, *94*, 1.

[18]   P. Raveendran, S. L. Wallen, *J. Phys. Chem. B* **2003**, *107*, 1473.

[19]   J. R. Fried, N. Hu, *Polymer (Guildf).* **2003**, *44*, 4363.

[20]   C. W. Bielawski, R. H. Grubbs, *Prog. Polym. Sci.* **2007**, *32*, 1.

[21]   T. A. Halgren, *J. Comput. Chem.* **1996**, *17*, 490.

[22]   T. A. Halgren, *J. Comput. Chem.* **1996**, *17*, 520.

[23]   T. A. Halgren, *J. Comput. Chem.* **1996**, *17*, 553.

[24]   M. D. Hanwell, D. E. Curtis, D. C. Lonie, T. Vandermeersch, E. Zurek, G. R. Hutchison, *J. Cheminform.* **2012**, *4*, 1.

[25]   P. M. Budd, B. S. Ghanem, S. Makhseed, N. B. McKeown, K. J. Msayib, C. E. Tattershall, *Chem. Commun.* **2004**, *4*, 230.

[26]   S. E. Doris, A. L. Ward, P. D. Frischmann, L. Li, B. A. Helms, *J. Mater. Chem. A* **2016**, *4*, 16946.

[27]   C. Li, A. L. Ward, S. E. Doris, T. A. Pascal, D. Prendergast, B. A. Helms, *Nano Lett.* **2015**, *15*, 5724.

[28]   S. Brunauer, P. H. Emmett, E. Teller, *J. Am. Chem. Soc.* **1938**, *60*, 309.

[29]   G. Kupgan, T. P. Liyana-Arachchi, C. M. Colina, *Langmuir* **2017**, *33*, 11138.

[30]   Y. Rogan, L. Starannikova, V. Ryzhikh, Y. Yampolskii, P. Bernardo, F. Bazzarelli, J. C. Jansen, N. B. McKeown, *Polym. Chem.* **2013**, *4*, 3813.

[31]   P. M. Budd, N. B. McKeown, B. S. Ghanem, K. J. Msayib, D. Fritsch, L. Starannikova, N. Belov, O. Sanfirova, Y. Yampolskii, V. Shantarovich, *J. Memb. Sci.* **2008**, *325*, 851.

[32]   C. G. Bezzu, M. Carta, M.-C. Ferrari, J. C. Jansen, M. Monteleone, E. Esposito, A. Fuoco, K. Hart, T. P. Liyana-Arachchi, C. M. Colina, N. B. McKeown, *J. Mater. Chem. A* **2018**, *6*, 10507.

[33]   R. Srinivasan, S. R. Auvil, P. M. Burban, *J. Memb. Sci.* **1994**, *86*, 67.

[34]   Y. Hu, M. Shiotsuki, F. Sanda, B. D. Freeman, T. Masuda, *Macromolecules* **2008**, *41*, 8525.

[35]   P. R. Bevington, D. K. Robinson, *Error Data Reduction and Error Analysis for the Physical Sciences*, **1992**.

[36]   M. Carta, M. Croad, R. Malpass-Evans, J. C. Jansen, P. Bernardo, G. Clarizia, K. Friess,

M. Lanč, N. B. McKeown, *Adv. Mater.* **2014**, *26*, 3526.

[37]   M. F. Costa Gomes, A. A. H. Pádua, *J. Phys. Chem. B* **2003**, *107*, 14020.

[38]   M. A. Hamza, G. Serratrice, M. J. Stébé, J. J. Delpuech, *J. Am. Chem. Soc.* **1981**, *103*, 3733.

[39]   D. F. Sanders, Z. P. Smith, R. Guo, L. M. Robeson, J. E. Mcgrath, D. R. Paul, B. D. Freeman, **2013**, *54*, 4729.

[40]   G. R. H. and D. R. P. M.W. Hellums, W.J. Koros, *J. Memb. Sci.* **1989**, *46*, 93.

[41]   L. M. Robeson, *J. Memb. Sci.* **1991**, *62*, 165.

[42]   L. M. Robeson, *J. Memb. Sci.* **2008**, *320*, 390.

[43]   L. M. Robeson, Z. P. Smith, B. D. Freeman, D. R. Paul, *J. Memb. Sci.* **2014**, *453*, 71.

[44]   B. D. Freeman, *Macromolecules* **1999**, *32*, 375.

[45]   E. Ricci, F. M. Benedetti, M. E. Dose, M. G. De Angelis, B. D. Freeman, D. R. Paul, *To be Submitt.* **n.d.**

[46]   L. M. Robeson, M. E. Dose, B. D. Freeman, D. R. Paul, *J. Memb. Sci.* **2017**, *525*, 18.

[47]   L. C. E. Struik, *Polym. Eng. Sci.* **1977**, *17*, 165.

[48]   Y. Huang, D. R. Paul, *Polymer (Guildf).* **2004**, *45*, 8377.

[49]   Y. Huang, D. R. Paul, *Macromolecules* **2005**, *38*, 10148.

[50]   J. H. Kim, W. J. Koros, D. R. Paul, *Polymer (Guildf).* **2006**, *47*, 3094.

[51]   H. Lin, *Curr. Opin. Chem. Eng.* **2014**, *4*, 54.

[52]   A. G. McDermott, P. M. Budd, N. B. McKeown, C. M. Colina, J. Runt, *J. Mater. Chem. A* **2014**, *2*, 11742.

[53]   J. S. Chiou, J. W. Barlow, D. R. Paul, *J. Appl. Polym. Sci.* **1985**, *30*, 2633.

[54]   A. Bos, I. G. M. Pünt, M. Wessling, H. Strathmann, *J. Memb. Sci.* **1999**, *155*, 67.

[55]   S. M. Jordan, G. K. Fleming, W. J. Koros, *J. Polym. Sci. Part B Polym. Phys.* **1990**, *28*, 2305.

[56]   N. R. Horn, D. R. Paul, *Polymer (Guildf).* **2011**, *52*, 1619.

[57]   A. Bos, I. G. M. Pünt, M. Wessling, H. Strathmann, *Sep. Purif. Technol.* **1998**, *14*, 27.

[58]   N. R. Horn, D. R. Paul, *Polymer (Guildf).* **2011**, *52*, 5587.

[59]   R. R. Tiwari, Z. P. Smith, H. Lin, B. D. Freeman, D. R. Paul, *Polymer (Guildf).* **2015**, *61*, 1.

[60]   R. R. Tiwari, J. Jin, B. D. Freeman, D. R. Paul, *J. Memb. Sci.* **2017**, *537*, 362.

[61]   R. Swaidan, B. Ghanem, E. Litwiller, I. Pinnau, *Macromolecules* **2015**, *48*, 6553.

[62]   D.-Y. Peng, D. B. Robinson, *Ind. Eng. Chem. Fundam.* **1976**, *15*, 59.

11. Conclusions

During the doctoral degree at the University of Bologna, I had the chance to get involved in many projects and develop a considerable amount of new materials for gas separation applications. I worked on a wide range of activities which led to the results I summarized in this dissertation.

Mixed Matrix Membranes based on ZIF-8/PPO, Zeolite/PPO with and without surface modification were developed. A synergic effect on the transport properties was generated, and performance often increased in comparison to the pure materials. The solvent evaporation rate played an important role in the preparation of the MMMs. It was shown that developing the conditions to obtain a homogeneous dispersion of the filler was necessary to prevent the formation of non-selective cavities between the two phases which would lead to a loss in mixed-gas selectivity. As shown by SEM images, the hydrophobic metal-organic filler was more compatible than the inorganic zeolite with the organic polymer. The density and the sorption of the MMMs prepared using ZIF-8 followed the additive rule. Permeability was modeled by means of the Maxwell-Wagner-Sillar model, obtaining an accurate prediction of permeability up to 15 wt.% of filler content. It was shown that transport properties can be tuned by controlling the concentration of the filler. For ZIF-8/PPO systems helium permeability was enhanced by a factor of eight, while He/CO_2 selectivity increased up to 15% at high content of ZIF (*i.e.*, 35 wt.%), possibly due to the activation of a transport mechanism which involved percolation. This allowed the composite systems to place their separation performance close to the 2008 Robeson upper bound for some industrially relevant gas pairs (*e.g.*, He/CO_2).The energetics of permeation and diffusion, as well as the sorption enthalpy, were calculated by investigating the transport properties of MMMs as a function of the temperature between 35 °C and 65 °C. Temperature-dependent results were described with the Arrhenius and van't Hoff equations. In this framework, it was possible to extrapolate the separation performance at higher temperature, similar to that operated by industrial processes, revealing enhanced He/CO_2 separation.

The study of CO_2/CH_4 mixed-gas sorption in novel materials such as HAB-6FDA polyimide, its TR450 analogues, and PIM-EA-TB, allowed to develop a fundamental understanding of the mechanisms

regulating the separation process in more realistic conditions. It was found that the concentration of both gases decreased in the multicomponent case, but CH_4 was more affected by the presence of the more soluble gas (*i.e.*, CO_2). This led to an increase of CO_2/CH_4 solubility selectivity. By coupling mixed-gas sorption results with mixed-gas permeation data from the literature, it was determined that in the multicomponent case solubility-selectivity is responsible for most of the selective behavior of the material. This is the opposite of the pure-gas case in which diffusivity-selectivity usually controls the efficiency of the separation. This finding is remarkable in the rational design of new polymer materials. A broad collection of mixed-gas data presented in this work provides a database for the validation of the Non-Equilibrium Thermodynamics for Glassy Polymers (NET-GP) model developed by the research group in Bologna. This approach can be used to predict the multicomponent behavior of materials from the knowledge of pure-gas data only, which is also widely available in the literature.

A dedicated study of the plasticization phenomenon was carried out on Matrimid® polyimide to develop a fundamental understanding of its mechanism. It was shown that relaxation of the glassy material was not an on-off phenomenon activated when plasticization pressure was reached, rather a continuous process whose intensity increases with penetrant concentration. The data collected by varying upstream and downstream pressure shown that plasticization pressure changed with the experimental conditions. This proved that the plasticization pressure is not a state of the system. This data provides experimental evidence to validate a modeling approach to predict the dependence of the plasticization phenomenon on operating pressure and design better-performing separation processes.

A new platform of ladder polymers based on the CANAL polymerization technique, was characterized for the first time for gas separation applications. These materials feature a contorted backbone structure which prevents their efficient packing while forming a film. This provides them with higher fractional free volume if compared with traditional single-strended polymers. High internal surface area, permeability, and solubility were common elements of this family of materials. It was shown how very small changes in the alkyl substituents included in the polymer chain affected the gas transport properties. Therefore, molecular weights, chain packing as well as permeability and sorption capacity can be tuned based on the flexibility of the new designs developed. The NBC CANALs were

324

hydrocarbon-based materials that do not feature heteroatoms, providing an ideal platform for fundamental investigation of the influence of fractional free volume on transport properties and of the connectivity of the free volume elements. It was determined that CANALs show both features of dense polymers and microporous materials by correlating the activation energy of the diffusion with the enthalpy of absorption and with the kinetic diameter squared.

The panorama of microporous materials for gas separation was further extended developing and characterizing ROMP polymers. This new family of materials feature a unique architecture made of rigid side-chains connected through a flexible backbone, to form the so-called "bottlebrush" polymers. Remarkably, CF_3-ROMP revealed ultrahigh CO_2 and H_2 permeability, being behind just to PIM-TMN-trip and PTMSP. A common characteristic of ROMPs is a very high resistance to CO_2-induced plasticization. Both CF_3-ROMP and OMe-ROMP did not reach the so-called plasticization pressure up to 51 bar of CO_2, with very little hysteresis compared to other high-performing materials such as PIM-1. On the other hand, OMe-ROMP showed to be much more selective, compromising on permeability, but also showed that properties can be tuned by changing the side-chain substituents. Despite the ultrahigh permeability, physical aging revealed to be reduced for small gases such as He and H_2, in comparison to materials with similar transport properties. Efforts to increase the diffusivity-selectivity by controlling the length of the side-chains more accurately are underway.

Abbreviation List

APDEMS	3-Aminopropyl(diethoxy)methylsilane
APTMS	(3-Aminopropyl)triethoxysilane
BP	Boiling Point
CA	Cellulose Acetate
CANAL	Catalytic Arene-Norbornene Annulation
CDR	Carbon Dioxide Removal
CMS	Carbon Molecular Sieves
DCM	Dichloromethane
DMS	Dual Mode Sorption
DOE	Department of Energy
DSC	Differential Scanning Calorimetry
EOR	Enhanced Oil Recovery
EoS	Equation of State
ETAC	Ethyl Acetate
FFV	Fractional Free Volume
GGR	Greenhouse Gas Removal
GPC	Gel permeation chromatography
IEA	International Energy Agency
IGCC	Integrated-Gasification Combined Cycle
IPCC	International Panel on Climate Change
LF	Lattice Fluid
LVE	Liquid Vapor Equilibrium
MMM	Mixed Matric Membrane
NE	Non-Equilibrium
NELF	Non-Equilibrium Lattice Fluid
NET-GP	Non-Equilibrium Thermodynamics for Glassy Polymers
NG	Natural Gas
NLDFT	Nonlocal Density Functional Theory
NMR	Nuclear Magnetic Resonance
PC	Polycarbonate
PDMS	Poly(dimethylsiloxane)
PEO	Poly(ethylene oxide)

PIM	Polymers of Intrinsic Microporosity
PPO	Poly(phenylene oxide)
PSA	Pressure Swing Adsorption
PSf	Polysulfone
PTMSP	Poly(1-trimethylsilyl-1-propyne)
pVT	Pressure Volume Temperature
ROMP	Ring-Opening Metathesis Polymerization
SAXW	Small-angle X-ray scattering
TCE	1,1,2-trichloroethylene
TGA	Thermogravimetric Analysis
THF	Tetrahydrofuran
TLC	Thin Layer Chromatography
TMS	Tetramethylsilane
TSA	Temperature Swing Adsorption
UNFCCC	United Nations Framework Convention on Climate Change
WAXS	Wide-angle X-ray scattering

Acknowledgements

As much as results, data, conclusions and achievements are what make a doctoral degree an actual qualification, there is nothing as important as the people that are part of this experience and make it special. This section of the dissertation is dedicated to them.

Something that I already knew, but I learned even more throughout the process of the PhD, is that alone we can do so little. But this is not as bad or sad as it sounds. Actually, it is the opposite. It is an opportunity, because the sooner we realize it, the sooner we start to increase the odds to do something greater, to learn something more every day, and for sure, to be happier. The main result of the 75-year-old Harvard study of adult development is, quoting the director Robert Waldinger, *good relationships keep us happier and healthier. Period.* Connection to family, friends and colleagues, as well as the quality of our close relationships is what matters, eventually. I do not have many opportunities to acknowledge this to the important people of my life, but this is one of them, and I want to say that I feel beyond fortunate today, because I am surrounded by a great number of people that care about me, and I hope I am doing as much as they do to make them feel the same.

There is something else that I have learned in the past few years. If you hold tight when difficulties arise, you will always find someone who believes in you more than you believe in yourself. This gives you access to energy and resources you forgot to have, making the best out of yourself. I am grateful to all the people that were than someone when I needed it the most, even though you may not even realize it.

I also consider myself extremely lucky because over the years of my PhD, every day, and a couple of nights, I was happy to wake up and go to the lab, because I was sure to find something new to be learned, or something that I have never thought or saw before. This is a great training for a person's mind, because often one needs to use his/her imagination and come up with solutions, which really helps in every day's life. I am grateful for this curiosity than never disappeared but rather increased over the years because of the interesting projects, the stimulating questions we were asking ourselves, and most of all the wonderful people I was often working with.

The warmest thank you goes to my family, because this PhD is the product of my efforts as much as their sacrifices. It must be mentally challenging to support a son who's technically still a student when he turned in his thirties. Thank you for the life-long encouragement to pursue my dreams, whatever they were over my whole life. You never questioned them. You have been always there for me and I will never take it for granted. To mom and dad, if one day I will have children, I hope to be a parent worth at least half of what you are worth, because it would be enough anyway to give him/her the chance to be happy and achieve everything in life. To Alessandra, you are a fantastic sister and an irreplaceable friend. I am proud to have you. To my grandpa and grandma, thank you for the stability you provided the family with and for your love. To all of you, you have taught me what cannot be learned in books.

I want to acknowledge my supervisor, Professor Maria Grazia De Angelis, for providing guidance to my work and for her full support in attending a series of international conferences that helped me sharing my work and developing my presentation skills. I am particularly grateful for her support in allowing me to work with collaborators. This took me away from Bologna for extended periods of time, but this freedom allowed me to develop some research interests I was enthusiastic about and meet friends and colleagues that really shaped my research and improved my experience to a great extent.

To Professor Giulio Cesare Sarti I want to say thank you for engaging me in the field of membrane-science starting from my Master's degree, allowing me to collaborate with the group or Professors Benny Freeman and Don Paul at the University of Texas at Austin. Thank you also for your contribution to the knowledge in the field of polymer and thermodynamics, and for founding the laboratory at the University of Bologna.

With gratitude I want to thank all the colleagues and friends I made in the lab in Bologna. Our job in the lab in highly collaborative, and without each other's help in solving problems of fixing equipment, everything would be much more difficult, if not impossible. I want to thank Dr. Luca Olivieri for his mentorship related to the use and maintenance of all the equipment when I started to work in the lab. His priceless guidance was particularly appreciated because he did not have to do so, but he did it anyway. To Eleonora Ricci I want to say thank you for all the daily support in the lab, for the solid knowledge in thermodynamics and transport phenomena which she is always willing to share, and for

her close friendship. Thank you also for the deep contribution to the research presented in this dissertation. Thanks also to Dr. Davide Venturi, Dr. Eleonora Lalli, Dr. Davide Pierleoni, Dr. Elisa Pavesi, Riccardo Rea, Matilde De Pascale e Mohamed Fawzy. I also wanted to thank all the labmates in the Smith group at *MIT*, who welcomed me from day one and were always ready to help: Dr. Lucas Chi, Dr. Andy Han, Sharon Lin, Qihui Qian, Albert Wu, Patrick Asinger and Katherine Mizrahi. To all of us I would like to report here what Professor Giovanni Astarita said when he was awarded the Alpha Chi Sigma award from the American Institute of Chemical Engineers: *the most valuable products of academic research are the researchers, even more than the outcome of the research itself*. This is meaningful to me because it means that we have all the tools to contribute to find the solution to problems that impact society, environmental and so forth, and we should always bare it in mind.

Non exactly members of the research lab in Bologna but almost, as members or supporters of the *Transport Phenomena* (rock band formed by PhD students and postdoctoral associates): thanks to Dr. Andrea Nuzzo for playing Pink Floyd ad David Gilmour and for your friendship, to Dr. Claudio Carletti, and to Francesco Maluta.

I also want to acknowledge Professor Michele Galizia, who was my co-advisor when I was at UT Austin, and that greatly helped me switching from ion exchange membranes for electrodialysis to dense and mixed matrix membranes for gas separation applications. His passion for teaching and caring behavior taught me a lot, and I will always be grateful for that. Thank you also for sharing with me the speech from Professor Astarita a long time ago.

My gratitude goes also to Tanja Mueller for the great support and strength provided while writing this dissertation, also for reading though some of the chapters to catch the English mistakes my eyse could not see anymore. Thank you for your tireless help.

Always Prof. Astarita in his speech said: *If you want to be a carpenter, you can do it everywhere, but if you want to be the Pope, then you need to go to Rome*. This does not mean I need, or I want, to become "the Pope", but for sure it means that when I started chemical engineering and a PhD program, I was ready and enthusiastic about the idea that it would have took me far from home.

Davide Simone. Thank for being the best group one can dream of while studying more than ten hours a day, every day.

Thanks also to all my friends from my hometown and from my band back in Urbania, Italy, that I never have the chance to see how much I would like to.

Thanks to Beatrice e Gabriele Bellini for their help when it was time to take important decisions.

A big thank you goes to Adrian Pylypec and Robin Manougian for making me part of their family when I am in the US.

This PhD has been a lifetime journey, with beautiful moments and tough days, but for sure it would have been impossible without all of you. Thank you.